

**Magnetic monopoles in chiral magnets &  
frustrated magnetism on the  
swedenborgite lattice**

**Magnetische monopolen in chirale  
magneten &  
gefrustreerd magnetisme op het  
Swedenborgite rooster**

(met een samenvatting in het Nederlands)

**Proefschrift**

ter verkrijging van de graad van doctor aan de Universiteit Utrecht op gezag van de rector magnificus, prof.dr. G.J. van der Zwaan, ingevolge het besluit van het college voor promoties in het openbaar te verdedigen op vrijdag 20 februari 2015 des ochtends te 10.30 uur

door

**Stefan Buhrandt**

geboren op 30 oktober 1986

te Troisdorf, Duitsland

Promotoren: Prof. dr. ir. H. Stoof  
Prof. dr. A. Rosch

Copromotor: Dr. L. Fritz

This thesis was partly accomplished with financial support from the University of Cologne and the Bonn-Cologne graduate school of physics and astronomy.

**Magnetic monopoles in chiral magnets &  
frustrated magnetism on the  
swedenborgite lattice**

**Inaugural-Dissertation**

zur

Erlangung des Doktorgrades

der Mathematisch-Naturwissenschaftlichen Fakultät

der Universität zu Köln

vorgelegt von

**Stefan Buhrandt**

aus Troisdorf

2015

Berichterstatter: Prof. Dr. H. Stoof  
Prof. Dr. A. Rosch

Dr. L. Fritz

Tag der letzten mündlichen Prüfung: 20.02.2015

# Abstract

This thesis deals with magnetic order in condensed matter systems and is divided into three parts. The first part gives a closed and self-contained introduction to the Monte Carlo methods used within this thesis with a special emphasis on a recently introduced feedback optimized parallel tempering algorithm.

The second part deals with chiral magnets, i. e. magnets without inversion symmetry in their crystal structure. In these systems, weak spin-orbit coupling leads to the formation of smooth helical structures with a long periodicity. In 2009, the existence of a novel magnetic phase consisting of topological stable whirls, so-called *skyrmions*, was discovered in these materials. Due to their topological stability and the fact that they can be packed very densely, skyrmions are currently considered as promising candidates for future data storage applications. In this part of the thesis, I analyze how the topological protection of these objects is destroyed during the phase transition into another (non-topological) phase. It turns out that the underlying microscopic process is governed by the movement of monopoles of an emergent magnetic field created by the skyrmions.

The third part of this thesis deals with frustrated spin systems. In these systems with antiferromagnetic interactions, a special lattice geometry excludes the simultaneous satisfaction of all competing interactions which often results in a macroscopic ground state degeneracy. Fluctuations between these different ground states prevent the system from developing long-range order and it remains disordered at all temperatures, which is why these systems are often referred to as “spin-liquids”. Interestingly, there exists an *intrinsic* effect called “order-by-disorder”, in which this degeneracy can be lifted at least partially at finite temperatures due to entropic reasons, provided that the ground states differ in their excitation spectra.

I present the first detailed theoretical study of the recently synthesized *swedenborgite* compounds and show that these systems realize spin-liquid ground states both for the Ising and Heisenberg model. In the latter case, the order-by-disorder effect is found to result in the entropic preference of coplanar ground states at low temperatures.



# Kurzzusammenfassung

Diese Arbeit befasst sich mit der magnetischen Ordnung in Festkörpern und gliedert sich in drei Themenkomplexe. Im ersten Teil werden zunächst die verwendeten Monte Carlo Methoden ausführlich und in sich geschlossen vorgestellt, wobei der in dieser Arbeit vielfach benutzte feedback optimierte Parallel Tempering Algorithmus gesondert behandelt wird.

Der zweite Teil befasst sich mit chiralen Magneten, d. h. Magneten ohne Inversionssymmetrie in der Kristallstruktur. In diesen Systemen führt die schwache Spin-Bahn Kopplung zur Bildung von helischen Strukturen mit langer Periode. Im Jahr 2009 wurde erstmals die Existenz einer neuartigen magnetischen Phase, bestehend aus topologisch stabilen magnetischen Wirbeln, sogenannten *Skyrmionen*, in diesen Systemen nachgewiesen. Aufgrund ihrer topologischen Stabilität und der Tatsache, dass sie auf kleinstem Raum nebeneinander existieren können, werden Skyrmionen derzeit u. a. als vielversprechende Möglichkeit zur Datenspeicherung diskutiert. In diesem Teil der Arbeit untersuche ich, wie der topologische Schutz dieser Objekte beim Phasenübergang in eine andere (nicht-topologische) Phase zerstört wird. Es stellt sich dabei heraus, dass der zugrunde liegende mikroskopische Prozess durch die Bewegung von Monopolen eines emergenten, d. h. von den Skyrmion erzeugten Magnetfeldes beschrieben werden kann.

Der dritte Teile dieser Arbeit befasst sich mit frustrierten Spinsystemen. In diesen Systemen mit antiferromagnetischen Wechselwirkungen ist aufgrund der besonderen Gitterstruktur eine gleichzeitige Befriedigung aller Wechselwirkungen nicht möglich, was oftmals in einem makroskopisch entarteten Grundzustand resultiert. Fluktuationen zwischen diesen Grundzuständen verhindern die Ausbildung von langreichweitiger Ordnung bei allen Temperaturen, weshalb diese Systeme häufig auch als "Spin-Flüssigkeit" bezeichnet werden. Die Entartung des Grundzustands kann durch einen als "Ordnung-durch-Unordnung" bekannten, *intrinsischen* Effekt teilweise wieder aufgehoben werden, vorausgesetzt, dass die Grundzustände sich in ihren Anregungsspektren unterscheiden.

In diesem Kontext präsentiere ich die erste systematische Studie der erst kürzlich synthetisch hergestellten *Schwedenborgit* Verbindungen und zeige, dass der Grundzustand dieser Systeme sowohl für das Ising-, als auch das Heisenberg-Modell Spin-Flüssigkeitsverhalten aufweist. Darüber hinaus zeige ich, dass der Ordnung-durch-Unordnung Effekt im Heisenberg-Modell auftritt und zur entropischen Bevorzugung von koplanaren Grundzuständen bei tiefen Temperaturen führt.





# Samenvatting

In dit proefschrift wordt in drie delen de magnetische ordering behandeld zoals deze in vaste stoffen voorkomt.

In het eerste deel wordt een op zichzelf staande introductie over de Monte Carlo simulatiemethoden gegeven. De nadruk zal worden gelegd op de recent in zwang geraakte methode van feedback optimized parallel tempering algoritmes.

Deel twee van dit proefschrift is gewijd aan chirale magneten. Chirale magneten bezitten geen inversie-symmetrie in hun kristalijne structuur. In dit type systemen leidt zwakke spin-baankoppeling tot de formatie van gladde helische structuren met een langdurige periodiciteit.

In 2009 werd het bestaan van een nieuwe magnetische fase, bestaand uit topologisch-stabiele wervelingen, ontdekt in deze materialen. Deze wervelingen noemt men skyrmionen. Door hun topologische stabiliteit en het feit dat ze zeer dicht opeengestapeld kunnen worden, worden materialen met deze fase gezien als veelbelovend voor digitale data opslag. Dit gedeelte van het proefschrift gaat tevens in op de opheffing van de topologische bescherming van de skyrmionen gedurende de faseovergang naar een andere fase. Het blijkt dat de onderliggende microscopische processen worden gedomineerd door de beweging van monopolen van een opkomend magnetisch veld, opgewekt door de skyrmionen.

In het derde en laatste deel van dit proefschrift worden anti-ferromagnetisch gefrustreerde spinsystemen beschouwd. In deze systemen verbiedt de specifieke geometrie van het rooster elke afzonderlijke spin te voldoen aan de optimale configuratie. Dit resulteert (doorgaans) in de ontaarding van een macroscopische grondtoestand. Fluctuaties tussen deze verschillende grondtoestanden voorkomen dat het systeem geordend raakt op grote lengteschalen. Op grote lengteschalen blijft zo'n systeem wanordelijk bij elke temperatuur. Dit is de reden dat men naar dit soort materialen refereert als spinvloeistoffen.

Er bestaat een intrinsiek effect dat orde-door-wanorde heet, waarbij de ontaarding (deels) wordt opgeheven bij eindige temperaturen. Dit effect is gestoeld op entropische redenen en de voorwaarde dat de grondtoestanden verschillen in hun excitatiespectrum.

Ik verschaf de eerste gedetailleerde theoretische studie van de recentelijk gesynthetiseerde zvedenborgiet-verbindingen en toon aan dat deze systemen spinvloeistofgrondtoestanden toelaten, voor zowel het Ising- en Heisenbergmodel. In het laatstgenoemde geval blijkt bij lage temperaturen het orde-door-wanorde-effect te resulteren in de entropisch gunstigere configuratie van co-planaire grondtoestanden.



# Publications

This thesis is based on the following publications:

- **S. Buhrandt** und L. Fritz, “Skyrmion lattice phase in three-dimensional chiral magnets from Monte Carlo simulations”, *Phys. Rev. B* **88**, 195137 (2013).
- P. Milde, D. Köhler, J. Seidel, L. M. Eng, A. Bauer, A. Chacon, J. Kinder-vater, S. Mühlbauer, C. Pfleiderer, **S. Buhrandt**, C. Schütte und A. Rosch, “Unwinding of a Skyrmion Lattice by Magnetic Monopoles”, *Science* **340**, 1076 (2013).
- **S. Buhrandt** und L. Fritz, “Spin-liquid phase and order by disorder of classical Heisenberg spins on the swedenborgite lattice”, *Phys. Rev. B* **90**, 020403(R) (2014).
- **S. Buhrandt** und L. Fritz, “Antiferromagnetic Ising model on the swedenborgite lattice”, *Phys. Rev. B* **90**, 094415 (2014).



# Contents

<b>Abstract / Kurzzusammenfassung / Samenvatting</b>	<b>v</b>
<b>Publications</b>	<b>xi</b>
<b>I. Monte Carlo methods for classical spin systems</b>	<b>1</b>
<b>1. Introduction</b>	<b>3</b>
1.1. The Metropolis algorithm . . . . .	4
1.2. Equilibration and auto-correlation times . . . . .	8
1.3. Determination of statistical errors . . . . .	9
1.4. Determination of critical exponents . . . . .	10
1.5. Implementation of Monte Carlo algorithms for continuous spin variables . . . . .	13
<b>2. Advanced Monte Carlo techniques</b>	<b>17</b>
2.1. Shortcomings of simple Monte Carlo algorithms . . . . .	17
2.2. Parallel tempering Monte Carlo . . . . .	19
2.3. Optimal choice of temperature points . . . . .	21
2.4. Other Monte Carlo techniques . . . . .	28
<b>II. Magnetic monopoles in chiral magnets</b>	<b>31</b>
<b>3. Introduction</b>	<b>33</b>
3.1. Chiral magnets . . . . .	34
3.2. Discovery of the skyrmion lattice . . . . .	37
3.3. Topological properties of the skyrmion lattice . . . . .	40
<b>4. Stabilization of the skyrmion lattice by thermal fluctuations</b>	<b>43</b>
4.1. Mean field theory for chiral magnets . . . . .	43
4.2. Thermal fluctuations in gaussian approximation . . . . .	49

<b>5. Phase diagram and thermodynamics from Monte Carlo simulations</b>	<b>53</b>
5.1. Numerical implementation and discretization of the continuum model . . . . .	53
5.2. Thermodynamic quantities . . . . .	57
5.3. Determination of the phase boundaries . . . . .	65
5.4. Structure factors . . . . .	70
<b>6. Emergent electrodynamics and magnetic monopoles</b>	<b>73</b>
6.1. Emergent electric and magnetic fields . . . . .	73
6.2. Topological Hall effect . . . . .	76
6.3. Experimental observation of the unwinding of a skyrmion lattice .	78
6.4. Emergent magnetic monopoles . . . . .	83
6.5. Conclusion and Outlook . . . . .	91
<b>III. Spin-liquid phase and order-by-disorder on the swedenborgite lattice</b>	<b>93</b>
<b>7. Introduction</b>	<b>95</b>
7.1. Magnetic frustration . . . . .	96
7.2. Ground state degeneracy . . . . .	98
7.3. Order-by-disorder . . . . .	101
7.4. Order-by-disorder on the kagome lattice . . . . .	104
7.5. Coulomb-phases . . . . .	110
<b>8. Swedenborgites</b>	<b>117</b>
8.1. Lattice structure and model . . . . .	117
8.2. Experiments and verification of the model . . . . .	120
<b>9. Classical Ising model on the swedenborgite lattice</b>	<b>123</b>
9.1. Residual entropy . . . . .	123
9.2. Ground state degeneracy and phase diagram for $B = 0$ . . . . .	124
9.3. Suppression of the crossover temperature for $J_2 \approx J_1$ . . . . .	128
9.4. Structure factors and correlations . . . . .	130
9.5. Ground state degeneracy and phase diagram for $B \neq 0$ . . . . .	136
<b>10. Classical Heisenberg model on the swedenborgite lattice</b>	<b>141</b>
10.1. Ground state degeneracy . . . . .	141
10.2. Nematic order parameter and order-by-disorder transition . . . . .	146
10.3. Spin-wave analysis . . . . .	152
10.4. Specific heat . . . . .	161

10.5. Phase diagram . . . . .	164
10.6. Structure factors and correlations . . . . .	167
10.7. Conclusion and experimental verification . . . . .	171
<b>IV. Appendices</b>	<b>175</b>
<b>A. Matrix elements for the spin-wave calculation</b>	<b>177</b>
<b>Bibliography</b>	<b>181</b>
<b>Statement of authorship/ Selbstständigkeitserklärung</b>	<b>191</b>
<b>Curriculum vitae</b>	<b>193</b>





Part I.

Monte Carlo methods for  
classical spin systems



# 1. Introduction

The thermodynamical properties of classical spin models can be determined analytically only in very rare cases. The probably most simple spin model is the nearest-neighbor Ising model

$$H = J \sum_{\langle ij \rangle} \sigma_i \sigma_j - B \sum_i \sigma_i, \quad (1.0.1)$$

where  $J$  is the ferromagnetic ( $J < 0$ ) or antiferromagnetic ( $J > 0$ ) coupling between two neighboring spins and the sum runs over all pairs of nearest-neighbors.  $B$  is an external magnetic field and each spin is represented by a variable  $\sigma$  which can only take the values  $\pm 1$ , representing “spin-up” and “spin-down” states. While this model is rather simple, it has only been solved analytically in one [1] and (for vanishing magnetic field) in two dimensions [2]. The problem that arises in the analysis of the Ising model is the large number of possible configurations  $s = \{\sigma_1, \sigma_2, \dots, \sigma_N\}$  that contribute to the calculation of the partition function

$$Z = \sum_{\sigma_1=\pm 1} \sum_{\sigma_2=\pm 1} \dots \sum_{\sigma_N=\pm 1} \exp(-H(s)/T). \quad (1.0.2)$$

On a lattice with  $N$  sites and two possible spin orientations (“up” and “down”) on each site, there are  $2^N$  states in total. In principle, one could simply sum up all these states in Eq. (1.0.2), but in practice, this is even numerically not possible for moderate system sizes (not to mention system sizes sufficiently close to the thermodynamic limit) due to the exponential growth of the phase space with system size. The general case of spins with continuous  $O(n)$  symmetry, like the XY- ( $n = 2$ ) or Heisenberg ( $n = 3$ ) model, has an even larger phase space and one thus needs efficient numerical simulation techniques to calculate all quantities of interest for these systems.

The probably most important technique, which is introduced in this part of the thesis, is importance sampling Monte Carlo (MC): Instead of taking into account *all* states in the calculation of expectation values etc., one uses only those states which have a significant statistical weight  $p \propto \exp(-H/T)$  at a given temperature. The heart of every Monte Carlo algorithm is the generation of these states in a Markov chain by using random numbers, hence the name “Monte Carlo”. While it is often the only applicable technique, it has also gained importance in

the last years due to ongoing advances in computer technologies which allow the treatment of very large model systems.

In this chapter, I closely follow Ref. 3 and give a full and self-contained introduction to fundamental Monte Carlo techniques for classical spin systems, starting with an introduction to the Metropolis algorithm in Sec. 1.1. The problem of thermal equilibration and auto-correlation times is addressed in Sec. 1.2, followed by a discussion of statistical errors and their origin in Sec. 1.3. In Sec. 1.4, it is shown how critical exponents can be determined by the means of finite-size scaling. Finally, this chapter closes with a discussion of the implementation of Monte Carlo methods for continuous spin-variables from a numerical point of view in Sec. 1.5. Ch. 2 deals with advanced Monte Carlo techniques and gives a detailed introduction to the feedback optimized parallel tempering algorithm that is used throughout this thesis.

## 1.1. The Metropolis algorithm

The calculation of expectation values is one of the main goals in statistical mechanics. For an observable  $O$ , the expectation value is defined as

$$\langle O \rangle = \frac{\sum_{\{s\}} O(s) \exp(-H(s)/T)}{\sum_{\{s\}} \exp(-H(s)/T)}, \quad (1.1.3)$$

where  $H$  is the Hamiltonian,  $T$  the temperature and the sum runs over all states  $s$  of the system. As mentioned in the introduction, the phase space grows exponentially with system size and it is impossible to take all states into account in Eq. (1.1.3).

However, one does not need to consider all possible states of a system since most of them will have an almost vanishing statistical weight, e. g. at very low temperatures, only states close to the ground state of the system will be occupied and contribute to the sum in Eq. (1.1.3). One therefore needs a method to generate states according to the Boltzmann distribution  $p(s) = \exp(-H(s)/T)/Z$ . An easy way of generating such an ensemble of states has been proposed by Metropolis [4] and later generalized by Hastings [5]. The idea behind their algorithm is to generate a Markov chain  $s_1 \rightarrow s_2 \rightarrow s_3 \rightarrow \dots$  of successive states, where the next state in the chain is chosen with a transition probability  $P(s_i \rightarrow s_{i+1})$  such that it occurs with a probability given by the Boltzmann distribution. The probability  $p_{i+1}(s)$  that the state  $s$  occurs at timestep  $(i+1)$  in the chain is

$$p_{i+1}(s) = p_i(s) + \sum_{s'} [p_i(s')P(s' \rightarrow s) - p_i(s)P(s \rightarrow s')], \quad (1.1.4)$$

where the sum is taken over all states  $s'$  of the system. The first term in the sum describes all transitions *reaching* state  $s$ , whereas the second term describes all states *leaving* state  $s$ . In the limit  $i \rightarrow \infty$ , the probability distribution  $p_i(s)$  should be stationary and coincide with the Boltzmann distribution. The stationarity condition demands that the probability that the state  $s$  occurs must be independent from the position in the chain, i. e.  $p_{i+1}(s) = p_i(s)$ , and one can rearrange Eq. (1.1.4) to obtain the *balance condition*

$$\sum_{s'} p(s')P(s' \rightarrow s) = \sum_{s'} p(s)P(s \rightarrow s'), \quad (1.1.5)$$

Using the constraint  $\sum_{s'} P(s \rightarrow s') = 1$  on the transition probabilities yields

$$p_i(s) = \sum_{s'} p_i(s')P(s' \rightarrow s), \quad (1.1.6)$$

which can be inserted in Eq. (1.1.4) again to obtain

$$p_{i+1}(s) = \sum_{s'} p_i(s')P(s' \rightarrow s). \quad (1.1.7)$$

If the Markov chain reaches a simple equilibrium state  $s$  as  $i \rightarrow \infty$ , this state has to satisfy

$$p_\infty(s) = \sum_{s'} p_\infty(s')P(s' \rightarrow s). \quad (1.1.8)$$

It is however also possible that the Markov chain reaches a *dynamic* equilibrium state in which the probability distribution repeats periodically in a cycle of length  $n$ , i. e.

$$p_\infty(s) = \sum_{s_{n-1}} P(s_{n-1} \rightarrow s) \dots \sum_{s_1} P(s_1 \rightarrow s_2) \sum_{s_0} P(s_0 \rightarrow s_1) p_\infty(s_0). \quad (1.1.9)$$

To exclude this undesired behavior, one can impose the *detailed balance* condition

$$p(s')P(s' \rightarrow s) = p(s)P(s \rightarrow s'), \quad (1.1.10)$$

which is a stronger constraint than Eq. (1.1.5). It demands that the system should go as often from state  $s$  to  $s'$  as it goes from  $s'$  to  $s$ . In a limit cycle as in Eq. (1.1.9), there must be states for which this condition is violated at any particular step in the Markov chain: In order for the occupation probability of a particular state to increase, there must be more transitions into that state than out of it. Imposing the detailed balance condition forbids any dynamics of that kind and hence ensures that no limit cycles occur.

## 1. Introduction

---

By inserting the equilibrium distribution  $p(s) = \exp(-H(s)/T)$  into Eq. (1.1.10), one finds the following condition for transition probabilities:

$$\begin{aligned} \frac{P(s \rightarrow s')}{P(s' \rightarrow s)} &= \frac{p(s')}{p(s)} \\ &= \exp(-(H(s') - H(s))/T) \\ &= \exp(-\Delta H(s, s')/T). \end{aligned} \tag{1.1.11}$$

There are several different choices for the transition probabilities that fulfill Eq. (1.1.11). Metropolis and Hastings suggested to choose

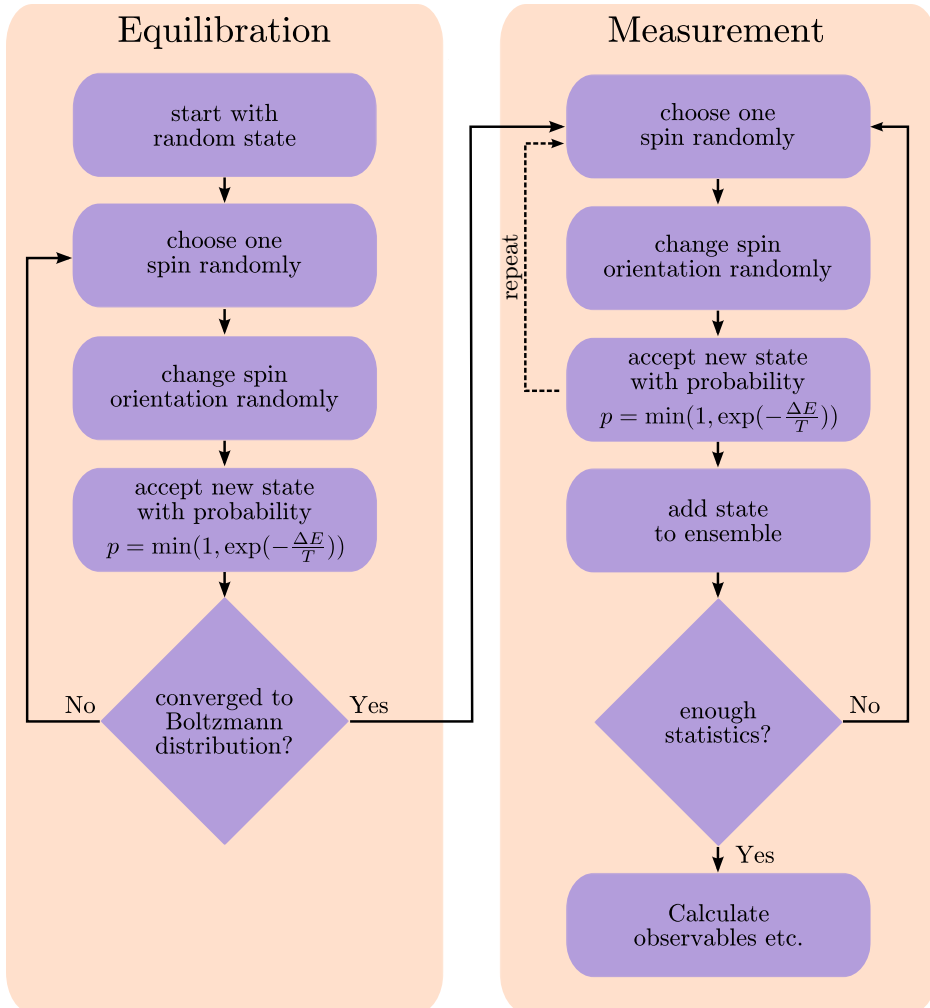
$$\begin{aligned} P(s \rightarrow s') &= \min(1, \exp(-\Delta E(s, s')/T)) \\ &= \begin{cases} 1 & \text{if } \Delta E(s, s') \leq 0 \\ \exp(-\Delta E(s, s')/T) & \text{if } \Delta E(s, s') > 0 \end{cases}. \end{aligned} \tag{1.1.12}$$

The move connecting the different states in the Markov chain can, in principle, be arbitrary. If the energy change associated with that move is too large, the probability that the move is accepted will be small. Hence, one often tries to change only the direction of a single spin at every step in the Markov-chain. These update schemes are often referred to as “single-site updates”.

After a certain number of time steps  $\tau_{\text{eq}}$  (also called equilibration time, c.f. Sec. 1.2), the states in the Markov chain will follow the Boltzmann-distribution and one can use the henceforth generated states to calculate observables, etc. Assuming that one takes  $N$  measurements of an observable  $O$  using the states  $s_i$ , the expectation value for this observable is approximately given by the mean value

$$\langle O \rangle \approx \sum_{i=1}^N O(s_i). \tag{1.1.13}$$

The statistical error of this approximation will be discussed in Sec. 1.3. Fig. 1.1.1 shows a schematic of the complete algorithm using a single-site update.



**Figure 1.1.1.:** Schematic illustration of the Metropolis-Hastings algorithm for the generation of an ensemble of states that are distributed according to the Boltzmann distribution. Typically, one tries to change the direction of every spin on the lattice instead of just a single spin before a state is added to the ensemble.

## 1.2. Equilibration and auto-correlation times

Since new states in a Markov chain are generated by modifications of a previous state, successive states are usually strongly correlated. If one starts the Markov chain with a random state, one has to wait a certain number of time steps, the equilibration time  $\tau_{\text{eq}}$ , until the states in the Markov chain indeed follow the Boltzmann distribution. Equilibration times can be measured simply by analyzing the time development of an observable: After  $\tau_{\text{eq}}$ , when equilibrium is reached, the value of the observable will only fluctuate around a well defined mean value which is constant in time. In general, equilibration times can be different for different observables, e.g. the energy usually equilibrates faster than other quantities such as the magnetization, and hence the equilibration times of *all* observables have to be taken into account.

The correlation of states in a Markov chain also affects the measurement of expectation values, etc. once equilibrium is reached. If two successive states are correlated, they do not yield two *independent* measurements of an observable and it will be shown in Sec. 1.3 that this influences the quality of the estimate of an expectation value by Eq. (1.1.13). The correlation of an observable  $O$  in a Markov chain is described by the so-called auto-correlation function

$$\begin{aligned}\chi(t) &= \int dt' [O(t') - \langle O \rangle][O(t'+t) - \langle O \rangle] \\ &= \int dt' [O(t')O(t'+t) - \langle O \rangle^2],\end{aligned}\tag{1.2.14}$$

where  $O(t)$  is the instantaneous value of the observable  $O$  at time  $t$  and  $\langle O \rangle$  is the average value. In a Monte Carlo simulation, one performs evenly spaced measurements up to some time  $t_{\text{max}}$  and one thus needs the discretized version of Eq. (1.2.14), which is given by [3]

$$\begin{aligned}\chi(t) &= \frac{1}{t_{\text{max}} - t} \sum_{t'=0}^{t_{\text{max}}-t} O(t')O(t'+t) \\ &\quad - \frac{1}{t_{\text{max}} - t} \sum_{t'=0}^{t_{\text{max}}-t} O(t') \times \frac{1}{t_{\text{max}} - t} \sum_{t'=0}^{t_{\text{max}}-t} O(t'+t).\end{aligned}\tag{1.2.15}$$

In general, the auto-correlation function behaves as  $\chi \propto \exp(-t/\tau)$ , where  $\tau$  is the auto-correlation time that defines the time one has to wait between two measurements until the correlations to have decreased by a factor of  $1/e$ . As it will be shown in the next section, it is possible (and desirable) to take measurements after times  $\Delta t$  which are smaller than the auto-correlation time  $\tau$ , and to account for this later in the calculation of statistical errors.



### 1.3. Determination of statistical errors

Since only a finite number of states is used in Eq. (1.1.13) for the approximation of expectation values, it is very important to know the statistical error of the calculated values. For most observables, this error is simply the error of the mean value,

$$\Delta O = \sqrt{\frac{\langle O^2 \rangle - \langle O \rangle^2}{N}}. \quad (1.3.16)$$

This expression assumes that all  $N$  measurements are statistically independent, which they might not be, if the measurements were recorded in time intervals  $\Delta t$  smaller than the correlation time  $\tau$ . It can be shown [3] that the correct expression in this case is

$$\Delta O = \sqrt{\frac{(1 + 2\tau/\Delta t)}{N} (\langle O^2 \rangle - \langle O \rangle^2)}. \quad (1.3.17)$$

For  $\Delta t \rightarrow \infty$ , this expression reduces again to Eq. (1.3.16), whereas for  $\Delta t \ll \tau$  one can ignore the 1 in the numerator and replace  $N = t_{\max}/\Delta t$  to obtain

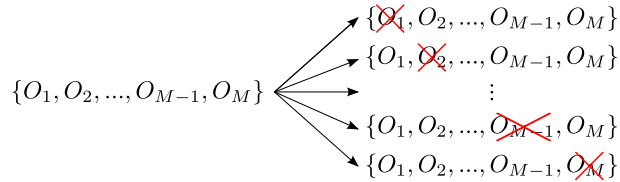
$$\Delta O = \sqrt{\frac{2\tau}{t_{\max}} (\langle O^2 \rangle - \langle O \rangle^2)}. \quad (1.3.18)$$

Since the error decreases as  $1/\sqrt{N}$ , one needs four times as many measurements in order to reduce the error by a factor of two.

There are other quantities for which the determination of the statistical error is not that simple, namely quantities which are directly calculated from the fluctuations, i. e. the variance, of an observable. The most important example is the specific heat  $c_V$ ,

$$c_V = \frac{\partial \langle H \rangle}{\partial T} = \frac{\partial}{\partial T} \frac{\sum_s H(s) \exp(-H(s)/T)}{\sum_s \exp(-H(s)/T)} = \frac{\langle H^2 \rangle - \langle H \rangle^2}{T^2}. \quad (1.3.19)$$

In order to calculate the statistical error of a quantity like this, one has to know the standard error of the variance, which is determined by the quality of the sample. The quality of a sample can be determined e. g. by statistical resampling of the available data, i. e. by analyzing different subsets of the sample. A very systematic and reproducible way to do this is the *jackknife method*: From an original sample of  $M$  independent measurements, one builds  $M$  new samples, each containing  $M - 1$  measurements, by neglecting the  $i^{\text{th}}$  measurement of the original sample in the construction of the  $i^{\text{th}}$  new sample, c. f. Fig. 1.3.2. These new samples can be used to calculate  $M - 1$  estimates for the variance, which on



**Figure 1.3.2.:** Illustration of the jackknife resampling method: From an original sample containing  $M$  measurements,  $M$  new samples, each containing  $M - 1$  measurements, are constructed by omitting one of the original measurements.

the other hand, can be used to estimate the standard error of the variance as

$$\Delta \text{Var}(O) = \sqrt{\frac{M-1}{M} \sum_{i=1}^{M-1} \left( \text{Var}(O)_i - \text{Var}(O) \right)^2}, \quad (1.3.20)$$

where  $\text{Var}(O)_i$  is the variance that has been calculated from the set with the  $i^{\text{th}}$  measurement left out. Other resampling approaches like *bootstrapping* generate new samples by randomly picking single measurements from the original one and allow the same measurement to be picked multiple times, which has the advantage that the original measurements do not need to be statistically independent [3]. Usually, already a couple of hundred resamplings give a very good estimate of the error [3], which makes bootstrapping the method of choice for simulations with a lot of measurements, where a full jackknife resampling is very elaborate.

## 1.4. Determination of critical exponents

If a system is close to a continuous phase transition, its behavior is governed by strong fluctuations on large length scales. This excludes the treatment of such critical systems by means of simple mean-field approximations which do not incorporate these fluctuations. Unfortunately, most of the interesting physics happens precisely in the critical region around a phase transition; the formation of a macroscopic magnetic moment at the Curie point in a ferromagnet, or critical opalescence, which causes large fluctuations in the refractive index of mixtures of certain liquids, are just two examples. It is thus desirable to use methods that can account for fluctuations in order to allow a description of these critical phenomena.

Another important aspect of phase transitions is the concept of *universality*. Close to a phase transition, many measurable properties of physical systems become independent of the microscopic parameters of the underlying model. For

classical spin systems with nearest neighbor interactions for instance, the interaction energy  $J$  between the spins does not influence the critical behavior. Only fairly gross properties like the dimensionality of the lattice, the range of the interactions and the broken symmetry enter [3]. This implies that phase transitions fall into a number of discrete *universality classes*. For instance, the phase transitions of a vapor/liquid system at its tricritical point and of the Ising model are, although describing two completely different systems, believed to fall into the same universality class and show remarkable similarities in the critical region.

Monte Carlo methods naturally incorporate fluctuations and can therefore be applied to systems close to a phase transition, but unfortunately it is exactly this region in which many algorithms suffer from critical slowing down, c. f. Sec. 2.1.

The most important quantities associated with a phase transition are the so-called critical exponents, which describe how thermodynamic quantities diverge as the phase transition is approached by lowering the reduced temperature  $t = (T - T_c)/T_c$  to 0. From the concept of universality, it follows that two systems within the same universality class also have the same critical exponents. The most important ones are

$$c_V \propto |t|^{-\alpha} \quad (\text{specific heat}) \quad (1.4.21)$$

$$\Psi \propto |t|^\beta \quad (\text{order parameter}) \quad (1.4.22)$$

$$\chi \propto |t|^{-\gamma} \quad (\text{order parameter susceptibility}) \quad (1.4.23)$$

$$\xi \propto |t|^{-\nu} \quad (\text{correlation length}) \quad (1.4.24)$$

Exactly at  $T = T_c$ , one further defines  $\delta$  and  $\nu$  according to

$$J \propto \Psi^\delta \quad (\text{source field}), \quad (1.4.25)$$

$$\langle \Psi(0)\Psi(r) \rangle \propto r^{-d+2-\eta} \quad (\text{decay of spatial corr. functions}), \quad (1.4.26)$$

where the source field  $J$  is given e. g. by the magnetic field in the case of a ferromagnet.

Only two of the critical exponents are independent, the others follow from the scaling relations

$$\begin{aligned} \nu d = 2 - \alpha = 2\beta + \gamma = \beta(\delta + 1) &= \gamma \frac{\delta + 1}{\delta - 1}, \\ 2 - \eta = \frac{\gamma}{\nu} &= d \frac{\delta - 1}{\delta + 1}, \end{aligned} \quad (1.4.27)$$

where  $d$  is the spatial dimension. Table 1.4.1 shows the critical exponents for various spin models with short ranged interactions.

The calculation of these exponents is a major challenge in every Monte Carlo

## 1. Introduction

---

	$\alpha$	$\beta$	$\gamma$	$\delta$	$\nu$	$\eta$
2d Ising	log	1/8	7/4	15	1	1/4
3d Ising	0.11	0.325	1.24	4.82	0.63	0.33
3d Heisenberg	?	0.365	1.39	4.80	0.705	0.034

**Table 1.4.1.:** Critical exponents for several models with short ranged interactions. The values for the 2d Ising model can be determined analytically, whereas other models require numerical calculations. The entry “log” represents a logarithmic divergence. Values taken from Ref. 6.

simulation. Since simulations are always carried out on finite systems, one will never observe a true phase transition since the correlation length is always limited by the system size and can never truly diverge. Instead, true thermodynamic singularities appear smoothly rounded in all simulations with a peak height that grows with system size. It is nevertheless possible to perform simulations for different lattice sizes and to extrapolate to the thermodynamic limit.

In the following, I illustrate the method of finite size scaling in some detail for the susceptibility following Ref. 3 and state the results for the other exponents at the end. One begins by expressing the susceptibility in terms of the correlation length. Eliminating the reduced temperature from Eq. (1.4.23) using Eq. (1.4.24), one obtains

$$\chi \propto \xi^{\gamma/\nu}. \quad (1.4.28)$$

In a system of finite (linear) size  $L$ , the correlation length is cut off as it approaches the system size. This can be accounted for mathematically by writing

$$\chi = \xi^{\gamma/\nu} \chi_0(L/\xi), \quad (1.4.29)$$

where the dimensionless scaling function  $\chi_0(x)$ , which behaves as

$$\chi_0(x) = \begin{cases} \text{const.} & x \gg 1 \\ \propto x^{\gamma/\nu} & x \rightarrow 0 \end{cases}, \quad (1.4.30)$$

has been introduced. The precise way in which the susceptibility is cut off close to the phase transition is completely contained in functional form of  $\chi_0$ . It is convention (and convenient) to introduce a further dimensionless function

$$\tilde{\chi}(x) = x^{-\gamma} \chi_0(x^\nu) \quad (1.4.31)$$

and express everything in terms of this function only. Using Eq. (1.4.24) once again and extending the above discussion to negative values of  $t$ , one finally obtains

$$\chi = L^{\gamma/\nu} \tilde{\chi}(L^{1/\nu} t). \quad (1.4.32)$$

This equation provides the backbone of the finite size scaling method: If one calculates the susceptibility for different lattice sizes and plots  $L^{-\gamma/\nu}\chi$  against  $L^{1/\nu}t$ , all curves should collapse on exactly one curve whose functional form is given by  $\tilde{\chi}$ , provided that one uses the *correct* values for the critical exponents and the critical temperature. Algorithms for the corresponding fitting procedure of these quantities are available, see e. g. Ref. 7.

The scaling relations for the other thermodynamic quantities can be derived in the same way and read [3]

$$c_V = L^{\alpha/\nu} \tilde{c}_V(L^{1/\nu}t), \quad (1.4.33)$$

$$\Psi = L^{-\beta/\nu} \tilde{\Psi}(L^{1/\nu}t). \quad (1.4.34)$$

The determination of the critical exponents with this method is in general very accurate if sufficient data for different lattice sizes is available. Usually, this method works better for larger exponents since the corresponding thermodynamic quantities depend more strongly on the lattice size.

Problems in the determination of the critical exponents can arise if the interactions possess a spatial anisotropy, e. g. if there are two distinct nearest-neighbor interactions for spins within the same and in adjacent planes,

$$H = J_{xy} \sum_{\substack{\langle i,j \rangle \in \\ \text{same plane}}} \mathbf{S}_i \cdot \mathbf{S}_j + J_z \sum_{\substack{\langle i,j \rangle \in \\ \text{diff. plane}}} \mathbf{S}_i \cdot \mathbf{S}_j. \quad (1.4.35)$$

This results in an anisotropic increase of the correlation lengths as the critical point is approached, and consequently, the finite size scaling method breaks down and cannot be applied in this case.

## 1.5. Implementation of Monte Carlo algorithms for continuous spin variables

**Spin update for  $O(3)$  spins** The numerical simulation of spin systems with continuous spin variables such as the XY-model or the Heisenberg model with  $O(2)$  and  $O(3)$  spins, respectively, is much more elaborate than the simulation of Ising-like spin variables due to their continuous degrees of freedom. This becomes evident by examining the spin update used in the Markov chain. A new configuration for an  $O(3)$  spin is in general proposed by evaluating two random numbers  $\varphi \in [0, 2\pi]$  and  $c = \cos(\theta) \in [-1, 1]$  and assigning the updated position

$$\mathbf{S}(\varphi, c) = \begin{pmatrix} \sqrt{1-c^2} \cos \varphi \\ \sqrt{1-c^2} \sin \varphi \\ c \end{pmatrix} \quad (1.5.36)$$

to the spin. Note that it is not possible to simply evaluate two evenly distributed angles  $\theta$  and  $\phi$  and assign a new position as

$$\mathbf{S}(\theta, \varphi) = \begin{pmatrix} \sin \theta \cos \varphi \\ \sin \theta \sin \varphi \\ \cos \theta \end{pmatrix} \quad (1.5.37)$$

since the configurations obtained by this update are not uniformly distributed over the unit-sphere. The update in Eq. (1.5.36) requires not only the construction of two random numbers, but also the evaluation of angular functions and square-roots and is hence numerically demanding when it is performed very often. If a simulation is carried out at sufficiently low temperatures, the probability that a proposed configuration is accepted, will drop exponentially as

$$p_{\text{accept}} \propto \exp\left(-\frac{\Delta E}{T}\right), \quad (1.5.38)$$

where  $\Delta E > 0$  is the energy difference between the old and new configuration. Most of the proposed updates will thus be rejected and the algorithm becomes inefficient. It is therefore desirable, to use a spin-update algorithm which changes the energy of a configuration only by a certain amount such that the acceptance rates do not drop below a certain threshold. This can be achieved according to Ref. 8 by tilting the spin only by some angle  $\delta$  out of its original position. Starting from an arbitrary spin direction  $\mathbf{S} = (S_x, S_y, S_z)^T$ , one can rotate this spin by the angle  $\alpha = \arccos(s^z)$  around the axis defined by

$$\hat{\mathbf{n}} = \frac{\mathbf{S} \times \hat{\mathbf{z}}}{\|\mathbf{S} \times \hat{\mathbf{z}}\|} \quad (1.5.39)$$

to align it parallel to the z-axis. Afterwards, one uses Eq. (1.5.36) to update the spin position with  $c$  not chosen randomly in  $[-1, 1]$  anymore, but in  $[c_{\min}, 1]$  with  $-1 \leq c_{\min} < 1$ . This restricts the new spin to lie in a spherical cap with opening angle  $\delta = \arccos(c_{\min})$  centered around the z-axis. At the end, the spin is rotated back into its original frame by an rotation around  $\hat{\mathbf{n}}$  by the angle  $-\alpha$ . The coordinates of the updated spin  $\mathbf{S}^{\text{new}}$  can be expressed in terms of the coordinates of the old spin  $\mathbf{S}^{\text{old}} = (S^x, S^y, S^z)^T$  as

$$\mathbf{S}^{\text{new}} = \begin{pmatrix} \frac{\sqrt{1-c^2}}{(S^x)^2+(S^y)^2} \left( [(S^x)^2 S^z + (S^y)^2] \cos \delta + (S^z - 1) S^x S^y \sin \delta \right) + c S^x \\ \frac{\sqrt{1-c^2}}{(S^x)^2+(S^y)^2} \left( (S^z - 1) S^x S^y \cos \delta + [(S^x)^2 + (S^y)^2 S^z] \sin \delta \right) + c S^y \\ -\sqrt{1-c^2} (S^x \cos \delta + S^y \sin \delta) + c S^z \end{pmatrix}. \quad (1.5.40)$$

A very intuitive method to determine the optimal value for  $c_{\min}$  iteratively is to measure the acceptance rate and to increase or decrease  $c_{\min}$ , depending on

whether the acceptance rate is lower or higher than the desired acceptance ratio. Empirically, acceptance rates of 50 – 70% have been found to be optimal. Note that the determination of  $c_{\min}$  should take place before one records measurements (e. g. during the thermalization process) since varying its value breaks detailed balance.

**Over-relaxation** A powerful and easy to implement method to reduce auto-correlation times is the over-relaxation method, which exploits symmetries of the Hamiltonian to create rejection free updates. For instance, each spin  $\mathbf{S}_i$  on the lattice can be rotated by an arbitrary angle around the effective field

$$\mathbf{H}_i^{\text{eff}} = \sum_j J_{ij} \mathbf{S}_j \quad (1.5.41)$$

without energy cost. By choosing a rotation by  $\pi$  around the local field,

$$\mathbf{S}_i \rightarrow -\mathbf{S}_i + 2 \frac{(\mathbf{S}_i \cdot \mathbf{H}_i^{\text{eff}})}{\|\mathbf{H}_i^{\text{eff}}\|^2} \mathbf{H}_i^{\text{eff}}, \quad (1.5.42)$$

one can change the spin configuration as much as possible to accelerate decorrelation. One should note that this update is non-ergodic since the energy does not change during the update. To restore ergodicity, it has to be combined with other methods, such as the single-site spin update discussed at the beginning of this section. Used together, these methods can reduce the auto-correlation time significantly compared to the random reorientation of single spins alone.





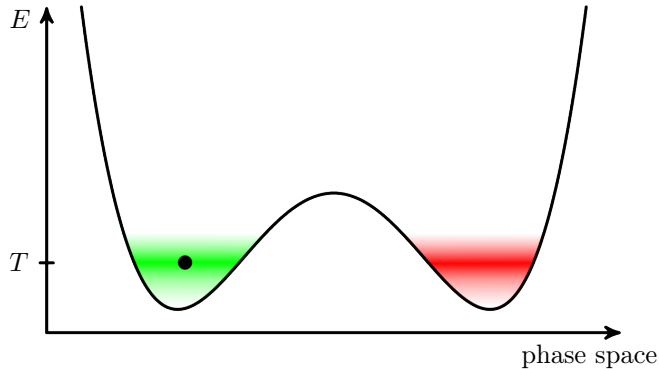
## 2. Advanced Monte Carlo techniques

This chapter gives an overview of advanced Monte Carlo techniques with an emphasis on the feedback-optimized parallel tempering algorithm that is used throughout this thesis. I start with an explanation why most simple Monte Carlo methods fail in practice and why more sophisticated methods are needed in Sec. 2.1. Afterwards, I introduce the concept of parallel tempering in Sec. 2.2, followed by a discussion on how the temperature points for a parallel tempering simulations have to be chosen in order to achieve optimal equilibration in Sec. 2.3. This chapter concludes with a brief overview of other Monte Carlo techniques in Sec. 2.4.

### 2.1. Shortcomings of simple Monte Carlo algorithms

In practice, many Monte Carlo algorithms suffer from severe problems when applied to real systems. Two of these problems, *ergodicity-breaking* and *critical slowing down*, deserve closer attention because almost every simple Monte Carlo algorithm encounters them. This section shall shed some light on the origin of these problems and explain the need for a more sophisticated algorithm. The probably most promising and versatile algorithm, parallel tempering Monte Carlo, is explained in full detail in Sec. 2.2.

**Ergodicity-breaking** An algorithm is called non-ergodic, if it fails to sample the phase space properly. A very intuitive example is a system with a one-dimensional potential featuring two minima of equal height, separated by a high energy barrier. If the temperature of the system is small compared to the height of this barrier, the system will most likely stay close to one of the two minima and never cross the barrier, c.f. Fig. 2.1.1. The phase space is thus effectively split into two parts of which only one is sampled properly. As a result, the calculated observables may differ from run to run, depending on which part of the phase space is sampled. To obtain correct measurements, it is important to use an ergodic algorithm which ensures that both parts of the phase space are sampled



**Figure 2.1.1.:** Illustration of a non-ergodic Monte Carlo algorithm. Once a system (black circle) has chosen a specific minimum, it will most likely stay there and fluctuate only into nearby states (green shaded). The states around the other minimum (red shaded) have a similar energy but are never sampled.

with their correct statistical weight. Real systems often have many separated minima, which a single simulation at a fixed temperature almost always fails to sample properly. Common examples are frustrated systems like spin-glasses and spin-ice. The most important method to solve the problem of ergodicity breaking is parallel tempering, which is explained in detail in Sec. 2.2. Another important method is entropic sampling [3], in which one tries to sample all states with a certain energy with equal probability. Some methods can be problem specific, e. g. there exists a loop-algorithm for spin-ice at low temperatures [9].

**Critical slowing down** For a given length of a simulation, the statistical error on measured quantities is influenced by two aspects, c. f. Eq. (1.3.17): The size of fluctuations,  $\langle O^2 \rangle - \langle O \rangle^2$ , and the auto-correlation time  $\tau$ . While the size of the fluctuations, characterized by the correlation length  $\xi$ , is specific for each model, the auto-correlation time depends solely on the spin-update algorithm that is used in the simulation. Since the correlation length diverges as the critical temperature is approached, one needs substantially more independent measurements in the critical region than in the non-critical-region to obtain results with the same accuracy. On the other hand, the auto-correlation time increases for many algorithms in the critical region: If correlations are large, a local-update algorithm that changes the direction of only a single spin at a time, needs a long time to change the state of a system in a way that correlations are lost. The resulting (algorithm-specific) increase in the auto-correlation time in the critical region is called *critical slowing down* and one major goal of any efficient Monte Carlo algorithms is to reduce or even completely eliminate this effect. This can be achieved

either by updating clusters of spins at once [3, 10] or by parallel tempering Monte Carlo. Since cluster algorithms are not suited for the problems addressed in this thesis, I only discuss the parallel tempering approach, c. f. Sec. 2.2.

## 2.2. Parallel tempering Monte Carlo

Parallel tempering Monte Carlo was originally developed for the simulation of glassy systems [11] and is considered as the most efficient way to evade the problems of ergodicity breaking and critical slowing down. This is achieved by simulating not only one system at a fixed temperature, but many *replicas* of the same system at different temperatures. If the temperatures are chosen close enough, there will be a substantial overlap of the energy histograms for two neighboring temperatures, or, in other words, there is a probability that a configuration sampled at a temperature  $T_1$  could as well be sampled at a different temperature  $T_2$ , c. f. Fig. 2.2.2. The aim of the parallel tempering approach is to allow the different replicas to exchange their configurations with each other. A replica, which may be stuck at a local minimum of the free energy at low temperatures, can move up in temperature space to a larger temperature, at which it can escape from this minimum. After spending some time at higher temperatures, where equilibration times are small, the replica will go to a low temperature again and probably occupy a different free energy minimum, ensuring that the phase space is sampled properly and ergodicity is not broken. This process is illustrated in Fig. 2.2.3.

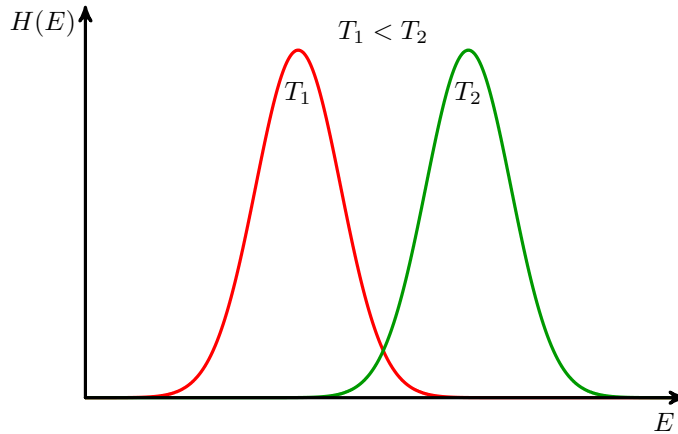
Additionally, the repeated swapping of configurations between replicas dramatically reduces auto-correlation times, which reduces the critical slowing down at phase transitions.

The detailed balance condition Eq. (1.1.10) for two replicas with different temperatures and energies reads

$$\begin{aligned} p(E_1, T_1)p(E_2, T_2)P((E_1, T_1), (E_2, T_2) \rightarrow (E_1, T_2), (E_2, T_1)) \\ = p(E_1, T_2)p(E_2, T_1)P((E_1, T_2), (E_2, T_1) \rightarrow (E_1, T_1), (E_2, T_2)), \end{aligned} \quad (2.2.1)$$

and the transition probabilities for replica exchange thus have to fulfill

$$\begin{aligned} \frac{P((E_1, T_1), (E_2, T_2) \rightarrow (E_1, T_2), (E_2, T_1))}{P((E_1, T_2), (E_2, T_1) \rightarrow (E_1, T_1), (E_2, T_2))} &= \frac{p(E_1, T_2)p(E_2, T_1)}{p(E_1, T_1)p(E_2, T_2)} \\ &= \frac{\exp(-E_1/T_2 - E_2/T_1)}{\exp(-E_1/T_1 - E_2/T_2)} \quad (2.2.2) \\ &= \exp \left[ \left( \frac{1}{T_1} - \frac{1}{T_2} \right) (E_1 - E_2) \right] \end{aligned}$$

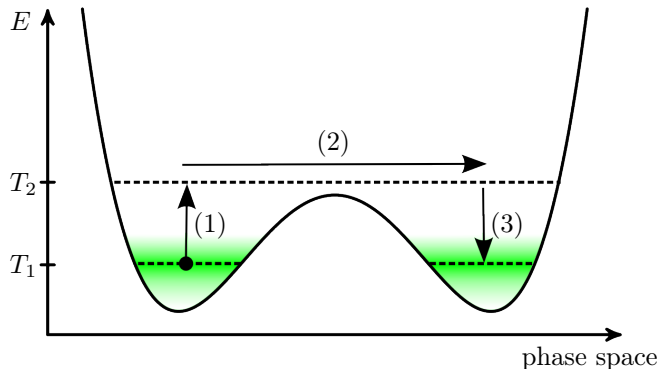


**Figure 2.2.2.:** Typical energy histograms for two replicas of the same system simulated at different temperatures  $T_1$  and  $T_2$  with  $T_1 < T_2$ . If the temperatures are close enough, there is a substantial overlap between the histograms and hence a finite probability that a configuration sampled at  $T_1$  could as well be sampled at  $T_2$ .

in order to fulfill detailed balance. A common choice for the transition probabilities that fulfills Eq. (2.2.2) is

$$p_{\text{swap}} = \min \left( 1, \exp \left[ (E_1 - E_2) \left( \frac{1}{T_1} - \frac{1}{T_2} \right) \right] \right). \quad (2.2.3)$$

From a computational point of view, parallel tempering algorithms can be parallelized with almost no numerical overhead. Often, one is interested in the value of observables over a wide range of temperatures and one would thus run separate simulations for all these temperatures anyway. Parallel tempering combines the measurements at these temperatures in a single simulation and improves the quality of the measurement as a whole by eliminating ergodicity-breaking and reducing critical slowing down.



**Figure 2.2.3.:** Illustration of the phase space sampling in a parallel tempering Monte Carlo simulation. **(1)** The replica residing in the left minimum moves “up” in temperature space from temperature  $T_1$  to  $T_2$ . **(2)** The replica passes the energy barrier between the two minima. **(3)** The replica moves down in temperature space to temperature  $T_1$  again and samples the right minimum.

### 2.3. Optimal choice of temperature points

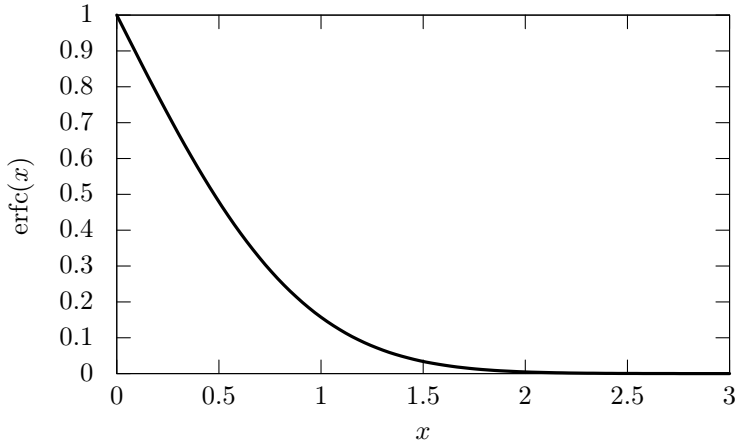
Before one begins to take measurements with parallel tempering Monte Carlo, one has to choose a set of temperatures  $\{T_1^0, \dots, T_M^0\}$  for the different replicas. The quality of this set influences the quality of the simulation in a crucial way: If the temperatures are separated too far, there will be no exchange of configurations at all, whereas computation time is wasted if temperatures are chosen too close. Assuming a piecewise constant specific heat, the acceptance rate for a replica exchange between two temperatures  $T_{i+1} > T_i$  is given by the incomplete beta-function law [12–15]

$$p_{\text{accept}}(T_i, T_{i+1}) = \text{erfc} \left( \frac{1 - T_i/T_{i+1}}{\sqrt{1 + (T_i/T_{i+1})^2}} \frac{\sqrt{N}c_V}{2} \right), \quad (2.3.4)$$

where  $c_V$  is the specific heat per spin in the interval  $[T_i, T_{i+1}]$ ,  $N$  the number of sites in the system and  $\text{erfc}(x)$  the complementary error function, c. f. Fig 2.3.4. For systems with constant, i. e. temperature-independent specific heat, Eq. (2.3.4) implies that a constant acceptance rate can be obtained if the ratio  $T_{i+1}/T_i$  is kept constant, i. e. if the temperatures follow a geometrical progression

$$T_i = T_{\min} \left( \frac{T_{\max}}{T_{\min}} \right)^{(i-1)/(M-1)} \quad \text{for } i = 1 \dots M. \quad (2.3.5)$$

Another consequence of Eq. (2.3.4) is that the acceptance rate will drop significantly if the specific heat becomes large, as it is the case at a phase transition.



**Figure 2.3.4.:** Behavior of the complementary error function  $\text{erfc}(x)$  that occurs in the incomplete beta-function law Eq. (2.3.4). As either the distance between neighboring temperatures or the specific heat increases, the acceptance rate for replica exchange decreases continuously.

Furthermore, one should note that it is necessary to increase the number of replicas with system size in order to keep the acceptance rate constant. Naively, one might expect that a temperature set with constant, i. e. temperature independent, acceptance probabilities for replica exchanges would be optimal. It has thus been the dominating approach in the past [16] to find algorithms which construct such a set of temperatures iteratively. One way to obtain such a set is to start with some temperature set  $\{T_1^0, \dots, T_M^0\}$  and to measure the acceptance rate  $a_i$  for each temperature point  $T_i^0$ . Afterwards, the next temperature set is obtained by

$$\begin{aligned}
 T_1^{(k+1)} &= T_{\min}^{(k)}, \\
 T_M^{(k+1)} &= T_{\max}^{(k)}, \\
 T_i^{(k+1)} &= T_{i-1}^{(k+1)} + \frac{a_i^{(k)} (T_i^{(k)} - T_{i-1}^{(k)})}{\sum_{i=2}^M a_i^{(k)} (T_i^{(k)} - T_{i-1}^{(k)})} (T_{\max} - T_{\min}), \quad i = 2 \dots M - 1,
 \end{aligned} \tag{2.3.6}$$

where  $k$  labels the iteration step. This iteration scheme keeps the two extremal temperatures fixed and increases or decreases the distance between intermediate temperature points depending on whether the acceptance rate is small or large. Kone and Kofke suggest in Ref. 17 that an average acceptance probability of

$\approx 20\%$  is optimal and adding further replicas does not improve the quality of the simulation. All these approaches do, however, not take the local diffusivity of a replica in temperature space into account. As it turns out, this quantity is of great importance in a parallel tempering simulation.

A recently introduced feedback-algorithm by Katzgraber *et al.* [16] aims at the construction of a temperature set which maximizes the actual quantity of interest in a parallel tempering simulation: the current of replicas drifting through temperature space. This is achieved by minimizing the average round trip time of a replica between the two extremal temperatures,  $T_{\max}$  and  $T_{\min}$ , and will in general result in a temperature set with non-constant acceptance probabilities. I closely follow Ref. 16 from now on and explain how this algorithm works in detail.

The diffusion of each replica through temperature space can be measured by assigning a label “up” or “down” to each replica, depending on which of the two extremal temperatures,  $T_{\min}$  or  $T_{\max}$ , it has visited most recently. A replica traveling “up” in temperature space will change its label to “down” once it has visited  $T_{\max}$  and vice versa, while the label remains unchanged on all intermediate temperatures. For a given set of temperatures, one can record two histograms,  $n_{\text{up}}(T_i)$  and  $n_{\text{down}}(T_i)$ , and evaluate the fraction

$$f(T_i) = \frac{n_{\text{up}}(T_i)}{n_{\text{up}}(T_i) + n_{\text{down}}(T_i)} \quad (2.3.7)$$

of replicas moving “up” in temperature space at all temperatures. This fraction is connected to a steady-state current  $j$  of “up”-moving replicas being produced at  $T_{\min}$  and absorbed at  $T_{\max}$ . In the following, it is assumed that  $T$  is a continuous variable, independent of the number of replicas. To first order in the derivative, the current  $j$  is then given by

$$j = D(T)\eta(T)\frac{df}{dT}, \quad (2.3.8)$$

where  $D(T)$  is the local diffusivity and  $\eta(T)$  is the probability distribution describing the probability for a replica to reside at temperature  $T$ .  $\eta(T)$  can be approximated by  $\eta(T) \approx C/\Delta T$ , where  $\Delta T = T_{i+1} - T_i$  is the width of the temperature interval around the temperature  $T$  located in the interval  $[T_i, T_{i+1}]$  in the current temperature set.  $C$  is a normalization constant chosen such that  $\int_{T_{\min}}^{T_{\max}} \eta(T)dT = 1$ . The derivative  $df/dT$  can be obtained from the measured data and Eq. (2.3.7) by a linear regression. Eq. (2.3.8) can be rearranged to give a measure for the local diffusivity,

$$D(T) \propto \frac{\Delta T}{df/dT}, \quad (2.3.9)$$

where the normalization constant as well as the current  $j$ , which are both constant for any specific choice of temperature set, have been dropped.

The aim of the algorithm is to maximize the current  $j$  by finding the optimal temperature set  $\{T_i^{\text{opt}}\}$ , or equivalently, the optimal probability distribution  $\eta^{\text{opt}}(T)$ . Eq. (2.3.8) already suggests that an optimal temperature set should have more temperature points in regions with low diffusivity and vice versa and it was indeed shown in Ref. 18 that the optimal probability distribution is connected to the local diffusivity  $D(T)$  by

$$\eta^{\text{opt}}(T) \propto \frac{1}{\sqrt{D(T)}}. \quad (2.3.10)$$

Inserting this in Eq. (2.3.8), one finds that the dependence of the current  $j$  on the local diffusivity can be eliminated completely by choosing a temperature set that fulfills

$$\frac{df^{\text{opt}}}{dT} = \eta^{\text{opt}}(T) \propto \frac{1}{\Delta T^{\text{opt}}}. \quad (2.3.11)$$

This implies that the optimal temperature set has a constant decay in the fraction of “up”-moving replicas,

$$\Delta f^{\text{opt}} = f(T_i) - f(T_{i+1}) = \frac{1}{M-1}, \quad (2.3.12)$$

where  $M$  is the number of replicas.

The optimal set of temperatures is found iteratively by measuring the local diffusivity from Eq. (2.3.9) followed by an adjustment of  $\eta(T)$  according to Eq. (2.3.10) as

$$\eta'(T) = \frac{C'}{\Delta T} \frac{df}{dT}, \quad (2.3.13)$$

with  $C'$  again chosen such that  $\int_{T_{\min}}^{T_{\max}} \eta'(T) dT = 1$ . The optimized intermediate temperatures  $T_i$  are then obtained by choosing them according to this distribution as

$$\int_{T_{\min}}^{T_i} \eta'(T) dT = \frac{i}{M}. \quad (2.3.14)$$

Depending on the quality of the initial temperature set and the strength of the bottlenecks in the local diffusivity, about one to five iterations of the whole algorithm are usually needed to obtain the fully optimized temperature set.

The algorithm can be summarized as follows:

- Start from an initial temperature set  $\{T_i\}$ . A temperature set with constant acceptance rates, as it can be constructed with the algorithm shown in Eq. 2.3.6, is usually a good choice. For systems with almost constant



specific heat, a geometrical progression as shown in Eq. 2.3.5 will result in approximately constant acceptance rates and might also be used.

- Repeat:

- Reset both histograms:  $n_{\text{up}}(T_i) = n_{\text{down}}(T_i) = 0$
- Perform a parallel tempering simulation with the current temperature set and record the two histograms  $n_{\text{up}}(T_i)$  and  $n_{\text{down}}(T_i)$ . Make sure that the simulation is long enough that steady state data is recorded.
- Calculate an estimate for the optimized probability density as

$$\eta'(T) = \frac{C'}{\Delta T} \frac{df}{dT}. \quad (2.3.15)$$

- Calculate the estimate for the optimized temperature set as

$$\int_{T_{\min}}^{T_i} \eta'(T) dT = \frac{i}{M}. \quad (2.3.16)$$

- Stop once the temperature set has converged.

If the system has a strong diffusion bottleneck for the replica current, i.e. a strong phase transition, the algorithm will locate many temperature points in this region. This can result in very low acceptance rates in other regions and it might be necessary to increase the total number of replicas. The number of replicas can, however, not be increased arbitrarily since the time a replica needs to move from one extremal temperature to the other will also increase. Assuming a 1d random walk (as it is the case for the optimal temperature set), the average time needed for a single trip between the two extremal temperatures scales as  $t \propto \sqrt{M}$ , where  $M$  is the number of replicas [19]. It is therefore desirable not to use more replicas than needed to obtain overall sufficient acceptance rates of about 20%.

**Example: The 2D-Ising model** Katzgraber *et al.* [16] have applied their algorithm i. a. to the well studied ferromagnetic Ising-model

$$H_{\text{Ising}} = J \sum_{\langle ij \rangle} \sigma_i \sigma_j, \quad (2.3.17)$$

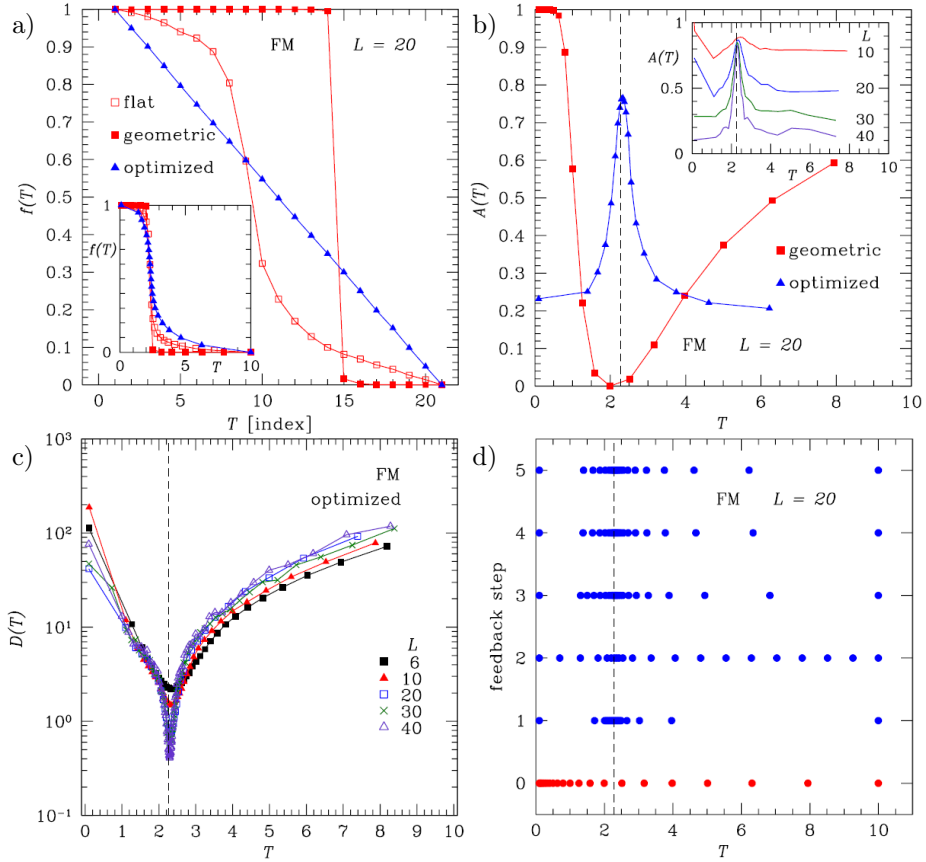
where  $J < 0$  is the ferromagnetic exchange constant, the sum extends over pairs of nearest neighbors and  $\sigma_i$  is a spin variable on lattice site  $i$ , taking the values  $\pm 1$ . Their results are summarized in Fig. 2.3.5.

Fig. 2.3.5 a) shows the fraction of the “up” drifting replicas in temperature

space according to Eq. (2.3.7) for different choices of temperature sets. The commonly chosen temperature set following a geometrical progression according to Eq. (2.3.5) shows a pronounced sharp step at the transition temperature  $T_c \approx 2.269 J$ , indicating that the phase transition is the bottleneck for the replica current since most replicas are not able to cross the critical temperature. The often recommended temperature set with a constant acceptance rate for replica exchange (here approx. 40%) still shows this feature, although it is not as sharp as for the geometrical progression. The optimized temperature set, however, does not have this problem and the fraction of “up” moving replicas shows a constant decay when plotted against the replica index, as expected.

Fig. 2.3.5 b) shows the acceptance rates for replica exchange moves in dependence on the temperature. The temperature set constructed by a geometrical progression shows a sharp drop in the acceptance rates around the phase transition, whereas the acceptance rates of the optimized temperature set peaks in this region. This is due to the fact that the local diffusivity is strongly suppressed at the phase transition, c. f. Fig. 2.3.5 c), which causes the algorithm to shift more temperature points in this region as required by Eq. (2.3.10). The evolution of the temperature set during the optimization, starting from a geometrical progression, is shown in Fig. 2.3.5 d) for five iterations. Already after three iterations, the temperature set does not change significantly any more.

### 2.3. Optimal choice of temperature points



**Figure 2.3.5.:** **a)** Fraction of replicas moving “up” in temperature space for different temperature sets against the replica index. The geometrical progression (filled squares) and a temperature set with almost constant acceptance rates of approx. 40% both show sharp steps in the curves, indicating that too few temperature points are located in a region with low diffusivity. The optimized temperature set shows a constant decay. Inset: fraction of replicas moving “up” in temperature space against temperature. The dashed line marks the critical temperature  $T_c \approx 2.269 J$ . **b)** Acceptance rates for replica exchange moves against temperature for different temperature sets. The optimized set has high acceptance rates at the phase transition (dashed line). Inset: acceptance rates for various system sizes  $N = L^2$ . **c)** Local diffusivity measured with the optimized temperature set for various system sizes. The diffusivity is strongly suppressed at the phase transition (dashed line) **d)** Evolution of the temperature set in five iterations starting from a geometrical progression. All pictures taken from Ref. 16.

## 2.4. Other Monte Carlo techniques

This section intends to give a short overview of other related Monte Carlo techniques. Monte Carlo integration is presented as an example how random numbers can be used to evaluate integrals. Two other simulation methods, simulated annealing and entropic sampling, are discussed for completeness. These methods are in general inferior to parallel tempering and thus only discussed briefly.

**Integration** Random numbers can also be used to approximate integrals. I show in the following that the (pure statistical) error of this approach is smaller compared to other traditional integration methods if the dimension of the integral is large.

In order to evaluate the integral

$$I = \int_V f(x) d^d x, \quad (2.4.18)$$

one evaluates the integrand  $N$  times at random points  $x_i \in V$ . A good estimate for the integral is then given by

$$I \approx \frac{V}{N} \sum_{i=1}^N f(x_i) \quad (2.4.19)$$

and the error of this approximation will decrease as  $\Delta I \propto 1/\sqrt{N}$ , independent of the dimension of the integral. The behavior of the error can be compared to other integration methods, where the integration volume is cut into equal pieces  $V_i$  and the integral is approximated as

$$I \approx \sum_{i=1}^N f(V_i) V_i. \quad (2.4.20)$$

For these methods, the error behaves as

$$\Delta I \propto \frac{1}{N^{\alpha/d}}, \quad (2.4.21)$$

where  $d$  is the dimension of the integral and  $\alpha$  is a method-dependent constant of order 1 (e. g.  $\alpha = 3$  for Simpson's rule) [20]. Since the error increases with the dimensionality of the integral, there is a critical dimension  $d_{\text{crit}} = 2\alpha$ , where Monte Carlo integration becomes superior to traditional integration methods ( $d_{\text{crit}} = 6$  for Simpson's rule). The efficiency of Monte Carlo integration can be increased by importance sampling, i. e. by sampling points not completely random in the integration volume, but with a probability distribution that allocates more points in regions where the integrand changes rapidly and less points in regions where the integrand is almost constant.

**Simulated annealing** Simulated annealing is a technique used to find the ground state of a function  $f(x_1, \dots, x_N)$ . The idea is to start with a random configuration  $\{x_1, \dots, x_N\}$  at a high temperature followed by a slow decrease of the temperature down to 0. During the cooling process, the configuration  $\{x_1, \dots, x_N\}$  is updated continuously by some update-scheme to a new configuration that is accepted according to the Metropolis-Hastings criterion Eq. (1.1.12), where the energy  $E$  is replaced by the value of  $f$ . The update-scheme can again be arbitrary, but the common choice would be to update only one variable in the configuration at a time to achieve reasonable acceptance rates.

If  $f(x_1, \dots, x_N)$  has a complex landscape with many minima, it is very likely that simulated annealing will break ergodicity at some point. Once one is trapped in a local minimum, other minima (and probably the global one) can not be reached anymore. Parallel tempering does not suffer this problem and is thus the superior method.

**Entropic sampling** The aim of entropic-sampling methods is to sample different states not with their Boltzmann probability proportional to  $e^{-E/T}$ , but with a probability proportional to  $1/\rho(E)$ , the reciprocal density of states. The probability that a certain state with an energy in the interval  $[E, E + dE]$  occurs in the Markov chain is then proportional to the product of the density of states,  $\rho(E)$ , and the probability to sample a state within that energy interval,  $1/\rho(E)$ . In other words, due to the particular choice of the sampling probability, one samples all energy values with a completely flat distribution and there is no Boltzmann weight anymore which makes it hard to cross energy barriers. A problem with this method is that the density of states is unknown at first and has to be determined before measurements can be taken. Once the density of states is known, the temperature dependence of an observable can be constructed from a single measurement. A good and detailed introduction to this method can be found e. g. in Ref. 3.



Part II.

# Magnetic monopoles in chiral magnets





### 3. Introduction

Besides the well known ferromagnetic and antiferromagnetic order, there also exist other interesting types of magnetic order in nature. A very interesting kind is found in so-called *chiral* magnets. In these systems, the lack of inversion symmetry in the atomic lattice gives rise to a Dzyaloshinskii-Moriya interaction, which causes the magnetization to twist like a helix around an axis which is determined either by crystal field anisotropies or an applied magnetic field. While these systems have been known to exist for more than 30 years [21], they recently gained a lot of interest when the magnetic structure of the so-called “A-phase” [22, 23] was identified in 2009 by Mühlbauer *et al.*, who discovered that this phase is a realization of a skyrmion lattice [24]. In this novel phase, topologically stable magnetic whirls, so-called *skyrmions*, stack on a regular triangular lattice and form a configuration similar to the vortex lattice in a type-II superconductor. Since its discovery, the skyrmion lattice has gained a lot of interest due to its extraordinary properties such as the very efficient coupling to electric currents [25], which makes it a promising candidate for future spintronic applications. The fact that skyrmions are topologically protected and thus very robust to perturbations also renders them promising candidates for data storage. Since they are already packed much closer than ordinary magnetic domains on hard-drives, they might allow the construction of devices with very high memory storage densities and lead to a further miniaturization in this area. In this context, the writing and deleting of single skyrmions has been reported by Romming *et al.* in 2013 for thin films [26].

In order to manipulate single skyrmions it is important to understand how their topological protection is destroyed, as it happens for instance during the phase transition from the skyrmion lattice to one of the other, non-topological phases. As I show in this part of the thesis, this process is mediated by artificial monopoles and anti-monopoles of an emergent magnetic field carried by the skyrmions. The charge of these monopoles is topologically quantized and they are either confined or deconfined, depending on temperature and magnetic field.

The structure of this part of the thesis is as follows: In this chapter, I give an introduction to chiral magnets with a special emphasis on the skyrmion lattice and its topological properties. In Ch. 4, I review the complete mean-field theory for chiral magnets and explain how the skyrmion lattice is stabilized by considering thermal fluctuations in gaussian order on top of the mean-field solution. A full

Monte Carlo study of chiral magnets, including fluctuations beyond gaussian order, is then presented in Ch. 5 and compared to experimental findings. Finally, I show in Ch. 6 how magnetic monopoles and anti-monopoles of an emergent magnetic field mediate the phase transition from the skyrmion lattice to other, non-topological phases.

## 3.1. Chiral magnets

In ferromagnets, the magnetic moments tend to align parallel, resulting in a uniform macroscopic magnetization. In a microscopic theory, this effect is typically captured by the simple nearest-neighbor Heisenberg Hamiltonian

$$H_{\text{FM}} = J \sum_{\langle ij \rangle} \mathbf{S}_i \cdot \mathbf{S}_j, \quad (3.1.1)$$

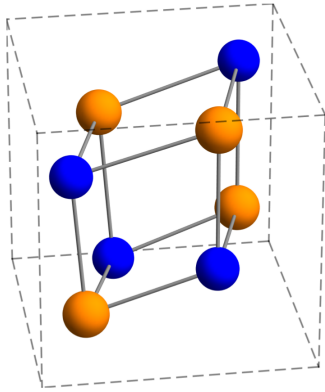
where  $\mathbf{S}_i$  denotes a classical  $O(3)$  spin on lattice site  $i$ ,  $J < 0$  is the ferromagnetic exchange constant and  $\sum_{\langle ij \rangle}$  denotes a sum over pairs of nearest neighbors. Usually, the ferromagnetic exchange is the dominant energy scale and corrections to this Hamiltonian are just anisotropies which favor either a certain plane or direction for the magnetization.

The symmetry of the underlying lattice imposes strong constraints on the allowed interactions and anisotropies. If, e. g., the crystal structure possesses an inversion symmetry, all interactions which transform odd under spatial inversion are forbidden. The B20 lattice structure, c. f. Fig. 3.1.1, that is usually realized in chiral magnets, lacks this symmetry, which gives rise to additional interactions. The leading additional contribution is the Dzyaloshinskii-Moriya (DM) interaction [27, 28]

$$H_{\text{DM}} = \sum_{\langle ij \rangle} \mathbf{D}_{ij} \cdot (\mathbf{S}_i \times \mathbf{S}_j), \quad (3.1.2)$$

where  $\mathbf{D}_{ij}$  is the so-called Dzyaloshinskii-Moriya vector, whose direction is constrained by the symmetries of the lattice. This interaction was first postulated by Dzyaloshinskii in 1958 [27] on the grounds of phenomenological considerations based on a Landau theory [27]. In 1960, Moriya identified the spin-orbit coupling as the microscopic mechanism that generates an interaction of this form [28].

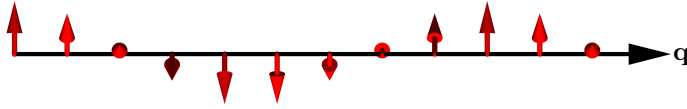
Since the expression  $(\mathbf{S}_i \times \mathbf{S}_j)$  vanishes for collinear spins, only non-collinear spin structures can benefit from such an interaction and the corresponding energy gain is maximized if the two neighboring spins entering Eq. (3.1.2) are perpendicular to each other. In competition with the much stronger ferromagnetic exchange, this leads to helical modulations of the magnetic structure with long wavelengths  $\lambda \propto J/D$ , c. f. Fig. 3.1.2. In small magnetic fields, the magnetic ground state



**Figure 3.1.1:** The atomic unit cell of the B20 crystal structure. Atoms are located at the relative positions  $(u, u, u)$ ,  $(1/2 + u, 1/2 - u, \bar{u})$ ,  $(1/2 - u, \bar{u}, 1/2 + u)$ ,  $(\bar{u}, 1/2 + u, 1/2 - u)$  where  $u$  is different for the orange and blue ions [29]. For MnSi, the Mn- and Si-ions are represented by the orange and blue balls, respectively, with  $u_{\text{Mn}} = 0.123$  and  $u_{\text{Si}} = 0.845$  [29]. Picture taken from Ref. 30.

of the system is thus a *helical phase* in which the propagation direction of these helices is determined solely by weak crystal anisotropies which favor a certain direction. For larger magnetic fields, it becomes energetically favorable for the system to have the propagation vector pointing along the direction of the field. All spins then point in a plane perpendicular to the field and the system can gain energy by simply tilting all spins continuously out of that plane towards the direction of the field, leading to a spiraling umbrella structure with a macroscopic magnetic moment, c. f. Fig. 3.1.3. Since the magnetization winds on cones around the wave-vector  $\mathbf{q}$ , this phase is also referred to as *conical phase*. Depending on the direction of the field, the helical and conical phase are either connected by a crossover or a first-order phase transition at some field value  $B_{c1}$ , where the energy gain from tilting all spins towards the field becomes larger than the crystal anisotropy energy difference between the two directions of the ordering wave vector. Upon further increasing the field, a continuous phase transition to a field polarized state takes place at some field  $B_{c2}$ . Fig. 3.1.4 shows schematically the expected phase diagram for chiral magnets. A complete and detailed mean-field analysis of these two states is presented in Sec. 4.1.

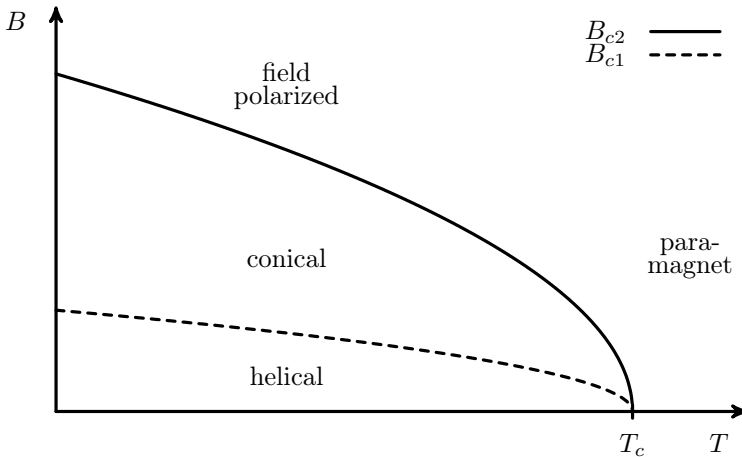
Experimentally, the conical phase can be identified in neutron scattering experiments with a magnetic field perpendicular to the incident neutron beam by a characteristic three-peak structure at  $\mathbf{Q} = 0$  and  $\mathbf{Q} = \pm\mathbf{q}$ , where the peak at  $\mathbf{Q} = 0$  originates from the uniform component of the magnetization. In the helical phase, there may exist several equivalent crystal directions preferred by some crystal anisotropy (there are e.g. four equivalent  $\langle 111 \rangle$  directions) and a sample will in general consist of multiple domains with different orientations of the propagation vector. Consequently, one observes peaks at  $\pm\mathbf{q}$  for each domain, resulting e.g. in eight peaks in total if the  $\langle 111 \rangle$  directions are favored. Fig. 3.1.5 shows neutron scattering images for the helical and conical phase in MnSi. Note



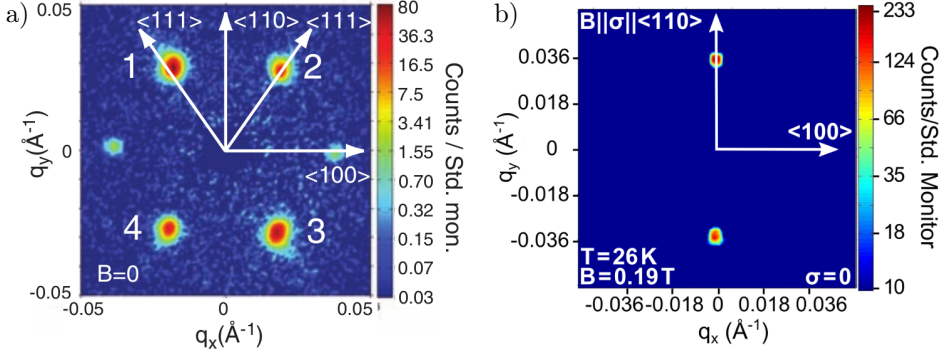
**Figure 3.1.2.:** In the helical phase, the magnetization winds around a propagation vector  $\mathbf{q}$  whose direction is defined by small crystal anisotropies. The magnetization is strictly perpendicular to  $\mathbf{q}$ .



**Figure 3.1.3.:** In the conical phase, the magnetization winds around a propagation vector  $\mathbf{q}$  which is parallel to the applied magnetic field. In contrast to the helical phase, all spins also tilt towards the direction of the field, leading to a conical umbrella structure with a macroscopic magnetic moment.



**Figure 3.1.4.:** The expected phase diagram for chiral magnets.  $B_{c2}$  denotes the transition to the fully field-polarized state, whereas  $B_{c1}$  denotes the transition/crossover between the helical and conical phase. The solid line represents a continuous phase transition, whereas the dashed line denotes either a first-order transition or a crossover, depending on the direction of the magnetic field.



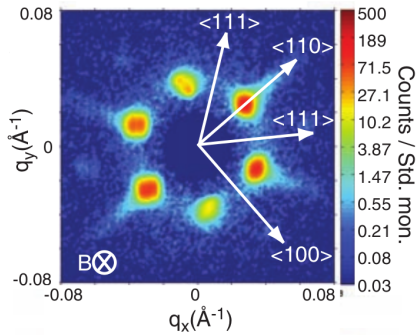
**Figure 3.1.5.:** **a)** Typical small angle neutron scattering (SANS) image for the helical phase in MnSi at  $T = 16$  K and  $B = 0$ . Crystal field anisotropies favor  $\langle 111 \rangle$  directions and the four equivalent  $\langle 111 \rangle$  directions lead to eight Bragg peaks in total, see main text. Picture taken from Ref. 24. **b)** Typical neutron scattering image for the conical phase in MnSi with a magnetic field applied in  $\langle 110 \rangle$  direction. Picture taken from Ref. 31.

that the aforementioned peak at  $\mathbf{Q} = 0$  is missing in these figures since one can experimentally not distinguish between unscattered neutrons and scattered neutrons with  $\mathbf{Q} = 0$ . The corresponding area around  $\mathbf{Q} = 0$  is therefore usually cut out from the images.

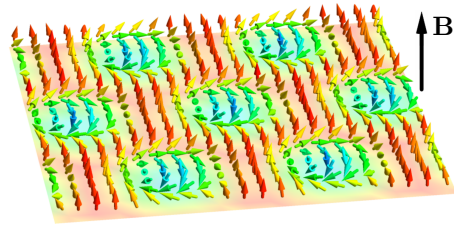
## 3.2. Discovery of the skyrmion lattice

Besides the well understood helical and conical phase, there was also a third phase known to exist [22, 23] in a very small pocket in the phase diagram at intermediate magnetic fields and temperatures just below the ordering temperature, c. f. phase diagram for MnSi in Fig. 3.2.8. Since the magnetic structure of this phase was not properly understood, it was first referred to as “A-phase”. For a long time, it was believed that it consisted of a single helix propagating perpendicular to the applied magnetic field [22, 23]. In 2009, Mühlbauer *et al.* showed that this interpretation is wrong and that the magnetic structure is much more interesting than thought before [24].

In contrast to previous experiments, they performed neutron scattering measurements with the magnetic field parallel instead of perpendicular to the incident neutron beam, the latter being the standard setup for measurements of the conical phase. They observed six Bragg spots arranged on a regular hexagon in the plane perpendicular to the magnetic field, c. f. Fig. 3.2.6, which indicates a multi- $\mathbf{q}$  structure comprised mainly out of three different helices with relative



**Figure 3.2.6.:** Small angle neutron scattering (SANS) image of the skyrmion lattice phase observed in MnSi at  $T = 26.45$  K and  $B = 0.164$  T. The magnetic field is aligned perpendicular to the scattering plane. Picture taken from Ref. 24.

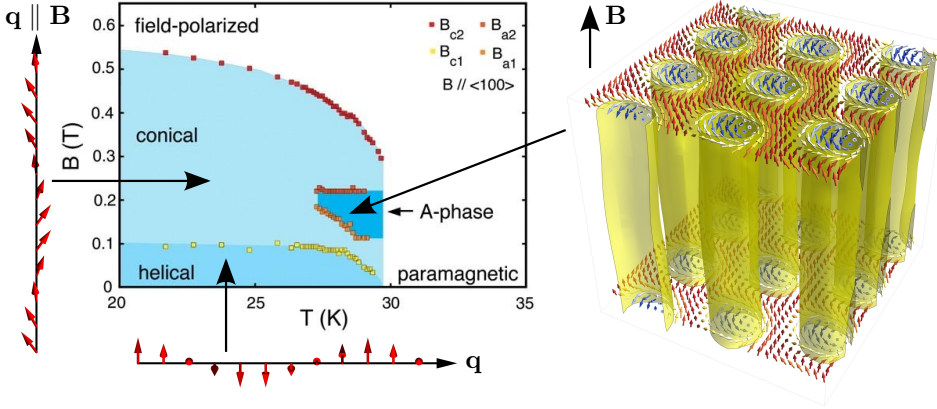


**Figure 3.2.7.:** Magnetic order in the skyrmion lattice phase: The magnetic structure forms a triangular lattice of skyrmions that is translationally invariant in the direction of the magnetic field and should therefore be visualized as an ordered arrangement of skyrmion tubes, c. f. Fig. 3.2.8, of which only one layer is shown here. Picture taken from Ref. 31.

angles of  $120^\circ$ .

A straightforward identification of the corresponding magnetic ground state in real space is not that easy since neutron scattering does not yield any information about the relative phases of the three helices to each other. The authors have therefore performed a detailed mean-field calculation which revealed that the energy of such a state is minimized if the relative phases are chosen such that the magnetic structure forms magnetic whirls, so-called *skyrmions*, in real space, which are arranged on a regular triangular lattice perpendicular to the magnetic field, c. f. Fig. 3.2.7 and the right part of Fig. 3.2.8. Interestingly, this phase appears only as a metastable state on mean-field level, but Mühlbauer *et al.* have shown that thermal fluctuations in gaussian order alone are already sufficient to stabilize it with respect to the competing conical phase. The mean-field calculation and fluctuation corrections are discussed in detail in Sec. 4.1 and 4.2, respectively.

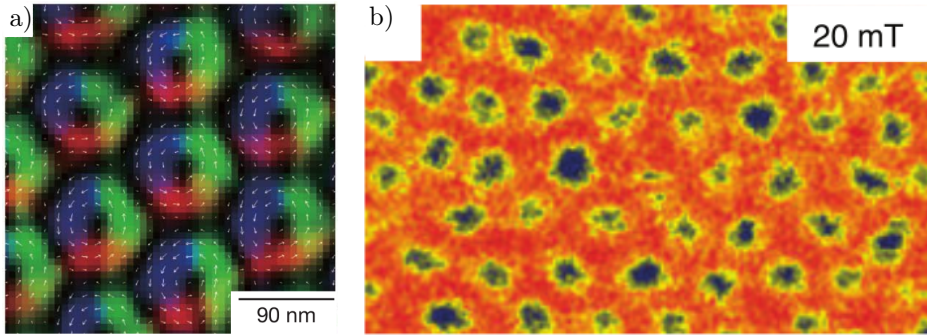
Since 2009, the skyrmion lattice phase has also been observed in many other materials such as the doped semiconductor  $\text{Fe}_{1-x}\text{Co}_x\text{Si}$  [32], iron and cobalt doped MnSi, i. e.  $\text{Mn}_{1-x}\text{Fe}_x\text{Si}$  and  $\text{Mn}_{1-x}\text{Co}_x\text{Si}$  [33], and the insulator  $\text{Cu}_2\text{OSeO}_3$  [34]. This is in agreement with the theoretical analysis, which predicts that the occurrence of a skyrmion lattice is a generic feature in chiral magnets. In fact, all above mentioned materials have a phase diagram similar to the one of MnSi shown in Fig. 3.2.8 [32–34].



**Figure 3.2.8.:** Magnetic phase diagram of MnSi. In a small pocket of the phase diagram at intermediate magnetic field and temperatures just below the ordering temperature of  $T \approx 29$  K, the skyrmion lattice is the magnetic ground state of the system. For historical reasons, the skyrmion lattice phase is named “A-phase” in the figure. The right figure shows the skyrmion lattice phase as an arrangement of magnetic whirls on a triangular lattice perpendicular to the applied field. Picture of the phase diagram taken from Ref. 24.

In addition to neutron scattering experiments, the skyrmion lattice has also been observed directly with real-space imaging techniques in thin films [35] and on surfaces of bulk materials [36, 37]. Fig. 3.2.9 a) shows a Lorentz transmission electron microscopy image (LTEM) of the skyrmion lattice phase in a thin film of  $\text{Fe}_{0.5}\text{Co}_{0.5}\text{Si}$  [36]. In this technique, one utilizes the deviation of an electron beam due to the Lorentz force resulting from the interaction with the magnetic moments in the sample to reconstruct the magnetic structure. Two drawbacks of this technique are that it can only be applied to electron transparent (i. e. very thin) samples and that it is only sensitive to the in-plane component of the magnetization, i. e. the component perpendicular to the electron beam.

Another technique, that is sensitive to the out-of-plane component of the magnetization, is magnetic force microscopy (MFM). For this method, one moves a magnetized tip directly over the surface of a sample. The interaction between the sample and the tip cause a deviation of the tip from which one can reconstruct the out-of-plane component of the surface magnetization. Fig. 3.2.9 b) shows the surface magnetization of a bulk sample of  $\text{Fe}_{0.5}\text{Co}_{0.5}\text{Si}$  in the skyrmion lattice phase as recorded with this technique [37].

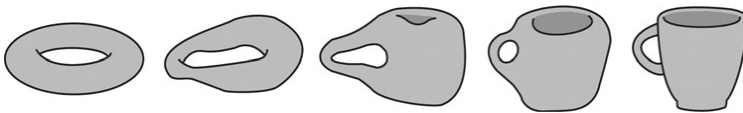


**Figure 3.2.9.:** a) Lorentz transmission electron microscopy image of the skyrmion lattice phase in a thin film of  $\text{Fe}_{0.5}\text{Co}_{0.5}\text{Si}$ . The color-code represents the in-plane magnetization distribution. Picture taken from Ref. 36. b) Magnetic force microscopy measurement of the surface of  $\text{Fe}_{0.5}\text{Co}_{0.5}\text{Si}$ . In red (blue) areas, the magnetization points out of (in) the plane. Picture taken from Ref. 37.

### 3.3. Topological properties of the skyrmion lattice

Topology is a branch of mathematics that deals with properties of systems that remain invariant under continuous deformations. This allows a classification of systems in terms of topological invariants, e. g. the number of “holes” in its shape. Based on this criterion, one would e. g. consider a doughnut and a coffee mug to be topologically equivalent since both have exactly one hole and can be continuously deformed into each another, c. f. Fig. 3.3.10. A doughnut and a cube, on the other hand, would be considered as topologically distinct since one would first have to drill a hole into the cube before it can be transformed into a doughnut.

The concept of topology has also proven to be very fruitful in the classification of condensed matter systems [39, 40] since many systems exhibit *topological phases* which are characterized by some non-local quantity depending solely on the global structure of the phase. The fact that topological order cannot be destroyed by continuous deformations leads to the concept of *topological stability*, which will



**Figure 3.3.10.:** Continuous transformation of a doughnut into a coffee mug. Picture taken from Ref. 38.



be of particular interest in this thesis.

The skyrmion lattice phase in chiral magnets is a realization of such a topological phase. The corresponding topological invariant is the winding number  $W$ , which is given by the integral over the skyrmion density

$$w_\mu = \frac{1}{8\pi} \epsilon_{\mu\nu\lambda} \hat{\mathbf{M}} \cdot \left( \partial_\nu \hat{\mathbf{M}} \times \partial_\lambda \hat{\mathbf{M}} \right), \quad (3.3.3)$$

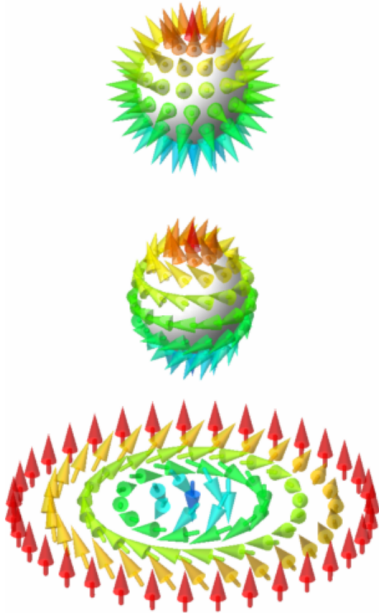
where  $\hat{\mathbf{M}}$  is a unit vector pointing in the direction of the local magnetization. For skyrmions located in the  $xy$ -plane, the winding number is given by

$$W = \frac{1}{4\pi} \int_A dx dy \hat{\mathbf{M}} \cdot \left( \frac{\partial \hat{\mathbf{M}}}{\partial x} \times \frac{\partial \hat{\mathbf{M}}}{\partial y} \right). \quad (3.3.4)$$

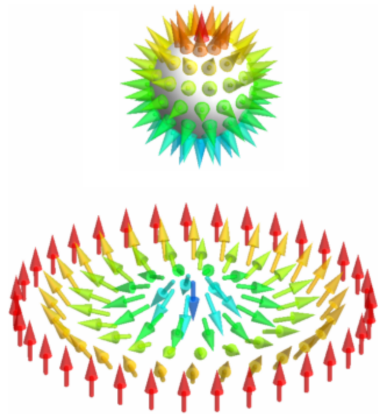
and simply counts how often the magnetization in a certain area  $A$  covers the unit sphere. Fig. 3.3.11 shows how a skyrmion can be obtained from a singular hedgehog configuration: First, the hedgehog is combed around the axis defined by the north and south pole, followed by a projection into the plane that obeys the rule that the magnetization at the north pole is mapped to a circle at infinity, whereas the magnetization at the south pole is mapped to a single point at the origin. This mapping reveals that the magnetization of a single skyrmion covers the unit sphere exactly once and the winding number per skyrmion is thus quantized to  $W = -1$ , where the sign comes from the fact that the magnetization in the center of the skyrmion points downwards. Strictly speaking, the observed skyrmions are thus *anti*-skyrmions, and skyrmions can be obtained from these by the transformation  $\mathbf{M} \rightarrow -\mathbf{M}$ .

If the hedgehog is not combed before it is projected into the plane, one obtains non-chiral skyrmions as shown in Fig. 3.3.12. These configurations also have a winding number of  $W = -1$  per skyrmion, but do not occur for the type of Dzyaloshinskii-Moriya interaction considered here, which always prefers a certain twist direction.

The helical and conical phases are, in contrast to the skyrmion lattice phase, not characterized by a topological invariant. Consequently, the phase transition between the skyrmion lattice and the conical phase is of particular interest since it goes along with a change in topology. As already mentioned in this section, this cannot be achieved by a smooth rearrangement of the magnetization and it turns out that the only way to convert one phase into the other is to suppress the amplitude  $|\mathbf{M}(\mathbf{r})|$  of the magnetization locally to zero, which is energetically very expensive. It will be shown in Ch. 6 that this phase conversion is mediated by monopoles and anti-monopoles of an emergent magnetic field.



**Figure 3.3.11.:** From a hedgehog configuration to a chiral skyrmion: First, the hedgehog is combed around an axis defined by the north and the south pole, followed by a projection into the plane. Picture taken from Ref. 31.



**Figure 3.3.12.:** From a hedgehog configuration to a non-chiral skyrmion: In contrast to chiral skyrmions, the hedgehog is not combed before the projection into the plane. Picture taken from Ref. 31.

# 4. Stabilization of the skyrmion lattice by thermal fluctuations

## 4.1. Mean field theory for chiral magnets

Landau mean-field theory is a phenomenological theory for the description of phase transitions, see e.g. Refs. 41 and 42 for an introduction. Central ingredient is the existence of an order parameter which is zero in the disordered phase and non-zero in the ordered phase. In the vicinity of a phase transition, the order parameter is small and one can expand the free energy in powers of the order parameter. Minimization of this functional with respect to the order parameter yields the thermodynamic equilibrium properties of the system under consideration, neglecting all fluctuations.

In a ferromagnet, the order parameter is given by the local magnetization  $\mathbf{M}(\mathbf{r})$  and the free energy  $G$  of a system can be expressed by the partition function  $Z$  as

$$e^{-G} = Z = \int \mathcal{D}\mathbf{M} e^{-F[\mathbf{M}]}, \quad (4.1.1)$$

where the functional  $F[\mathbf{M}]$  respects all symmetries of the system.

To first order, the free energy of the system is simply given by its mean-field value, which is defined as

$$G \approx \min[F[\mathbf{M}]] \equiv F[\mathbf{M}_0], \quad (4.1.2)$$

where  $\mathbf{M}_0$  is the magnetic structure that minimizes the functional  $F[\mathbf{M}]$ . From now on, I closely follow Refs. 24 and 43 for the review of the mean-field theory for chiral magnets.

**Mean-field theory for ferromagnets with inversion symmetry** For a ferromagnet with inversion symmetry exposed to an external magnetic field  $\mathbf{B}$ , the free energy functional  $F[\mathbf{M}]$  takes the form

$$F[\mathbf{M}] = \int d^3r \left( J(\nabla\mathbf{M})^2 + r_0\mathbf{M}^2 + U\mathbf{M}^4 - \mathbf{B} \cdot \mathbf{M} + \dots \right), \quad (4.1.3)$$

where  $J > 0$ ,  $r_0$  and  $U > 0$  are phenomenological parameters that have to be derived from a microscopical theory of the system under consideration. The first term proportional to  $J$  is the coarse-grained version of Eq. (3.1.1) and accounts for the ferromagnetic character of the system by favoring a parallel alignment of the magnetization. The second term changes its sign at the phase transition (i. e.  $r_0 \propto T - T_c$ , where  $T_c$  is the critical temperature) and is responsible for the spontaneous symmetry breaking, whereas the term proportional to  $U$  ensures stability of the system by preventing arbitrary large magnetizations. The last term accounts for the Zeeman-energy gain due to the external magnetic field.

Eq. (4.1.3) is invariant under rotations and translations in space, spatial inversions, the transformation defined by  $(\mathbf{M}, \mathbf{B}) \rightarrow (-\mathbf{M}, -\mathbf{B})$  as well as a combined rotation of space and spin space around the axis defined by  $\mathbf{B}$  (or an arbitrary axis if  $\mathbf{B} = 0$ ). Other terms containing e. g. only one spatial derivative are forbidden since they transform as  $\nabla \rightarrow -\nabla$  under spatial inversion and hence do not respect the inversion symmetry of the underlying system.

Without an external magnetic field, the free energy functional is minimized for  $T < T_c$  by a uniform and spatial independent (i. e.  $\nabla \mathbf{M}(\mathbf{r}) = 0$ ) magnetization with a magnitude given by

$$M = \sqrt{-\frac{r_0}{2U}}. \quad (4.1.4)$$

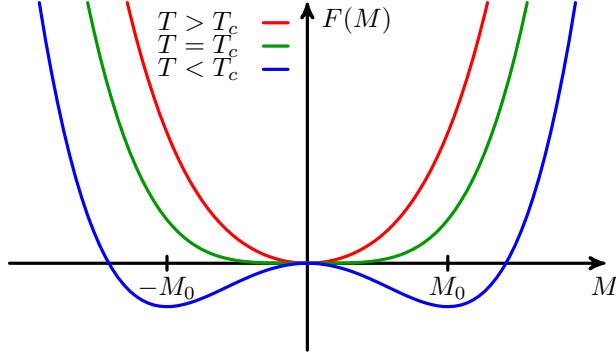
Since the free energy functional Eq. (4.1.3) is rotationally invariant, the direction of  $\mathbf{M}$  is not determined by this solution. This degeneracy is lifted either by a magnetic field or crystal anisotropies which favor a certain direction in space. For temperatures  $T > T_c$ , the only minimum of  $F[\mathbf{M}]$  is given by  $\mathbf{M}(\mathbf{r}) = 0$ , which corresponds to a paramagnetic state.

Fig. 4.1.1 shows schematically the behavior of the free energy functional for  $T < T_c$ ,  $T = T_c$  and  $T > T_c$  in dependence on the uniform magnetization.

**Mean-field theory for chiral magnets** For systems without inversion symmetry, one has to extend the free energy functional to include terms containing odd powers of the spatial derivative. The leading term is the Dzyaloshinskii-Moriya (DM) interaction [27, 28], whose coarse grained version (c. f. Eq. (3.1.2)) is linear in the gradient and given by

$$F_{\text{DM}} = \int d^3r \, 2D \mathbf{M} \cdot (\nabla \times \mathbf{M}), \quad (4.1.5)$$

where the energy scale  $D$  is set by the spin-orbit coupling strength  $\lambda_{\text{SO}}$  and the sign of  $D$  depends on the particular system. It will be shown later that  $\nabla \times \mathbf{k} \propto D$ , which makes the DM interaction term in Eq. (4.1.5) in fact *second* order in the spin-orbit coupling.



**Figure 4.1.1.:** Schematic behavior of the free energy functional  $F$ , Eq. (4.1.3), for  $T < T_c$ ,  $T = T_c$  and  $T > T_c$  and a uniform magnetization.

In order to minimize the corresponding full free energy functional, it is useful to first simplify the expression by rescaling the parameters as

$$\mathbf{r} \rightarrow \frac{D}{J}\mathbf{r}, \quad \mathbf{M} \rightarrow \frac{\sqrt{JU}}{D}\mathbf{M}, \quad \mathbf{B} \rightarrow \sqrt{\frac{UJ^3}{D^3}}\mathbf{B} \quad (4.1.6)$$

and introducing

$$t = \frac{r_0 J}{D^2}, \quad \gamma = \frac{JD}{U} \quad (4.1.7)$$

to obtain

$$F[\mathbf{M}] = \gamma \int d^3r \left( (\nabla \mathbf{M})^2 + 2\mathbf{M} \cdot (\nabla \times \mathbf{M}) + (1+t)\mathbf{M}^2 + \mathbf{M}^4 - \mathbf{B} \cdot \mathbf{M} \right). \quad (4.1.8)$$

The complete physics of the mean-field theory is thus determined by the parameters  $t$  and  $\mathbf{B}$ . The next step is to exploit the translation symmetry of the system by performing a Fourier transform of the magnetization to momentum space,

$$\mathbf{M}(\mathbf{r}) = \sum_{\mathbf{k}} e^{i\mathbf{k}\mathbf{r}} \mathbf{M}_{\mathbf{k}}. \quad (4.1.9)$$

Since the magnetization is real, the Fourier components have to satisfy  $\mathbf{M}_{\mathbf{k}} = \mathbf{M}_{-\mathbf{k}}^*$ . This allows to rewrite Eq. (4.1.8) as a sum of quadratic terms and a



**Figure 4.1.2.:** The conical mean-field solution of the free energy functional with Dzyaloshinskii-Moriya interaction.

constant,

$$\begin{aligned} \frac{F[\mathbf{M}]}{\gamma} = & -V \frac{t^2 - \mathbf{B}^2}{4} + V \sum_{\mathbf{k} \neq 0} M_{-\mathbf{k}}^i [(1 + \mathbf{k}^2)\delta_{ij} - 2i\epsilon_{ijk}k^k] M_{\mathbf{k}}^j \\ & + \int d^3r \left( \mathbf{M}^2 + \frac{t}{2} \right)^2 + V \left( \mathbf{M}_f - \frac{1}{2}\mathbf{B} \right)^2, \end{aligned} \quad (4.1.10)$$

where  $M_f \equiv M_{\mathbf{k}=0}$  is the field-polarized component of the magnetization and  $V$  the volume of the system.

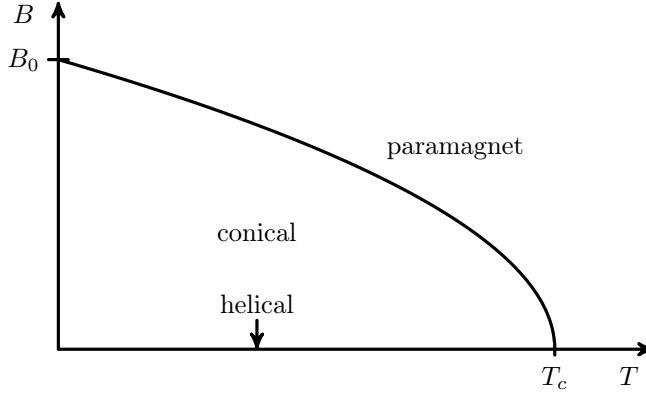
The matrix  $[(1 + \mathbf{k}^2)\delta_{ij} - 2i\epsilon_{ijk}k^k]$  has the eigenvalues  $\{(1 - k)^2, 1 + k^2, (1 + k)^2\}$  with  $k = |\mathbf{k}|$  and is thus positive semi-definite, as are the last two terms in Eq. (4.1.10). The free energy is therefore bounded from below by  $F_{\min} = -\gamma V(t^2 - \mathbf{B}^2)/4$  and the mean field solution can be found by minimizing all quadratic terms individually. For a magnetic field in z-direction and  $B < \sqrt{-2t}$ , the solution is given by

$$\mathbf{M}(\mathbf{r}) = \begin{pmatrix} \Phi \cos(kz) \\ \Phi \sin(kz) \\ M_f \end{pmatrix} \quad (4.1.11)$$

with

$$M_f = \frac{1}{2}B, \quad \Phi = \frac{\sqrt{-2t - B^2}}{2}, \quad k = \frac{2\pi}{\lambda} = 1, \quad \mathbf{k} \parallel \mathbf{B}, \quad (4.1.12)$$

which describes an umbrella like conical structure propagating in direction of the magnetic field, c.f. Fig. 4.1.2. For  $B > \sqrt{-2t}$ , the ground state of the system is described by a fully polarized phase with a magnetic moment  $M_f = B/2$  in the direction of the field. As the magnetic field is reduced to zero, the uniform magnetization  $M_f$  vanishes continuously. Exactly at  $\mathbf{B} = 0$ , the propagation direction of the helical structure is not determined by the free energy functional. This degeneracy is usually lifted by small anisotropies which favor a certain direction in space. One of these anisotropy terms that is allowed by the  $P2_13$  space group of the B20 crystal structure is in lowest order of the spin-orbit coupling



**Figure 4.1.3.:** Mean field phase diagram of a ferromagnet with additional DM interaction according to Eq. (4.1.8) and  $B_0 = \sqrt{2Dr_0(T=0)}/J^2U$ .

( $\propto \lambda_{\text{SO}}^4$ ) given by [31]

$$\begin{aligned} F_{\text{anisotropy}} &= A \int d^3r \mathbf{M}(\mathbf{r})(\partial_x^4 + \partial_y^4 + \partial_z^4)\mathbf{M}(\mathbf{r}) \\ &= AV \sum_{\mathbf{k}} (k_x^4 + k_y^4 + k_z^4) |\mathbf{M}_{\mathbf{k}}|^2, \end{aligned} \quad (4.1.13)$$

and locks the propagation direction either in  $\langle 111 \rangle$  ( $A > 0$ ) or  $\langle 100 \rangle$  ( $A < 0$ ) direction. A detailed overview of all terms up to sixth order in  $\mathbf{k}$  allowed by the symmetry of the  $P2_13$  space group can be found in Ref. 31.

In non-rescaled units, the wavelength  $\lambda$  of the helical modulations is given by  $\lambda = 2\pi J/D$  (and thus of the order  $\lambda_{\text{SO}}^{-1}$ ), which is large compared to crystallographic distances. The magnetic structure thus effectively decouples from the crystal lattice and varies very smoothly through the whole system.

The phase boundary between the conical and paramagnetic phase is according to Eq. (4.1.12) given by  $B = \sqrt{-2t}$ , or in original units by

$$B = \sqrt{\frac{2Dr_0}{J^2U}} \quad (4.1.14)$$

Fig. 4.1.3 shows the corresponding mean-field phase diagram.

**Mean-field theory for the skyrmion lattice** The characteristic signal of a skyrmion lattice in neutron scattering experiments are the six Bragg spots

#### 4. Stabilization of the skyrmion lattice by thermal fluctuations

---

with relative angles of  $60^\circ$  in the plane perpendicular to the magnetic field, c. f. Fig. 3.2.6. This implies that the skyrmion lattice basically consists out of three different Fourier modes  $\{\mathbf{k}_1, \mathbf{k}_2, \mathbf{k}_3\} \perp \mathbf{B}$ , with same magnitude  $k \equiv |\mathbf{k}_1| = |\mathbf{k}_2| = |\mathbf{k}_3|$  and  $\mathbf{k}_1 + \mathbf{k}_2 + \mathbf{k}_3 = 0$ , as imposed by the  $60^\circ$  pattern<sup>1</sup>. In the following, I discuss how such a structure can gain energy from the quartic term in the free energy functional (although this is not sufficient to stabilize it on mean-field level).

As a first step, the  $\mathbf{q} = 0$  component  $\mathbf{M}_f$ , which corresponds to the field polarized part of the magnetization, is singled out to obtain the “true” order parameter  $\Psi = \mathbf{M} - \mathbf{M}_f$ . Expanding the quartic interaction term of the free energy functional Eq. (4.1.8) yields

$$\int d^3r \mathbf{M}^4 = \int d^3r \left( \mathbf{M}_f^4 + 4\mathbf{M}_f^2(\mathbf{M}_f \cdot \Psi) + 2\mathbf{M}_f^2\Psi^2 + 4(\mathbf{M}_f \cdot \Psi)^2 + 4\Psi^2(\mathbf{M}_f \cdot \Psi) + \Psi^4 \right). \quad (4.1.15)$$

The skyrmion lattice can gain energy from the term which is cubic in the order parameter  $\Psi$ . Its Fourier transform reads

$$\int d^3r \Psi^2(\mathbf{M}_f \cdot \Psi) = \sum_{\mathbf{k}_1, \mathbf{k}_2, \mathbf{k}_3 \neq 0} (\mathbf{M}_f \cdot \mathbf{M}_{\mathbf{k}_1})(\mathbf{M}_{\mathbf{k}_2} \cdot \mathbf{M}_{\mathbf{k}_3})\delta(\mathbf{k}_1 + \mathbf{k}_2 + \mathbf{k}_3). \quad (4.1.16)$$

The only possibility to gain energy from this term is if the magnetic structure contains Fourier modes of three wave vectors with  $\mathbf{k}_1 + \mathbf{k}_2 + \mathbf{k}_3 = 0$ . Since the modulus of the wave vectors is fixed by  $k = D/J$ , the three wave vectors have to lie in the same plane with relative angles of  $120^\circ$  in between them, c. f. Fig. 4.1.4. This already accounts for the six Bragg spots with relative angles of  $60^\circ$  observed in experiments.

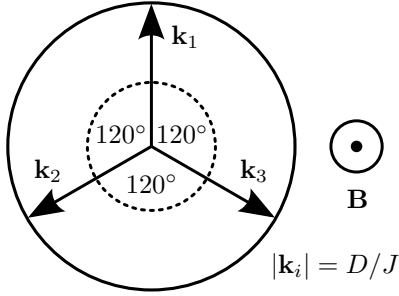
A direct calculation [24, 43] shows that the vector  $\int d^3r \Psi^2\Psi$  aligns orthogonal to the plane spanned by  $\mathbf{k}_1, \mathbf{k}_2$  and  $\mathbf{k}_3$ , with a prefactor that depends on the relative phases of the three helices. The energy of the cubic term is thus minimized if  $\mathbf{k}_1, \mathbf{k}_2$  and  $\mathbf{k}_3$  are orthogonal to  $\mathbf{M}_f$  and hence also orthogonal to  $\mathbf{B}$ . The relative phases between the different helices then ensure that  $\int d^3r \Psi^2\Psi$  becomes maximally anti-parallel to  $\mathbf{M}_f$ , which minimizes the energy gain by the cubic term. This explains the second experimental observation that the six Bragg spots occur in a plane perpendicular to the applied magnetic field.

Although this argument can already explain how the skyrmion lattice can gain energy from the quartic term in the free energy functional, a more profound

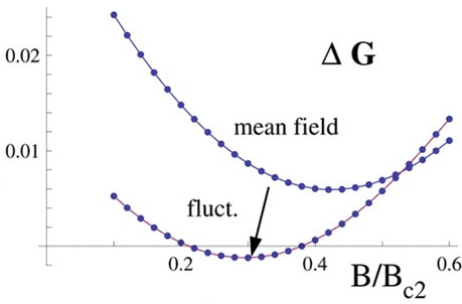
---

<sup>1</sup>Since the magnetization is real, each Fourier mode gives rise to two Bragg peaks at  $\pm\mathbf{k}$ , which implies that the relative angle between the three helices is  $120^\circ$ , leading to the condition  $\mathbf{k}_1 + \mathbf{k}_2 + \mathbf{k}_3 = 0$ .





**Figure 4.1.4:** Alignment of the three wave vectors in the skyrmion lattice solution.



**Figure 4.1.5:** The free energy difference  $\Delta G = G_{\text{skyrmion}} - G_{\text{conical}}$  between the conical and the skyrmion phase in dependence on the magnetic field for  $t = -3.5$ . The free energy difference is plotted in units of  $\gamma t/4$ , which is the energy difference between the ferromagnetic state and the conical phase at  $B = 0$ . Thermal fluctuations lower the free energy of the skyrmion phase below the energy of the conical phase, c.f. Sec. 4.2. Picture taken from Ref. 24.

analysis is necessary to make quantitative statements about its stability. A full study [24, 43] that takes into account also higher Fourier modes  $\mathbf{k}$  up to some cut-off  $\Lambda$  (these modes have also been observed experimentally, c.f. Ref. 44), followed by a numerical minimization, reveals that the skyrmion lattice phase only occurs as a local minimum of the free energy whereas the global minimum is still given by the conical phase. The energy difference between these two phases is however very small, in particular for intermediate magnetic fields, c.f. Fig. 4.1.5.

## 4.2. Thermal fluctuations in gaussian approximation

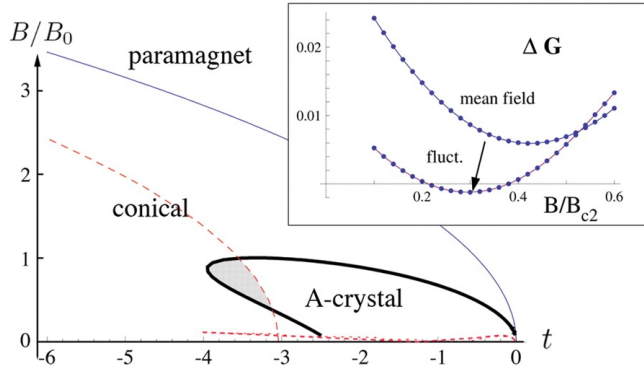
The small energy difference between the skyrmion lattice and the conical phase, which appears on mean-field level and favors the latter one, is in contradiction to the observed stability of the skyrmion lattice in experiments. The fact that the skyrmion lattice phase is observed just in a small pocket below the critical temperature and vanishes again as the temperature is reduced further hints that thermal fluctuations might be responsible for its stabilization. The leading order

correction to the mean-field solution is given by gaussian fluctuations [24],

$$\Delta G = \frac{1}{2} \ln \det \left( \frac{\delta^2 F}{\delta \mathbf{M} \delta \mathbf{M}} \right) \Big|_{\mathbf{M}_0}, \quad (4.2.17)$$

where  $\mathbf{M}_0$  is the mean-field solution that minimizes  $F[\mathbf{M}]$ . Mühlbauer *et al.* have calculated the energy gain from thermal fluctuations for the conical and the skyrmion lattice phase in Ref. 24. They find that especially the skyrmion lattice benefits from fluctuations, which eventually leads to its stabilization with respect to the competing conical phase for a certain field range, c. f. Fig. 4.1.5 for a comparison to the mean-field energies. Fig. 4.2.6 shows the obtained phase diagram including gaussian fluctuations. As observed in the experiment (c. f. phase diagram in Fig. 3.2.8), the skyrmion lattice phase is stable only in a small pocket close to the critical temperature for intermediate magnetic fields. On the right hand side of the vertical red dashed line, the fluctuation corrections to the dominant Fourier modes become larger than 20%, i. e.  $\delta \mathbf{M}_{\mathbf{k}}^{\text{fluct}} > 0.2 \mathbf{M}_{\mathbf{k}}^0$ , and the perturbative treatment breaks down. On the left hand side of this line, the perturbative treatment is controlled in the sense that the fluctuation corrections are small (<20%) and the existence of the skyrmion lattice phase can be guaranteed in the gray colored pocket. Below the lower horizontal red dashed line, the skyrmion lattice becomes unstable again.

This fluctuation analysis remarkably shows that no additional interactions or phenomenological parameters are required to stabilize the skyrmion lattice phase, as proposed by several authors [45–49], which implies that the formation of a skyrmion lattice is a generic feature of chiral magnets.



**Figure 4.2.6.:** Phase diagram for chiral magnets incorporating gaussian thermal fluctuations. The skyrmion lattice phase (called “A-crystal” in the figure) becomes unstable with respect to the conical phase below the horizontal red dashed line. On the right hand side of the vertical red dashed line, the fluctuation contribution to the magnetic structure becomes larger than 20% and the perturbation theory breaks down. On the left hand side of this line, fluctuations are small enough ( $<20\%$ ) to justify the perturbative treatment and the existence of the skyrmion lattice phase can be guaranteed in the gray colored pocket. The inset is explained in Fig. 4.1.5. Picture taken from Ref. 24.



# 5. Phase diagram and thermodynamics from Monte Carlo simulations

In this section, I extend the fluctuation analysis presented by Mühlbauer *et al.* in Ref. 24 by a large scale classical Monte Carlo simulation. This approach includes fluctuations beyond gaussian order in a non-perturbative manner and is thus ideally suited to test the stability of the skyrmion lattice phase, especially in the region close to  $T_c$ , where the perturbative treatment breaks down due to the strong thermal fluctuations.

Simulations for two-dimensional systems have been performed before [36, 50] and the phase diagrams obtained are in excellent agreement with recent experiments on thin films of  $\text{Fe}_{0.5}\text{Co}_{0.5}\text{Si}$  [36]. So far, these simulations have not yet been extended to three dimensions since they are numerically very demanding. In this chapter, I close this gap and present the first complete Monte Carlo study of three-dimensional chiral magnets. Most of the results presented in this chapter have been published in Ref. 51.

The structure of this chapter is as follows: I first discuss the numerical implementation with a special emphasis on the discretization of the continuum model in Sec. 5.1. In Sec. 5.2, I present several thermodynamical quantities across the temperature driven phase transition and compare them to experimental data. Finally, I conclude this chapter with a presentation of the full phase diagram in Sec. 5.3 and a discussion of the numerically obtained structure factors in Sec. 5.4.

## 5.1. Numerical implementation and discretization of the continuum model

A major reason why the previous Monte Carlo studies for two-dimensional systems have not been extended to three-dimensional systems yet (except for an energy minimization study that does not take into account thermal fluctuations [52]) is the high computational effort: One has to simulate very large systems in order to observe multiple twists of the helical structure. Since the length of

the helical modulations is controlled solely by the ratio  $J/D$ , one might naively think that one can simply reduce the pitch-length by increasing the DM interaction. If, however, the magnetization varies significantly from site to site, as it does for short pitch-lengths, the assumption of a continuum model is not justified anymore. In fact, it will be shown below that the discretized model used for the Monte Carlo simulations deviates from the continuum model in terms which are in leading order proportional to  $k^4$  and thus relevant for all pitch-lengths that are accessible in numerical simulations.

Assuming a slow variation of the magnetization, one can resort to the already introduced Hamiltonian (c.f. Sec. 4.1)

$$H = \int d^3r \left[ J (\nabla \mathbf{M}(\mathbf{r}))^2 + 2D \mathbf{M}(\mathbf{r}) \cdot (\nabla \times \mathbf{M}(\mathbf{r})) - \mathbf{B} \cdot \mathbf{M}(\mathbf{r}) \right], \quad (5.1.1)$$

for the description of chiral magnets [21, 24]. Instead of using e.g. the full B20 structure, that is often found in chiral magnets, for the Monte Carlo simulations, one can also implement this model on a simple cubic lattice, which, in principle, has inversion symmetry, unless it is explicitly broken as it is done below. Extending the lattice Hamiltonian proposed in Refs. 36 and 50 to three-dimensional systems yields<sup>1</sup>

$$\begin{aligned} H = & -J \sum_{\mathbf{r}} \mathbf{S}_{\mathbf{r}} \cdot (\mathbf{S}_{\mathbf{r}+\hat{\mathbf{x}}} + \mathbf{S}_{\mathbf{r}+\hat{\mathbf{y}}} + \mathbf{S}_{\mathbf{r}+\hat{\mathbf{z}}}) - \mathbf{B} \cdot \sum_{\mathbf{r}} \mathbf{S}_{\mathbf{r}} \\ & - D \sum_{\mathbf{r}} (\mathbf{S}_{\mathbf{r}} \times \mathbf{S}_{\mathbf{r}+\hat{\mathbf{x}}} \cdot \hat{\mathbf{x}} + \mathbf{S}_{\mathbf{r}} \times \mathbf{S}_{\mathbf{r}+\hat{\mathbf{y}}} \cdot \hat{\mathbf{y}} + \mathbf{S}_{\mathbf{r}} \times \mathbf{S}_{\mathbf{r}+\hat{\mathbf{z}}} \cdot \hat{\mathbf{z}}), \end{aligned} \quad (5.1.2)$$

where  $\hat{\mathbf{x}}, \hat{\mathbf{y}}$  and  $\hat{\mathbf{z}}$  are the basis vectors of the simple cubic lattice. Even though this Hamiltonian does not provide any explicit anisotropies that favor a certain crystal direction at  $\mathbf{B} = 0$ , such anisotropies are automatically generated in the lattice model due to discretization errors and finite size effects and it is thus not necessary to add these terms explicitly to the Hamiltonian.

Using feedback optimized parallel tempering (c.f. Sec. 2.2 and 2.3), it was possible to equilibrate the transition from the paramagnetic to the ordered phases for lattice sizes up to  $N = L^3$ ,  $L = 20$  spins by using up to 600 replicas. At  $L = 30$ , a significantly larger number of replicas would have been necessary, which is the reason why the analysis is mostly restricted to  $L = 20$ .

Several things have to be taken into account in the selection of suitable parameters  $J$  and  $D$  for the simulation: On the one hand, one would like to have a

---

<sup>1</sup>Note that the parameters  $J, D$  and  $B$  from the continuum model Eq. (5.1.1) and the discretized version Eq. (5.1.2) are not in one-to-one correspondence due to the coarse graining procedure.

large pitch-length such that the magnetization varies smoothly enough that the assumption of the continuum model Eq. (5.1.1) is justified, whereas, on the other hand, one would like to observe multiple twists of the magnetization within a system size that is still tractable in a numerical simulation. A reasonable compromise is given by a pitch length of 10 lattice sites, which can be obtained in the lattice model by choosing<sup>2</sup>  $D/J = \tan(2\pi/10) \approx 0.727$ . As mentioned before, these relatively short pitch lengths lead to deviations between the lattice model and the continuum model which have to be taken seriously. This can be seen as follows: On the lattice, the Fourier transform of the ferromagnetic Heisenberg interaction term reads

$$H_{\text{FM}} = J \sum_{\mathbf{k}} \alpha_{\mathbf{k}} \mathbf{S}_{\mathbf{k}} \cdot \mathbf{S}_{-\mathbf{k}}, \quad (5.1.3)$$

with

$$\begin{aligned} \alpha_{\mathbf{k}} &= -(\cos(k_x) + \cos(k_y) + \cos(k_z)) \\ &= -3 + \frac{1}{2}(k_x^2 + k_y^2 + k_z^2) - \frac{1}{24}(k_x^4 + k_y^4 + k_z^4) + \mathcal{O}(k^6), \end{aligned} \quad (5.1.4)$$

which implies that all kinds of higher order momentum terms are generated (the constant term only shifts the energies). Comparing this to the Fourier transform of the ferromagnetic Heisenberg term of the continuum model ( $\propto (\nabla \mathbf{M})^2$ ), one finds that only terms quadratic in  $k$  are present there. In principle, one would not be worried about the higher-order terms in the series if the ordered state was described by a uniform spin texture, as it is e.g. the case in the purely ferromagnetic Heisenberg model. In general, however, the critical modes do not become soft at zero momentum, but at a finite-ordering wave-vector  $\mathbf{Q} \neq 0$ . Due to the use of relatively small lattice sizes in the numerical simulations (compared to the modulation period of the helices),  $|\mathbf{Q}|$  is in general of the order  $\lesssim 1$  (for a pitch length of 10 lattice sites one has  $|\mathbf{Q}| \approx 0.63$ ). Consequently, the contribution of the higher order terms in Eq. (5.1.4) is not negligible and spoils the analysis. In fact, it turns out that it is impossible to reproduce the experimentally observed shape of the phase diagram for the chosen pitch-length, c.f. Sec. 5.3.

In order to compensate these induced anisotropies, one can add next-nearest-neighbor interactions  $H'$  to the Hamiltonian, chosen such that they do not break any symmetries of the underlying system and give a better approximation of the continuum field theory in the sense that they compensate the higher order terms.

---

<sup>2</sup>The energy for a helix with wave vector  $\mathbf{k}$  is according to lattice Hamiltonian in Eq. 5.1.2 given by  $E = -J \cos(k) - K \sin(k)$  and thus minimized for  $\tan(k) = D/J$ . For small  $k$ , one has  $\tan(k) = k + \mathcal{O}(k^3)$ , and this result agrees with the result  $k = D/J$  from the continuum theory. See Ref. 50 for details.

They assume the form

$$\begin{aligned}
 H' = & J' \sum_{\mathbf{r}} \mathbf{S}_{\mathbf{r}} \cdot (\mathbf{S}_{\mathbf{r}+2\hat{x}} + \mathbf{S}_{\mathbf{r}+2\hat{y}} + \mathbf{S}_{\mathbf{r}+2\hat{z}}) \\
 & + D' \sum_{\mathbf{r}} (\mathbf{S}_{\mathbf{r}} \times \mathbf{S}_{\mathbf{r}+2\hat{x}} \cdot \hat{x} + \mathbf{S}_{\mathbf{r}} \times \mathbf{S}_{\mathbf{r}+2\hat{y}} \cdot \hat{y} + \mathbf{S}_{\mathbf{r}} \times \mathbf{S}_{\mathbf{r}+2\hat{z}} \cdot \hat{z}).
 \end{aligned} \tag{5.1.5}$$

The full  $\alpha_{\mathbf{k}}$  of the ferromagnetic Heisenberg term, c. f. Eq. (5.1.3), is then given by

$$\begin{aligned}
 \alpha_{\mathbf{k}} = & -3 \left(1 - \frac{J'}{J}\right) + \frac{1}{2} \left(1 - \frac{4J'}{J}\right) (k_x^2 + k_y^2 + k_z^2) \\
 & - \frac{1}{24} \left(1 - \frac{16J'}{J}\right) (k_x^4 + k_y^4 + k_z^4) + \mathcal{O}(k^6),
 \end{aligned} \tag{5.1.6}$$

which immediately shows that one can compensate the anisotropies in leading order by choosing  $J' = J/16$ . Repeating the same procedure for the DM interaction leads to  $D' = D/8$ . One should note that this compensation rescales the effective  $J$  and  $D$  (given by the prefactors of leading order terms in  $k$ ) both by the same factor of  $3/4$ . In addition to that, there is also a modification of the pitch-length of the helical structure, which becomes slightly shorter than with nearest neighbor interactions alone.

To conclude, the reason for the need of this compensation is that the approximation of the gradient terms in the continuum theory Eq. (5.1.1) solely by nearest-neighbor interactions as in Eq. (5.1.2) is not accurate if the spin configuration varies significantly from site to site. If one could simulate larger lattices, one could use a smaller value of  $D$ , which, in turn, increases the modulation period of the helices. The spin configuration would then vary more smoothly, and consequently, the nearest-neighbor approximation of the lattice model Eq. (5.1.2) improves.

The concept using next-nearest-neighbors to improve the approximation of derivatives is also known for ordinary functions which are given on an equally spaced grid with distance  $h$ . While a simple central approximation

$$f'(x_i) = \frac{f(x_i + h) - f(x_i - h)}{2h} \tag{5.1.7}$$

that takes into account only function values next to the point at which the derivative is approximated, i. e. at  $x_i \pm h$ , yields an error of  $\mathcal{O}(f'''(y)h^2)$ , where  $y \in [x-h, x+h]$  [20], a better approximation can be achieved if one also considers function values at  $x_i \pm 2h$ . For instance, the approximation

$$f'(x_i) = \frac{f(x_i - 2h) - 8f(x_i - h) + 8f(x_i + h) - f(x_i + 2h)}{12h} \tag{5.1.8}$$



yields an error which only scales as  $\mathcal{O}(f^{(5)}(y)h^4)$ , where  $y \in [x - 2h, x + 2h]$  [20] and is thus more accurate. Details on this topic can be found e. g. in Ref. 20.

Another problem related to the pitch-length is the choice of optimal boundary conditions. For periodic boundary conditions, one can expect strong finite size effects since it is not possible to choose the parameters such that helices with different orientations, e. g. in the  $\langle 100 \rangle$  and  $\langle 111 \rangle$  direction, fit perfectly on the lattice at the same time. Additionally, the shape of a cubic system of size  $L^3$  is incompatible with the triangular skyrmion lattice, which penalizes this phase in particular. One might thus think that open boundary conditions might be better suited for numerical simulations, but these lead to polarized spins on the boundaries due to missing nearest-neighbor ferromagnetic and DM interactions, which makes these spins profit maximally from an alignment in the magnetic field. Therefore, periodic boundary conditions have been used in all simulations and it was found that these did not lead to major complications in the simulations for the chosen parameters  $J$  and  $D$  in the sense that all results compare very well to experimental findings.

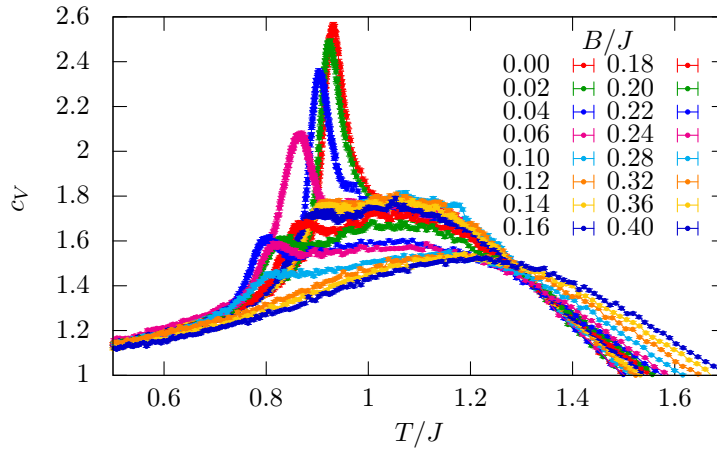
The most severe problem one encounters in the Monte Carlo simulation is, however, given by the topological stability of the skyrmion lattice phase. Even in a feedback optimized parallel tempering simulation according to Sec. 2.2 and 2.3, it is not possible to equilibrate the phase transition from the skyrmion lattice to the conical phase and the former one remains as a metastable state down to lowest temperatures. This metastability can also be observed experimentally [37] and, even though it makes the determination of the phase boundaries difficult, it can be utilized to get some fundamental insight into the topological unwinding of the skyrmion lattice as it is shown in Ch. 6. Strong hysteresis is also observed for the helical to conical transition, where it is very difficult to drive the reorientation of the helical propagation vector solely by local Monte Carlo updates once a specific orientation is selected.

## 5.2. Thermodynamic quantities

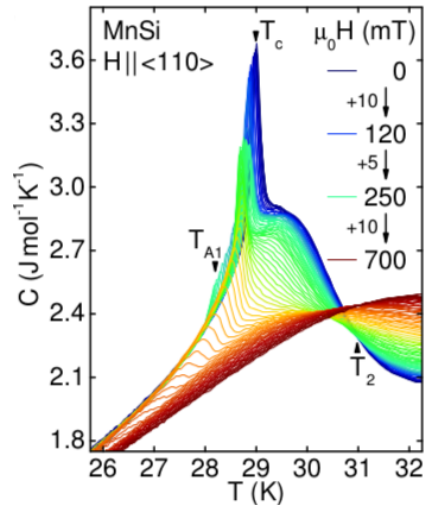
Fig. 5.2.1 shows the results for specific heat

$$c_V = \frac{\partial E}{\partial T} = \frac{\langle E^2 \rangle - \langle E \rangle^2}{NT^2} \quad (5.2.9)$$

obtained by Monte Carlo simulations for a system size  $N = L^3$ ,  $L = 20$  in dependence on temperature for different magnetic fields.



**Figure 5.2.1:** The specific heat in dependence on temperature for various fields strengths at  $L = 20$ . The broadened first-order peak vanishes continuously as the field is increased. The crossing point at  $T/J \approx 1.3$  marks a Vohllhardt-invariance, see main text.



**Figure 5.2.2:** Experimentally measured specific heat of MnSi.  $T_c$  marks the position of the first-order peak at low fields,  $T_2$  the Vohllhardt-invariance and  $T_{A1}$  the transition from the skyrmion lattice to the conical phase. See Ref. 53 for more details and images of single curves. Picture taken from Ref. 53.

First of all, one finds a crossing point for all curves at  $T/J = T^*/J \approx 1.3$ . This crossing point, a so-called Vollhardt-invariance [54], has also been observed experimentally in MnSi [53, 55] and is (in this case) related to a turning point in the magnetic susceptibility  $\chi$ . To see this, one notes that the universality of the specific heat at  $T = T^*$  implies

$$0 = \left. \frac{\partial}{\partial B} c_V \right|_{T=T^*} = T \left. \frac{\partial^2 S}{\partial B \partial T} \right|_{T=T^*}, \quad (5.2.10)$$

which can be rearranged using the Maxwell relation  $\partial S/\partial B = \partial M/\partial T$  to

$$0 = T \left. \frac{\partial^2 M}{\partial T^2} \right|_{T=T^*} = TB \left. \frac{\partial^2 \chi}{\partial T^2} \right|_{T=T^*}, \quad (5.2.11)$$

where it was used that  $M = \chi B$  for sufficiently small fields. The appearance of a turning point in the magnetic susceptibility has been explained recently by the occurrence of a Brazovskii-scenario [56, 57], which describes how the abundance of soft chiral fluctuations close to the critical point drives the transition to the helical phase weakly first-order. This abundance of soft modes originates from the fact that the helical modulations do not become soft at a single point in  $k$ -space but on a sphere with radius  $k = D/J$ . Consequently, the density of states for critical fluctuations exhibits a one-dimensional singularity so that interaction corrections are expected to drive a strong suppression of the correlation length and, eventually, a fluctuation-induced first-order transition [57].

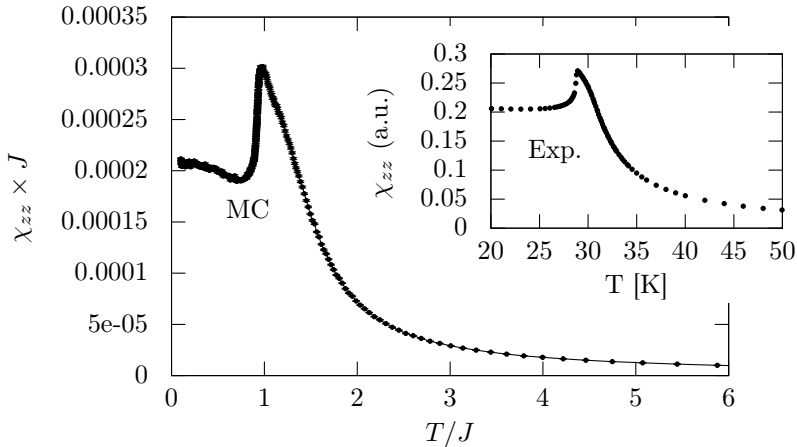
Fig. 5.2.3 shows the experimentally measured magnetic susceptibility for MnSi at zero-field as published in Ref. 57 (c. f. also Ref. 58 and 59 for other experimental data) together with the data obtained from the Monte Carlo simulations, which has been calculated from the magnetization per spin in direction of the magnetic field ( $\mathbf{B} = B\hat{\mathbf{z}}$ ) as

$$\chi_{zz} = \frac{\partial M_z}{\partial B_z} = \frac{\langle M_z^2 \rangle - \langle M_z \rangle^2}{T}. \quad (5.2.12)$$

The similarity between the two curves is striking, in particular the Monte Carlo data also features the above mentioned turning point related to the Vollhardt invariance at  $T/J = T^*/J \approx 1.3$ .

In the following, I discuss the remaining Monte Carlo data for each of the three ordered phases separately.

**Helical phase** At low fields, the specific heat features a slightly broadened first-order peak on top of a broader shoulder, indicating the transition to the helical phase. The broadening of the peak is typical for a fluctuation driven first-order transition [53, 57]. As the magnetic field is increased, the height of the peak

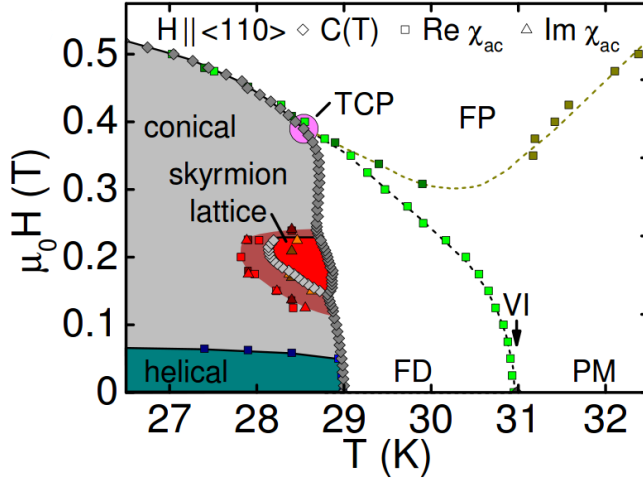


**Figure 5.2.3.:** Magnetic susceptibility  $\chi_{zz}$  as measured in the Monte Carlo simulation for  $L = 20$  (large image) and in MnSi (inset). The experimental data has been provided by A. Bauer and was published in Ref. 57.

decreases continuously, as it is also observed experimentally upon approaching the tricritical point located at larger fields [53], c. f. Figs. 5.2.2 and 5.2.4.

In the Monte Carlo simulations, the direction of the helical wave-vector depends on system size. For the size of  $N = 20^3$  that was used in the parallel tempering simulations, the helical propagation vector aligns roughly in a  $\langle 110 \rangle$  direction since the length of the system in that direction,  $L_{\langle 110 \rangle} = 20\sqrt{2} \approx 28.3$ , is approximately compatible with the chosen pitch-length of  $\lambda = 10$  lattice sites. For simulated annealing runs with a lattice size of  $L = 30$ , the helical propagation vector aligned roughly in a  $\langle 111 \rangle$  direction, which is again approximately compatible with the length of the helical modulations ( $L_{\langle 111 \rangle} = 30\sqrt{3} \approx 52$ ).

**Skyrmion lattice phase** In order to identify a phase transition into the skyrmion lattice phase, one has to define a suitable order parameter which is sensitive to the formation of skyrmions. A good choice is the topological winding number since it is independent of many details such as the orientation and pitch-length of the helices that build up the skyrmion lattice. For the calculation of the average winding number per layer perpendicular to the applied field, the bottom of each unit cell of every layer is divided into two triangles as shown in Fig. 5.2.5. Afterwards, the solid angle  $\Omega_i$  covered by the three spins on the edges of every



**Figure 5.2.4.:** Magnetic phase diagram of MnSi derived from the specific heat (diamonds) and the real part (squares) and imaginary part (triangles) of the ac susceptibility. One distinguishes the following regimes: helical order, conical order, skyrmion lattice, fluctuation disordered (FD), paramagnetic (PM) and field-polarized (FP). TCP denotes the tricritical point and VI the Völler-Hardt-invariance. Picture taken from Ref. 53.

triangle is computed using the Oosterom-Strackee algorithm [60]

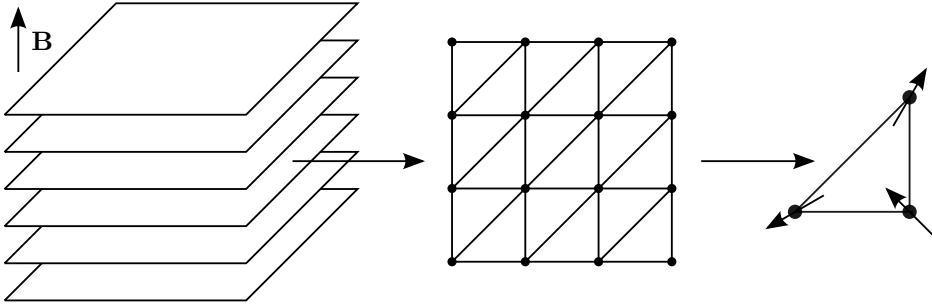
$$\Omega_i = \frac{\mathbf{S}_1 \cdot (\mathbf{S}_2 \times \mathbf{S}_3)}{1 + \mathbf{S}_1 \cdot \mathbf{S}_2 + \mathbf{S}_2 \cdot \mathbf{S}_3 + \mathbf{S}_3 \cdot \mathbf{S}_1}. \quad (5.2.13)$$

The total winding number of a layer is then obtained by summing over all triangles in that layer and dividing by  $4\pi$ ,

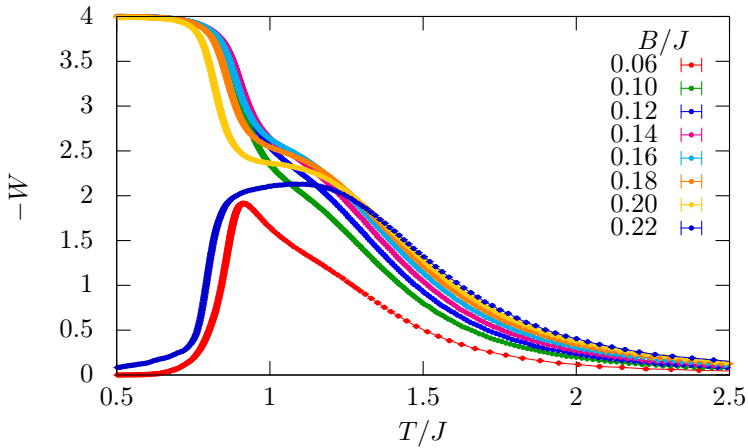
$$W = \frac{1}{4\pi} \sum_i \Omega_i. \quad (5.2.14)$$

Fig. 5.2.6 shows the average winding number per layer in dependence on temperature for various field strengths. For all field values, one finds the above mentioned strongly fluctuating regime at  $T \approx J$ , in which the winding number is non-zero on average. Below a temperature of  $T/J \approx 0.9$ , the winding number drops to zero except in the intermediate field range  $0.10 \lesssim B \lesssim 0.20$ , where it approaches exactly the constant value 4, indicating the transition to a skyrmion lattice phase with four skyrmion tubes (the number of skyrmions is limited by the lattice size  $L = 20$ ), whereas it enters a non-topological phase with vanishing winding number for all other field values.

Since skyrmions are topologically protected, it is very difficult to destroy the



**Figure 5.2.5.:** Calculation of the winding number: The system is first divided into layers perpendicular to the magnetic field. Afterwards, the bottom of every unit cell in each layer is divided into two triangles and for each triangle, the solid angle covered by the spins on its corners is calculated using the Oosterom-Strackee algorithm, see main text.



**Figure 5.2.6.:** Average winding number per layer in dependence on temperature for various field strengths at  $L = 20$ . For  $0.10 \lesssim B \lesssim 0.20$ , the winding number approaches exactly the constant value 4 as the temperature is lowered, indicating a skyrmion lattice phase with four skyrmion tubes.

skyrmion lattice phase at low temperatures, where thermal fluctuations are weak. In fact, it turns out that even a feedback optimized parallel tempering algorithm according to Sec. 2.2 and 2.3 is not able to equilibrate the phase transition from the skyrmion lattice to the conical phase. Instead, one finds that the system always remains in the (metastable) skyrmion lattice phase down to lowest temperature, which is the reason why one does not observe the winding number decrease to zero again for smaller temperatures in Fig. 5.2.5. It is nevertheless possible to determine the phase boundary between the two competing phases, c. f. Sec. 5.3.

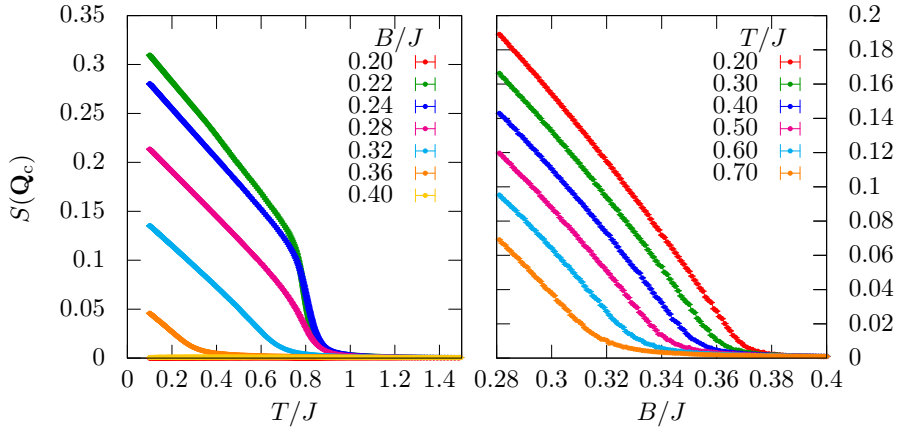
**Conical phase** The conical phase can be detected e. g. by the magnetic structure factor

$$S(\mathbf{Q}_c) = \frac{1}{N^2} \sum_{ij} e^{-i\mathbf{Q}_c \cdot (\mathbf{r}_i - \mathbf{r}_j)} \langle \mathbf{S}_i \cdot \mathbf{S}_j \rangle, \quad (5.2.15)$$

at the conical wave-vector<sup>3</sup>  $\mathbf{Q}_c = (0, 0, \text{atan}(D/J))$ . Fig. 5.2.7 shows the magnetic structure factor as a function of temperature for different field strengths as well as a function of field for different temperatures. As the system is cooled at constant field, the structure factor becomes non-zero below a certain temperature, indicating a phase transition to the conical phase. If the field is just above the level for which the skyrmion lattice is still stabilized, i. e.  $B/J \approx 0.20$ , the structure factor seems to jump discontinuously at the phase transition, whereas it rises continuously for larger field values. From a numerical point of view, it is in general difficult to make statements about the nature of a phase transition just by the analysis of the temperature dependence of the structure factor. An unambiguous statement can, however, be made by recording a frequency histogram of the structure factor exactly at the critical temperature: If the phase transition is second order, there will be only one peak in the histogram since the structure factor rises continuously. If, on the other hand, the transition is first-order, i. e. if there is phase coexistence, one should find two separated peaks in the histogram, corresponding to the values in the respective phases. Fig. 5.2.8 shows the structure factor histograms for various values of the magnetic field. One can clearly see that a double peak structure is present for values just above the level for which the skyrmion lattice is still stabilized, whereas only a single-peak structure is visible for larger field values. This observation is consistent with the phase transition turning from first- to second-order at a tricritical point as the magnetic field is increased. This tricritical point has also been observed experimentally in MnSi [53], c. f. Fig. 5.2.4.

If the field is increased at constant temperature (right part of Fig. 5.2.7), the

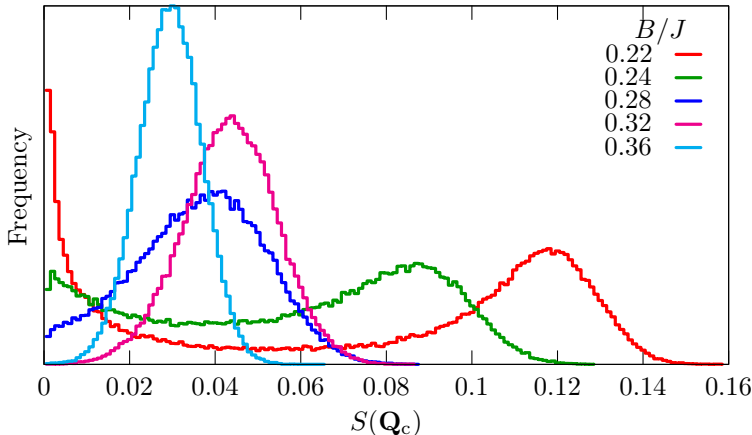
<sup>3</sup>In the simulations, the magnetic field is applied along z-direction, i. e.  $\mathbf{B} = B\hat{\mathbf{z}}$



**Figure 5.2.7.:** The structure factor at the conical wave-vector  $\mathbf{Q}_c$  (Eq. (5.2.15)) as a function of temperature for different magnetic fields (left) and as a function of the magnetic field for different temperatures (right).

structure factor decreases continuously to zero as the system enters a fully polarized phase. The continuity of the structure factor at the transition implies that the nature of the phase transition is second order.





**Figure 5.2.8.:** Frequency histograms of structure factor at the conical wave-vector  $\mathbf{Q}_c$  (Eq. (5.2.15)) and at the critical temperature for several magnetic fields at  $L = 20$ .

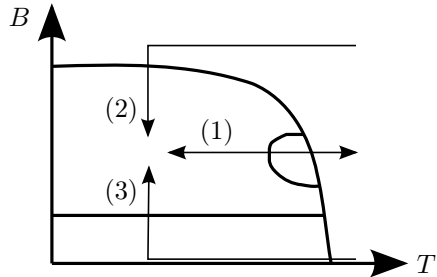
### 5.3. Determination of the phase boundaries

The phase boundaries between the paramagnetic and the various ordered phases have been determined from the peak in the specific heat (helical phase) as well as the susceptibilities of the corresponding order parameters, i. e. winding number (skyrmion lattice) and structure factor at the conical wave-vector  $\mathbf{Q}_c$  (conical phase). The inner phase boundaries between the ordered phases can unfortunately not be determined that easily. Even in a parallel tempering simulation with an optimized temperature set according to Secs. 2.2 and 2.3, the skyrmion lattice phase remains metastable down to the lowest temperatures and no transition to the conical phase is observed. The reason for this is that the skyrmion phase is topologically protected and hence very difficult to destroy. The topological unwinding of this phase is discussed in more detail in Ch. 6.

For the transition between the helical and the conical phase, one also observes a large hysteresis since it is very difficult to change the orientation of the helical structure with *local* spin updates alone. In order to determine the phase boundaries between the ordered phases, one has to compare their free energies. Unfortunately, the free energy is (in contrast to the energy) a quantity which can not be accessed that easily within a Monte Carlo simulation. One way to estimate the free energy difference between two states is to simulate both states at the same temperature and magnetic field and to record the transition probabilities

$$P(s \rightarrow s') = \min(1, \exp((E_s - E_{s'})/T)) \quad (5.3.16)$$

**Figure 5.3.9:** Different cooling paths used to determine the phase boundaries in a schematic phase diagram: (1) Cooling at intermediate magnetic fields, (2) field cooling at high field and subsequent decrease of the field to the target value, (3) zero-field cooling and subsequent increase of the field to the target value.



from one state to the other throughout the simulation, without ever performing the actual spin update. Since the free energy is related to the probability  $p(s)$  that a certain state  $s$  is occupied, i. e.  $F(s) = -T \log(p(s))$ , one can use the detailed balance condition Eq. (1.1.10) to estimate the free energy difference between two states according to Ref. [61] as

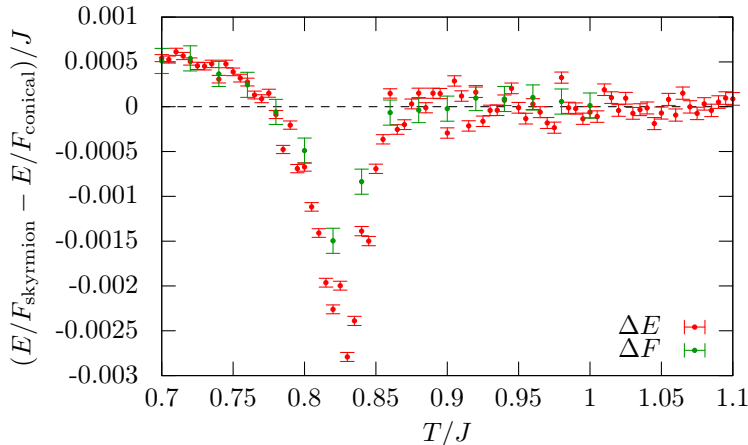
$$\Delta F = -T \log \left( \frac{p(s)}{p(s')} \right) = -T \log \left( \frac{P(s' \rightarrow s)}{P(s \rightarrow s')} \right). \quad (5.3.17)$$

Unfortunately, this method requires very large statistics in order to determine the phase boundary with a sufficient accuracy. For convenience, the energy difference between two states was used most of the time to estimate the phase boundary. Although this is strictly speaking not correct, it is discussed below that it leads to almost identical results.

The energies for the skyrmion lattice phase can be obtained from the parallel tempering simulation (path 1 in Fig. 5.3.9), whereas the energies for the conical phase can be measured by cooling the system at high field to the desired temperature followed by decreasing the field to the target value (path 2 in Fig. 5.3.9). This way, the system enters the conical phase without ever being in the topologically protected skyrmion phase. The energies are then measured for different temperatures up to the paramagnetic transition. Throughout this process, it is checked that the system never leaves the conical phase by monitoring the corresponding order parameter.

Fig. 5.3.10 shows the energy as well as the free energy difference between the skyrmion and the conical phase for a linear lattice size of  $L = 20$  and  $B/J = 0.16$ . The zero crossings of the energy and the free energy differences are almost identical, which justifies to use the energy difference to a good approximation.

For small system sizes, one can expect that the *triangular* skyrmion lattice, which is incompatible with two boundaries of the simulated *cubic* cell, is penalized by rather strong finite size effects, whereas the conical phase, which is at most incompatible with one boundary, should be less affected. For larger lattices, however, one can expect that the measured energies are closer to the respective

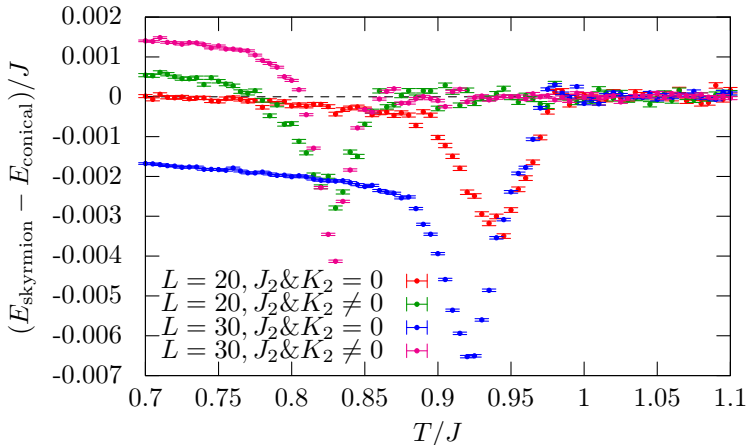


**Figure 5.3.10.:** The energy and free energy difference between the skyrmion lattice and the conical phase for  $L = 20$  and  $B/J = 0.16$  with discretization anisotropy compensation by next-nearest neighbor interactions according to Sec. 5.1. The free energy difference has been rescaled by a factor of 80 to fit on the same scale.

values in the thermodynamic limit since finite size effects become less important. Fig. 5.3.11 shows the energy differences between the skyrmion lattice and the conical phase exemplarily for fixed field in dependence on temperature for different systems sizes. Simulations with and without next-nearest neighbor interactions have been performed at  $B/J = 0.16$  and  $B/J = 0.21\bar{3}$ , respectively. These values differ by a factor of  $4/3$  to account for the modification of the effective  $J$ , c. f. Sec. 5.1 for details.

For  $L = 20$ , where the skyrmion lattice is penalized by rather strong finite size effects, the conical phase becomes eventually the ground state at low temperatures even without the anisotropy compensation, but the skyrmion phase extends over a wide range in temperature. With the compensation, the skyrmion phase remains restricted only to a temperature range close to  $T_c$ , as it also observed experimentally. At  $L = 30$ , the need for the anisotropy compensation becomes even more evident: Without the compensation, the skyrmion lattice remains the ground state down to  $T = 0$  since it is less penalized by finite size effects. With the compensation, however, it remains restricted to a small temperature region again.

In order to obtain the energy difference between the helical and conical phase in dependence on the field strength, the system is cooled to a target temperature

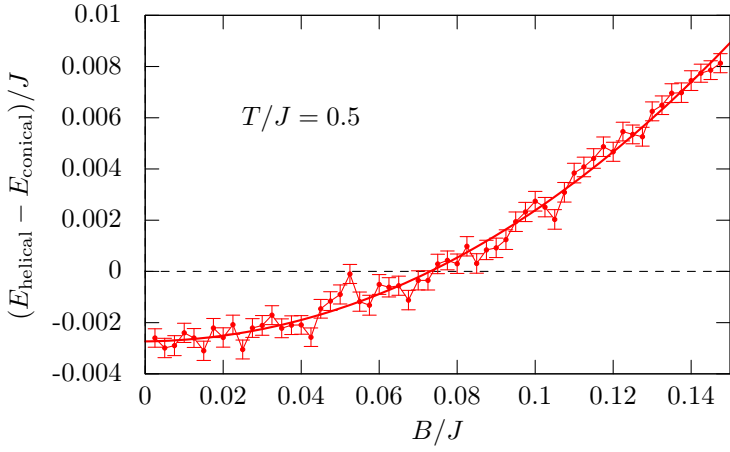


**Figure 5.3.11.:** The energy difference per spin between the skyrmion lattice and the conical phase for different lattice sizes with and without discretization anisotropy compensation by next-nearest neighbor interactions. Simulations without (with) anisotropy compensation were recorded at  $B/J = 0.213$  ( $B/J = 0.16$ ), see main text for explanations. Note that the effective  $J$  is rescaled by a factor  $3/4$  in the case of finite next-nearest neighbor interactions, c. f. Sec. 5.1.

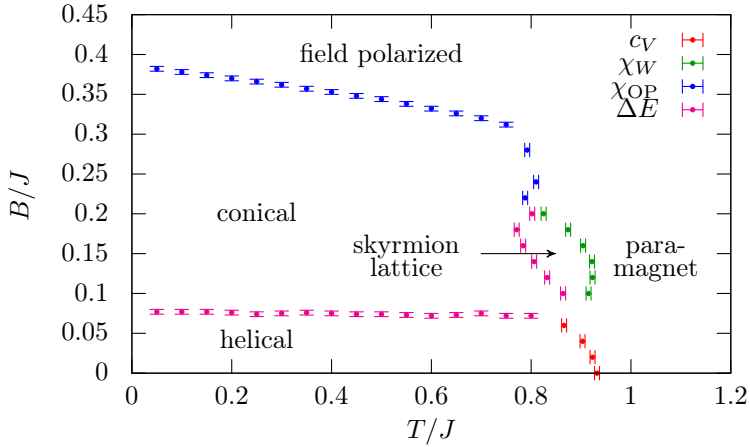
both at large and at zero field (paths 2 and 3 in Fig. 5.3.9) such that the system is in the spin polarized or helical phase, respectively. Afterwards, the field is reduced or increased, respectively, while the energies are measured. Fig. 5.3.12 shows exemplarily the energy difference between the two phases in dependence on the magnetic field at constant temperature. The phase boundary is then determined from the zero-crossing of a fit to the corresponding data.

Fig. 5.3.13 shows the phase diagram for a lattice size of  $L = 20$ . The similarity with the experimentally observed phase diagrams (c. f. Fig. 3.2.8 and 5.2.4) is striking and proves that the minimal model Eq. (5.1.2) is indeed sufficient to reproduce all experimental findings. In particular, it proves that thermal fluctuations alone are indeed sufficient to stabilize the skyrmion lattice and that this assertion holds beyond gaussian order. Furthermore, it was conclusively shown that no additional interactions or anisotropies are needed to stabilize the skyrmion lattice as it was proposed by several authors [45–49].

From a simulation point of view, the crucial role of lattice discretization anisotropies was identified and a possible way to compensate them has been proposed and implemented.



**Figure 5.3.12.:** The energy difference per spin between the helical and the conical phase in dependence on the magnetic field at  $T/J = 0.5$  for  $L = 20$ . The solid line represents a fit to the data.

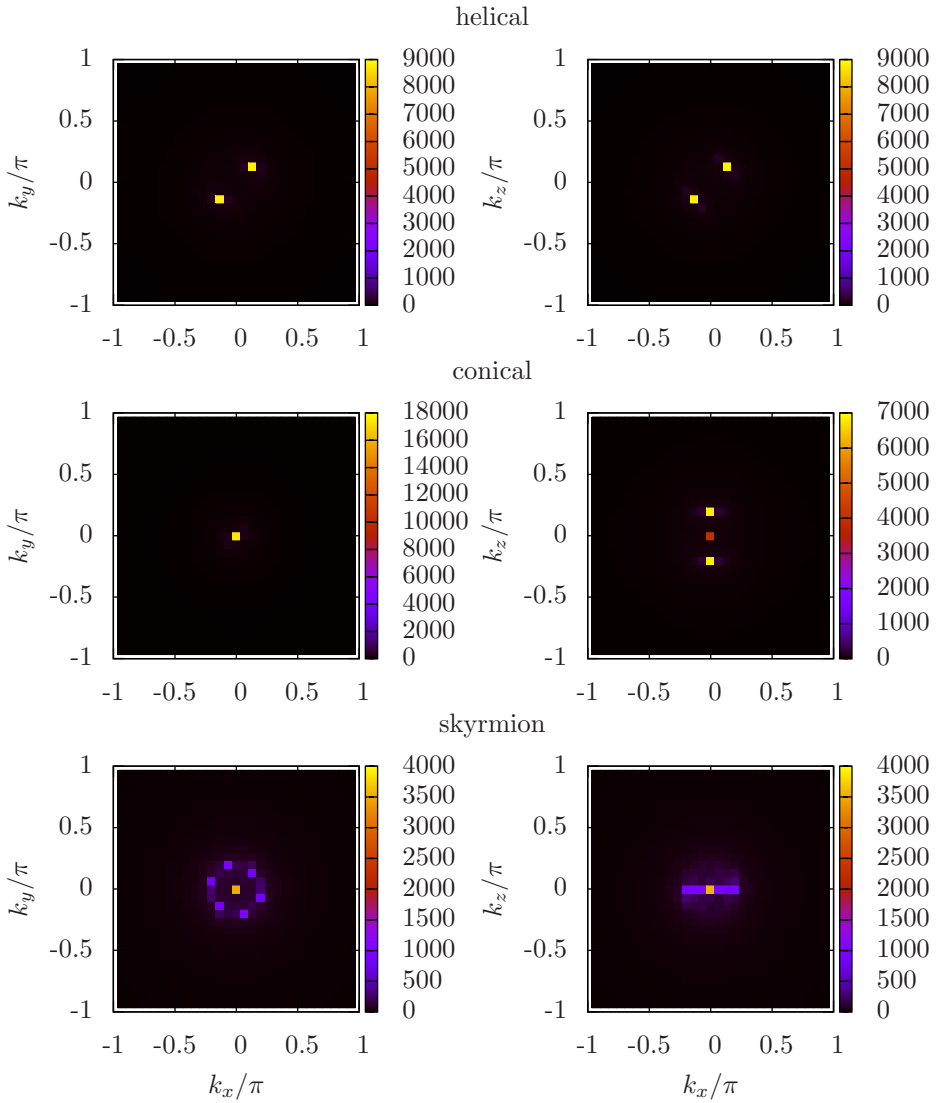


**Figure 5.3.13.:** Phase diagram for  $L = 20$  as determined by the peak in the specific heat ( $c_V$ ), the peak in susceptibility of the winding number ( $\chi_W$ ) or conical order parameter ( $\chi_{OP}$ ) and the crossing of the respective energies of the competing phases ( $\Delta E$ ). The error-bars are due to the uncertainty in the determination of the maximum of the thermodynamic quantity or zero-crossing of the energy difference.

## 5.4. Structure factors

To conclude this chapter, the structure factors of the three different ordered phases are shown in Fig. 5.4.14 for a system of size  $L = 30$ . The states used for the calculation of the structure factor have been obtained by simulated annealing (skyrmion and helical phase) or by decreasing the field at constant temperature (conical phase). The larger lattice size was chosen to obtain a better resolution in  $k$ -space. Simulations with  $L = 20$  lead to identical results except that the helical propagation vector changes roughly to  $\langle 110 \rangle$ . Note that the structure factors have been integrated over the  $k$ -direction perpendicular to the plane shown in the figure to allow an easier identification of the phases.

As all other quantities before, the structure factors show a remarkable similarity to experimental findings, c. f. Fig. 3.1.5 and 3.2.6.



**Figure 5.4.14.:** Magnetic structure factors for the three different phases that occur in chiral magnets in the  $k_x-k_y$  and  $k_x-k_z$  plane, integrated over the  $k$ -direction perpendicular to the respective planes. The states used for the calculation of the structure factors have been obtained by simulated annealing (helical and skyrmion phase) and decreasing the field at constant temperature (conical phase). Parameters are  $(B, T) = (0, 0.5)$  (helical phase),  $(0.16, 0.84)$  (skyrmion phase) and  $(0.16, 0)$  (conical phase) as well as  $L = 30$ .





# 6. Emergent electrodynamics and magnetic monopoles

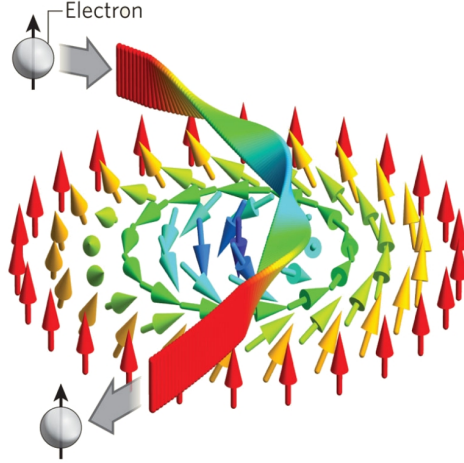
This chapter deals with the phase transition from the skyrmion lattice to the conical phase. Since the conical phase is, in contrast to the skyrmion lattice, an ordinary, non-topological phase, it is a question of fundamental interest how the system manages to unwind the topologically stable skyrmions during this transition. It turns out that this process is mediated by monopoles of an emergent magnetic field associated with the skyrmions.

Sec. 6.1 reviews the derivation of these fields in detail by analyzing the influence of a smoothly varying magnetic structure on conduction electrons. Sec. 6.2 deals with the measurement of the emergent magnetic field via the so-called topological Hall-effect in experiments. The experimental observation of the phase transition from the skyrmion to the conical phase by magnetic force microscopy and small angle neutron scattering experiments is discussed in Sec. 6.3. The underlying microscopic process of the phase conversion by magnetic monopoles is explained with the support of Monte Carlo simulations and topological arguments in Sec. 6.4. Sec. 6.5 concludes this chapter with a short comparison of these emergent monopoles to the monopoles found in frustrated “spin-ice” materials.

## 6.1. Emergent electric and magnetic fields

In this section, I closely follow Ref. 62 and review how conduction electrons are affected by a magnetic structure that contains skyrmions. It is shown that the movement of the electrons can be described elegantly in terms of *emergent* electric and magnetic fields carried by the skyrmions. These fields turn out to be *topologically* quantized and their influence on the electron movement can be measured e. g. in Hall-effect experiments.

Since the magnetic texture of a chiral magnet is usually very smooth in the sense that the magnetization twists on length scales much larger than the lattice spacing (e. g. in MnSi the pitch-length is about  $190 \text{ \AA}$  whereas the lattice spacing is on about  $4.56 \text{ \AA}$  [24]), one can assume that the spin of a conduction electron adjusts adiabatically to the direction of the local magnetization, c. f. Fig. 6.1.1.



**Figure 6.1.1.:** Adiabatic adjustment of the spin of a conduction electron as it passes the magnetic texture of a skyrmion. Picture taken from Ref. 63.

Assuming a free conduction electron whose spin couples to the direction of the local magnetization  $\hat{\mathbf{M}}(\mathbf{r}, t) = \mathbf{M}(\mathbf{r}, t)/|\mathbf{M}(\mathbf{r}, t)|$ , one can start with the simple Hamiltonian

$$H = \frac{\mathbf{p}^2}{2m} + J\boldsymbol{\sigma} \cdot \hat{\mathbf{M}}(\mathbf{r}), \quad (6.1.1)$$

where  $\mathbf{p}$  denotes the momentum of the electron,  $\boldsymbol{\sigma}$  is the vector of the three Pauli matrices and  $J < 0$  accounts for the coupling between the spin of the conduction electron and the local magnetization. The corresponding equation of motion for the wave function  $\psi$  of the conduction electron reads

$$i\partial_t\psi(\mathbf{r}, t) = \left[ \frac{\mathbf{p}^2}{2m} + J\boldsymbol{\sigma} \cdot \hat{\mathbf{M}}(\mathbf{r}) \right] \psi(\mathbf{r}, t). \quad (6.1.2)$$

In order to diagonalize the Hamiltonian, one can perform a unitary transformation  $U(\mathbf{r}, t)$  on the wave function which rotates the local coordinate system such that the local  $\hat{\mathbf{z}}$ -axis points always in the direction of the local magnetization and  $J\boldsymbol{\sigma} \cdot \hat{\mathbf{M}}(\mathbf{r})$  goes over into  $J\sigma_z$ . This transformation is given by

$$U(\mathbf{r}, t) = \exp(-i\theta\boldsymbol{\sigma} \cdot \mathbf{n}(\mathbf{r}, t)/2), \quad (6.1.3)$$

with  $\theta$  being the angle of the rotation and  $\mathbf{n}(\mathbf{r}, t) = \hat{\mathbf{z}} \times \hat{\mathbf{M}}(\mathbf{r})/|\hat{\mathbf{z}} \times \hat{\mathbf{M}}(\mathbf{r})|$  being the local rotation axis. Writing  $\psi(\mathbf{r}, t) = U(\mathbf{r}, t)\xi(\mathbf{r}, t)$  in Eq. (6.1.2) and multiplying

with  $U^\dagger(\mathbf{r}, t)$  from the left, one obtains

$$i\partial_t\xi(\mathbf{r}, t) = \left[ -iU^\dagger\partial_tU + \frac{(\mathbf{p} + iU^\dagger\nabla U)^2}{2m} + J\sigma_z \right] \xi(\mathbf{r}, t). \quad (6.1.4)$$

By identifying the emergent scalar and vector potentials,

$$V^e(\mathbf{r}, t) = -(i/q^e)U^\dagger(\mathbf{r}, t)\partial_tU(\mathbf{r}, t), \quad (6.1.5)$$

$$\mathbf{A}^e(\mathbf{r}, t) = -(i/q^e)U^\dagger(\mathbf{r}, t)\nabla U(\mathbf{r}, t), \quad (6.1.6)$$

one can rewrite the Hamiltonian in the familiar form known from minimal coupling,

$$i\partial_t\xi(\mathbf{r}, t) = \left[ q^eV^e + \frac{(\mathbf{p} - q^e\mathbf{A}^e)^2}{2m} + J\sigma_z \right] \xi(\mathbf{r}, t). \quad (6.1.7)$$

The meaning of the *emergent* charge  $q^e$ , which so far drops out in these expressions, will become clear shortly.

The adiabatic approximation justifies to treat the emergent potentials as a perturbation to the free Hamiltonian

$$H_0 = \frac{\mathbf{p}^2}{2m} + J\sigma_z, \quad (6.1.8)$$

which describes two bands, one corresponding to majority spins (spin pointing in direction of the local magnetization) and one to minority spins (spin pointing in the opposite direction). Since the spin-flip scattering length is estimated to be much larger than the distance between skyrmions [25], one can neglect spin-flip scattering and consider only the diagonal parts of the emergent potentials  $V^e$  and  $\mathbf{A}^e$  by projecting these onto the two bands, which yields [62]

$$E_i^e = -\partial_iV^e - \partial_tA_i^e = \mp \frac{1}{2q^e}\hat{\mathbf{M}} \cdot \left( \partial_i\hat{\mathbf{M}} \times \partial_t\hat{\mathbf{M}} \right), \quad (6.1.9)$$

$$B_i^e = \epsilon_{ijk}\partial_jA_k^e = \mp \frac{\epsilon_{ijk}}{4q^e}\hat{\mathbf{M}} \cdot \left( \partial_j\hat{\mathbf{M}} \times \partial_k\hat{\mathbf{M}} \right). \quad (6.1.10)$$

These two fields account for the Berry phase picked up by an electron on a closed path in its parameter space as its spin adiabatically follows the direction of the local magnetization. The sign of this phase is opposite for majority and minority spins [64] which motivates to define the emergent charge  $q^e$  as  $-1/2$  for majority and as  $+1/2$  for minority spins.

The emergent fields then have the same sign for both bands and are given by

$$E_i^e = \hat{\mathbf{M}} \cdot \left( \partial_i\hat{\mathbf{M}} \times \partial_t\hat{\mathbf{M}} \right), \quad (6.1.11)$$

$$B_i^e = \frac{\epsilon_{ijk}}{2}\hat{\mathbf{M}} \cdot \left( \partial_j\hat{\mathbf{M}} \times \partial_k\hat{\mathbf{M}} \right). \quad (6.1.12)$$

Eq. (6.1.11) implies that an emergent electric field can only exist if the direction of the magnetic structure is both space and time dependent. The space dependence is naturally given in chiral magnets, whereas the time dependence has to be created from outside. This can e. g. be achieved by driving a current through the sample, which causes a drift of the skyrmion lattice [25, 31, 65].

An emergent magnetic field can only arise in the skyrmion lattice phase since it is directly proportional to the skyrmion density  $\epsilon_{ijk}\hat{\mathbf{M}} \cdot (\partial_j\hat{\mathbf{M}} \times \partial_k\hat{\mathbf{M}})$ , c. f. Eqs. (3.3.3) and (3.3.4). Furthermore, the quantization of the winding number enforces the flux of the emergent magnetic field to be quantized as well and consequently each skyrmion carries exactly one (negative) flux quantum  $\Phi_0$ ,

$$\int_{\text{UC}} \mathbf{B}^e \cdot d\mathbf{A} = -\frac{2\pi}{|q^e|} \equiv -\Phi_0, \quad (6.1.13)$$

where UC denotes the magnetic unit cell of the skyrmion lattice.

## 6.2. Topological Hall effect

The emergent magnetic field can be observed experimentally by its influence on the movement of conduction electrons in Hall-effect measurements. Since the origin of the emergent magnetic field is rooted in the non-trivial topology of the magnetic structure, this effect is often referred to as the *topological* Hall-effect [66].

The normal Hall-effect occurs when electrons with charge  $q = -e$  and density  $n$  move with drift velocity  $\mathbf{v}_d$  through a sample in the presence of an external magnetic field  $\mathbf{B}$ , c. f. Fig. 6.2.2. The Lorentz force

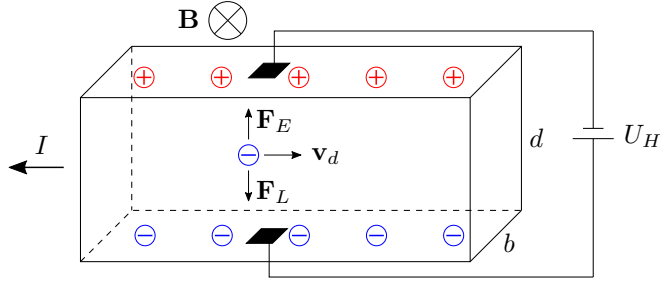
$$\mathbf{F}_L = -e\mathbf{v}_d \times \mathbf{B} \quad (6.2.14)$$

accelerates the electrons towards one end of the sample where they accumulate. This charge separation gives rise to an electric field  $\mathbf{E}$  and results in a force

$$\mathbf{F}_E = e\mathbf{E}, \quad (6.2.15)$$

which is oriented opposite to the Lorentz force.

Eventually, the two forces balance each other and the electrons drift unaffected by the magnetic and electric fields through the sample. The charge separation



**Figure 6.2.2.:** Illustration of the Hall effect. Electrons move from the left to the right with drift velocity  $\mathbf{v}_d$  through the sample. The Lorentz-force causes the electrons to move downwards leading to an excess of electrons at the bottom and a shortage at the top of the sample. This charge separation gives rise to an electric field which forces the electrons to move upwards again. The acting forces compensate each other and a Hall voltage can be measured between the top and bottom of the sample.

on the two sides of the sample (which effectively forms a capacitor) leads to a voltage drop  $U_H$ , the so-called Hall voltage, given by

$$U_H = Ed = \frac{1}{ne} \frac{IB}{d}, \quad (6.2.16)$$

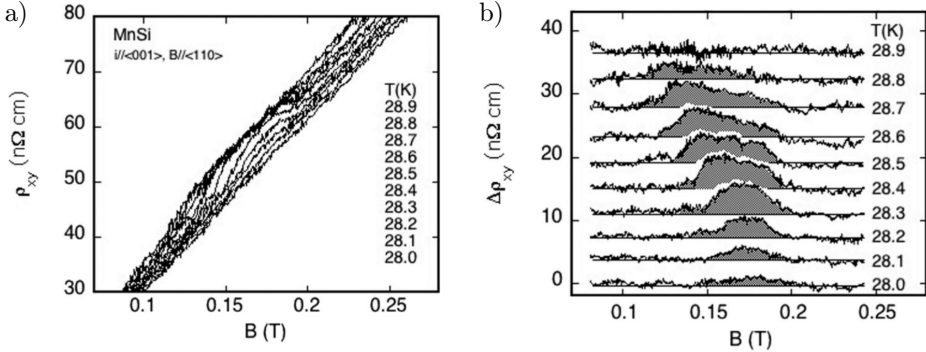
where it was used that the current  $I$  is given by  $I = nev_d b d$  (c. f. Fig. 6.2.2 for the definition of the geometric dimensions  $b$  and  $d$ ).

Experimentally, one typically measures the hall resistivity

$$R_H = \frac{U_H}{I} = \frac{B}{ned} \quad (6.2.17)$$

in dependence on the magnetic field. One would thus expect that the Hall resistivity rises linearly with the applied field and exhibits an additional contribution due to the emergent magnetic field, which is present only in the skyrmion lattice phase.

This has been experimentally verified e. g. in MnSi by Neubauer *et al.* [66], who measured the magnetic field dependence of the Hall resistivity for different temperatures in and around the small pocket in the phase diagram where the skyrmion lattice phase exists, c. f. Fig. 6.2.3 a). While the Hall resistivity rises overall linearly with increasing magnetic field, one can observe a small additional contribution in the skyrmion lattice phase. To extract only this additional contribution, the authors subtracted the linear background due to the normal Hall-effect from their data, c. f. Fig. 6.2.3 b).



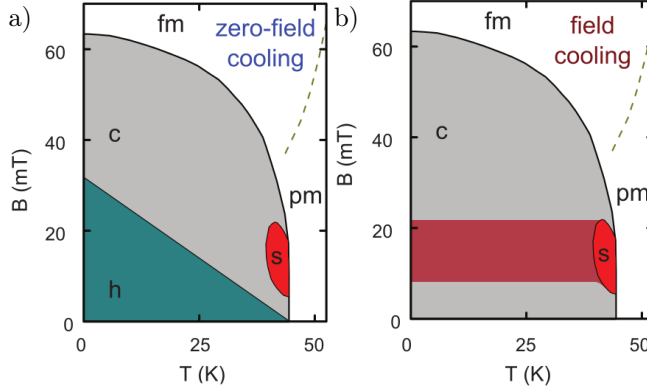
**Figure 6.2.3.:** a) Hall resistivity of MnSi in dependence on the magnetic field for different temperatures. b) Additional contribution due to the emergent magnetic field obtained by subtraction of the linear background caused by the common Hall-effect. The additional contribution is only present in the skyrmion lattice phase, c. f. Fig. 3.2.8. Picture taken from Ref. 66.

### 6.3. Experimental observation of the unwinding of a skyrmion lattice

Since topological and non-topological phases are both realized in chiral magnets, these systems are ideally suited for the observation of a topological phase transition. In 2013, Milde *et al.* analyzed the phase transition from the skyrmion lattice to the helical phase by means of magnetic force microscopy (MFM) measurements on the surface of bulk  $\text{Fe}_{0.5}\text{Co}_{0.5}\text{Si}$  [37]. This composition was chosen because the periodicity of the helical modulations of  $\sim 90$  nm is large compared to the resolution of  $\sim 20$  nm of MFM [67], which allows to observe single skyrmions on its surface.

Fig. 6.3.4 shows the magnetic phase diagram of this compound. Interestingly, one observes strong hysteresis, i. e. the observed state at a point in the phase diagram depends strongly on how this point was reached. Under zero-field cooling, i. e. cooling without magnetic field, helimagnetic order with a propagation vector in  $\langle 100 \rangle$  direction occurs below a temperature of  $T_c \approx 45$  K. As the magnetic field is subsequently increased at  $T < T_c$ , the system first undergoes a spin-flop transition to a conical phase at  $B_{c1}$  followed by a transition to a field-polarized state at  $B_{c2}$ . Additionally, the skyrmion phase is stabilized in a small pocket just below the ordering temperature at intermediate magnetic fields.

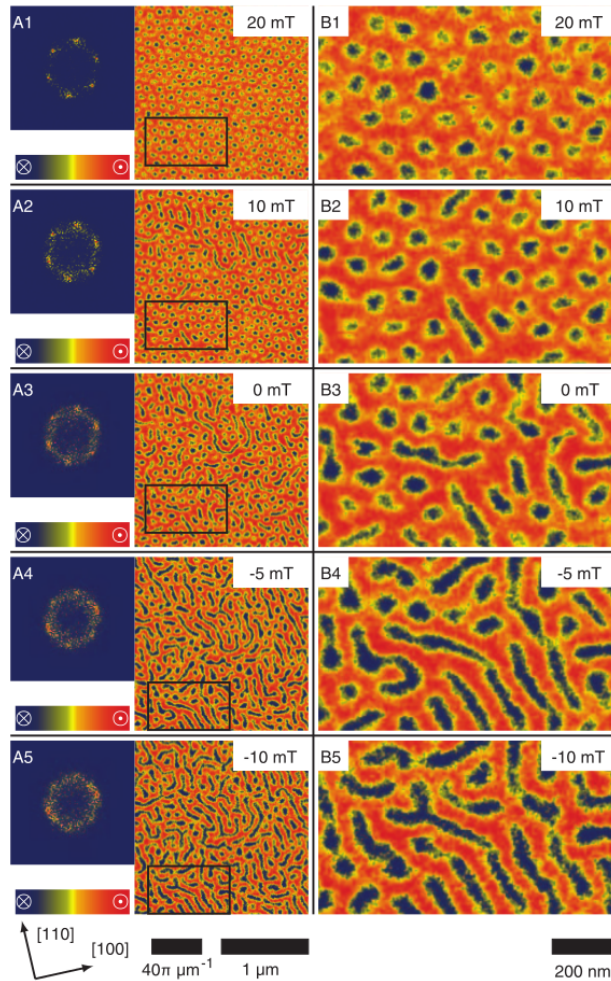
Under field cooling, i. e. cooling at a constant magnetic field, one observes strong hysteresis in the sense that there is only a transition from the paramagnetic to the conical or skyrmion lattice phase, but not to the helical phase. Furthermore,



**Figure 6.3.4.:** a) Phase diagram of  $\text{Fe}_{0.5}\text{Co}_{0.5}\text{Si}$  observed under zero-field cooling. The skyrmion lattice phase is confined to a small pocket just below the ordering temperature. b) Phase diagram observed under field cooling. The skyrmion lattice phase persists as a metastable phase down to  $T = 0$ , whereas the helical phase is never observed at finite fields. Picture taken from Ref. 37.

upon cooling at field values in the range of the skyrmion lattice phase, this phase survives as a metastable state down to the lowest temperatures. This facilitates MFM measurements in two ways: First, the magnetic moments increase at small temperatures which substantially improves the contrast of the MFM data. Second, the topological stability of skyrmions is based on the fact that the amplitude of the local magnetization is finite everywhere. Strong thermal amplitude fluctuations close to  $T_c$  might in principle weaken their stability, whereas for  $T \ll T_c$ , one can expect to observe the pure mechanism of the topological unwinding.

Fig. 6.3.5 shows typical MFM images recorded for decreasing applied field after an initial cool-down to  $T = 10$  K at  $B = 20$  mT as well as Fourier transforms of the surface magnetization. The image for  $B = 20$  mT (panel B1) was recorded directly after the initial cool-down and shows a triangular lattice of skyrmions (blue spots). As the magnetic field is lowered, one observes that neighboring skyrmions coalesce and form an elongated pattern (see e.g. panel B2). Upon lowering the field further, more skyrmions merge and the resulting structures grow in length (panels B3 to B5). Eventually, a striped pattern containing various defects is formed. Such a pattern is typical for helically modulated phases and a Fourier transform of the magnetization (panels A4 and A5) reveals that the helices propagate mainly in  $\langle 100 \rangle$  direction which is the easy axis in this compound. The lifetime of the metastable skyrmion lattice was found to be long compared to the time needed to record each image ( $\sim 17$  minutes) and only small



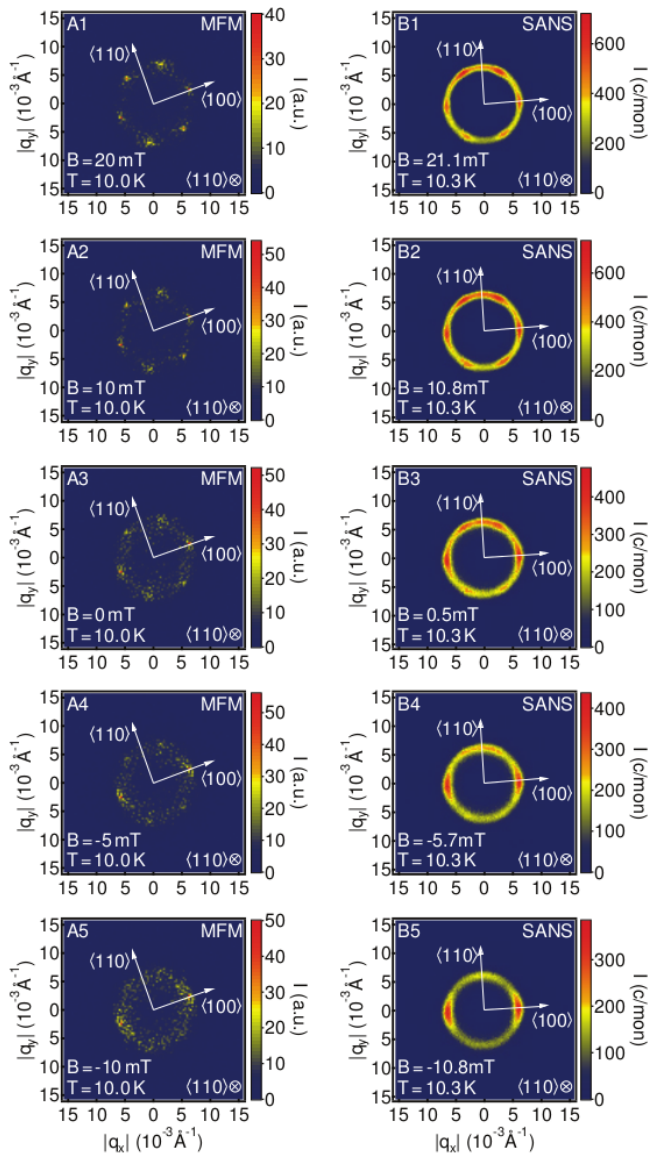
**Figure 6.3.5.:** Typical magnetic force microscopy images at the surface of  $\text{Fe}_{0.5}\text{Co}_{0.5}\text{Si}$ . Red (blue) areas correspond to a magnetization pointing parallel (anti-parallel) to the line of sight out of (into) the surface. The magnetic field is pointing out of the surface. Panels (A1) through (A5): Images recorded as a function of magnetic field after field cooling at  $B = +20$  mT down to  $T = 10$  K. Panel (A1) shows the image obtained immediately after field cooling. After the initial cool-down, the field was reduced at a fixed temperature of  $T = 10$  K (A2 to A5). During this process, the skyrmions, which appear as blue spots in the images, merge and form elongated, line-like structures. The left inset shows the Fourier transform of the real-space signal. Panels (B1) to (B5) enlarge the region marked by the black rectangle in panels (A1) to (A5). Picture taken from Ref. 37.



changes in the MFM data has been observed after a waiting time of 15 hours [37, 67].

To summarize, the MFM data suggests that the mechanism for the unwinding of the skyrmion lattice is the coalescence of skyrmions into helical domains. To check whether the same process takes also place in the bulk of the material, Milde *et al.* performed small angle neutron scattering experiments with the same sample that was used for the MFM measurements. The observed scattering patterns, shown in Fig. 6.3.6, basically agree with the Fourier transforms obtained from the MFM data, which lends further support to the assumption that the coalescence of skyrmions is not just a surface effect but also takes place in the bulk of the material. The SANS measurements show an additional ring of intensity that is not observed in the MFM data. The authors attribute this ring to the presence of disorder and the fact that the MFM measurements only probe a very small part of the sample, whereas the SANS measurements reflect its whole volume.

The interesting questions which are still unanswered are, on the one hand, how the merging of skyrmions can be understood from a microscopic point of view, and, on the other hand, how the topology changes during this process. To answer these questions, it is desirable to model the system e.g. in a Monte Carlo simulation, which allows to observe every magnetic moment in the vicinity of the point where two skyrmions merge. The next section explains the details of such a simulation and the conclusions that can be drawn from it regarding the topological properties of the points of coalescence.



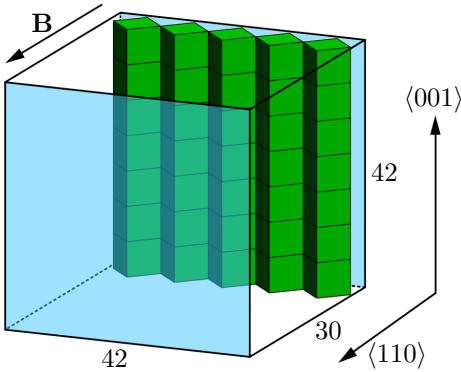
**Figure 6.3.6.:** Comparison of the Fourier transforms of the magnetic force microscopy data (left column) with small angle neutron scattering (right column). The same sample of  $\text{Fe}_{0.5}\text{Co}_{0.5}\text{Si}$  was used for all measurements. Picture taken from Ref. 67.

## 6.4. Emergent magnetic monopoles

In order to get some insight into the fundamental microscopic process responsible for the merging of neighboring skyrmions, I performed classical Monte Carlo simulations following the experimental setup and protocol used in Ref. 37 as closely as possible. As it was already discussed in Sec. 5.3, one observes strong hysteresis in the Monte Carlo simulations, including the metastability of the skyrmion lattice phase under field-cooling, which is also observed experimentally. In this section, I exploit this fact and analyze in detail the phase transition from the skyrmion lattice to the helical phase upon decreasing the magnetic field.

After presenting the results from the Monte Carlo simulation, I discuss the topological aspects of this phase transition and show that it is mediated by magnetic monopoles and antimonopoles of the emergent magnetic field. At the end of this section, I discuss another numerical approach that takes into account the real-time dynamics of the magnetic moments by solving the stochastic Landau-Lifshitz-Gilbert equation, leading to qualitatively identical results.

**Monte Carlo study** Simulations were performed using the lattice Hamiltonian Eq. (5.1.2) with  $D/J = \arctan(2\pi/10) \approx 0.73$  and the anisotropy compensation by next-nearest neighbor interactions (c.f. Sec. 5.3) on a simple cubic lattice consisting of  $42 \times 42 \times 30$  lattice sites with open boundary conditions in  $\langle 110 \rangle$  direction and periodic boundary conditions in the other two directions. As in the experimental setup, the magnetic field is applied along a  $\langle 110 \rangle$  direction and thus perpendicular to the surfaces with open boundary conditions, c.f. Fig. 6.4.7. Having a real surface along this direction is important in order to reproduce the experimental setup and allows a comparison with the MFM measurements.



**Figure 6.4.7:** Orientation of the simple cubic lattice of size  $42 \times 42 \times 30$  used in the Monte Carlo simulations and direction of the magnetic field. The blue shaded areas mark the surfaces with open boundary conditions and the green boxes denote unit cells of the simple cubic lattice. Note that only a few unit cells are shown for simplicity to illustrate their arrangement inside the simulated cell. Picture taken from Ref. 67.

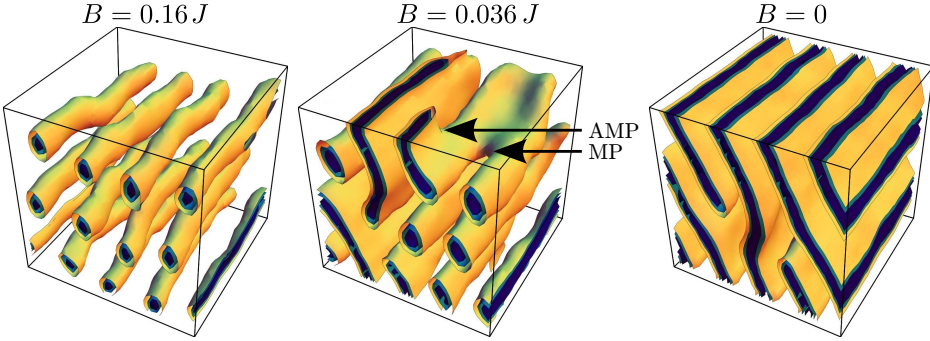
As described in Sec. 6.3, the experiment explores the metastability of the skyrmion lattice by cooling the system at a constant field that is subsequently reduced at a fixed temperature. To be able to track metastable states in the Monte Carlo simulation, it is necessary to perform a *single* simulation with *local* updates, i. e. random reorientations of *single* randomly chosen spins (this excludes parallel tempering due to the constant exchange of replicas). Using single-site updates, the system is cooled down slowly at  $B/J = 0.16$  to various temperatures ranging from  $T/J = 0.4$  to  $0.7$ . As observed in the experiment, the skyrmion lattice phase remains intact upon cooling despite the fact that the conical phase is the thermodynamically stable ground state at these temperatures, c. f. Sec. 5.3. Following the initial cool-down, the field is reduced linearly at a rate of  $\Delta B/J = 5 \cdot 10^{-4}$  after 250 Monte Carlo lattice sweeps. At each value of the magnetic field, the state of the system is then averaged over 250 configurations separated by 30 lattice sweeps for later analysis. These timescales have been found to average out some thermal fluctuations but still allow to monitor the changes of the magnetic structure during the phase conversion. Fig. 6.4.8 shows typical snapshots of the spin configuration immediately after the initial cool-down, at low fields and at zero field. Instead of showing the individual magnetic moments in the system, it is (for reasons that will become clear shortly) very useful to show surfaces of constant magnetization in the direction of the field, which provides a clear view on the skyrmion tubes running through the system.

In contrast to the experiments, the simulation allows to monitor the process responsible for the merging of skyrmions not just at the surface but also in the bulk of the system and is thus of great importance for the understanding of the phase conversion. As the field is decreased, the neighboring skyrmion tubes touch and merge into a single tube, reducing the winding number in the corresponding layer by 1 and thus indicating a change of topology. The pattern at the front of the simulated system (corresponding to a surface with open boundary conditions) shows remarkable similarities to the MFM data, c. f. Fig. 6.3.5.

**Topological aspects** The topological aspects of the observed merging of skyrmions is best described in the language of the emergent electric and magnetic fields introduced in Sec. 6.1. The most important result of this section was that the emergent magnetic flux through a surface intersected by a skyrmion tube is exactly given by one (negative) flux quantum  $-\Phi_0$ ,

$$\int_{\text{UC}} \mathbf{B}^e d\mathbf{A} = -\frac{2\pi}{|q^e|} \equiv -\Phi_0. \quad (6.4.18)$$

Fig. 6.4.9 shows schematically the merging of two skyrmion tubes in the bulk. Going from the top to the bottom in this figure, the magnetic flux through the layers jumps discontinuously from  $-2\Phi_0$  to  $-\Phi_0$  in the layer where the two



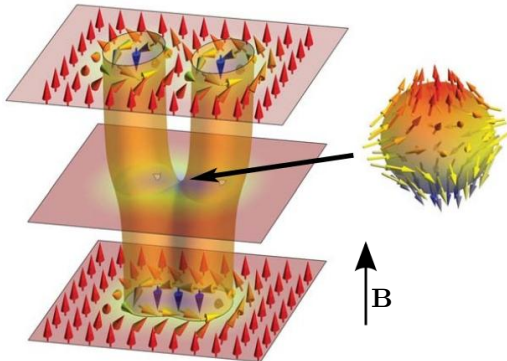
**Figure 6.4.8.:** Monte Carlo simulation of the phase conversion. The system was first field cooled at  $B/J = 0.16$  ( $B \parallel \langle 110 \rangle$ ) down to  $T/J = 0.6$ , followed by a linear decrease of the field at constant temperature. Below a critical field  $B_c^-$ , the skyrmion tubes touch and merge. The arrows labeled MP and AMP point to a monopole and antimonopole, respectively.

skyrmion tubes merge. Due to the topological nature of the skyrmions, this is only possible by a singular field configuration for which the magnetization vanishes locally at one point in space. Such a configuration is exactly generated by the hedgehog defect shown in the right part of Fig. 6.4.9. The implications on the emergent magnetic field can be seen by integrating the field over a closed surface  $\partial\Omega$  of an infinitesimal volume  $\Omega$  surrounding this point,

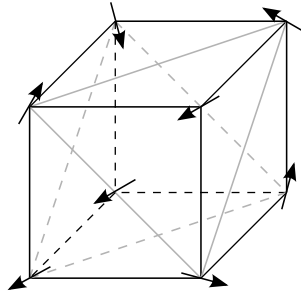
$$\begin{aligned}
 \int_{\partial\Omega} \mathbf{B}^e \cdot d\mathbf{A} &= \int_{\Omega} \nabla \cdot \mathbf{B}^e dV \\
 &= -\Phi_0 (N_{\text{out}}^s - N_{\text{in}}^s) \\
 &= -\Phi_0,
 \end{aligned} \tag{6.4.19}$$

where  $N_{\text{out}}^s$  ( $N_{\text{in}}^s$ ) is the number of skyrmion tubes going out of (into) the volume  $\Omega$ . The singular hedgehog configuration at the merging point has thus winding number  $-1$  and creates exactly one negative quantum of emergent magnetic flux. In that sense, the hedgehog defect carries a magnetic charge and can be interpreted as *emergent magnetic antimonopole*. The corresponding monopoles are given by defects with winding number  $+1$ , which carry a positive flux quantum. Note that the position of a monopole (MP) and an antimonopole (AMP) is also marked in the numerical data presented in Fig. 6.4.8.

In order to find topological defects in the Monte Carlo simulation, it is necessary to perform the volume integral in Eq. (6.4.19) numerically. The winding number of the eight magnetic moments around each unit cell can be computed by a triangulation of the surface of the unit cell according to Fig. 6.4.10. Each of the



**Figure 6.4.9.:** Schematic illustration describing the merging of two skyrmions. At the merging point the magnetization vanishes at a singular point (arrow). The corresponding hedgehog defect can be interpreted as an emergent magnetic antimonopole, which acts like the slider of a zipper connecting two skyrmion tubes. Picture taken from Ref. 37.



**Figure 6.4.10.:** Triangulation of a unit cell of the simple cubic lattice. To find topological defects, the surface of the cube is split into twelve triangles (gray lines). For each triangle, the solid angle covered by the spins on its corners is calculated using the Oosterom-Strackee algorithm Eq. (6.4.20). The sum of all solid angles divided by  $4\pi$  yields the winding number of the cube.

six surfaces is therefore split into two triangles and for every triangle the solid angle covered by the three magnetic moments  $\mathbf{S}_i$  on its corners is computed by the Oosterom-Strackee algorithm [60]

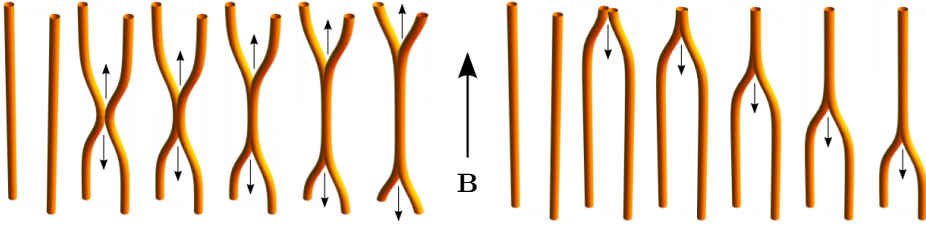
$$\Omega_i = \frac{\mathbf{S}_1 \cdot (\mathbf{S}_2 \times \mathbf{S}_3)}{1 + \mathbf{S}_1 \cdot \mathbf{S}_2 + \mathbf{S}_2 \cdot \mathbf{S}_3 + \mathbf{S}_3 \cdot \mathbf{S}_1}. \quad (6.4.20)$$

The winding number of the unit cell is then given by

$$W = \frac{1}{4\pi} \sum_{i=1}^{12} \Omega_i \quad (6.4.21)$$

and can by construction only take the values  $-1$ ,  $0$  and  $+1$ , where  $+1$  and  $-1$  correspond to a monopole or antimonopole, respectively. Additionally, the winding number for every layer perpendicular to the magnetic field was calculated as described in Sec. 5.2.

Since winding numbers are additive, the total winding number for an arbitrary closed surface can be computed by adding the winding numbers of the elementary cubes within the volume surrounded by the surface. Local Monte Carlo updates (or thermal fluctuations in the experiment) can therefore only create monopole-antimonopole *pairs* in the bulk of the system. Single monopoles or



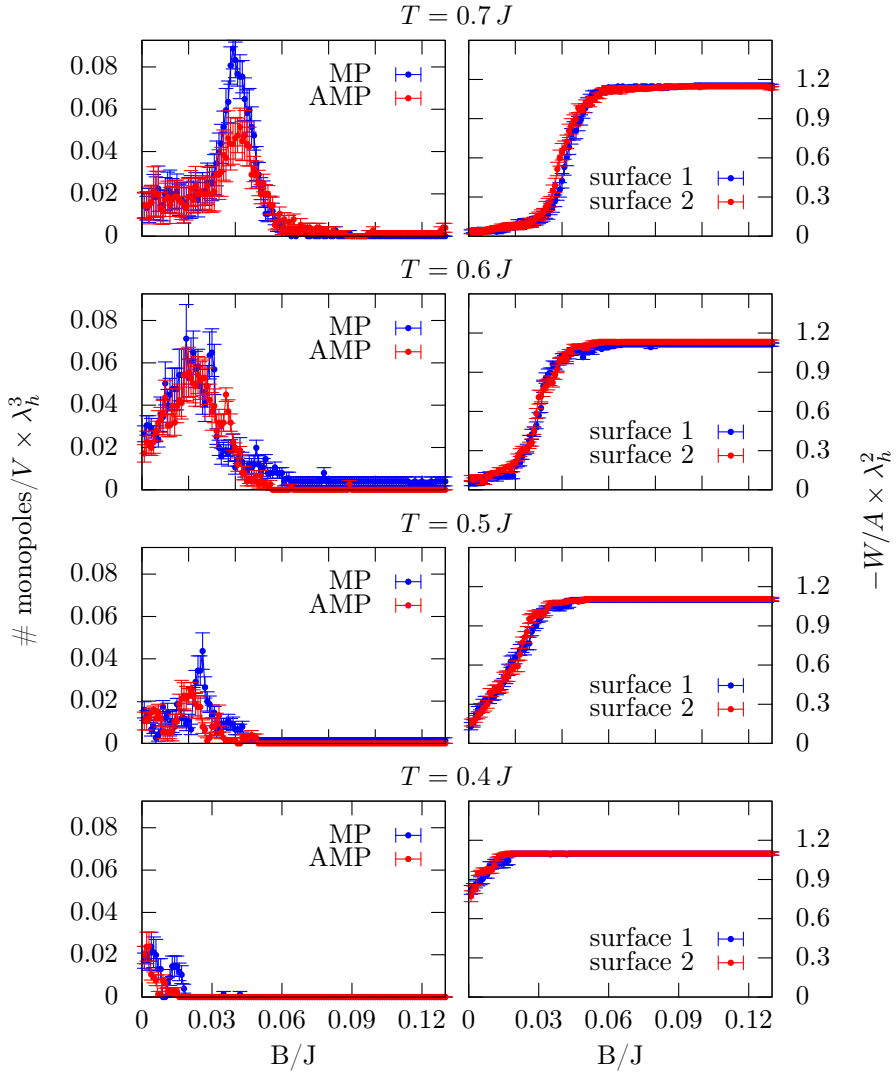
**Figure 6.4.11.:** **Left row:** Two skyrmion tubes merge in the bulk and create a monopole-antimonopole pair. The two monopoles move in opposite direction through the system, zipping the tubes together like the slider of a zipper. **Right row:** Two skyrmion tubes merge at the surface and create a single monopole which again acts like the slider of zipper when moving through the system.

antimonopoles can only be created at the surface. During the Monte Carlo simulation, the monopoles and antimonopoles move through the sample and merge neighboring skyrmion tubes like the slider of a zipper. Fig. 6.4.11 shows these processes schematically. Since the energy cost for creating single monopoles and antimonopoles is only half as large as for the creation of a pair (the magnetization has to be suppressed only once locally), the creation of single defects at the surface of the sample is much more likely. This is also in agreement with the Monte Carlo simulations, in which almost all “free” defects are created at the surfaces, whereas most pairs created in the bulk annihilate again after a short time before they separate. For larger systems, one will probably observe that the largest fraction of monopoles and antimonopoles is nevertheless created in the bulk, since the surface contribution to the overall creation rate becomes neglectable in the thermodynamic limit.

Fig. 6.4.12 shows the monopole density and the winding number on the two surfaces during the decrease of the magnetic field (averaged over 15 independent runs) after an initial cool-down to four different temperatures. As a lot of monopole-antimonopole pairs are frequently generated and destroyed by thermal fluctuations, all pairs with a distance smaller than three lattice sites have not been taken into account in the counting and only the number of the remaining “free” monopoles, which are responsible for the phase conversion, is shown.

For each temperature, there is a certain field value  $B_c^-$ , below which monopoles and antimonopoles are created and the winding number on the two surfaces decreases. When thermal fluctuations become weaker with decreasing temperature, less monopoles and antimonopoles are excited. Consequently, the metastable region<sup>1</sup> of the phase diagram grows and one observes that  $B_c^-$  is shifted to smaller

<sup>1</sup>All statements about the metastable region have to be thought of in the context of a sufficiently small time scale that allows to observe the metastability.



**Figure 6.4.12.:** **Left:** Density of monopoles (MP) and antimonopoles (AMP) as a function of the magnetic field for four different temperatures. The density is normalized to a volume given by  $\lambda_h^3$ , where  $\lambda_h$  is the wavelength of the helical state. The errorbars indicate standard deviations of the mean obtained after averaging over 15 different runs. **Right:** winding number per area  $\lambda_h^2$  on the two surfaces with open boundary conditions.



field values. If the temperature is chosen low enough, the skyrmion phase remains metastable even down to  $B = 0$  in the simulations.

For some intermediate temperatures, the phase conversion does not take place completely as the field is lowered to  $B = 0$ , i.e. the winding number on the surfaces remains finite and there are still monopoles and antimonopoles present in the bulk of the sample. An analysis of the magnetic structure reveals that the remaining monopoles are associated to frozen-in topological defects of a helical state, typically with a propagation vector parallel to the surface, c.f. picture for  $B = 0$  in Fig. 6.4.8.

On average, the density of monopoles and antimonopoles is identical. This is rooted in the fact that time reversal  $\mathbf{M} \rightarrow -\mathbf{M}$  followed by an rotation by  $\pi$  around an arbitrary axis perpendicular to the field is a symmetry of the system which maps monopoles to antimonopoles and vice versa.

Finally, one can consider what happens if the phase transition out of the skyrmion lattice phase is induced by increasing instead of decreasing the magnetic field. In this case, there exists again a certain field value  $B_c^+$ , at which the skyrmion tubes are either cut into two tubes by the creation of a monopole/antimonopole pair at some splitting point in the bulk or unwound piece-by-piece by a monopole or antimonopole moving from the surface along the tube into the bulk. The latter case is again preferred due to energetic reasons.

**Micromagnetic simulations** Since the phase conversion is a non-equilibrium process, it is a question of fundamental importance whether the artificial Monte Carlo dynamics and the real-time dynamics lead qualitatively to the same results. C. Schütte has studied the spin dynamics [37, 68] taking into account the precession of spins, their damping as well as thermal fluctuations in a micromagnetic simulation governed by the stochastic Landau-Lifshitz-Gilbert (sLLG) equation [69]

$$\frac{d\mathbf{S}(\mathbf{r}, t)}{dt} = -\mathbf{S}(\mathbf{r}, t) \times [\mathbf{B}^{\text{eff}}(\mathbf{r}, t) + \mathbf{B}^{\text{fl}}(\mathbf{r}, t)] + \alpha \mathbf{S}(\mathbf{r}, t) \times \frac{d\mathbf{S}(\mathbf{r}, t)}{dt}, \quad (6.4.22)$$

with  $\mathbf{B}^{\text{eff}}(\mathbf{r}, t) = -\delta H / \delta \mathbf{S}(\mathbf{r}, t)$ , where  $H$  is the Hamiltonian Eq. (5.1.2) of the full system (including the anisotropy compensation by next-nearest neighbor interactions, c.f. Sec. 5.3),  $\alpha$  the dimensionless Gilbert damping and  $\mathbf{B}^{\text{fl}}(\mathbf{r}, t)$  a randomly fluctuating field used to describe thermal fluctuations of the magnetic moments. Its properties are determined completely by the fluctuation-dissipation theorem, i. e.

$$\langle \mathbf{B}^{\text{fl}}(\mathbf{r}, t) \rangle = 0, \quad \langle \mathbf{B}^{\text{fl}}(\mathbf{r}_i, t) \mathbf{B}^{\text{fl}}(\mathbf{r}_j, t') \rangle = 2\alpha T \delta_{ij} \delta(t - t'). \quad (6.4.23)$$

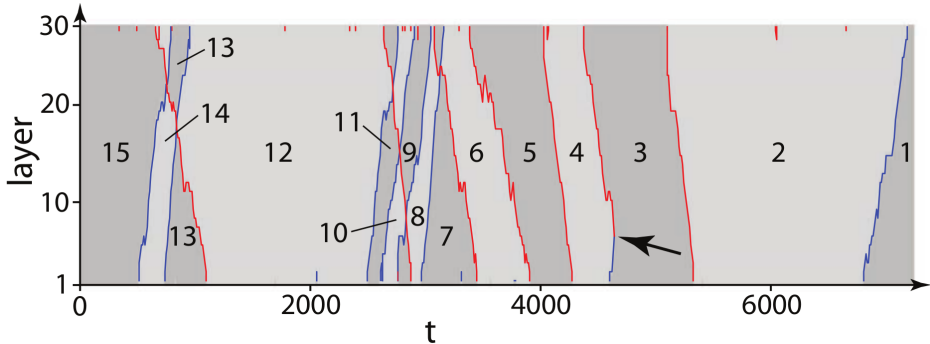
A numerical integration of the sLLG equation (6.4.22) yields the correct thermal equilibrium properties and allows to study the real-time dynamics of the phase

conversion driven by thermal fluctuations.

As in the Monte Carlo study, a system size of  $42 \times 42 \times 30$  spins was used with a magnetic field applied along a  $\langle 110 \rangle$  direction. A Gilbert damping of  $\alpha = 0.04$  was chosen to account for magnetic relaxation. At the beginning of the simulation, an initial skyrmion state with a lattice constant compatible with  $D/J = \arctan(2\pi/10)$  was initialized and relaxed for a time  $t_{\text{init}} = 1000/J$  at  $T/J = 0.5$  in a constant field of  $B^{\text{ext}}/J = 0.16$  by integrating the sLLG equation (6.4.22). The magnetic field was then switched off completely at  $t = 0$  to investigate the dynamics of monopoles and antimonopoles. Snapshots of the spin configuration were taken throughout the simulation and averaged over a short time interval of  $\Delta t = 10/J$  to suppress spurious monopole-antimonopole pairs at short distances, which are frequently created and destroyed during the simulation.

Fig. 6.4.13 shows the distance of the monopoles (red) and antimonopoles (blue) from the bottom surface of the simulated box as a function of time. Monopoles (antimonopoles) are created at the top (bottom) surface and move down (up) through the system. As a monopole or antimonopole passes a layer in the box, the winding number of that layer (shown by the numbers in the figure) is reduced by one. The black arrow in the figure marks an event where a monopole and an antimonopole meet and annihilate. As mentioned before, the creation of monopole-antimonopole pairs is energetically very costly and one hence observes only the creation of single defects at the surfaces.

Overall, the results from the real-time dynamics are in agreement with the Monte Carlo simulation concerning the underlying process of the phase conversion.



**Figure 6.4.13.:** Movement of monopoles through a sample after a sudden quench of the magnetic field, based on micromagnetic simulations of the sLLG equation. Starting in the skyrmion phase, an initial external magnetic field of  $B^{\text{ext}}/J = 0.16$  is set to 0 at  $t = 0$ . The distance of the monopoles (red) and antimonopoles (blue) to the lower surface is shown in dependence on the time (in units of  $J^{-1}$ ). The numbers in the figure denote the winding number in each layer. The black arrow marks a point where a monopole and an antimonopole meet and annihilate. Picture taken from Ref. 67.

## 6.5. Conclusion and Outlook

It was shown that monopoles and anti-monopoles of an emergent magnetic field are responsible for the unwinding of the topologically stable skyrmion lattice in chiral magnets. Understanding the details of this process is important for future data storage applications and provides the theoretical background for the controlled writing and deleting of single skyrmions (which has already been achieved experimentally in two dimensions [26]).

Since magnetic monopoles have also been reported for so-called “spin-ice” [70, 71], it is instructive to compare those monopoles with the emergent monopoles found in chiral magnets. While monopoles in spin-ice are sources of the “real” magnetic field, their charge is *not* quantized and depends on several microscopic details such as the lattice spacing. By contrast, the monopoles considered here are sources of the *emergent* magnetic field and follow Dirac’s quantization condition [72] for monopoles, i. e. they carry exactly one quantum of emergent magnetic flux.

Furthermore, in spin-ice at zero field, the monopoles are deconfined, i. e. it requires only a finite energy to separate monopoles and antimonopoles to an infinite distance. In chiral magnets, the situation is different. Deep in the skyrmion phase, it requires a finite amount of energy per length to merge two skyrmions together and there is consequently a linear potential (i. e. a finite string tension) holding monopoles and antimonopoles together. Outside of the skyrmion phase,

this string tension vanishes or becomes negative which allows the monopoles to separate to arbitrary distances. It would be interesting to study disordered materials, where the string tension may be a random function at every lattice site which could result in a pinning of the monopoles.

Another interesting open question is whether phases of deconfined monopoles may exist in chiral magnets. One candidate for such a phase is the metallic state of MnSi under high pressure, which shows non Fermi-liquid behavior [73] with many properties that differ significantly from those of conventional metals, e.g. it features a resistivity proportional to  $T^{3/2}$  over almost three decades in temperature [33] as well as partial magnetic order on intermediate time and length scales [74] and an unconventional Hall signature [75].

## Part III.

# Spin-liquid phase and order-by-disorder on the swedenborgite lattice



## 7. Introduction

This part of the thesis deals with so-called “frustrated” spin systems. The name refers to the fact that a simultaneous satisfaction of competing interactions in these systems is impossible, which can often be traced back to a lattice geometry that is incompatible with antiferromagnetic exchange interactions. Depending on the particular lattice, frustration results in many cases in a macroscopically degenerate ground state which is only restricted by local constraints on small clusters of spins. Such states do not show long-ranged magnetic correlations and are often referred to as “spin-liquids”, as they are magnetically disordered much in the way that liquid water is disordered compared to crystalline ice.

The search for spin-liquid materials is one of the current challenges in condensed matter physics. From a theoretical point of view, there are a handful of *classical* systems known to exhibit spin-liquid behavior, but often these systems are either not realized in nature or the corresponding *quantum* system orders in some way. It was therefore not before 2012 until the first good evidence of a system exhibiting a spin-liquid ground state was found in so-called Herbertsmithite  $\text{ZnCu}_3(\text{OD})_6\text{Cl}$  [76].

Usually, the ground state degeneracy in spin-liquids is very fragile and can be easily lifted by small perturbations. As pointed out first by Villain [77] and later by Chalker [78], there exists also an intrinsic way to lift the ground state degeneracy, provided that some ground states have softer excitations than others. Such states promote fluctuations (which can be of thermal or quantum nature) into nearby low energy configurations and are thus entropically favored, resulting in a selection of these states at low temperatures in an “order-by-disorder” transition. Even though a few systems are known to exhibit this effect (see e. g. Ref. 78–81) such a transition has not yet been observed experimentally since most of these systems simply do not exist in nature.

In this part of the thesis, I analyze a new class of highly frustrated spin systems, the so-called swedenborgites, consisting of stacked kagome and triangular layers. These compounds are relatively new and have not received a lot of attention from the scientific community yet. In the following chapters, I close this gap by presenting the first systematic theoretical study of the simplest model believed to describe these compounds. Using a combination of analytical arguments and numerical simulations, it is found that this model features a large spin-liquid regime as well as an order-by-disorder transition. The fact that these compounds are not only realized in nature but also offer a very favorable tunability and convenient

energy scales renders them prime candidates for further experimental studies.

In the remaining part of this chapter, I first explain the concept of frustration and how it can lead to degenerate ground states. This introduction is followed by an explanation of the order-by-disorder effect together with a review of the antiferromagnetic Heisenberg model on the kagome lattice, which is known to exhibit this effect. The chapter concludes with a short explanation of emergent “Coulomb-phases” in frustrated systems.

In Ch. 8, I discuss the swedenborgite lattice structure, introduce the minimal model that is believed to describe these compounds and compare its predictions to some experimental findings.

The Ising model with and without magnetic field on this lattice is then analyzed in Ch. 9. It turns out that even though this particular model is probably not realized in nature, it features very rich physics in terms of competing degenerate ground state manifolds and is thus of great conceptual interest in the context of spin-liquids.

The experimentally relevant Heisenberg model is finally considered in Ch. 10. It is found that the ground state of this model is either unique or largely degenerate, depending on the ratio of the exchange interactions. A harmonic spin-wave analysis around coplanar ground states reveals that these states feature soft modes which are not present in generic ground states. Numerical evidence for the therefore expected order-by-disorder transition is presented together with a detailed analysis of the low-temperature behavior of the specific heat.

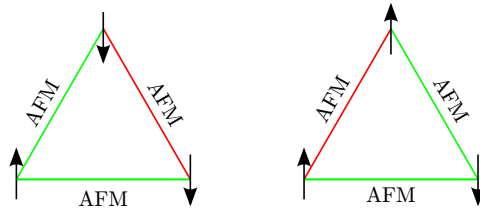
This part ends with some concluding remarks on a possible experimental verification of the order-by-disorder transition.

### 7.1. Magnetic frustration

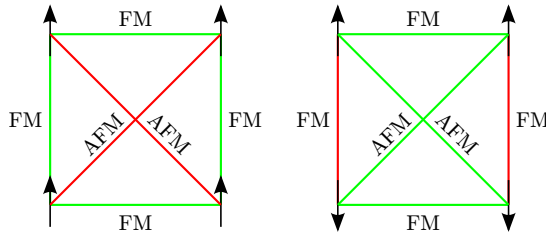
Magnetic frustration refers to the inability of a spin system to fully satisfy competing interactions simultaneously and is often present in systems with antiferromagnetic interactions (see e. g. Ref. 82 and 83 for reviews). It can arise either from a lattice geometry that is incompatible with these interactions or from competing interactions beyond nearest neighbors.

The former one is referred to as *geometrical frustration* and is found e. g. in any antiferromagnetic nearest-neighbor spin model on a single triangle, c. f. Fig. 7.1.1. In general, antiferromagnetic interactions are satisfied by aligning neighboring spins anti-parallel to each other. The special geometry of the triangle, however, makes it impossible to choose a spin configuration which completely satisfies the interactions on all three bonds *simultaneously*. Once two spins in the triangle are aligned anti-parallel, a third spin on the remaining site cannot be aligned anti-parallel to both of them.





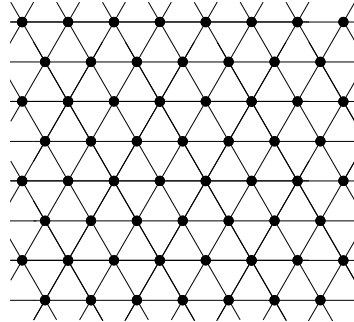
**Figure 7.1.1.:** Geometric frustration on a single triangle: Once the two spins on the bottom are aligned anti-parallel, it is not longer possible for the third spin to align anti-parallel to both of them, resulting in an unsatisfied interaction between the two parallel aligned spins. Satisfied bond-interactions are shown in green, unsatisfied ones in red.



**Figure 7.1.2.:** Exchange frustration due to next-nearest neighbor interactions on a single square: Nearest neighbors are coupled ferromagnetically, while next-nearest neighbors are coupled antiferromagnetically. It is never possible to satisfy the interactions on all bonds simultaneously. The two configurations shown in the figure have different satisfied and unsatisfied bonds (shown in green and red, respectively).

The second kind of frustration is often referred to as *exchange frustration* and can be found e.g. on a single square with ferromagnetic nearest neighbor and antiferromagnetic next-nearest neighbor interactions, c.f. Fig. 7.1.2. Once the interactions on the bonds to the nearest neighbors are satisfied, the interactions on the bonds to the next-nearest neighbors cannot be satisfied any more and vice versa.

In both cases, the impossibility of a simultaneous minimization of all interactions also translates to every lattice constructed out of these frustrated units. It is shown in the next section that the resulting magnetic ground state is either a spin-liquid or magnetically long-range ordered, depending on several details of the particular system.



**Figure 7.2.3:** The triangular lattice consisting of edge-sharing triangles. Neighboring triangles have two common spins and each lattice site has six nearest neighbors, indicating the strong connectedness of the lattice.

## 7.2. Ground state degeneracy

The nature of the ground state in a frustrated spin system depends strongly on the symmetry of the spin variables and the geometry of the underlying lattice structure. In this section, it is shown how Ising and Heisenberg spins face the problem of geometrical frustration on the triangular and kagome lattice. While Ising spins remain disordered on both lattices, Heisenberg spins have at least on the triangular lattice a unique ground state<sup>1</sup>.

**Triangular lattice** The triangular lattice, consisting of edge sharing triangles, is shown in Fig. 7.2.3. The nearest neighbor antiferromagnetic Heisenberg Hamiltonian for  $O(3)$  Heisenberg spins  $\mathbf{S}$  on this lattice is given by

$$H = J \sum_{\langle ij \rangle} \mathbf{S}_i \cdot \mathbf{S}_j \quad (7.2.1)$$

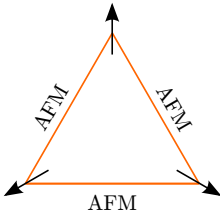
where  $\langle i, j \rangle$  denotes pairs of nearest neighbors and  $J > 0$  is the antiferromagnetic exchange interaction. Eq. (7.2.1) can be written more conveniently as

$$H = \frac{J}{2} \sum_{\Delta} (\mathbf{S}_{\Delta}^1 + \mathbf{S}_{\Delta}^2 + \mathbf{S}_{\Delta}^3)^2 + \text{const.}, \quad (7.2.2)$$

where  $\mathbf{S}_{\Delta}^i$  labels the  $i^{\text{th}}$  spin on a certain triangle  $\Delta$  and the sum runs over all triangles of the lattice. The special form of the Hamiltonian in Eq. (7.2.2) allows to read off the ground state constraints immediately: The first term in Eq. (7.2.2) is positive semi-definite and the energy is thus minimized if the total spin  $\mathbf{L}_{\Delta}$  vanishes on every triangle, i. e. if

$$\mathbf{L}_{\Delta} \equiv \mathbf{S}_{\Delta}^1 + \mathbf{S}_{\Delta}^2 + \mathbf{S}_{\Delta}^3 = 0. \quad (7.2.3)$$

<sup>1</sup>Note that only classical systems are considered here.



**Figure 7.2.4:** The unique  $120^\circ$  ground state for  $O(3)$  Heisenberg spins on a triangle with antiferromagnetic couplings. None of the bond interactions is satisfied completely, indicated by an orange color.

This leads to the ground state configuration shown in Fig. 7.2.4 with  $120^\circ$  angles between neighboring spins in every triangle of the lattice. In this state, the inability to fulfill all interactions simultaneously is not manifested at specific bonds anymore, but is rather distributed along all bonds which are now equally unsatisfied. After a specific spin configuration is chosen in one triangle, the spin configuration in a neighboring triangle is also fixed by Eq. (7.2.3) since both triangles share two spins. Consequently, this implies that *all* spins on the lattice are uniquely fixed once the spin configuration in a single triangle is chosen. The resulting ground state is thus unique up to global rotations and the exchange of sub-lattices.

The situation changes completely if the  $O(3)$  Heisenberg spins are replaced by Ising spins. The Hamiltonian now reads

$$H = J \sum_{\langle ij \rangle} \sigma_i \sigma_j, \quad (7.2.4)$$

where  $\sigma$  is a spin variable that can only take the values  $\pm 1$ . In analogy to Eq. (7.2.3), the total spin

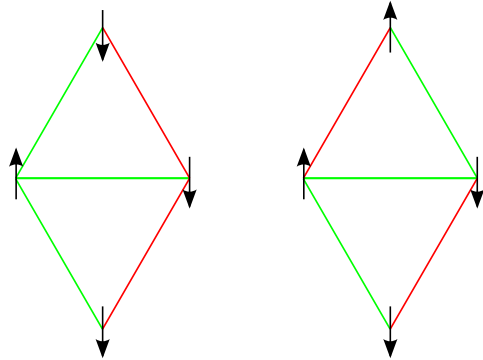
$$L_\Delta = \sigma_\Delta^1 + \sigma_\Delta^2 + \sigma_\Delta^3 \quad (7.2.5)$$

must vanish in the ground state. Interestingly, this is not possible any more due to the discrete symmetry of the Ising spins. Instead, optimal configurations have to fulfill

$$L_\Delta = \sigma_\Delta^1 + \sigma_\Delta^2 + \sigma_\Delta^3 = \pm 1 \quad (7.2.6)$$

on every triangle. The fact that this constraint is not as strict as the corresponding constraint on Heisenberg spins has a strong influence on the ground state manifold. After choosing the spin orientations in one triangle, the orientation of the non-mutual spin in the neighboring triangle can still be chosen independently, provided that two shared spins are anti-parallel to each other, c. f. Fig. 7.2.5. The resulting ground state is extensively degenerate and different ground states are connected by fluctuations that consist of flipping chains of neighboring anti-parallel spins along a closed loop in the system. These fluctuations cost no energy because the total spin on each triangle remains restricted

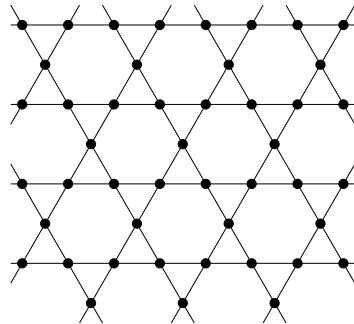
**Figure 7.2.5:** Two neighboring triangles on a triangular lattice with Ising spins. After the spin configuration on the lower triangle is fixed, one can still choose the orientation of the top spin on the upper triangle in two ways without violating the ground state constraint Eq. (7.2.6).



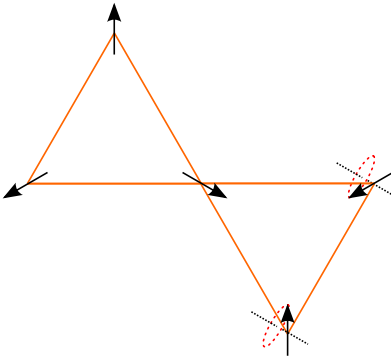
to  $\pm 1$ . Any ordering in a specific state is thus suppressed and the system is an example for a spin-liquid [84, 85].

**Kagome lattice** The kagome lattice is shown in Fig. 7.2.6. It can be constructed from the triangular lattice by removing one third of the lattice sites, which reduces the coordination number from 6 to 4. In contrast to the triangular lattice, the single triangles are now *corner*- instead of *edge*-sharing; a fact which has important consequences for the ground state degeneracy.

The antiferromagnetic Heisenberg Hamiltonian on this lattice has the same structure as on the triangular lattice, c.f. Eq. (7.2.1), and consequently, one finds again that the total spin on every triangle has to vanish in the ground state, c.f. Eq. (7.2.3). Since two neighboring triangles only share *one* spin, choosing a specific  $120^\circ$  configuration on one triangle does not fix the spin configuration on the other one completely as it did on the triangular lattice. The associated degree of freedom is the rotation of the two outer spins of the second triangle around the axis defined by the shared spin, c.f. Fig. 7.2.7. Consequently, the spin-planes of neighboring triangles can be different, resulting in a macroscopic ground state



**Figure 7.2.6:** The two-dimensional kagome lattice consisting of corner-sharing triangles. It can be constructed from the triangular lattice by removing one third of the lattice sites which reduces the coordination number from 6 down to 4.



**Figure 7.2.7:** The ground state degeneracy of the antiferromagnetic Heisenberg model on the kagome lattice: It is possible to rotate the spins on neighboring triangles around the axis defined by the mutual spin without violating Eq. (7.2.3) and thus without energy cost. A part of the degeneracy is removed again once all triangles on the lattice are connected.

degeneracy. A part of this degeneracy is removed again once the additional constraints imposed by connecting all triangles on the lattice are taken into account.

For the Ising model, the ground state on the kagome lattice is again only restricted by the constraint given by Eq. (7.2.6) on every triangle. The fact that the kagome lattice is less connected than the triangular lattice results in a larger ground state degeneracy on the former one. Considering two neighboring triangles with a fixed ground state configuration in the first one, there is a huge freedom in choosing an allowed spin configuration in the second one since only one spin of this triangle is already fixed.

A quantitative measure for the ground state degeneracy is the residual entropy  $S_{\text{res}}$  at  $T = 0$  which will be discussed in detail in Sec. 9.1. For the triangular lattice one finds  $S_{\text{res}} \approx 0.47 \ln 2$  [86] per spin, whereas one finds  $S_{\text{res}} \approx 0.72 \ln 2$  [86, 87] on the kagome lattice.

Other lattices exhibiting spin liquid phases for both the Ising and the Heisenberg model are usually constructed out of *corner*-sharing frustrated units. Famous examples in three dimensions are the Pyrochlore lattice [79, 88, 89], consisting of corner-sharing tetrahedra, and the hyper-kagome [90], a generalization of the kagome lattice to three dimensions.

### 7.3. Order-by-disorder

Spin-liquid phases are usually very fragile in the sense that small perturbations can easily lift the ground state degeneracy. Known mechanisms are e. g. dipolar interactions and disorder [91], spin-lattice coupling [92], and Dzyaloshinskii-Moriya interaction [93]. There exists, however, an intrinsic mechanism known as “order-by-disorder”, in which the degeneracy is lifted purely due to entropic

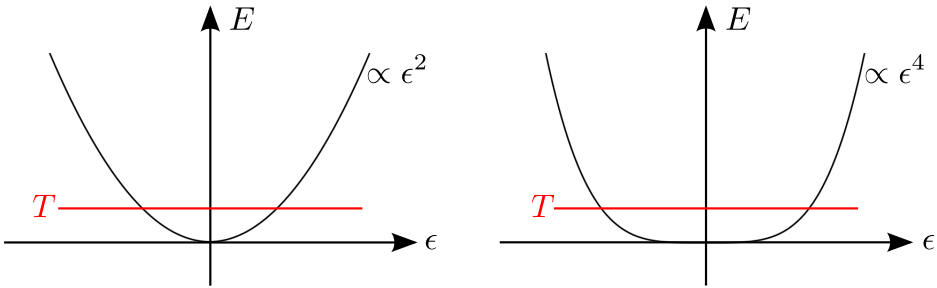
reasons. This effect was first mentioned by Villain in 1980 [77] for the diluted 2d Ising model and gained more interest in 1987 when Henley showed that thermal fluctuations alone are sufficient to provide an ordering mechanism for antiferromagnetically coupled  $O(3)$  spins on fcc lattices [94, 95]. In 1992, Chalker showed that the same mechanism is also present for  $O(3)$  spins on the kagome lattice [78]. The name “order-by-disorder” originates from the fact that the two quantities *temperature* and *entropy*, both usually associated with disorder, can under certain circumstances drive an ordering mechanism in which specific states out of a degenerate ground state manifold are selected. The decisive quantity is the free energy

$$F = E - TS, \tag{7.3.7}$$

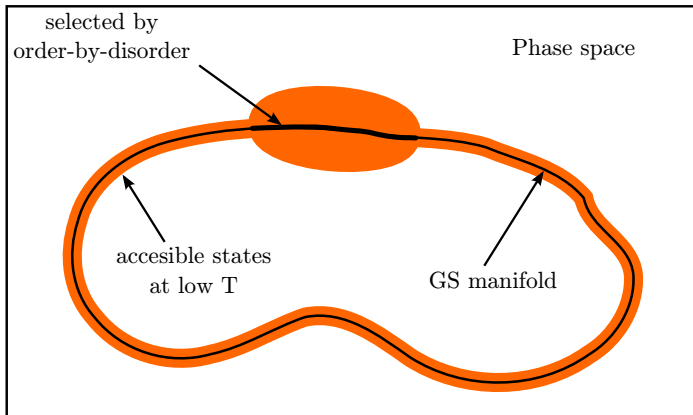
where  $E$  is the energy,  $T$  the temperature and  $S$  the entropy. Due to the entropic contribution to the free energy, states with the same internal energy can still differ in their free energy depending on how well the system can fluctuate into nearby low energy configurations. This is shown schematically in Fig 7.3.8: The two degenerate ground states shown have exactly the same energy, but as soon as small thermal fluctuations are considered, the neighborhood of the ground states becomes important as well. In the vicinity of a ground state, one can expand the energy in the deviation  $\epsilon$  of the spins from their respective ground state positions. If the temperature is sufficiently small, it is justified to stop the expansion after the leading order. For a generic ground state, this gives rise to an effective quadratic potential around the ground state, c.f. left part of Fig 7.3.8. For some states, it *might* happen that the leading order in the series expansion is not quadratic but e.g quartic, resulting in a very flat potential around these ground states as shown in the right part of Fig 7.3.8. These states promote fluctuations into nearby low energy configurations and are thus entropically favored. Consequently, these states have a lower free energy and are eventually selected at low temperatures.

The same process is also shown schematically in Fig. 7.3.9 in a phase space picture. The black line denotes the ground state manifold and the orange shaded region marks the part of the phase space that the system can fluctuate into at a small temperature. The ground states with many nearby low energy configurations (thick black line) are eventually selected at low temperatures. It is important to note that the ground state manifold does not necessarily have to be connected as shown in the figure.

The question whether an order-by-disorder transition can occur in a system with a degenerate ground state manifold depends again on several details. One necessary condition is of course the presence of entropically favored ground states that feature softer excitations than others. This condition is, however, not sufficient, as it was shown by Moessner and Chalker in Ref. 79, who found that the answer



**Figure 7.3.8.:** Schematic comparison of the neighborhood of two degenerate ground states. The left figure shows the generic case that the energy cost for deviating spins out of the ground state is quadratic in the deviation  $\epsilon$ . The right figure shows a special ground state with an excitation energy that is quartic in the deviation from the ground state. At a finite (small) temperature, one would associate a larger entropy with the right ground state since the system can fluctuate into more nearby low energy configurations than in the left ground state. As a consequence, the right state has a lower free energy than the left one and the degeneracy between the two ground states is lifted.



**Figure 7.3.9.:** Schematic view of the phase space and the order-by-disorder effect: A part of the ground state manifold has more nearby low energy excitations than the rest and is thus preferred at low temperatures. Note that the ground state manifold does not necessarily have to be connected.

to this question strongly depends on the degeneracy of the ground state manifold and can be expressed in a rather simple counting argument: If there are degrees of freedom left after fulfilling all ground state constraints, the system remains disordered at all temperatures<sup>2</sup>. Otherwise, an order-by-disorder transition will occur at some small temperature.

On the kagome lattice, there are three degrees of freedom per triangle since each spin has two angular degrees of freedom and is shared by two triangles. Eq. (7.2.3), on the other hand, implies three constraints per triangle and there are hence no degrees of freedom left. Consequently, the kagome lattice is a candidate for the order-by-disorder effect and it is shown in Sec. 7.4 that this effect is indeed observed in numerical simulations.

The Pyrochlore lattice, consisting of corner-sharing tetrahedra, does in contrast not show order-by-disorder: Each tetrahedron consists of four spins which are each shared by two tetrahedra and has accordingly four degrees of freedom. In analogy to Eq. (7.2.3) for the triangle, one can derive that the total spin on each tetrahedron has to vanish in the ground state, yielding three constraints per tetrahedron. The ground state is thus (extensively) under-constrained with one remaining degree of freedom per tetrahedron. Consequently, the system is able to explore the whole ground state manifold without crossing any energy barriers and there is no reason why the system should stay in a specific ground state.

It is important to note that the counting argument can easily go wrong if the ground state constraints are not independent. A detailed discussion can be found in Ref. 79.

### 7.4. Order-by-disorder on the kagome lattice

The occurrence of order-by-disorder on the kagome lattice was first described and verified by Chalker *et al.* in 1992 [78]. He argued that coplanar ground states, i. e. ground states with a mutual spin plane for all triangles of the lattice, have a soft excitation which is not present in non-coplanar ground states and are hence entropically favored at low temperatures. Since the breaking of continuous symmetries in two-dimensional systems is forbidden at finite temperatures due to the Mermin-Wagner theorem [96], this preference is, however, only a local effect with a temperature-dependent correlation length  $\xi \propto \exp(T^{-1})$ . In the following, I briefly review Chalker's arguments as presented in Ref. 78.

Fluctuations around a coplanar ground state can be described best by a suitable

---

<sup>2</sup>The fact that there are as many constraints as degrees of freedom does not necessarily lead to a unique ground state with magnetic long-range order, as one might naively think. Instead, this often results only in *local* constraints for single clusters of spins, as it was shown e. g. in Sec. 7.2 for the antiferromagnetic Heisenberg model on the kagome lattice.



coordinate system oriented with respect to the local spin positions in the ground state: At each lattice site  $i$ , one can choose a coordinate system with  $\hat{\mathbf{z}}_i$  parallel to  $\mathbf{S}_i$  in the particular ground state position and  $\hat{\mathbf{y}}_i$  orthogonal to the ground state plane and all  $\hat{\mathbf{y}}_i$  mutually parallel. The remaining coordinate  $\hat{\mathbf{x}}_i$  is chosen such that the resulting coordinate system  $\{\hat{\mathbf{x}}_i, \hat{\mathbf{y}}_i, \hat{\mathbf{z}}_i\}$  is right handed on every lattice site. Remarkably, this coordinate system allows to analyze fluctuations around *all* coplanar ground states without making any further assumptions. The spin directions can be parametrized in terms of their in-plane and out-of-plane deviations from the ground state,  $\epsilon_i^x$  and  $\epsilon_i^y$ , as

$$\mathbf{S}_i = \left( \epsilon_i^x, \epsilon_i^y, \sqrt{1 - (\epsilon_i^x)^2 - (\epsilon_i^y)^2} \right)^T. \quad (7.4.8)$$

Inserting this parametrization into the Heisenberg Hamiltonian

$$H = J \sum_{\langle ij \rangle} \mathbf{S}_i \cdot \mathbf{S}_j \quad (7.4.9)$$

and using that

$$(\hat{\mathbf{x}}_i \cdot \hat{\mathbf{x}}_j) = -\frac{1}{2}, \quad (\hat{\mathbf{y}}_i \cdot \hat{\mathbf{y}}_j) = 1, \quad (\hat{\mathbf{z}}_i \cdot \hat{\mathbf{z}}_j) = -\frac{1}{2} \quad (7.4.10)$$

for neighboring spins (all terms for non-neighboring spins vanish), one can expand the Hamiltonian up to second order in the deviations and obtains

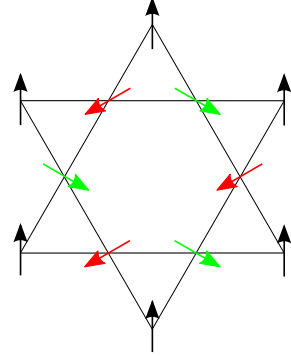
$$H = E_{\text{GS}} + \frac{J}{2} \sum_{ij} \left( (3\delta_{ij} - M_{ij}) \epsilon_i^x \epsilon_j^x + 2M_{ij} \epsilon_i^y \epsilon_j^y \right) + \mathcal{O}(\epsilon^4), \quad (7.4.11)$$

where  $E_{\text{GS}}$  is the ground state energy and

$$M_{ij} = \begin{cases} 1 & \text{if } i = j \\ \frac{1}{2} & \text{if } i \text{ and } j \text{ are nearest neighbors} \\ 0 & \text{else} \end{cases} \quad (7.4.12)$$

From Eq. (7.4.11) it becomes clear that the in-plane and out-of-plane excitations are not coupled in the harmonic approximation. The translational invariance of the lattice can be exploited by a Fourier transform. The eigenvalues of the resulting  $3 \times 3$  matrix  $M(\mathbf{q})$  can be calculated analytically and are given by

$$\begin{aligned} \lambda_0(\mathbf{q}) &= 0, \\ \lambda_{\pm}(\mathbf{q}) &= \frac{3}{2} \left( 1 \pm \sqrt{1 - \frac{8}{9} \left( 1 - \cos\left(\frac{q_1}{2}\right) \cos\left(\frac{q_2}{2}\right) \cos\left(\frac{q_1 - q_2}{2}\right) \right)} \right). \end{aligned} \quad (7.4.13)$$



**Figure 7.4.10:** The soft mode with excitation energy  $E \propto \epsilon^4$  on the kagome lattice: The black spins remain idle while the red and green spins tilt out of the ground state plane in an alternating fashion by the same amount.

The fact that there is an eigenvalue that vanishes for all  $\mathbf{q}$  implies that there is an excitation mode whose excitation costs no energy up to second order in the deviation  $\epsilon$ . The corresponding eigenvector can again be Fourier transformed to visualize the associated mode in real space, c. f. Fig. 7.4.10. It is localized around a hexagon and consists of tilting neighboring spins out of the ground state plane by the same amount in an alternating fashion. The energy of this mode is proportional to  $\epsilon^4$  as can be seen by plugging the corresponding eigenvector into Eq. (7.4.11).

The presence of this soft mode in coplanar ground states (and its absence in generic, non-coplanar ground states) is eventually responsible for the preference of these states at low temperatures.

This selection of a common spin plane does not remove the ground state degeneracy completely: coplanar ground states are built up out of three different spins  $A$ ,  $B$  and  $C$ , each of which must occur exactly once on every triangle on the lattice. Since neighboring triangles share only one spin, there is still an extensively large number of allowed ground states and consequently no magnetic long-range order. Instead, quasi long-range order develops in the correlation function

$$g(|\mathbf{r}_i - \mathbf{r}_j|) \propto \langle \boldsymbol{\kappa}_i \cdot \boldsymbol{\kappa}_j \rangle \quad (7.4.14)$$

where

$$\boldsymbol{\kappa}_i = \frac{2}{3\sqrt{3}} (\mathbf{S}_i^1 \times \mathbf{S}_i^2 + \mathbf{S}_i^2 \times \mathbf{S}_i^3 + \mathbf{S}_i^3 \times \mathbf{S}_i^1) \quad (7.4.15)$$

is a vector that specifies the spin plane of the  $i^{\text{th}}$  triangle [78]. In general, a continuous symmetry can not be spontaneously broken at finite temperature due to the Mermin-Wagner theorem [96] and consequently these correlations exist only on a length scale  $\xi \propto \exp(T^{-1})$ . This implies that the system *locally* chooses a common spin plane which slowly tilts on a length scale set by  $\xi$ . At small

temperatures, however, this correlation length is much larger than all system sizes accessible in computer simulations and the order misleadingly appears to be long-ranged.

It is later shown in Sec. 10.2 that a fully equivalent description of the same broken symmetry as described by Eq. (7.4.14) is given by the more convenient two component on-site nematic order tensor [90]

$$Q^{\alpha\beta} = \frac{1}{N} \sum_i \left( S_i^\alpha S_i^\beta - \frac{1}{3} \delta^{\alpha\beta} \right). \quad (7.4.16)$$

For a long time it was believed that this is the primary order parameter for the kagome antiferromagnet. In 2008, however, Zhitomirsky showed in Ref. 90 that this is just a secondary order parameter that couples in a Landau theory to the primary octupolar order parameter

$$T^{\alpha\beta\gamma} = \frac{1}{N} \sum_i \left( S_i^\alpha S_i^\beta S_i^\gamma - \frac{1}{5} S_i^\alpha \delta^{\beta\gamma} - \frac{1}{5} S_i^\beta \delta^{\alpha\gamma} - \frac{1}{5} S_i^\gamma \delta^{\alpha\beta} \right) \quad (7.4.17)$$

via the rotational invariant term

$$\Delta F_{QT} = Q^{\alpha\beta} T^{\alpha\mu\nu} T^{\beta\mu\nu}. \quad (7.4.18)$$

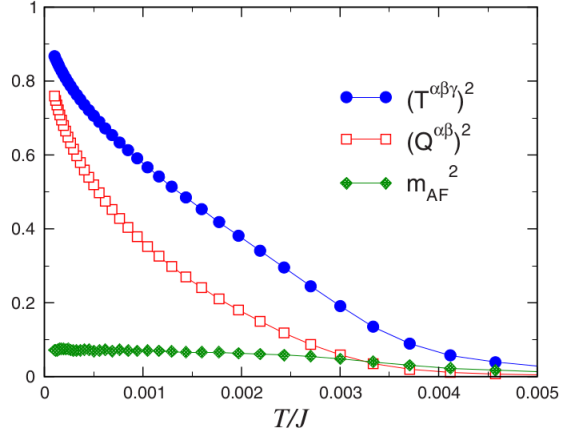
If  $T^{\alpha\beta\gamma}$  takes a finite value, it will act as field  $Q^{\alpha\beta}$  and consequently induce a finite value of  $Q^{\alpha\beta}$ . It is, however, also possible that  $Q^{\alpha\beta}$  induces a finite value of  $T^{\alpha\beta\gamma}$ , but this process is in contrast to the former one non-generic<sup>3</sup>. To identify the primary order parameter, Zhitomirsky performed classical Monte Carlo simulations to find out which order parameter rises first as the temperature of the system is lowered. The results, shown in Fig. 7.4.11, clearly prove that the octupolar order parameter is the primary one.

The presence of soft modes in the excitation spectrum also affects the low-temperature behavior of the specific heat. The equipartition theorem states that each quadratic (quartic) mode, contributes a factor  $T/2$  ( $T/4$ ) to the thermal expectation value of the energy. The specific heat, given by  $c_V = dE/dT$ , for these modes is consequently  $1/2$  and  $1/4$  per spin, respectively. For the coplanar ordered ground states, three quadratic in-plane as well as two quadratic and one quartic out-of-plane modes were found. Assuming that these modes are equally occupied, one would expect a specific heat of

$$c_V = \underbrace{\left( \frac{3}{3} \times \frac{1}{2} \right)}_{\text{in-plane}} + \underbrace{\left( \frac{2}{3} \times \frac{1}{2} + \frac{1}{3} \times \frac{1}{4} \right)}_{\text{out-of-plane}} = \frac{11}{12} \quad (7.4.19)$$

<sup>3</sup>This can only happen upon a sign change of the complete prefactor (which depends on temperature and  $Q$ ) of the term proportional to the square of the octupolar order parameter in Landau theory.

**Figure 7.4.11:** Comparison of the nematic and octupolar order parameter: The primary octupolar order parameter rises first upon cooling and induces the nematic order parameter.  $m_{\text{AF}}$  is the order parameter of the  $\sqrt{3} \times \sqrt{3}$  structure (see Ref. 90 for details). Picture taken from Ref. 90.



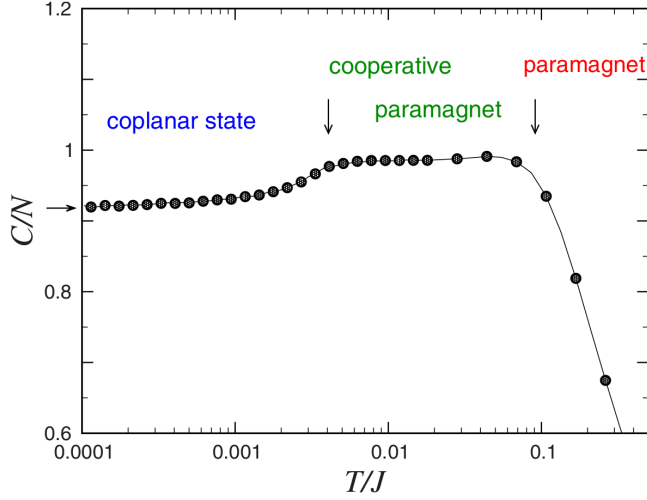
in the limit of low temperatures. Fig. 7.4.12 shows the specific heat per spin as calculated by Zhitomirsky in a classical Monte Carlo simulation [90]. One can clearly identify three different regimes: At high temperatures, the system is in the paramagnetic state and the specific heat slowly rises as the temperature is lowered. At a temperature of the order  $\mathcal{O}(10^{-1} J)$ , the specific heat approaches 1, indicating a crossover into the spin liquid regime where the ground state constraint Eq. (7.2.3) is fulfilled on every triangle and all excitation energies are quadratic in the deviations of the spins from the (in general non-coplanar) ground state. Eventually, the system selects coplanar ground states at a temperature of the order  $\mathcal{O}(10^{-3} J)$  and the specific heat is consequently reduced to the expected value  $11/12$ , where it remains all the way down to zero temperature.

The short ranged correlations in the spin liquid regime also result in a broadening of the peaks in the magnetic structure factor

$$S(\mathbf{q}) = \frac{1}{N} \sum_{ij} \langle \mathbf{S}_i \cdot \mathbf{S}_j \rangle e^{i\mathbf{q}(\mathbf{r}_i - \mathbf{r}_j)}, \quad (7.4.20)$$

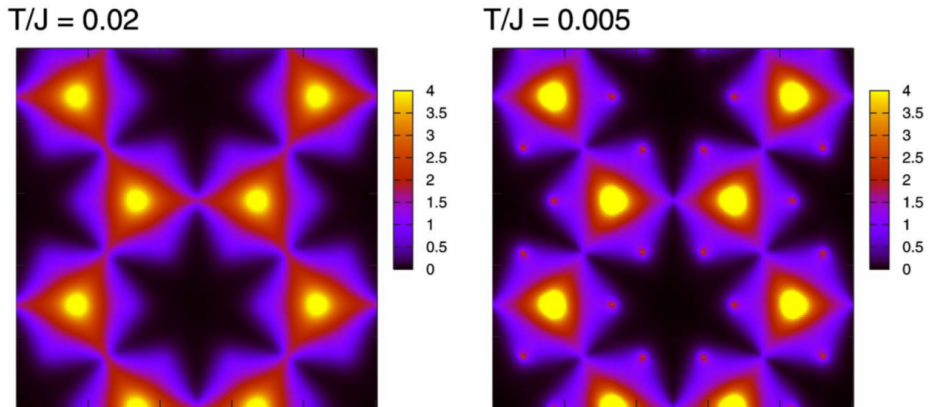
which is shown in Fig. 7.4.13 for  $T/J = 0.02$  (spin-liquid phase) and  $T/J = 0.005$  (coplanar ordered phase). Interestingly, the selection of coplanar ordered states goes along with the development of correlations at the antiferromagnetic wave vector  $\mathbf{Q} = (4\pi/3, 0)$  and wave vectors related by symmetry. Zhitomirsky concludes in Ref. 90 that these additional peaks are not true Bragg peaks in the sense that their intensity does not increase linearly with the system size.

There is, however, an ongoing discussion about whether the unique ground state with ordering wave vector  $\mathbf{Q} = (4\pi/3, 0)$  (also called “ $\sqrt{3} \times \sqrt{3}$  state” in the literature) is eventually selected out of all coplanar ground states at low temper-



**Figure 7.4.12.:** The specific heat per spin of the kagome antiferromagnet in dependence on the temperature for a system consisting of  $N = 3 \times 36^2 = 3888$  spins. The black arrow on the specific heat axis marks the value  $11/12$  that is expected from the mode counting argument. Picture taken from Ref. 90.

atures. Unfortunately, most simple Monte Carlo methods are non-ergodic in the sense that they fail to sample all coplanar spin configurations due to high energy barriers between these states and can thus not be used to settle the question. Chern and Moessner have thus developed a special algorithm [97] that allows transitions between different coplanar states and further identified that the effective low energy Hamiltonian corresponds to a three-state Potts model with a weak ( $J_2 \approx 0.019$ ) second neighbor exchange interaction. Studying very large systems with about  $10^6$  lattice sites for this effective model, they indeed observed a small but finite magnetic moment corresponding to order at  $\mathbf{Q} = (4\pi/3, 0)$ . A completely independent approach to this problem has been presented by Sachdev in Ref. 98, where he constructed a mean-field theory that takes into account quantum effects by starting from the Schwinger boson representation of the spin operators. He reports that there are two competing ground states with ordering vectors  $\mathbf{Q} = (4\pi/3, 0)$  and  $\mathbf{Q} = \mathbf{0}$  and also argues in favor of the first one due to its lower energy.



**Figure 7.4.13.:** The magnetic structure factor of the Heisenberg model on the kagome lattice in the spin-liquid regime (left) and the coplanar ordered state (right). Shown is a region of size  $8\pi \times 8\pi$  in reciprocal space. One can clearly observe additional correlations at the antiferromagnetic wave vector  $\mathbf{Q} = (4\pi/3, 0)$  and wave vectors related by symmetry in the coplanar ordered phase. Picture taken from Ref. 90.

## 7.5. Coulomb-phases

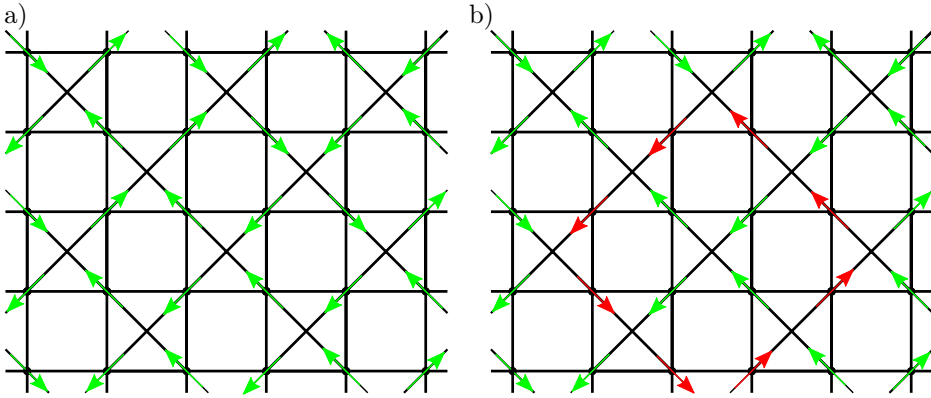
The ground state manifold of some frustrated systems can be described as a so-called Coulomb-phase. The name originates from the fact that excitations above the degenerate ground state in these systems occur as pairwise local charge defects which interact in three dimensions via an effective Coulomb potential  $V(r) \propto (Q_1 Q_2)/r$ , where  $r$  is the spatial distance between the charges. This section intends to give a short introduction into the concept and follows closely the presentation in Ref. 99.

It was shown in Sec. 7.2 that many frustrated system are governed by a local constraint of the type

$$\sum_i \mathbf{S}_i = 0 \quad (7.5.21)$$

on every cluster (i. e. triangle, tetrahedron, etc.) on the lattice. Even though this constraint is *local*, it has a strong influence on the long distance behavior of the system and allows a description of its low energy behavior in terms of an emergent electrodynamic theory.

Eq. (7.5.21) can also be understood as a local conservation law if one identifies the spin variables as an artificial “lattice flux”. This flux can be coarse-grained to a continuous vector field  $\mathbf{p}(\mathbf{r})$  by taking its mean value over a spherical volume centered at  $\mathbf{r}$  with a radius much bigger than the lattice spacing but much smaller



**Figure 7.5.14.:** a) The square lattice with double crossings. The spin configuration shown is a possible ground state obeying the “2in-2out” ice-rule with vanishing total flux in every square. b) A zero-energy loop flip that does not violate the ice-rule and thus allows fluctuations between different ground state configurations.

than the system size. The ground state constraint Eq. (7.5.21) then translates into

$$\nabla \cdot \mathbf{p}(\mathbf{r}) = 0. \quad (7.5.22)$$

which is exactly the zero-divergence condition an electric or magnetic field would satisfy in the absence of charges.

As an example, one can consider Ising spins on the two-dimensional square lattice with crossings shown in Fig. 7.5.14 a). If one takes the diagonals of the squares as spin axes, each spin can point either into the center of a square or out of it, and the ground state constraint Eq. (7.5.21) becomes a so-called “ice-rule”, which states that every square must have two in and two out-pointing spins<sup>4</sup>. Fluctuations between different ground states consist of flipping all spins along a closed loop in the system such that the ice-rule is never violated, c. f. Fig. 7.5.14 b). Obviously, states with total polarization  $\mathbf{P} \equiv \int \mathbf{p}(\mathbf{r})dV = 0$  have the largest number of flippable loops. Consequently, the number of configurations  $N(\mathbf{P})$  for a given total polarization is maximal at  $\mathbf{P} = 0$  and goes to zero as  $\mathbf{P}$  approaches its saturated value. The Central Limit theorem states that for a large system,  $N(\mathbf{P})$

<sup>4</sup>The name “ice-rule” comes from the fact that in the hexagonal ice phase of water, every oxygen atom is bound to 4 hydrogen atoms with two of these bonds being strong and the other two being much weaker. Consequently, every oxygen atoms has two “near” and two “far” protons, but it is not determined which of the 4 protons are “near” and “far”, respectively [100].

will take the form of a Gaussian distribution

$$N(\mathbf{P}) \propto \exp(-\mathbf{P}^2/2\sigma^2). \quad (7.5.23)$$

From this distribution, one can calculate the entropy  $S = \ln(N(\mathbf{P}))$  and finds that the entropic part of the free energy  $F = E - TS$  is in lowest order given by

$$F \propto \mathbf{P}^2. \quad (7.5.24)$$

Correlations can be evaluated by transforming Eq. (7.5.22) to momentum space,

$$\mathbf{q} \cdot \mathbf{P}(\mathbf{q}) = 0, \quad (7.5.25)$$

which implies that all components of  $\mathbf{P}$  parallel to  $\mathbf{q}$  must vanish. This implies that all correlations of  $\mathbf{P}$  have no component in the direction of  $\mathbf{q}$ , i. e.

$$\langle P^\mu(-\mathbf{q})P^\nu(\mathbf{q}') \rangle \propto \left( \delta_{\mu\nu} - \frac{q_\mu q_\nu}{\mathbf{q}^2} \right) \delta_{\mathbf{q}\mathbf{q}'}. \quad (7.5.26)$$

Every physical observable  $\Phi(\mathbf{r})$  has (if not forbidden by any symmetry) usually a contribution proportional to  $\mathbf{P}$ , i. e.

$$\Phi_a(\mathbf{r}) = \Phi_a^0(\mathbf{r}) + \sum_{\mu} c_{a\mu} P_{\mu}(\mathbf{r}), \quad (7.5.27)$$

where  $\Phi_a^0(\mathbf{r})$  is the  $a^{\text{th}}$  component of the  $\mathbf{P}$  independent part of  $\Phi_a(\mathbf{r})$  and  $c_{a\mu}$  are matrix coefficients that obey the symmetry of the lattice. The experimentally measured magnetic structure factor is thus given by

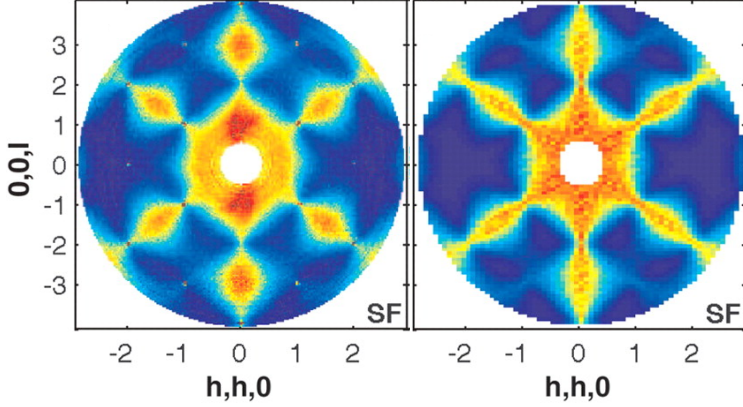
$$\begin{aligned} S_{ab}(\mathbf{q}) &= \langle S_a(\mathbf{q})S_b(-\mathbf{q}) \rangle \\ &= \sum_{\mu\nu\mathbf{Q}} f_{ab\mu\nu}(\mathbf{Q}) \langle P^\mu(-\mathbf{q} + \mathbf{Q})P^\nu(\mathbf{q} - \mathbf{Q}) \rangle \end{aligned} \quad (7.5.28)$$

with  $f_{ab\mu\nu}(\mathbf{Q})$  being a form factor derived from the  $c_{a\mu}$ 's. The singular nature of Eq. (7.5.26) leads to so-called ‘‘pinch-points’’ in reciprocal space which show a strong dependence on how the singular point at  $\mathbf{q} = 0$  is approached. This singularity is translated by the form factor in Eq. (7.5.28) to other values of  $\mathbf{q}$ . Fig. 7.5.15 shows the magnetic structure factor for so-called ‘‘spin-ice’’, the antiferromagnetic Ising model on the pyrochlore lattice, obtained from Monte Carlo simulations compared to measurements with the compound  $\text{Ho}_2\text{Ti}_2\text{O}_7$ .

If one Fourier transforms the structure factor back to real space, one finds

$$\langle P_{\mu}(0)P_{\nu}(\mathbf{r}) \rangle \propto \frac{\delta_{\mu\nu} - d\hat{r}_{\mu}\hat{r}_{\nu}}{r^d}, \quad (7.5.29)$$





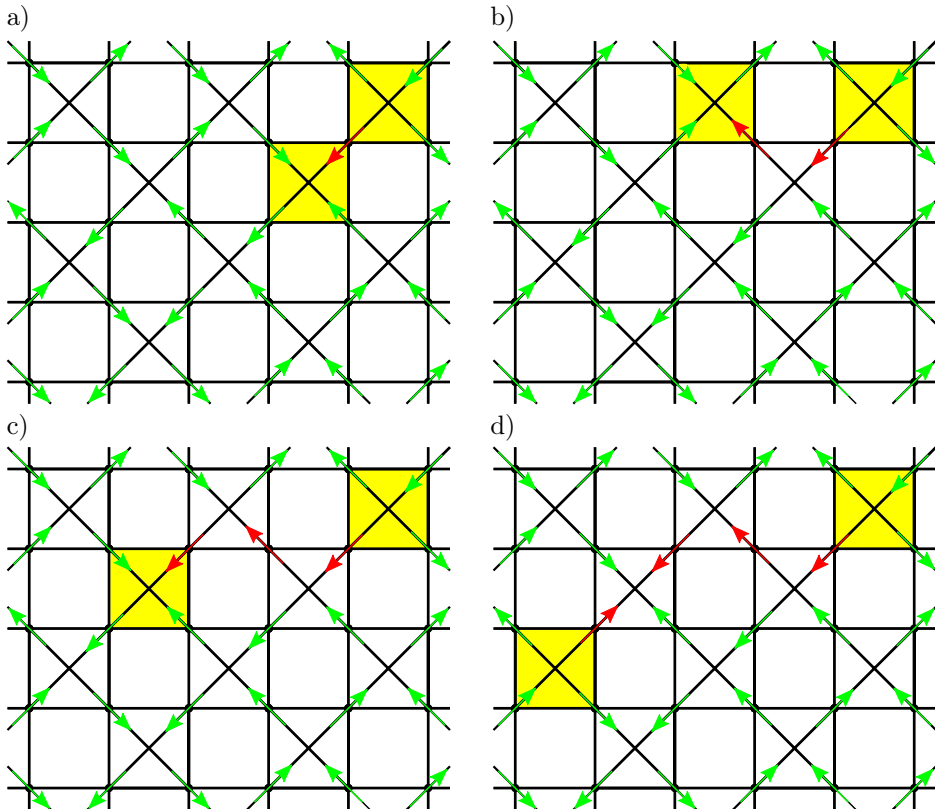
**Figure 7.5.15.:** The structure factor in the reciprocal  $hhl$  plane obtained from experiments on the spin-ice compound  $\text{Ho}_2\text{Ti}_2\text{O}_7$  at  $T = 1.7$  K (left) and from Monte Carlo simulations (right). Picture taken from Ref. 101.

where  $d$  is the spatial dimension and  $\hat{\mathbf{r}} = \mathbf{r}/|\mathbf{r}|$ , i.e. correlations decay with a power law and have the spatial dependence of a dipole-dipole interaction.

Finally, one can also consider local violations of the ground state condition Eq. (7.5.21). In the continuum theory, these defects can be understood as local charges acting as sources and sinks of the vector field  $\mathbf{p}(\mathbf{r})$ . In the example of the square lattice with crossings, such defects are in lowest order given by defect squares with “3-in-1-out” or “1-in-3-out” configurations and carry the charge  $Q = N_{\text{in}} - N_{\text{out}} = \pm 2$ , where  $N_{\text{in}}$  and  $N_{\text{out}}$  are the number of ingoing and outgoing flux arrows (spins) per square. These defects are always created pairwise on neighboring squares by single spin flips, c.f. Fig. 7.5.16 a) and can propagate through the system without any energy cost by flipping an additional spin of a defect square, c.f. Fig. 7.5.16 b)-d). By integrating the partition function under the condition that two defects with charges  $Q_1$  and  $Q_2$  are placed at positions  $\mathbf{r}_1$  and  $\mathbf{r}_2$ , one finds the interesting result that these charges interact in three dimensions via an effective Coulomb potential [99]

$$V(\mathbf{r}_1, \mathbf{r}_2) \propto \frac{Q_1 Q_2}{|\mathbf{r}_1 - \mathbf{r}_2|}. \quad (7.5.30)$$

This interaction is a purely entropic effect as the separation of defect squares costs no energy since no further defect squares are produced during the movement of a defect square through the system, c.f. Fig. 7.5.16. In three dimensions (not necessarily in two dimensions) these charges are *deconfined*, i.e. it takes only a finite energy to separate the charges to an infinite distance.



**Figure 7.5.16.:** **a)** Elementary excitation consisting of a single flipped spin (red) leading to two defect squares with violated ice-rules (yellow). **b)-d)** Movement of a defect square through the system along a chain of flipped spins (red). The movement costs no energy since the number of defect squares stays constant.

It is important to note that Coulomb-phases do not automatically occur in all frustrated systems governed by local constraints. Henley states the following conditions for the appearance of a Coulomb-phase in Ref. 99:

1. The *premedial* lattice, i. e. the lattice which has its sites inside the elementary frustrated units of the original lattice, has to be bipartite (e. g. the premedial lattice of the square lattice with crossings is again the square lattice and the premedial lattice of the kagome is the honeycomb).
2. The spin variables can be mapped uniquely to a signed flux  $\mathbf{p}_i$  running around the  $i^{\text{th}}$  bond of the premedial lattice.
3. The spin variables obey hard constraints such that the sum of the incoming and outgoing fluxes at each lattice site of the premedial lattice is zero in the ground state.
4. The system has a highly disordered ground state without any long-range ordered pattern.

For lattices with an even number  $N$  of spins in each frustrated unit (square lattice with crossings, pyrochlore, ...), the lattices fluxes  $\mathbf{p}_i$  are simply given by the spin directions  $\mathbf{S}_i$  and the mapping to the Coulomb-phase is relatively obvious. Since the ground states of these systems are described by ice-rules of the type “ $N/2$ -in- $N/2$ -out” on every site of the premedial lattice, these models are also called “ice-models”. The best known model is probably the already mentioned “spin-ice”, the antiferromagnetic Ising model on the triangular lattice [70].

If the number of spins in the frustrated units is odd, the mapping to a Coulomb-phase is not that obvious. Sometimes, the ground state of these models can be mapped to a hardcore dimer covering and one can define weighted fluxes depending on whether a dimer crosses a bond of the premedial lattice. Examples are i. a. the Ising model on the triangular lattice [102] and the Heisenberg-Kitaev model on the honeycomb lattice [103].



## 8. Swedenborgites

In this chapter, I discuss the swedenborgite compounds as a realization of a frustrated system with a very unusual lattice geometry. After a detailed discussion of the lattice structure, I introduce the model that is believed to describe the interactions in these compounds. At the end, I give a brief overview of neutron scattering experiments that confirm the validity of this model.

### 8.1. Lattice structure and model

Swedenborgites are a class of materials that are structurally equivalent to the mineral swedenborgite  $\text{SbNaBe}_4\text{O}_7$ , which was first discovered by the Swedish mineralogist Gregori Aminoff 1924 in Långban (Sweden) [104]. It is named after Emanuel Swedenborg, a Swedish scientist and theologian of the 18<sup>th</sup> century. This class of materials recently gained interest [105–113] when it was noticed that the Sb, Na and Be ions of the mineral could be replaced by other ions, including magnetic ones like cobalt and iron [108, 113]. Known magnetic representatives of this class are i. a.  $\text{YBaCo}_4\text{O}_7$ ,  $\text{YBaCo}_3\text{FeO}_7$ ,  $\text{YBaCo}_2\text{Fe}_2\text{O}_7$ ,  $\text{Y}_{0.5}\text{Ca}_{0.5}\text{BaCo}_4\text{O}_7$ ,  $\text{CaBaFe}_4\text{O}_7$  and  $\text{CaBaCo}_2\text{Fe}_2\text{O}_7$ . These compounds consist of corner sharing  $\text{CoO}_4$  and  $\text{FeO}_4$  tetrahedra arranged in an alternating stack of triangular and kagome layers, c. f. Fig. 8.1.1.

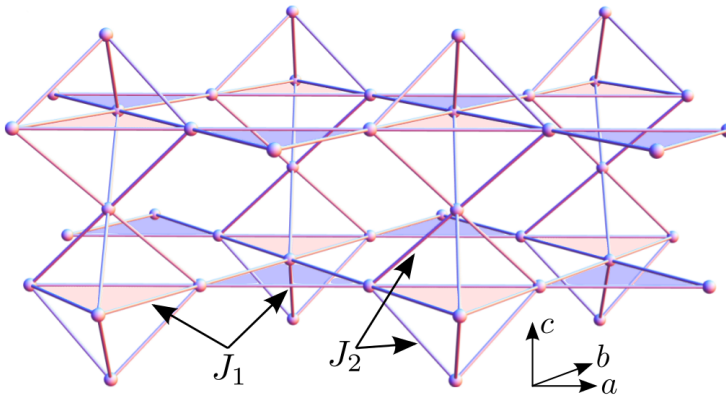
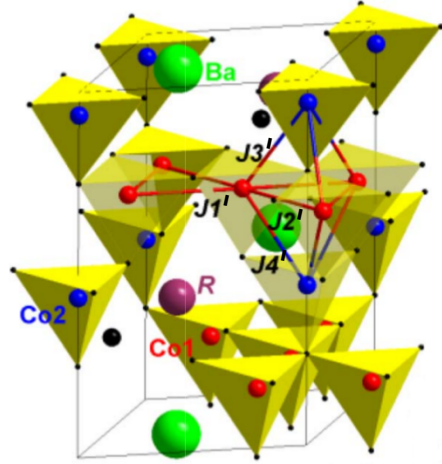
Neglecting all non-magnetic ions, one finds that the remaining magnetic ions reside on the lattice shown in Fig. 8.1.2, which is from now on simply referred to as the *swedenborgite lattice*. It has a hexagonal structure and is spanned by the three basis vectors

$$\mathbf{a} = \begin{pmatrix} 1 \\ 0 \\ 0 \end{pmatrix}, \quad \mathbf{b} = \begin{pmatrix} 1/2 \\ \sqrt{3}/2 \\ 0 \end{pmatrix}, \quad \mathbf{c} = \begin{pmatrix} 0 \\ 0 \\ 1 \end{pmatrix}, \quad (8.1.1)$$

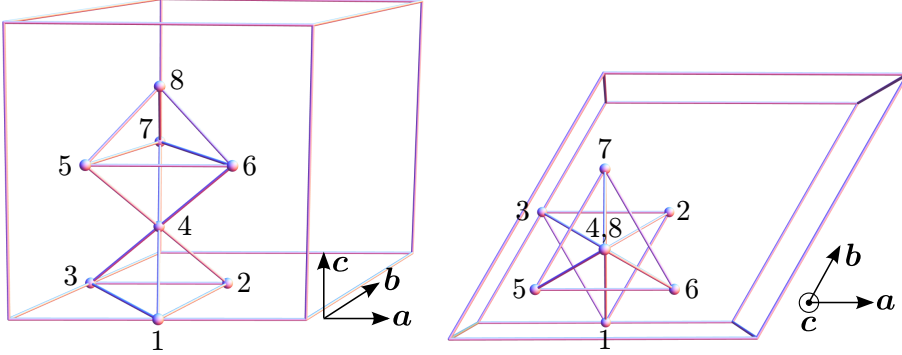
together with a magnetic unit cell comprised of eight atoms, c. f. Fig. 8.1.3.

It can be thought of either as a layered structure consisting of an alternating stack of triangular and kagome lattices in an ABAC...-pattern or as a lattice of triangle sharing bipyramids stacked along c-direction. The latter point of view emphasizes the unique exchange topology of the lattice: Typically, frustrated lattices are constructed out of small *corner*-sharing frustrated clusters like triangles on the kagome or tetrahedra on the pyrochlore lattice. In swedenborgites, however, the

**Figure 8.1.1:** The hexagonal lattice structure of  $R\text{BaCo}_4\text{O}_7$  as a network of corner-sharing  $\text{CoO}_4$  tetrahedra. The magnetic Co-ions in the kagome and triangular layers are denoted as  $\text{Co}_1$  (red) and  $\text{Co}_2$  (blue), respectively.  $R$  denotes a rare earth ion and oxygen ions are shown as black dots on the corners of the tetrahedra.  $J'_1, J'_2, J'_3$  and  $J'_4$  denote the four different exchange interactions allowed by the  $P6_3mc$  symmetry of the lattice, see main text. Picture taken from Ref. 110.



**Figure 8.1.2.:** The lattice formed by the magnetic ions in swedenborgite compounds. The filled triangles denote the kagome planes. Red triangles fully belong to a single bipyramid, whereas blue triangles connect three neighboring bipyramids.



$$\begin{array}{lll}
 \mathbf{r}_1 = (1/2, 0, 0) & \mathbf{r}_4 = (1/3, 1/3, 1/4) & \mathbf{r}_7 = (1/6, 2/3, 1/2) \\
 \mathbf{r}_2 = (1/2, 1/2, 0) & \mathbf{r}_5 = (1/6, 1/6, 1/2) & \mathbf{r}_8 = (1/3, 1/3, 3/4) \\
 \mathbf{r}_3 = (0, 1/2, 0) & \mathbf{r}_6 = (2/3, 1/6, 1/2) & 
 \end{array}$$

**Figure 8.1.3.:** The unit cell of the swedenborgite lattice and the relative position of the magnetic ions in terms of the lattice vectors.

lattice is constructed out of *triangle*-sharing frustrated bipyramidal clusters, i. e. frustrated clusters which are connected by other frustrated clusters. The influence of this fact on the ground state degeneracy is discussed in detail in Sec. 10.1.

The hexagonal symmetry (space group  $P6_3mc$  [110]) of the lattice allows in principle for four distinct nearest neighbor exchange interactions  $J'_1, J'_2, J'_3$  and  $J'_4$ ; the first two inside the kagome planes and the last two between ions in the kagome planes and adjacent triangular layers, c. f. Fig. 8.1.1. Using a spin-dimer analysis based on molecular orbital electronic-structure calculations, Khalyavin *et al.* have shown in Ref. 110 for cobalt oxides  $RBaCo_4O_7$  ( $R$  denotes a rare earth atom) that the in-plane interactions differ by less than 5% and the out-of-plane interactions by less than 10%. It is thus to a good approximation justified to use a simpler model with only two distinct exchange interactions<sup>1</sup>:  $J_1$ , accounting for the exchange inside the kagome planes and  $J_2$ , describing the exchange between the kagome planes and adjacent triangular layers. One can thus adopt the simplified Heisenberg Hamiltonian

$$H = J_1 \sum_{\langle ij \rangle \in \text{same layer}} \mathbf{S}_i \cdot \mathbf{S}_j + J_2 \sum_{\langle ij \rangle \in \text{diff. layer}} \mathbf{S}_i \cdot \mathbf{S}_j, \quad (8.1.2)$$

<sup>1</sup>This results in a model with exact frustration, c. f. Sec. 10.1.

where  $J_1, J_2 > 0$  are antiferromagnetic exchange interactions and  $\sum_{\langle ij \rangle}$  indicates a sum over nearest neighbors. It is shown in the next section that this minimal model agrees well with experimental findings if the ratio  $J_2/J_1$  is chosen appropriate for the particular compound under consideration.

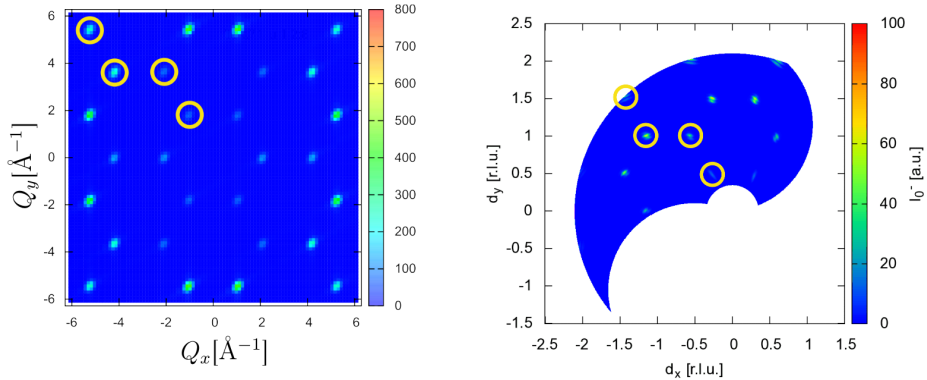
## 8.2. Experiments and verification of the model

In order to show the validity of the Hamiltonian Eq. (8.1.2) that was introduced in Sec. 8.1, it is desirable to compare the predictions that can be drawn from it to experimental findings. Unfortunately, there are only a limited number of experimental studies available at this time. A major reason for this is that the swedenborgite compounds have so far been overlooked by a large part of the scientific community, which can be traced back to the lack of a systematic theoretical study. This thesis intends to close this gap by showing that the playground offered by these systems is much richer than thought before. This should in turn motivate further experimental studies.

Most available experimental studies aim at the reconstruction of the magnetic ground state from neutron scattering data. Typically, the Hamiltonian Eq. (8.1.2) is therefore implemented in a classical Monte Carlo simulation, from which the thermally averaged magnetic structure factor is calculated and compared to the experimental findings. It turns out that very good agreement between the model and experiments can be achieved by tuning the ratio  $J_2/J_1$  in the range from 0 to  $3/2$ . In the following, I focus on the two compounds  $\text{CaBaCo}_2\text{Fe}_2\text{O}_7$  and  $\text{YBaCo}_4\text{O}_7$ , for which the magnetic structure factor has been measured using single crystals. Measurements with powder samples of other compounds have been published e. g. in Refs. 114 and 111.

The right part of Fig. 8.2.4 shows the magnetic structure factor of  $\text{CaBaCo}_2\text{Fe}_2\text{O}_7$  in the reciprocal  $hk0$  plane at  $T = 4$  K [115, 116]. One can clearly observe sharp Bragg peaks at  $\mathbf{q} \neq 0$ , indicating a long-range ordered antiferromagnetic ground state. The left part of Fig. 8.2.4 shows the magnetic structure factor obtained by a classical Monte Carlo simulation of Eq. (8.1.2) with  $J_2/J_1 = 3/2$  at  $T \ll J_1$  [115, 116]. The agreement between experiment and theory is striking, lending important experimental support for the assumption of the simplified model. It is shown in Sec. 10.1 by a detailed analysis of the Hamiltonian Eq. (8.1.2) that its magnetic ground state is long-range ordered and independent of  $J_2/J_1$  in the regime  $J_2/J_1 \geq 3/2$ . The actual ratio  $J_2/J_1$  in  $\text{CaBaCo}_2\text{Fe}_2\text{O}_7$  might thus be even larger than  $3/2$ .





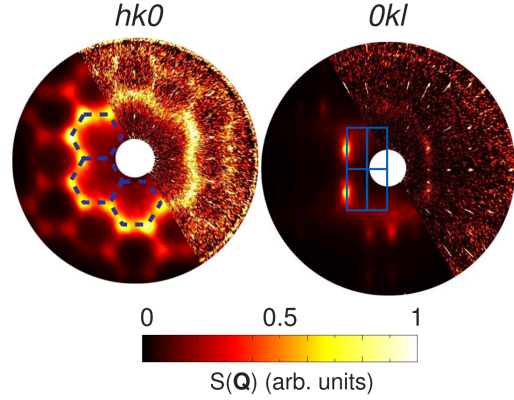
**Figure 8.2.4.:** Magnetic structure factor in the  $(q_x, q_y, 0)$  plane obtained from Monte Carlo simulations of the Hamiltonian Eq. (8.1.2) with  $J_2/J_1 = 3/2$  and  $T \ll J_1$  (left) and neutron scattering measurements with  $\text{CaBaCo}_2\text{Fe}_2\text{O}_7$  at  $T = 4\text{ K}$  (right). Pictures taken from Ref. 115.

Manuel *et al.* studied single crystals of the compound  $\text{YBaCo}_4\text{O}_7$  in Ref. 109. Fig. 8.2.5 shows the magnetic structure factor for this compound in the reciprocal  $hk0$  and  $hhl$  planes. The right hand side of the two images shows the experimentally measured data, whereas the left hand side shows again results from a classical Monte Carlo simulation of Eq. (8.1.2) [109], where the ratio  $J_2/J_1 = 1$  has been chosen to match the experimental data. Again, theory and experiment show a remarkable agreement in the sense that all observed features in the structure factor can be reproduced from the simplified model. The very broad peaks in the magnetic structure factor indicate short correlations, which can be traced back to the magnetic frustration in the system. It is shown in Sec. 10.1 that the ground state of the Hamiltonian is macroscopically degenerate for  $J_2/J_1 < 3/2$ , with a degeneracy that increases as  $J_2/J_1$  is lowered.

Some swedenborgite compounds, e.g.  $\text{YBaCo}_4\text{O}_7$ , also undergo a structural phase transition, in which the symmetry of the crystal lattice is lowered from hexagonal (space group  $P6_3mc$ ) or trigonal<sup>2</sup> (space group  $P3_1c$ ) to orthorhombic (space group  $Pbn2_1$ ) [117]. This symmetry lowering relieves the geometric frustration of the original lattice structure, c.f. Sec. 10.1, and the assumption of the simplified Hamiltonian with only two distinct nearest neighbor interactions is not justified anymore. Eventually, this leads to the selection of a unique long-range

<sup>2</sup>Huq *et al.* report in Ref. 117 that the trigonal  $P3_1c$  symmetry agrees slightly better with their measurements than the hexagonal  $P6_3mc$  symmetry reported e.g. by Khalyavin *et al.* for  $\text{RBaCo}_4\text{O}_7$  in Ref. 110

**Figure 8.2.5:** Magnetic structure factor for  $\text{YBaCo}_4\text{O}_7$  in the  $hk0$  (left panel) and  $0kl$  (right panel) reciprocal planes. Each map shows the data obtained from Monte Carlo simulations of the Hamiltonian Eq. (8.1.2) with  $J_2/J_1 = 1$  at  $T/J_1 = 4$  (left hand side) and experimental measurements at  $T = 130$  K with subtracted nuclear scattering (right hand side). Picture taken from Ref. 109.



**Table 8.2.1:** An overview of some swedenborgite compounds with the corresponding value  $J_2/J_1$  in the Hamiltonian Eq. 8.1.2 that reproduces the measured magnetic structure factor.

Compound	$J_2/J_1$	Ref.
$\text{CaBaCo}_2\text{Fe}_2\text{O}_7$	$\geq 3/2$	115
$\text{YBaCo}_4\text{O}_7$	$\approx 1$	109
$\text{YBaCo}_3\text{FeO}_7$	$\approx 1/2$	114
$\text{Y}_{0.5}\text{Ca}_{0.5}\text{BaCo}_4\text{O}_7$	$\gtrsim 0$	111, 118

ordered antiferromagnetic ground state at low temperatures [117].

Since the aim of this section is only to show the validity of the simplified Hamiltonian, it is beyond the scope of this work to give a full and detailed overview of all experimental studies on swedenborgite compounds. More data on the magnetic structure factors is e.g. published in Refs. 114 and 111.

Tab. 8.2.1 shows an overview of some swedenborgite compounds with the corresponding ratio  $J_2/J_1$  as derived from a comparison of Monte Carlo simulations of the Hamiltonian Eq. (8.1.2) with neutron scattering experiments.

## 9. Classical Ising model on the swedenborgite lattice

In this section, I analyze the Ising model with and without magnetic field in detail. It turns out that even though this particular model is probably not realized in any swedenborgite compound, it features very rich physics in terms of competing degenerate ground state manifolds and is thus of great conceptual interest in the context of spin-liquids.

I first introduce the concept of the residual entropy as a quantitative measure for the ground state degeneracy and calculate it for different ratios  $J_2/J_1$ . At zero field, two different ground state manifolds, separated by a first-order transition at  $T = 0$  and equal exchange couplings, are found. In the vicinity of this point, the crossover temperature turns out to be linearly suppressed as a result of the almost equal energy of the two ground state regimes. For a finite magnetic field, one finds a rich phase diagram with six phases, in which the degeneracy is lifted either partially or completely. Most of the results presented in this chapter have been published in Ref. 119.

### 9.1. Residual entropy

For systems with a vanishing specific heat  $c_V$  in the limit  $T \rightarrow 0$  and known entropy in the disordered phase, it is possible to calculate the residual entropy (ground state entropy) at  $T = 0$  by integrating the Maxwell relation

$$\frac{dS}{dT} = \frac{c_V}{T} \quad (9.1.1)$$

from  $T = 0$  to  $T = \infty$ . For classical systems with continuous spin variables, where  $c_V \rightarrow \text{const.}$  as  $T \rightarrow 0$ , this integral diverges logarithmically at  $T = 0$  and the method cannot be applied. The fact that  $dS/dT$  diverges for low temperatures is a general problem of classical models. Models that take into account the quantum nature of spins do not encounter this problem, but are analytically and numerically much less tractable. For discrete Ising spins, however, the specific heat vanishes as  $T \rightarrow 0$  due to the gapped excitation spectrum and the integral over Eq. (9.1.1) converges.

Since each Ising spin has two possible orientations (up and down) that occur with

**Table 9.1.1:** Known values of the residual entropy for the Ising model without magnetic field on different lattices.

Lattice	$S_{\text{res}}/\ln 2$	Ref.
Triangular	$\approx 0.47$	86
Kagome	$\approx 0.72$	86, 87
Pyrochlore	$\approx 0.32$	88

the same probability in the disordered phase, the entropy per spin at  $T = \infty$  is simply  $\ln 2$ . The residual entropy  $S_{\text{res}}$  at  $T = 0$  is then given by

$$S_{\text{res}} = \ln 2 - \int_0^\infty \frac{c_V}{T} dT. \quad (9.1.2)$$

The specific heat that occurs in the integral is not known analytically in most cases. It can, however, be calculated numerically, e. g. in a Monte Carlo simulation.

The ratio  $S_{\text{res}}/\ln 2$  is a measure for the ground state degeneracy. It ranges from 0 for a unique or sub-extensively degenerate ground state to 1 for a system without any ground state constraints. Tab. 9.1.1 shows the residual entropies for the antiferromagnetic Ising model on various lattices.

## 9.2. Ground state degeneracy and phase diagram for $\mathbf{B} = 0$

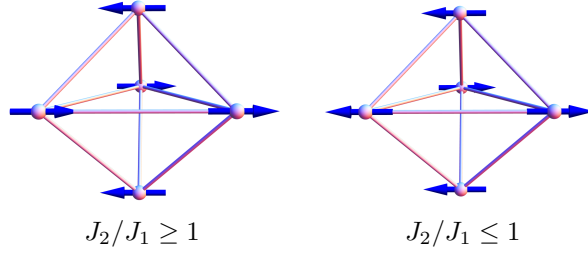
The ground state of the Ising model on the swedenborgite can be determined conveniently by analyzing the building blocks of the lattice, i. e. bipyramids and intermediate triangles, independently.

For the intermediate triangles, it was already shown in Sec. 7.2 that ground state configurations have to fulfill

$$\sigma_\Delta^1 + \sigma_\Delta^2 + \sigma_\Delta^3 = \pm 1 \quad (9.2.3)$$

on every triangle, resulting in a six-fold degeneracy per triangle as long as they are isolated.

For the bipyramids, the situation is slightly more complicated. While the out-of-plane interaction  $J_2$  favors states with all three kagome spins of a bipyramid aligned anti-parallel to the mutually parallel triangular spins, the in-plane interaction  $J_1$  favors states in which the kagome spins obey Eq. (9.2.3), excluding a full satisfaction of the out-of-plane interaction. The ground state configuration of the bipyramids thus depends on the ratio  $J_2/J_1$ . For  $J_2/J_1 > 1$ , the three kagome spins are aligned mutually parallel and anti-parallel to the triangular spins, c. f. left part of Fig. 9.2.1. This configuration with energy  $E = -12J_2 + 6J_1$  per unit cell is not degenerate if one assumes that the triangular spins are fixed. In the



**Figure 9.2.1.:** The bipyramid ground state configurations for  $J_2/J_1 \geq 1$  and  $J_2/J_1 \leq 1$ .

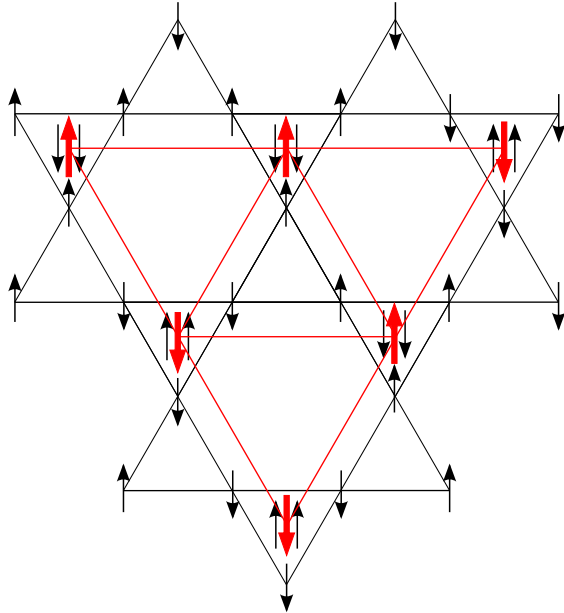
allowed bipyramid configurations	
$J_2/J_1 > 1$	
$J_2/J_1 = 1$	
$J_2/J_1 < 1$	

**Table 9.2.2.:** Degeneracy of the bipyramid configurations in the different ground state regimes. The two spins in the center of each triangle denote the triangular spins of a bipyramid, which are assumed to be already fixed in “up” direction. The configurations for  $J_2/J_1 > 1$  and  $J_2/J_1 < 1$  have an energy per unit cell of  $E = -12J_2 + 6J_1$  and  $E = -8J_2 + 2J_1$ , respectively.

regime  $J_2/J_1 < 1$ , where the in-plane interaction dominates, it becomes favorable for the system to flip one of the three kagome spins in each bipyramid to align it parallel with the triangular spins, c. f. right part of Fig. 9.2.1. In this configuration with energy  $E = -8J_2 + 2J_1$  per unit cell, each bipyramid is three-fold degenerate. For  $J_2/J_1 = 1$ , both above mentioned bipyramid configurations have the same energy and the bipyramids are thus four-fold degenerate. Tab. 9.2.2 summarizes the bipyramid degeneracy in dependence on  $J_2/J_1$ .

The ground state of the whole system is constructed by connecting the bipyramids via the intermediate triangles in the kagome planes. For  $J_2/J_1 > 1$ , the stacked bipyramids are ordered along  $c$ -direction and it is sufficient to choose the spin directions of the bipyramids and intermediate triangles in *one* plane

**Figure 9.2.2:** The mapping between the original ground state on the swedenborgite lattice and the Ising model on the triangular lattice for  $J_2/J_1 > 1$ . Shown is one layer of kagome spins with the triangular spins above and below (black). Replacing all bipyramids with a single spin pointing in direction of the respective kagome spins, one can map the ground state to a triangular lattice (red). Note that the spin configuration repeats itself in c-direction, i. e. in the direction orthogonal to the plane shown.

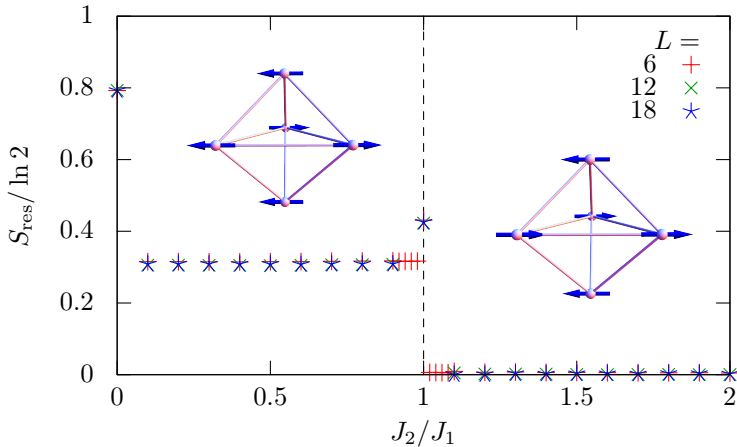


to fix *all* remaining spins in the system. The problem is therefore effectively reduced to the two-dimensional problem of Ising spins on the triangular lattice, c. f. Fig. 9.2.2. The resulting ground state degeneracy is thus *sub-extensive* and the residual entropy per spin vanishes in the thermodynamic limit.

For  $J_2/J_1 < 1$ , fixing one plane of bipyramids and intermediate triangles does not fix the whole ground state since bipyramids on top of each other can choose independent kagome spin configurations. Although the triangular spins are fixed along c-direction, the kagome planes remain degenerate, resulting in an extensively degenerate ground state.

At the equal coupling point  $J_2/J_1 = 1$ , the degeneracy is larger than for  $J_2/J_1 < 1$  since there are four types of bipyramids instead of three to choose from, c. f. Tab. 9.2.2. Based on this argument, one can expect the ground state degeneracy at  $J_2/J_1 = 1$  to be larger than at  $J_2/J_1 < 1$ .

The residual entropy was calculated numerically for various ratios  $J_2/J_1$  in the range from 0 to 2 to quantify the degeneracy in the different ground state regimes. The specific heat, which is required for this according to Eq. (9.1.2), was obtained using feedback optimized parallel tempering Monte Carlo as described in Sec. 2.2 and 2.3. A direct comparison to simulated annealing algorithms has shown that the latter ones are not able to sample the degenerate ground state manifold properly, especially if the couplings  $J_1$  and  $J_2$  are of the same size or if  $J_2$  is much



**Figure 9.2.3.:** Residual entropy for the Ising model on the swedenborgite lattice in dependence on  $J_2/J_1$ . The spin configurations shown are the bypyramid ground state configuration for  $J_2/J_1 < 1$  (left) and  $J_2/J_1 > 1$  (right).

smaller than  $J_1$ . The ground states obtained upon cooling have often shown frozen defects like single defect bipyramids. The feedback optimized parallel tempering algorithm, on the other hand, was able to overcome these problems. Monitoring the drift of the replicas through temperature space as described in Sec. 2.3, it was found that equilibration could be achieved for *all* values  $J_2/J_1$ . It is thus strictly necessary to use the more sophisticated parallel tempering algorithm in order to obtain correct results. The final integration of  $c_V/T$  according to Eq. (9.1.2) has been carried out using the standard trapezoidal rule for numerical integration [20].

Fig. 9.2.3 shows the residual entropy in dependence on  $J_2/J_1$ . For  $J_2/J_1 < 1$ , one finds a value of  $S_{\text{res}}/\ln 2 \approx 0.32$ , which is clearly smaller than the values reported for the antiferromagnetic Ising model on the triangular lattice ( $S_{\text{res}}/\ln 2 \approx 0.47$  [86]) and the kagome lattice ( $S_{\text{res}}/\ln 2 \approx 0.72$  [86, 87]), but of the same size as for so-called “spin-ice”, the antiferromagnetic Ising model on the pyrochlore lattice ( $S_{\text{res}}/\ln 2 \approx 0.32$  [88]), c.f. Tab. 9.1.1. For equal exchange couplings, the enhanced degeneracy of the bipyramids results in a larger residual entropy of  $S_{\text{res}}/\ln 2 \approx 0.43$ , a value which is compatible with the assumption that the ground state degeneracy at  $J_2/J_1 = 1$  is larger than at  $J_2/J_1 < 1$  as mentioned above. For  $J_2/J_1 > 1$ , the residual entropy vanishes, consistent with the assumption of a sub-extensively degenerate ground state.

To check the above results for consistency, one can also estimate the residual

entropy by a counting argument following Ref. 88. Starting from stacked bipyramids, there are 9 ( $J_2/J_1 < 1$ ) or 16 ( $J_2 = J_1$ ) ground state configurations per unit cell, if one assumes that the triangular spins are aligned parallel in c-direction. This results in  $9^{N/8}$  ( $J_2/J_1 < 1$ ) or  $16^{N/8}$  ( $J_2/J_1 = 1$ ) allowed ground states on a lattice with  $N$  sites. Since the direction of the triangular spins inside the columns is a priori not fixed, there is an additional factor of 2 for each of the  $(N/8)^{2/3}$  columns. The influence of the intermediate triangles can be taken into account by deflating these numbers by the probability of 6/8 that the  $N/4$  intermediate triangles are in a ground state configuration, leading to the estimates

$$\frac{S_{\text{res}}}{N} = \begin{cases} \frac{1}{N} \ln \left( 9^{N/8} \left(\frac{6}{8}\right)^{N/4} 2^{(N/8)^{2/3}} \right) \approx 0.29 \ln 2 + \mathcal{O}(N^{-1/3}) & J_2/J_1 < 1 \\ \frac{1}{N} \ln \left( 16^{N/8} \left(\frac{6}{8}\right)^{N/4} 2^{(N/8)^{2/3}} \right) \approx 0.40 \ln 2 + \mathcal{O}(N^{-1/3}) & J_2/J_1 = 1 \end{cases} \quad (9.2.4)$$

Both values are very close to the values obtained from the Monte Carlo simulation.

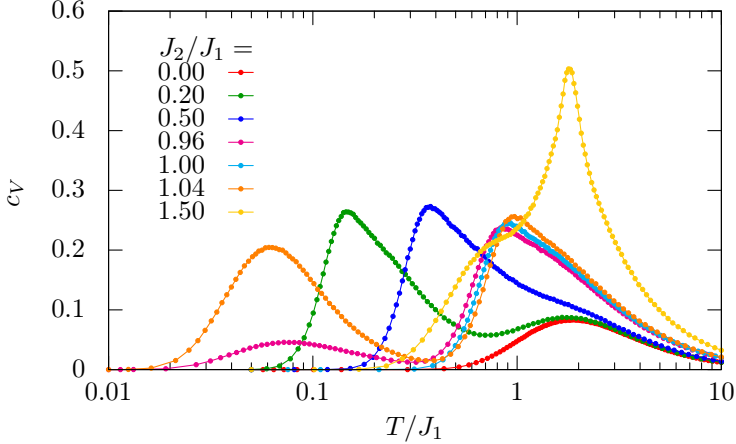
### 9.3. Suppression of the crossover temperature for $J_2 \approx J_1$

It was shown in the last section that the ground state manifold for the antiferromagnetic Ising model on the swedenborgite lattice is mainly characterized by the two possible configurations of the bipyramids for  $J_2/J_1 < 1$  and  $J_2/J_1 > 1$ . If the exchange couplings in the system are equal, both bipyramid configurations have the same energy and the ground state can be constructed using both types, resulting in a larger ground state degeneracy and residual entropy at the single point  $J_2/J_1 = 1$ .

In this section, the focus is on the temperature at which the crossover to the ground state manifold occurs, in particular its dependence on the ratio  $J_2/J_1$ . It is shown that the crossover temperature can be significantly suppressed if the exchange couplings  $J_1$  and  $J_2$  are *almost* equal.

The crossover temperature can be determined e. g. from the specific heat. Whenever the system locks into a specific ground state manifold, its entropy decreases due to the truncation of the available phase space. Rearranging Eq. (9.1.1), one finds  $c_V = TdS/dT$ , i. e. this release of entropy must be accompanied by a hump in the specific heat. Fig. 9.3.4 shows the specific heat for different ratios  $J_2/J_1$ . If the kagome planes are decoupled, i. e.  $J_2 = 0$ , there is only one hump in the specific heat that signals the selection of an up-up-down or up-down-down configuration on each triangle.

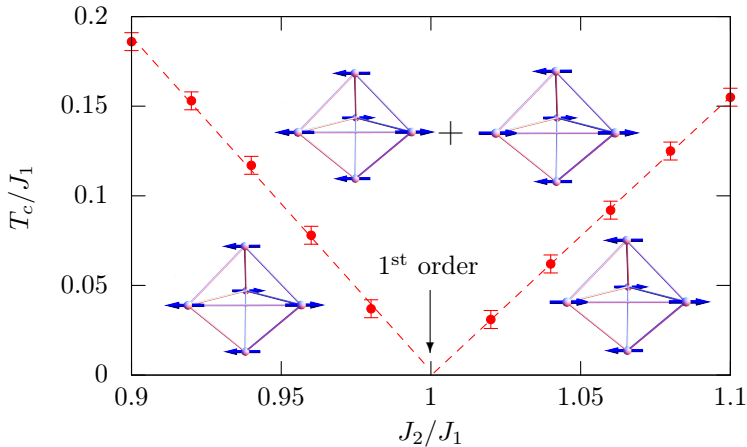




**Figure 9.3.4.:** The specific heat of the Ising model on the swedenborgite lattice in dependence on temperature for various ratios  $J_2/J_1$ . A well separated double peak structure emerges if the ratio  $J_2/J_1$  is close to 1 or if  $J_2/J_1 \ll 1$ . In both cases, the low-temperature peak is pushed to  $T = 0$  as  $J_2/J_1$  approaches 1 or 0, respectively.

If the out-of-plane coupling is much weaker than the in-plane coupling, the system crosses over into its ground state manifold in two steps. First, *all* triangles in the kagome planes select up-up-down and up-down-down states, resulting in a hump at a temperature of the order  $\mathcal{O}(J_1)$ , whereas the triangular spins remain disordered until a much lower temperature of the order  $\mathcal{O}(J_2)$ , where the bipyramids eventually enter their respective ground state configurations, accompanied by a second peak in the specific heat. These two peaks merge into one broad peak as  $J_2/J_1$  is increased above  $\approx 0.3$  and the two crossovers cannot be separated any more.

Another interesting parameter region is given by almost equal exchange couplings. Exactly at  $J_2/J_1 = 1$ , one finds only one hump at a temperature of  $\mathcal{O}(J_1)$ , indicating that the intermediate triangles and the bipyramids enter their respective ground state manifold at the same time. In the vicinity of this point, i. e.  $J_2 = J_1 \pm \delta$ , one observes an additional well separated hump at low temperatures which is pushed towards  $T = 0$  as  $\delta \rightarrow 0$ . This feature originates from the fact that the two relevant bipyramid configurations, which are truly degenerate at  $J_2 = J_1$ , appear almost degenerate for  $J_2 \approx J_1$  until the temperature becomes of the order of their energy splitting  $\Delta E = |J_2 - J_1|/2$  per spin. As a consequence, the position of the associated hump in the specific heat is found to approach  $T = 0$  linearly as  $J_2/J_1$  approaches 1, c. f. Fig. 9.3.5. The crossover temperature



**Figure 9.3.5.:** The crossover temperature to the different ground state regimes determined from the position of the low-temperature hump in the specific heat as a function of  $J_2/J_1$ . Close to  $J_2/J_1 = 1$ , both relevant bipyramid configurations appear almost degenerate until the temperature is low enough for the system to distinguish between them. The dashed lines represent a linear regression.

in these systems can thus be substantially smaller than one would expect it based on the strength of the exchange interactions. Exactly at  $J_2/J_1 = 1$  and  $T = 0$ , there is a first-order phase transition between the two ground state regimes due to a level crossing of the energies of the two bipyramid configurations.

For values of  $J_2/J_1$  significantly larger than 1, one finds again a weakly separated double peak structure in the specific heat. The first peak at a temperature of order  $\mathcal{O}(J_2)$  signals the formation ordered columns of bipyramids along c-direction, whereas the broad second peak indicates the alignment of these columns in a way that all intermediate triangles are either in an up-up-down or up-down-down configuration according to Eq. (9.2.3).

## 9.4. Structure factors and correlations

One can expect from the analysis of the ground state constraints on the bipyramids and intermediate triangles in Sec. 9.2 that the different ground state regimes feature different spin-spin correlations. Due to the degeneracy of the intermediate triangles, correlations in the ab-plane always remain short ranged and are expected to decay on the lattice scale. Correlations along c-direction can, however, be different for kagome and triangular spins depending on the ratio  $J_2/J_1$ :

The triangular spins in each bipyramid are always aligned parallel and consequently long-range ordered in  $c$ -direction. For  $J_2/J_1 > 1$ , the kagome spins in every bipyramid are aligned anti-parallel to the respective triangular spins and hence also long-range ordered along  $c$ -direction. For  $J_2/J_1 = 1$  and  $J_2/J_1 < 1$ , however, the probability that a kagome spin in a bipyramid is anti-parallel to the respective triangular spin is only  $3/4$  and  $2/3$ , respectively, c. f. Tab. 9.2.2. This leads to the conclusion that the spin-spin correlation function

$$g(\mathbf{r} - \mathbf{r}') = \langle \sigma(\mathbf{r})\sigma(\mathbf{r}') \rangle \quad (9.4.5)$$

as well as the magnetic structure factor

$$S(\mathbf{q}) = \frac{1}{N} \sum_{ij} \langle \sigma_i \sigma_j \rangle e^{i\mathbf{q}(\mathbf{r}_i - \mathbf{r}_j)}, \quad (9.4.6)$$

should show a strong anisotropic decay of correlations and behave differently for  $J_2/J_1 = 1$ ,  $J_2/J_1 < 1$  and  $J_2/J_1 > 1$ .

The structure factor was calculated numerically in a Monte Carlo simulation for all three regimes. As expected, it was found that the precise value of  $J_2/J_1$  has no influence on the result in the latter two regimes. The values  $J_2/J_1 = 1/2$  and  $3/2$  have been simulated as representative values for these regimes since they were relatively easy to equilibrate and thus allowed to simulate a larger lattice size of  $L = 30$ , which increases the resolution in  $k$ -space.

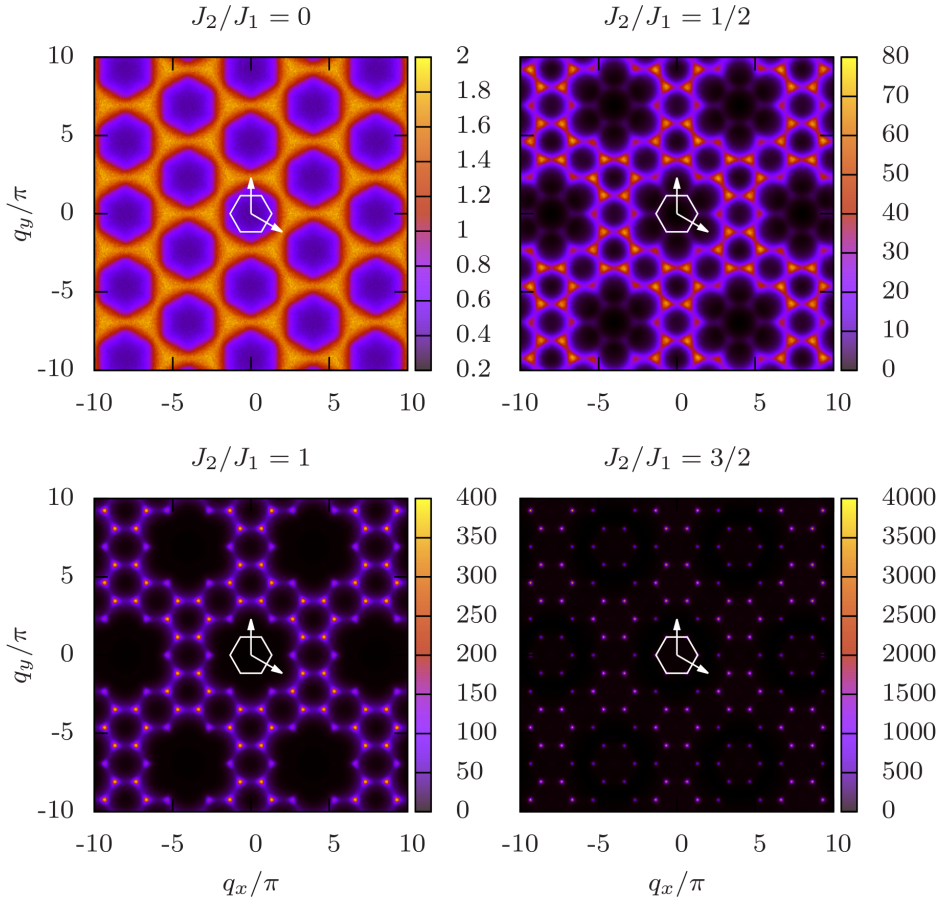
Figs. 9.4.6 and 9.4.7 show the structure factor in the three different regimes averaged over several cooling cycles down to  $T = 0$  in the  $(q_x, q_y, q_z = 0)$  and  $(q_{xy}, q_{xy}, q_z)$  plane, respectively. The white arrows in these figures represent the reciprocal lattice vectors

$$\mathbf{k}_1 = 2\pi \begin{pmatrix} 1 \\ -1/\sqrt{3} \\ 0 \end{pmatrix}, \quad \mathbf{k}_2 = 2\pi \begin{pmatrix} 0 \\ 2/\sqrt{3} \\ 0 \end{pmatrix}, \quad \mathbf{k}_3 = 2\pi \begin{pmatrix} 0 \\ 0 \\ 1 \end{pmatrix} \quad (9.4.7)$$

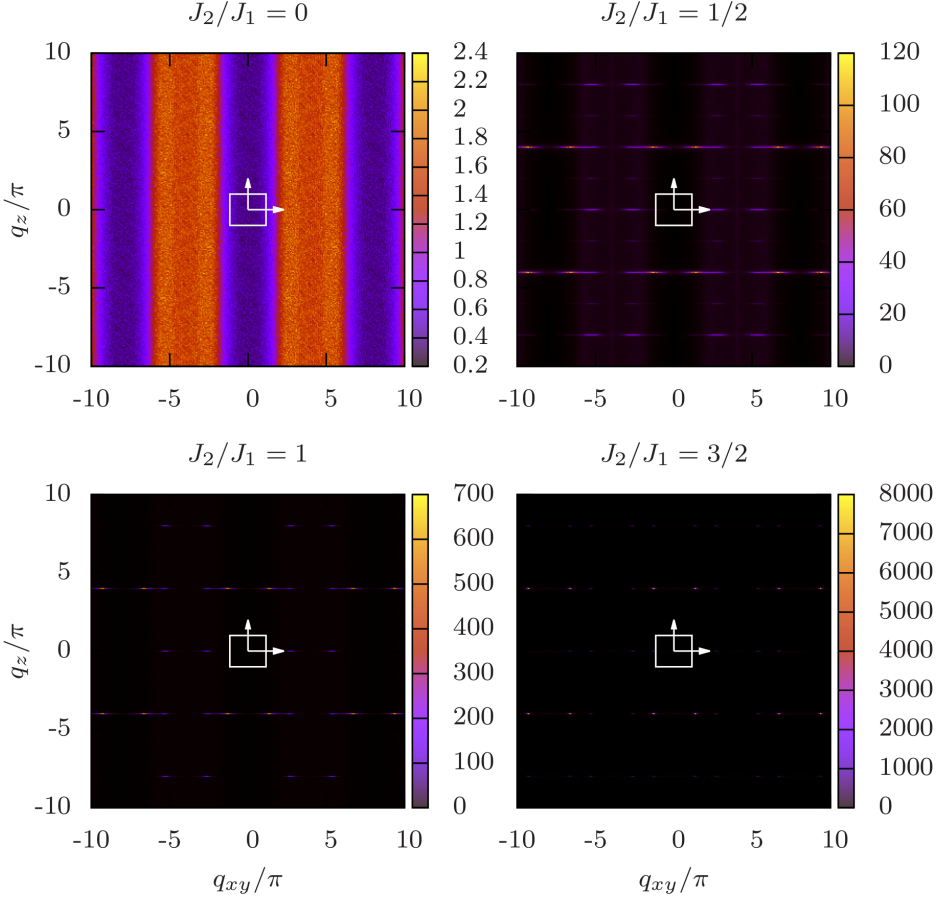
which have been obtained from the basis vectors of the lattice in real space, c. f. Eq. (8.1.1), by

$$\mathbf{k}_1 = 2\pi \frac{\mathbf{b} \times \mathbf{c}}{\mathbf{a} \cdot (\mathbf{b} \times \mathbf{c})}, \quad \mathbf{k}_2 = 2\pi \frac{\mathbf{c} \times \mathbf{a}}{\mathbf{a} \cdot (\mathbf{b} \times \mathbf{c})}, \quad \mathbf{k}_3 = 2\pi \frac{\mathbf{a} \times \mathbf{b}}{\mathbf{a} \cdot (\mathbf{b} \times \mathbf{c})} \quad (9.4.8)$$

and the white hexagons and rectangles show the first Brillouin zone. As expected, the enhanced degeneracy of the bipyramids for  $J_2/J_1 \leq 1$  leads to weaker correlations, indicated by the broadening of the peaks in the  $q_x$ - $q_y$  plane. Correlations along  $c$ -direction, on the other hand, remain long-ranged as long as  $J_2$  is finite. For  $J_2 = 0$ , the kagome planes are completely decoupled, resulting in vanishing correlations along  $c$ -direction and very weak and short-ranged correlations in the



**Figure 9.4.6.:** The magnetic structure factor Eq. (9.4.6) for different ratios  $J_2/J_1$  at  $T = 0$  in the  $(q_x, q_y, q_z = 0)$  plane. The white arrows denote the reciprocal lattice vectors and the white hexagon represents the first Brillouin zone. One can clearly observe a broadening of the peaks for  $J_2/J_1 \leq 1$ . Note the different scales of the color code in the different images.



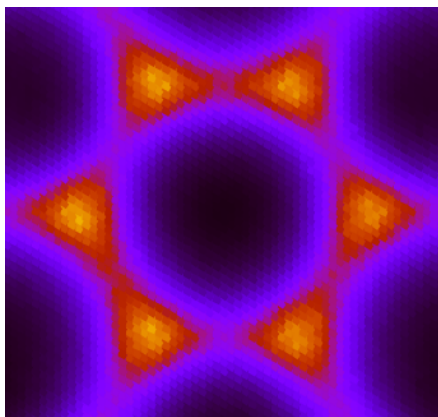
**Figure 9.4.7.:** The magnetic structure factor Eq. (9.4.6) for different ratios  $J_2/J_1$  at  $T = 0$  in the  $(q_{xy}, q_{xy}, q_z)$  plane. The white arrows denote the reciprocal lattice vectors and the white rectangle represents the first Brillouin zone. One can observe a broadening of the peaks along the  $q_{xy}$  direction for  $J_2/J_1 \leq 1$ . Note the different scales of the color code in the different images.

ab-plane.

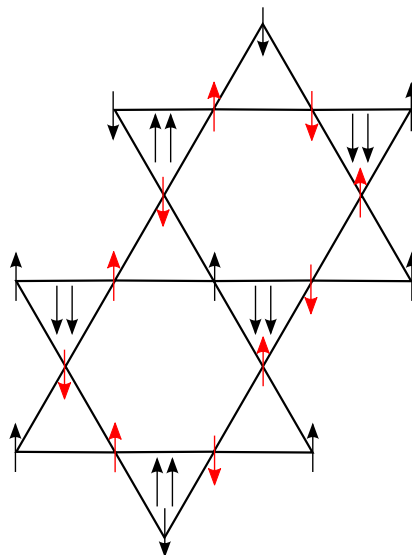
For  $0 < J_2/J_1 < 1$ , the structure factor shows bow-tie like structures reminiscent of the pinch-points which occur in Coulomb-phases, c. f. Sec. 7.5. A close inspection of these structures, c. f. Fig. 9.4.8, reveals, however, that there is no direction in which the correlations vanish completely as one moves away from the center of the bow-tie, as it should for a real pinch-point according to Eq. (7.5.26) and Fig. 7.5.15. Since the structure factor was obtained strictly at  $T = 0$ , thermal broadening of a true pinch-point cannot be the reason for this observation.

It was mentioned in Sec. 7.5 that Coulomb-phases can only exist if one can describe the ground state manifold either by an ice-rule or a hardcore dimer covering. The fact that the bipyramids and triangles on the swedenborgite lattice consist of an odd number of spins excludes an ice-rule description and it was also not possible to find any mapping of the ground state manifold to a dimer covering. The observed bow-tie like features thus do not seem to be pinch-points originating from a Coulomb-phase.

There are nevertheless some similarities between a Coulomb-phase and the ground state manifold for  $J_2/J_1 < 1$ . As it was shown in Sec. 7.5, Coulomb-phases are well known to host closed loops of zero-energy spin flips that connect different ground states with each other. It was shown in Fig. 7.5.16 that non-closed loops also allow defects (i. e. local violations of the ground state constraints) to move through the system without energy cost and that these loops are thus the origin of the defect mobility in these phases. One can find similar loops within the kagome layers of the swedenborgite lattice, consisting of neighboring anti-parallel aligned spins, c. f. Fig. 9.4.9. In contrast to Coulomb-phases, it is however not possible to reach every ground state by flipping such loops since the spins on the triangular lattice remain unaffected. Nevertheless, non-closed loops can mediate the movement of single defects, in lowest order described by bipyramids with three instead of two kagome spins anti-parallel to the triangular ones, within the kagome planes. One can also easily construct zero energy spin flips for  $J_2/J_1 = 1$ , where the loops do not necessarily have to be closed due to the enhanced degeneracy of the ground state manifold, whereas no such loops exist for  $J_2/J_1 > 1$ .



**Figure 9.4.8.:** Close-up of the pinch-point like structure in the  $(q_x, q_y, q_z = 0)$  plane for  $J_2/J_1 = 0.5$  at  $T = 0$ . There is no direction in which the correlations vanish completely as one moves away from the center of the bow-tie as it should for a real pinch-point according to Eq. (7.5.26).



**Figure 9.4.9.:** A zero-energy loop spin flip in the ground state manifold for  $J_2/J_1 < 1$ . Flipping the chain of red spins at the same time does not cost any energy and the system remains in the ground state manifold.

## 9.5. Ground state degeneracy and phase diagram for $B \neq 0$

In this section, I study the effect of a magnetic field on the ground state degeneracy and consider the Hamiltonian

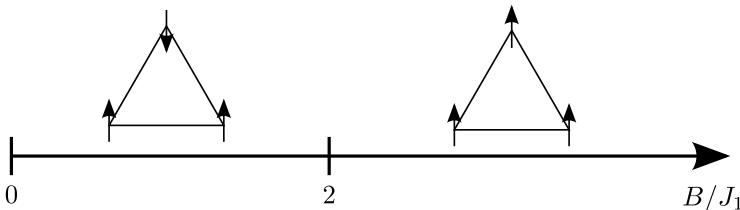
$$H = J_1 \sum_{\substack{\langle ij \rangle \in \\ \text{same layer}}} \sigma_i \sigma_j + J_2 \sum_{\substack{\langle ij \rangle \in \\ \text{diff. layer}}} \sigma_i \sigma_j - B \sum_i \sigma_i \quad (9.5.9)$$

with the magnetic field  $B$  applied in the direction of the Ising axis. A magnetic field in a different direction would lead to a quantum model that favors spin flips. As in Sec. 9.2, the ground state of the system is again constructed piecewise by considering isolated triangles and stacked bipyramidal clusters independently. It turns out that connecting these units at finite field is much more complicated than in the zero-field case. The resulting phase diagram shows a large variety of six phases with different magnetizations and degeneracies. In two of these phases, the degeneracy is lifted only partially by the magnetic field.

On the intermediate triangles, an infinitesimal magnetic field already favors the up-up-down configurations and thus reduces the degeneracy by a factor of two to three-fold. These configurations with energy  $E = -J_1 - B$  per triangle become unfavorable with respect to the (non-degenerate) fully polarized states with energy  $E = 3J_1 - 3B$  per triangle at  $B/J_1 = 2$ . Fig. 9.5.10 shows the corresponding phase diagram.


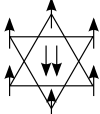

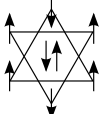
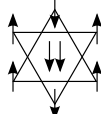

Of all possible stacked bipyramid configurations, only those which can gain energy from a magnetic field are of interest. These states and their corresponding energies are shown in Tab. 9.5.3. The  $T = 0$  mean-field phase diagram in the  $B - J_2$  plane can be found by comparing their energies and is shown in Fig. 9.5.11.

While the determination of the phase diagram for isolated triangles and stacked bipyramids is rather straightforward, the situation becomes much more compli-

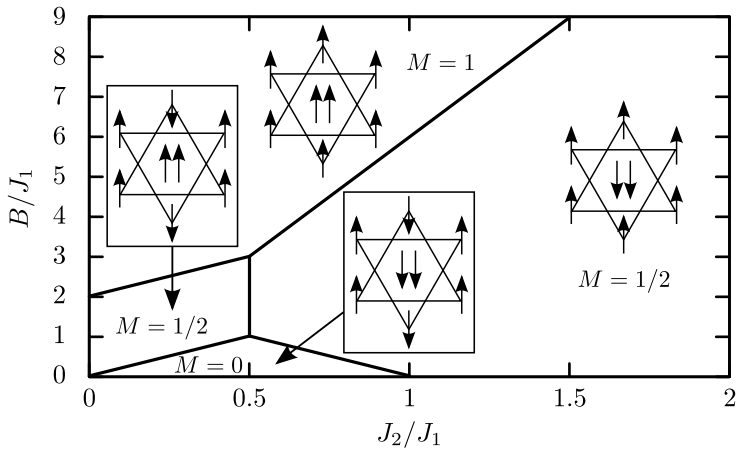


**Figure 9.5.10.:** The phase diagram for a single triangle in a magnetic field at  $T = 0$ .



State	Energy	State	Energy
	$12J_2 + 6J_1 - 8B$		$-12J_2 + 6J_1 - 4B$
	$6J_1 - 6B$		$-2J_1 - 2B$
	$-4J_2 - 2J_1$		$4J_2 - 2J_1 - 4B$

**Table 9.5.3.:** All spin configurations of a unit cell (two stacked bipyramids) that can gain energy from a magnetic field (pointing in “up” direction) and their corresponding energy (per unit cell). The two triangles belong to different kagome layers and are thus pointing in opposite directions. The two spins inside the triangles denote the two triangular spins in the unit cell. The resulting phase diagram is shown in Fig. 9.5.11.

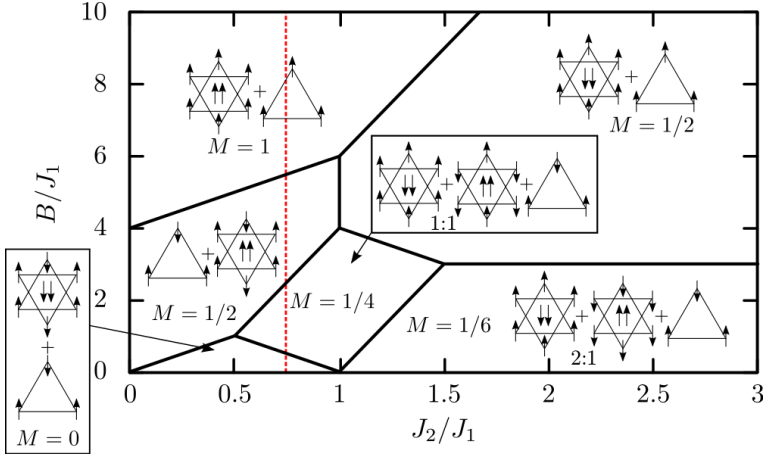


**Figure 9.5.11.:**  $T = 0$  phase diagram for columns of isolated stacked bipyramids in a magnetic field. The energies per unit cell are shown in Tab. 9.5.3.  $M$  denotes the magnetization per spin.

cated when they are connected as on the swedenborgite lattice. There are certain bipyramid configurations (e. g. the top right configuration in Tab. 9.5.3) that can not be connected to every site of an intermediate up-up-down triangle without an energy penalty due to the magnetic field, even though the isolated bipyramids might be able to gain energy from the field if rotated in the right direction. On the other hand, it might be favorable to have up-up-down configurations on the intermediate triangles once they are connected to certain bipyramids, even though an isolated triangle would prefer to be fully polarized. The only way to find the phase diagram is to systematically write down all possible bipyramid configurations and combine them with intermediate up-up-down or (polarized) up-up-up triangles. This task becomes even more complicated if one takes into account that not all bipyramids need to have the same configuration. A detailed analysis of all possible combinations results in the phase diagram shown in Fig. 9.5.12, which was also checked against Monte Carlo simulations for several points to ensure consistency.

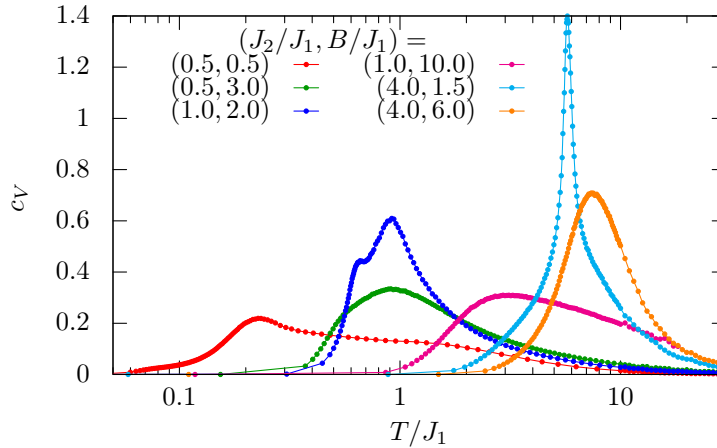
One finds that there are in total six different phases at finite magnetic field, four of which differ in their magnetization. If the magnetic field is the dominating energy scale, i. e.  $B \gg J_2, J_1$ , the ground state is a completely polarized phase with all spins pointing in direction of the field. On the other hand, if  $J_2$  dominates, i. e.  $J_2 \gg B, J_1$ , the bipyramids take the antiferromagnetic configuration shown in the left part of Fig 9.2.1 where the kagome spins inside the bipyramid align anti-parallel to the triangular spins. Depending on the strength of the magnetic field compared to  $J_1$ , these bipyramids are then connected either by up-up-down or fully polarized triangles. The other three phases can not be understood intuitively due to the lack of a dominating energy scale. All transitions between the different phases are again first-order since they originate from level crossings of the respective energies.

Fig. 9.5.13 shows the specific heat at single points within the six different phases for which the residual entropy has again been calculated using Eq. (9.1.2). One finds that only the  $M = 0$  phase ( $S_{\text{res}}/\ln 2 \approx 0.24$ ) and the  $M = 1/2$  phase for  $J_2/J_1 < 1$  ( $S_{\text{res}}/\ln 2 \approx 0.11$ ) have an extensive ground state degeneracy. In general, the ground state degeneracy is always smaller than for zero-field, as expected. There are, however, regions in the phase diagram where the degeneracy changes unexpectedly as the field is varied at constant  $J_2/J_1$ . Following the red line in Fig. 9.5.12, the residual entropy changes according to  $0.24 \ln 2 \rightarrow 0 \rightarrow 0.11 \ln 2 \rightarrow 0$  in the different phases as the magnetic field is increased, i. e. there are regions in the phase diagram where an increase of the magnetic field counter-intuitively leads to an increase of the degeneracy. The reason is rooted in the fact that the ground state manifold is more rigid in the intermediate  $M = 1/4$  zero entropy phase than the two adjacent finite entropy phases. The difference in the residual entropy between the two phases traces back to the fact that,



**Figure 9.5.12.:**  $T = 0$  Phase diagram of the Ising model on the swedenborgite lattice in an external magnetic field. “up” pointing triangles represent the blue intermediate triangles from Fig. 8.1.2 and “down” pointing triangles represent the triangles inside the bipyramids (red triangles in Fig. 8.1.2) with the two triangular spins shown inside.  $M$  denotes the magnetization per spin and if a ratio is given, it denotes the ratio of the different bipyramid configurations in the ground state. All transitions between the different phases are first-order. Along the red line the residual entropy changes as  $0.24 \ln 2 \rightarrow 0 \rightarrow 0.11 \ln 2 \rightarrow 0$  in the different phases as the magnetic field is increased.

while in the  $M = 0$  phase the bipyramids are two-fold degenerate with respect to their orientation in the field, a certain alignment of the bipyramids is favored in the  $M = 1/2$ ,  $J_2/J_1 < 1$  phase, c.f. insets of Fig. 9.5.12. Exactly at the phase boundary between the two phases with finite residual entropy, one can again expect an increase of the entropy as in Fig. 9.2.3 due to the enhanced degeneracy of the bipyramids. These entropy spikes upon increasing the magnetic field are also known to occur e.g. in spin-ice at the transition from the  $M = 1/3$  to the  $M = 1/2$  magnetization plateau [120]. Tab. 9.5.4 gives an overview of the calculated residual entropies on the swedenborgite lattice with and without magnetic field in comparison to other lattices.



**Figure 9.5.13.:** The specific heat for different values  $J_2/J_1$  and  $B$  corresponding to points within the six different phases of the Ising model with magnetic field, c.f. Fig. 9.5.12. The parallel tempering feedback algorithm has been used up to  $T_{\max} = 10 J_1$ .

Lattice	$S_{\text{res}}/\ln 2$	Ref.
Kagome	$\approx 0.72$	86, 87
Triangular	$\approx 0.47$	86
Swedenborgite $J_2/J_1 = 1, B = 0$	$\approx 0.43$	this work
Swedenborgite $J_2/J_1 < 1, B = 0$	$\approx 0.32$	this work
Pyrochlore	$\approx 0.32$	88
Swedenborgite $M = 0$ phase for $B \neq 0$	$\approx 0.24$	this work
Swedenborgite $M = 1/2$ phase for $B \neq 0, J_2 < 1$	$\approx 0.11$	this work

**Table 9.5.4.:** Values for the residual entropy for the Ising model on different lattices in descending order. The different phases for the swedenborgite lattice in finite magnetic field are shown in Fig. 9.5.12.

# 10. Classical Heisenberg model on the swedenborgite lattice

In this chapter, I analyze the experimentally relevant Heisenberg model on the swedenborgite lattice.

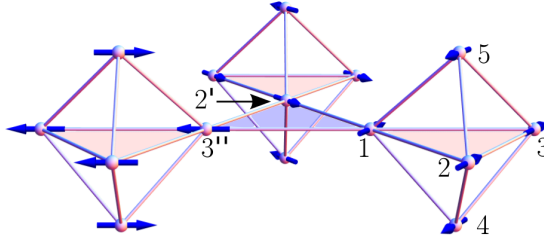
It is first shown in Sec. 10.1 that the continuous nature of the spin variables has a strong influence on the nature of the ground state. Depending on the ratio of the exchange interactions, the ground state is found to be either unique or highly degenerate. In the latter case, it is shown by elaborate Monte Carlo simulations in Sec. 10.2 that the system undergoes an order-by-disorder transition to coplanar ordered ground states at low temperatures. In section 10.3, I present a harmonic spin-wave analysis which reveals that these states feature soft excitations which are absent in generic ground states, explaining their preference according to Sec. 7.3. As on the kagome lattice, c. f. Sec. 7.4, the presence of these excitations also reduces the low temperature value of the specific heat, which is analyzed in detail in Sec. 10.4.

At the end of this chapter, I conclude with some remarks on a possible experimental verification of the order-by-disorder transition with an emphasis on additional interactions which are not accounted for in the model under consideration. Most results presented in this chapter have been published in Ref. 121.

## 10.1. Ground state degeneracy

In this section, I discuss how the geometric frustration on the swedenborgite lattice can result either in a unique ground state with magnetic long-range order, a spin liquid with quasi one-dimensional ordering, or independent copies of decoupled kagome spin liquids, depending on the ratio of the exchange interactions  $J_2/J_1$ .

The constraints on the ground state manifold can be derived by minimizing the energy on the bipyramidal clusters and the interlacing triangles simultaneously. The Hamiltonian Eq. (8.1.2) is therefore decomposed into two parts: One part describing the interactions between the spins on the intermediate triangles and one part accounting for the interactions inside the bipyramids. Using the notation from Fig. 10.1.1, the Hamiltonians for these particular units can be written



**Figure 10.1.1.:** Three bipyramids and an intermediate triangle as the elementary building blocks of the swedenborgite lattice. The spin configuration shown is the ground state for  $J_2/J_1 \geq 3/2$ .

as

$$\begin{aligned}
 H_{\text{triangle}} &= \frac{J_1}{2} (\mathbf{S}_1 + \mathbf{S}_{2'} + \mathbf{S}_{3''})^2 + \text{const.}, \\
 H_{\text{bipyramid}} &= \frac{J_1}{2} \left( \mathbf{S}_1 + \mathbf{S}_2 + \mathbf{S}_3 + \frac{J_2}{J_1} (\mathbf{S}_4 + \mathbf{S}_5) \right)^2 \\
 &\quad + \frac{J_2^2}{2J_1} (\mathbf{S}_4 - \mathbf{S}_5)^2 + \text{const.},
 \end{aligned} \tag{10.1.1}$$

where the second term in the bipyramid Hamiltonian was introduced to remove the artificial interaction between the triangular spins 4 and 5 that is generated by the first term.

It was already shown in Sec. 7.2 that optimal configurations on a triangle have vanishing total spin,

$$\mathbf{S}_1 + \mathbf{S}_{2'} + \mathbf{S}_{3''} = 0, \tag{10.1.2}$$

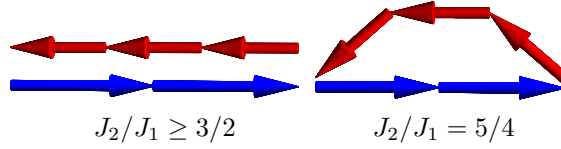
which leads to  $120^\circ$  order as shown in Fig. 7.2.4.

From Eq. (10.1.1), one can also read off the ground state constraints on the bipyramids immediately:

$$\mathbf{S}_4 - \mathbf{S}_5 = 0, \tag{10.1.3}$$

$$\mathbf{S}_1 + \mathbf{S}_2 + \mathbf{S}_3 + \frac{J_2}{J_1} (\mathbf{S}_4 + \mathbf{S}_5) = 0. \tag{10.1.4}$$

The first term wants to align the two triangular spins on each bipyramid parallel. Since the bipyramids are stacked in  $c$ -direction, this results in mutually parallel triangular spins in all bipyramids along that direction. The second term requires the total spin on each bipyramid (with  $\mathbf{S}_4$  and  $\mathbf{S}_5$  rescaled by a factor  $J_2/J_1$ ) to vanish in the ground state. Interestingly, the number of solutions to this equation is the same as for Heisenberg spins on a single triangle<sup>2</sup> in a magnetic



**Figure 10.1.2.:** **Left:** Unique ground state spin configuration for  $J_2/J_1 \geq 3/2$ . **Right:** A possible ground state configuration for  $J_2/J_1 = 5/4$ . Kagome spins are shown in red, triangular spins are shown in blue and rescaled by a factor  $J_2/J_1$  in both figures.

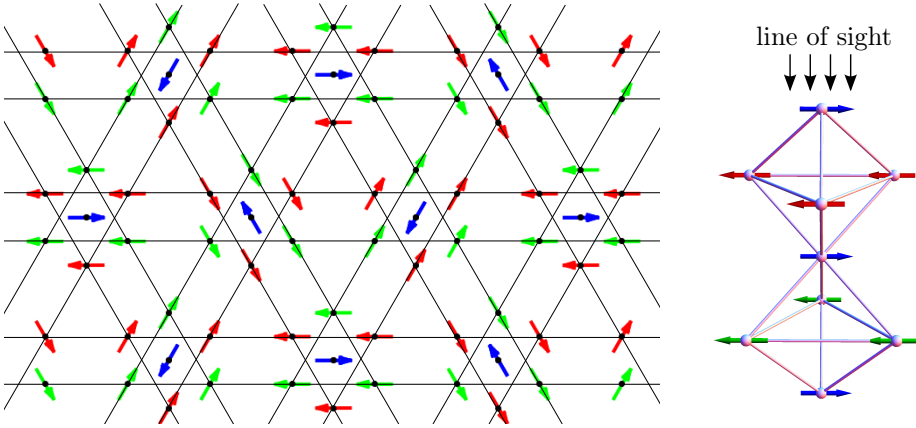
field  $\mathbf{B} = -J_2/J_1(\mathbf{S}_4 + \mathbf{S}_5)$  [122, 123], if one considers the triangular spins as fixed. In the following, the different regimes  $J_2/J_1 \geq 3/2$ ,  $0 < J_2/J_1 < 3/2$  and  $J_2/J_1 = 0$  are discussed separately.

**$\mathbf{J}_2/\mathbf{J}_1 \geq 3/2$**  With the triangular spins being parallel, there exists a unique solution to Eq. (10.1.4) only for  $J_2/J_1 = 3/2$ , which is that the three kagome spins in each bipyramid are aligned mutually parallel and anti-parallel to the two triangular spins as shown in the left hand side of Fig. 10.1.2. To construct the ground state of the full system, one has to stack the bipyramids in  $c$ -direction and ensure  $120^\circ$  order at the intermediate triangles. The complete ground state spin configuration is shown in Fig. 10.1.1 for three bipyramids with an intermediate triangle and in Fig. 10.1.3 as seen along the  $c$ -axis. Obviously, this state is magnetically long-range ordered with the staggered magnetization  $\mathbf{M}(\mathbf{q})$ ,  $\mathbf{q} = (4\pi/3, 0, 0)^T$  as corresponding order parameter.

Even though the ground state condition in Eq. (10.1.4) cannot be satisfied any more for  $J_2/J_1 > 3/2$ , this configuration still remains the ground state in this regime since there is no better configuration than to align all kagome spin completely anti-parallel to the triangular spins if the (antiferromagnetic) out-of-plane interaction  $J_2$  is increased further.

**$0 < \mathbf{J}_2/\mathbf{J}_1 < 3/2$**  In this case, the effective length of the triangular spins is reduced below a critical threshold and there exist many solutions to Eq. (10.1.4). A possible ground state configuration for  $J_2/J_1 = 5/4$  is shown in the right part of Fig. 10.1.2. To quantify the degree of the degeneracy in dependence on  $J_2/J_1$ , one can generate random configurations for the kagome spins inside a bipyramid with parallel triangular spins and check whether Eq. (10.1.4) is fulfilled up to some small  $\delta$ , i. e. if

$$\left\| \mathbf{S}_1 + \mathbf{S}_2 + \mathbf{S}_3 + \frac{J_2}{J_1} (\mathbf{S}_4 + \mathbf{S}_5) \right\| < \delta. \quad (10.1.5)$$



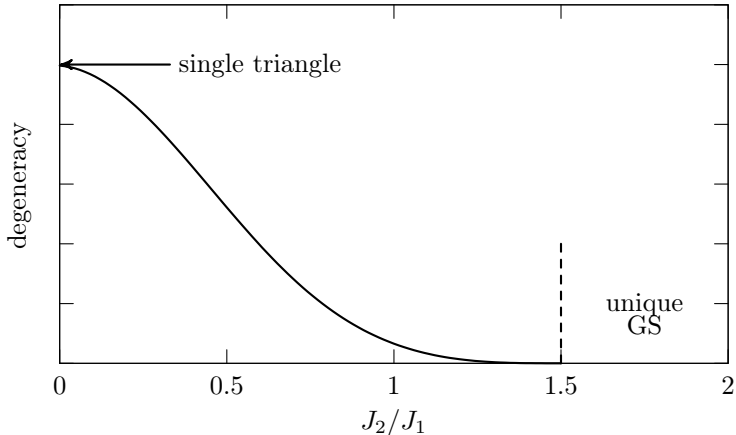
**Figure 10.1.3.:** The unique ground state configuration for  $J_2/J_1 \geq 3/2$  as seen along the  $c$ -axis. Blue spins reside on the triangular lattices, red and green spins reside on the two non-equivalent kagome planes.

Fig. 10.1.4 shows the fraction of  $10^8$  generated spin configurations that fulfill Eq. (10.1.5) for  $\delta = 0.1$ . The data has been normalized to the value at  $J_2 = 0$ , which reflects the degeneracy of a single triangle without triangular spins. Starting from  $J_2/J_1 = 3/2$ , the degeneracy of the bipyramids continuously increases as  $J_2/J_1$  is lowered to zero.

A part of this degeneracy is later removed when the bipyramids are connected by the intermediate triangles. Nevertheless, this still allows for an extensive number of degenerate ground states since each bipyramid is only restricted by a *local* constraint. Knowing the spin configuration in one bipyramid, one cannot predict the configuration in another one, and there is consequently no long-range order.

An interesting consequence of the exchange topology of the swedenborgite lattice is an anisotropic decay of correlations in the regime  $0 < J_2/J_1 < 3/2$ . Counterintuitively, the correlation length in the  $ab$ -plane, i. e. within the kagome and triangular layers, depends on the out-of-plane coupling  $J_2$ : If  $J_2$  is close to  $3/2$ , the bipyramids have only little freedom in choosing a spin configuration compatible with Eq. (10.1.4), i. e. the kagome spins inside the bipyramids will be *almost* completely anti-parallel to the triangular spins. Connecting these bipyramids by intermediate triangles with  $120^\circ$  configurations leads to a ground state which differs *locally* only slightly from the unique ground state for  $J_2/J_1 \geq 3/2$  and features very slow decaying correlations in the  $ab$ -plane. For small  $J_2/J_1$ , on the other hand, the kagome spins inside the bipyramids can arrange in more



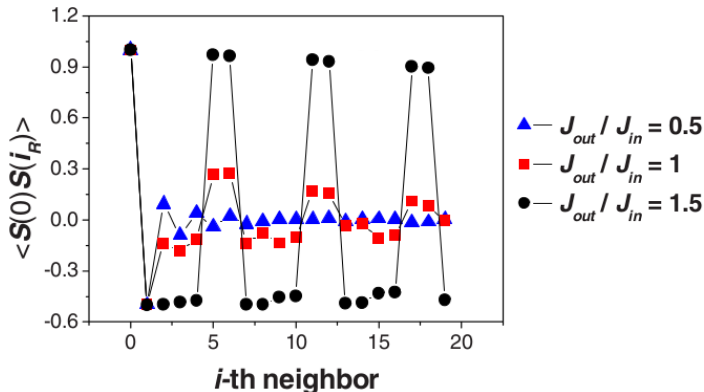


**Figure 10.1.4.:** Degeneracy of a single bipyramid as a function of  $J_2$ . Shown is the fraction of randomly initialized spins on a bipyramid that fulfill Eq. (10.1.5).

ways without violating Eq. (10.1.4), which effectively destroys correlations in the ab-plane after a few lattice sites. Khalyavin *et al.* have calculated the correlations of the kagome spins inside the ab-plane for a system consisting  $21 \times 21 \times 13$  unit cells with open boundary conditions in Ref. 110. Their results, shown in Fig. 10.1.5, confirm this anisotropic decay of correlations.

As in the regime  $J_2/J_1 \geq 3/2$ , the triangular spins within the same column of stacked bipyramids are still aligned parallel and thus long-range ordered along c-direction. The kagome spins of that column are restricted by Eq. (10.1.4) and will thus on average have an ( $J_2/J_1$  dependent) anti-parallel component to the respective triangular spins of the particular column. Consequently, the kagome spins are also long-range ordered along c-direction.

**$\mathbf{J}_2/\mathbf{J}_1 = \mathbf{0}$**  In this limit, the system consists of decoupled kagome layers. According to the discussion in Sec. 7.4, these layers form individual two-dimensional kagome spin-liquids on their own, which undergo independent order-by-disorder transitions to coplanar ground states at  $T/J_1 \approx 10^{-3}$ . Since the layers are decoupled, there exists however no common spin plane for the system as a whole.



**Figure 10.1.5.:** The correlation function of the kagome spins along the direction of the nearest neighbor bonds in the  $ab$ -plane for a system consisting of  $21 \times 21 \times 13$  unit cells with open boundary conditions.  $J_{out}$  and  $J_{in}$  correspond to  $J_2$  and  $J_1$  in the notation used in this thesis. Picture taken from Ref. 110.

## 10.2. Nematic order parameter and order-by-disorder transition

In this section, I introduce the nematic order parameter which can be used to measure whether a spin configuration is coplanar. For these states, the magnetization itself is not an order parameter since the average  $\langle \mathbf{S}_i \rangle$  still vanishes if no specific direction inside the spin plane is preferred [124, 125]. Since the selection of a common spin plane lowers the symmetry of the ground state from  $O(3)$  to  $O(2)$ , it is desirable to have an order parameter which is sensitive to this type of symmetry breaking.

In general, it is not possible to describe *nematic* phases, i. e. phases in which the spins align in certain planes or along certain axes, by a simple vector order parameter and one has to consider higher harmonics, i. e. tensors, instead. A natural extension is the  $3 \times 3$  second rank tensor

$$Q^{\alpha\beta} = \frac{1}{N} \sum_i \left( S_i^\alpha S_i^\beta - \frac{1}{3} \delta^{\alpha\beta} \right), \quad \alpha, \beta = \{x, y, z\}, \quad (10.2.6)$$

which has the following properties [125]:

1. It is a symmetric tensor, i. e.  $Q^{\alpha\beta} = Q^{\beta\alpha}$ .
2. It is traceless, i. e.  $Q^{\alpha\alpha} = 0$ .

3. The first two properties reduce the number of independent components from nine to five.
4. It vanishes in the isotropic phase where no specific plane or axis is preferred. To prove this one can transform into spherical coordinates

$$\begin{aligned}
 S_i^x &= \sin \theta \cos \phi, \\
 S_i^y &= \sin \theta \sin \phi, \\
 S_i^z &= \cos \theta
 \end{aligned}
 \tag{10.2.7}$$

and obtains

$$Q^{\alpha\beta} = \int_0^{2\pi} d\phi \int_0^\pi \sin \theta d\theta P(\theta, \phi) \left( S_i^\alpha S_i^\beta - \frac{1}{3} \delta^{\alpha\beta} \right), \tag{10.2.8}$$

where  $P(\theta, \phi)$  is the probability that a spin is aligned in the direction described by the angles  $\theta$  and  $\phi$ . In the isotropic phase,  $P(\theta, \phi)$  is constant and takes the value  $P_{\text{iso}}(\theta, \phi) = 1/(4\pi)$  as required by the normalization condition  $\int_0^{2\pi} d\phi \int_0^\pi \sin \theta d\theta P(\theta, \phi) = 1$ . It is obvious that all off-diagonal components  $Q^{xy}$ ,  $Q^{xz}$  and  $Q^{yz}$  vanish in the isotropic phase due to the integration over  $\phi$ . For the diagonal components, this is not that easy to see. For  $Q^{zz}$ , one obtains

$$\begin{aligned}
 Q^{zz} &= \int_0^{2\pi} d\phi \int_0^\pi \sin \theta d\theta \frac{1}{4\pi} \left( \cos^2 \theta - \frac{1}{3} \right) \\
 &= \frac{1}{2} \int_{-1}^1 d(\cos \theta) \left( \cos^2 \theta - \frac{1}{3} \right) \\
 &= \frac{1}{6} [\cos^3 \theta - \cos \theta]_{\cos \theta = -1}^{\cos \theta = 1} \\
 &= 0.
 \end{aligned}
 \tag{10.2.9}$$

In a similar fashion it can be shown that  $Q^{xx} = Q^{yy} = 0$ .

5. In a perfect coplanar spin configuration with  $S_i^z = 0$ ,  $Q$  becomes

$$Q = \begin{pmatrix} 1/6 & 0 & 0 \\ 0 & 1/6 & 0 \\ 0 & 0 & -1/3 \end{pmatrix}. \tag{10.2.10}$$

Again, the off-diagonal components vanish due to the integration over  $\phi$ .

Using  $P(\theta, \phi) = \delta(\theta - \pi/2)/2\pi$ , one obtains for  $Q^{zz}$

$$\begin{aligned} Q^{zz} &= \int_0^{2\pi} d\phi \int_0^\pi \sin \theta d\theta \frac{\delta(\theta - \pi/2)}{2\pi} \left( \cos^2 \theta - \frac{1}{3} \right) \\ &= \left[ \cos^2 \theta - \frac{1}{3} \right]_{\theta=\pi/2} \\ &= -\frac{1}{3}. \end{aligned} \tag{10.2.11}$$

The other diagonal components follow from this as  $Q^{xx} = Q^{yy} = -Q^{zz}/2$  due to the symmetry of the spin configuration and the tracelessness of the tensor.

6. If all spins point either parallel or anti-parallel to the z-axis,  $Q$  becomes

$$Q = \begin{pmatrix} -1/3 & 0 & 0 \\ 0 & -1/3 & 0 \\ 0 & 0 & 2/3 \end{pmatrix}. \tag{10.2.12}$$

To prove this, it is again sufficient to calculate only  $Q^{zz}$  using  $P(\theta, \phi) = (\delta(\theta) + \delta(\theta - \pi))\delta(\phi)/2$ ,

$$\begin{aligned} Q^{zz} &= \int_0^{2\pi} d\phi \int_0^\pi \sin \theta d\theta \frac{\delta(\theta) + \delta(\theta - \pi)}{2} \delta(\phi) \left( \cos^2 \theta - \frac{1}{3} \right) \\ &= \frac{1}{2} \left( \left[ \cos^2 \theta - \frac{1}{3} \right]_{\theta=0} + \left[ \cos^2 \theta - \frac{1}{3} \right]_{\theta=\pi} \right) \\ &= \frac{2}{3}. \end{aligned} \tag{10.2.13}$$

To construct a Landau mean-field theory, one has to build scalar quantities out of the tensor order parameter by taking traces. The leading terms in this expansion take the form

$$F = A Q^{\alpha\beta} Q^{\beta\alpha} + B Q^{\alpha\beta} Q^{\beta\gamma} Q^{\gamma\alpha} + C Q^{\alpha\beta} Q^{\beta\alpha} Q^{\gamma\delta} Q^{\delta\gamma} + \mathcal{O}(Q^5), \tag{10.2.14}$$

where  $A, B$  and  $C$  are the parameters of the expansion. The fact that the cubic term is not forbidden by any symmetry implies that any transition with this order parameter is generically first-order [126].

Usually, one does not know the spin-plane or spin-axis in advance, and in an arbitrary basis, the order parameter tensor will in general not be diagonal. It is

thus more convenient to measure the trace of this tensor and its powers which are basis independent. The first non-vanishing trace is

$$\begin{aligned} Q^{\alpha\beta}Q^{\beta\alpha} &= \frac{1}{N^2} \sum_{ij} \left( S_i^\alpha S_i^\beta - \frac{1}{3}\delta_{\alpha\beta} \right) \left( S_j^\alpha S_j^\beta - \frac{1}{3}\delta_{\alpha\beta} \right) \\ &= \frac{1}{N^2} \sum_{ij} \left( (\mathbf{S}_i \cdot \mathbf{S}_j)^2 - \frac{1}{3} \right) \end{aligned} \quad (10.2.15)$$

and can be easily measured in numerical simulations. In a completely coplanar or uni-axial state, this quantity takes the values  $1/6$  and  $2/3$ , respectively, as can be seen by transforming to a basis where  $Q$  is diagonal and Eqs. (10.2.10) and (10.2.12) hold. By taking the trace of this quantity, one has lost all directional information about the nematic, i. e. one cannot specify the spin-plane or spin-axis from  $Q^{\alpha\beta}Q^{\beta\alpha}$  alone anymore.

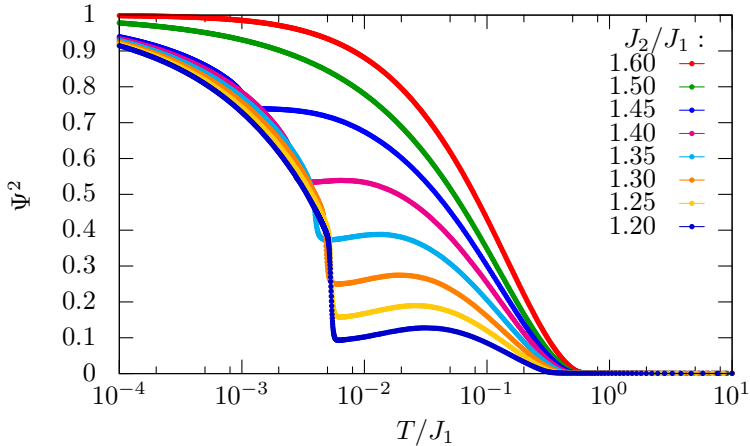
Being mainly interested in coplanar ordered states, the normalized scalar order parameter

$$\Psi^2 = \frac{6}{N^2} \sum_{ij} \left( (\mathbf{S}_i \cdot \mathbf{S}_j)^2 - \frac{1}{3} \right). \quad (10.2.16)$$

is considered from now on. Fig. 10.2.6 shows this order parameter as obtained from Monte Carlo simulations for several values of  $J_2/J_1$  at  $L = 9$ .

For  $J_2/J_1 \geq 3/2$ , the order parameter rises straight to 1 due to the coplanarity of the unique ordered ground state in this regime. As  $J_2/J_1$  is reduced below  $3/2$ , the order parameter rises first to a plateau, whose height depends on the ratio  $J_2/J_1$ , before it eventually rises to 1 at a much lower temperature. The plateau originates from the fact that the ground state constraint on the bipyramids (Eq. (10.1.4)) already imposes some  $J_2/J_1$ -dependent local coplanarity to the ground state which is further enhanced by the periodic boundary conditions. This interpretation is backed up further by the fact that the height of the plateau decreases for smaller ratios  $J_2/J_1$ , where the ground state constraint is not so restrictive anymore and allows for more configurations.

The second rise of the order parameter corresponds to the actual transition to the coplanar ordered phase. For smaller ratios  $J_2/J_1$ , the order parameter seems to jump discontinuously at the transition, indicating that the transition is first-order. From a numerical point of view, it is in general difficult to make statements about the nature of a phase transition just by the analysis of the temperature dependence of the order parameter. An unambiguous statement can, however, be made by recording a frequency histogram of the order parameter exactly at the critical temperature: If the phase transition is second order, there will be only one peak in the histogram since the order parameter rises continuously. If, on the other hand, the transition is first-order, i. e. if there is phase coexistence, one



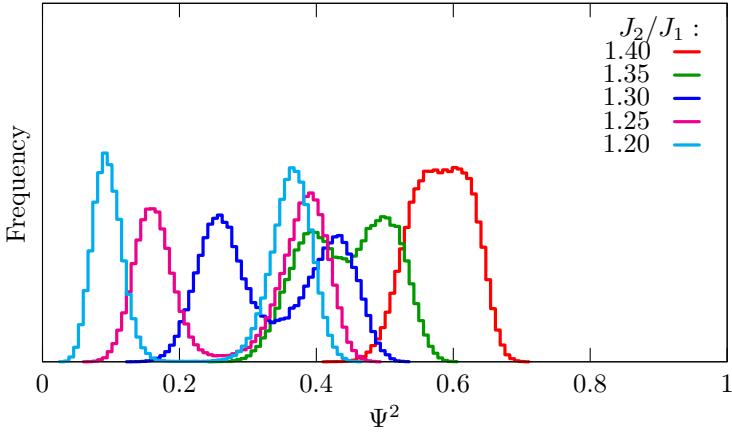
**Figure 10.2.6.:** Temperature dependence of the nematic order parameter for  $L = 9$  obtained by Monte Carlo simulations. For  $J_2/J_1 < 1.20$  the first-order transition could not be equilibrated anymore and the corresponding curves are thus not shown.

should find two separated peaks in the histogram, corresponding to the values in the respective phases. Fig. 10.2.7 shows the order parameter histograms for different values  $J_2/J_1$  at  $L = 9$ . One can clearly observe how the aforementioned double peak structure emerges for  $J_2/J_1 \lesssim 1.40$ , yielding proof that the transition is indeed first-order. For values  $J_2/J_1 \gtrsim 1.40$ , the discontinuity  $\Delta\Psi^2$  is of the same size as the peak width and the two peaks cannot be separated anymore. For  $J_2/J_1 < 1.20$ , it was not possible to equilibrate the first-order transition anymore and the corresponding curves are thus only shown for temperatures above the transition.

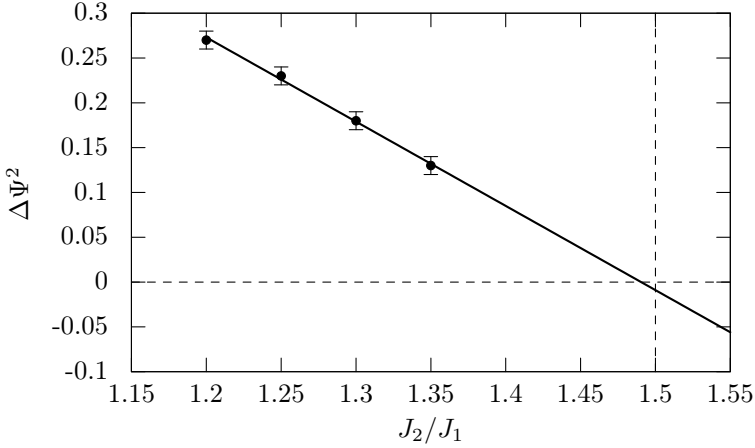
Fig. 10.2.8 shows the dependence of  $\Delta\Psi^2$  on  $J_2/J_1$ . Fitting a linear function to the data points yields

$$\Delta\Psi^2 = (-0.940 \pm 0.035) J_2/J_1 + (1.401 \pm 0.044) \quad (10.2.17)$$

which can be extrapolated to larger values of  $J_2/J_1$  to find that the discontinuity vanishes at  $J_2/J_1 = 1.49 \pm 0.07$ . This is consistent with the assumption that the transition to the coplanar ordered ground states is always first-order for  $J_2/J_1 < 3/2$ , whereas, for  $J_2/J_1 \geq 3/2$ , the (unique) ground state is always coplanar and the order-by-disorder transition ceases to exist.



**Figure 10.2.7.:** Frequency histograms of the nematic order parameter for various ratios  $J_2/J_1$  at  $L = 9$ .



**Figure 10.2.8.:** The discontinuity  $\Delta\Psi^2$  of the order parameter at the phase transition in dependence on  $J_2/J_1$  for  $L = 9$ . For  $J_2/J_1 \gtrsim 1.40$ , the two peaks in the histogram could not be separated due to a large overlap, whereas the phase transition could not be equilibrated anymore for  $J_2/J_1 < 1.20$ . The straight line is a linear fit to the data points. Extrapolating to larger values  $J_2/J_1$ , one finds that the discontinuity vanishes at  $J_2/J_1 = 1.49 \pm 0.07$ .

### 10.3. Spin-wave analysis

It was shown in the previous section that coplanar ground states are selected out of the degenerate ground state manifold in a first-order transition at low temperatures. In this section, I present a harmonic spin-wave analysis following the lines of Chalker [78] that explains *why* this selection takes place and proof that it exists in the whole regime  $0 < J_2/J_1 < 3/2$ . I first discuss fluctuations around a finite number of spins located around a single hexagon in the kagome plane for pedagogical purposes, followed by a full spin-wave analysis around the unique ground state for  $J_2/J_1 \geq 3/2$ . At the the end, the analysis is extended to arbitrary degenerate coplanar ground states for  $J_2/J_1 < 3/2$ .

**Fluctuations around a single hexagon** The unique ground state for  $J_2/J_1 \geq 3/2$  can be described completely using only three different types of spins  $\mathbf{S}_A^{\text{GS}}$ ,  $\mathbf{S}_B^{\text{GS}}$  and  $\mathbf{S}_C^{\text{GS}}$  (and their anti-parallel counterparts), which one can choose to be

$$\begin{aligned}\mathbf{S}_A^{\text{GS}} &= (0, 1, 0)^T, \\ \mathbf{S}_B^{\text{GS}} &= (\sqrt{3}/2, -1/2, 0)^T, \\ \mathbf{S}_C^{\text{GS}} &= (-\sqrt{3}/2, -1/2, 0)^T.\end{aligned}\tag{10.3.18}$$

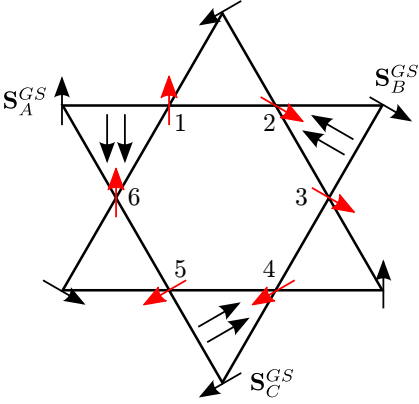
In the anticipation that a possible soft mode will show some similarity with the soft mode known from the kagome lattice, I first consider a finite system consisting of only one hexagon as shown in Fig. 10.3.9 and allow only the spins on the inner hexagon to tilt out of the ground state plane. These six spins can be parametrized as (c. f. Fig. 10.3.9 for the labeling of the spins).

$$\begin{aligned}\mathbf{S}_1 &= \sqrt{1 - \epsilon_1^2} \mathbf{S}_A^{\text{GS}} + \epsilon_1 (0, 0, 1)^T, \\ \mathbf{S}_2 &= \sqrt{1 - \epsilon_2^2} \mathbf{S}_B^{\text{GS}} + \epsilon_2 (0, 0, 1)^T, \\ \mathbf{S}_3 &= \sqrt{1 - \epsilon_3^2} \mathbf{S}_B^{\text{GS}} + \epsilon_3 (0, 0, 1)^T, \\ \mathbf{S}_4 &= \sqrt{1 - \epsilon_4^2} \mathbf{S}_C^{\text{GS}} + \epsilon_4 (0, 0, 1)^T, \\ \mathbf{S}_5 &= \sqrt{1 - \epsilon_5^2} \mathbf{S}_C^{\text{GS}} + \epsilon_5 (0, 0, 1)^T, \\ \mathbf{S}_6 &= \sqrt{1 - \epsilon_6^2} \mathbf{S}_A^{\text{GS}} + \epsilon_6 (0, 0, 1)^T.\end{aligned}\tag{10.3.19}$$

Expanding the Hamiltonian Eq. (8.1.2) up to second order in these deviations yields

$$H = E_{\text{GS}} + \boldsymbol{\epsilon}^T H_2 \boldsymbol{\epsilon} + \mathcal{O}(|\boldsymbol{\epsilon}|^4)\tag{10.3.20}$$





**Figure 10.3.9:** Spin-wave analysis for a single hexagon. The red spins are allowed to tilt out of the ground state plane whereas the black spins are fixed in their respective ground state positions. Note that the ground state is completely built out of the spins  $\pm\mathbf{S}_A^{\text{GS}}$ ,  $\pm\mathbf{S}_B^{\text{GS}}$  and  $\pm\mathbf{S}_C^{\text{GS}}$ , c.f. Eq. (10.3.18).

with  $E_{\text{GS}} = -3J_2^2/J_1 - 9J_1/2$  being the ground state energy,  $\epsilon = (\epsilon_1, \dots, \epsilon_6)^T$  and

$$H_2 = \begin{pmatrix} J_2 - \frac{J_1}{2} & \frac{J_1}{2} & 0 & 0 & 0 & \frac{J_1}{2} \\ \frac{J_1}{2} & J_2 - \frac{J_1}{2} & \frac{J_1}{2} & 0 & 0 & 0 \\ 0 & \frac{J_1}{2} & J_2 - \frac{J_1}{2} & \frac{J_1}{2} & 0 & 0 \\ 0 & 0 & \frac{J_1}{2} & J_2 - \frac{J_1}{2} & \frac{J_1}{2} & 0 \\ 0 & 0 & 0 & \frac{J_1}{2} & J_2 - \frac{J_1}{2} & \frac{J_1}{2} \\ \frac{J_1}{2} & 0 & 0 & 0 & \frac{J_1}{2} & J_2 - \frac{J_1}{2} \end{pmatrix}. \quad (10.3.21)$$

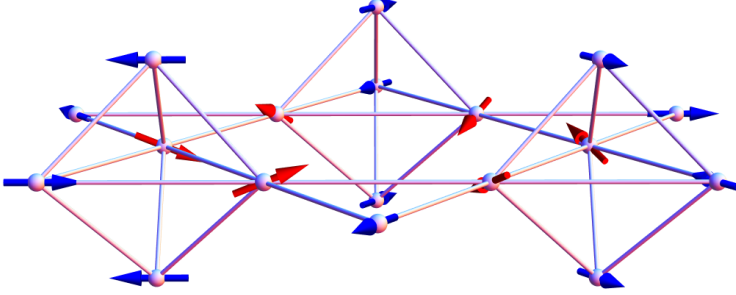
This matrix has an eigenvalue  $\omega = J_2 - 3J_1/2$  that vanishes exactly at  $J_2/J_1 = 3/2$ , i. e. when the ground state is about to become degenerate. For  $J_2/J_1 < 3/2$ , the eigenvalue does not become negative as one might naively think. Instead, the above analysis breaks down since one has to expand the Hamiltonian around a different ground state.

The eigenvector corresponding to the above mentioned eigenvalue is

$$\epsilon = \epsilon(+1, -1, +1, -1, +1, -1)^T, \quad (10.3.22)$$

implying that the soft mode is given by the spins on the hexagon tilting out of the ground state plane in an alternating fashion by the same amount, c.f. Fig. 10.3.10. Apparently, this mode is closely connected to the mode already known from the kagome lattice, c.f. Fig. 7.4.10. Inserting the eigenvector back in the Hamiltonian Eq. (8.1.2), one finds that the excitation energy of this mode at  $J_2/J_1 = 3/2$  is quartic in leading order,

$$E = \frac{15J_1}{8}\epsilon^4 + \mathcal{O}(\epsilon^6). \quad (10.3.23)$$



**Figure 10.3.10.:** Local soft mode in coplanar ground state configurations for  $J_2/J_1 = 3/2$ : blue spins are idle while red spins tilt out of the plane by  $\pm\epsilon$  in an alternating fashion.

**Fluctuations around the unique ground state for  $J_2/J_1 \geq 3/2$**  After this pedagogical introduction, I continue by presenting a *full* harmonic spin-wave analysis around the unique ground state, i. e. *all* spins are now allowed to tilt out of their respective ground state positions. As in Sec. 7.4, fluctuations around the ground state can be parametrized best in a local basis on each lattice site  $i$  with  $\hat{\mathbf{z}}_i$  parallel to  $\mathbf{S}_i$  in the respective ground state position and  $\hat{\mathbf{y}}_i$  orthogonal to the ground state plane with all  $\hat{\mathbf{y}}_i$  mutually parallel. The remaining coordinate  $\hat{\mathbf{x}}_i$  is chosen such that the resulting coordinate system is right handed on every lattice site. Using this coordinate system, every spin can be parametrized by the in-plane and out-of-plane deviations from the ground state,  $\epsilon_i^x$  and  $\epsilon_i^y$ , as

$$\mathbf{S}_i = \left( \epsilon_i^x, \epsilon_i^y, \sqrt{1 - (\epsilon_i^x)^2 - (\epsilon_i^y)^2} \right)^T. \quad (10.3.24)$$

Inserting this into the Hamiltonian Eq. (8.1.2), one obtains

$$\begin{aligned} H = E_{\text{GS}} + \sum_{\langle ij \rangle} & \left( \epsilon_i^x J_{ij} (\hat{\mathbf{x}}_i \cdot \hat{\mathbf{x}}_j) \epsilon_j^x + \epsilon_i^y J_{ij} (\hat{\mathbf{y}}_i \cdot \hat{\mathbf{y}}_j) \epsilon_j^y \right. \\ & \left. + \sqrt{1 - (\epsilon_i^x)^2 - (\epsilon_i^y)^2} J_{ij} (\hat{\mathbf{z}}_i \cdot \hat{\mathbf{z}}_j) \sqrt{1 - (\epsilon_j^x)^2 - (\epsilon_j^y)^2} \right), \end{aligned} \quad (10.3.25)$$

where  $E_{\text{GS}} = (-J_2^2/2J_1 - 3J_1/4)N$  is the ground state energy and  $N$  the number of lattice sites. In the harmonic approximation, all terms beyond quadratic order

are neglected and Eq. (10.3.25) becomes

$$H = E_{\text{GS}} + \sum_{\langle ij \rangle} \left( \epsilon_i^x J_{ij} (\hat{\mathbf{x}}_i \cdot \hat{\mathbf{x}}_j) \epsilon_j^x + \epsilon_i^y J_{ij} (\hat{\mathbf{y}}_i \cdot \hat{\mathbf{y}}_j) \epsilon_j^y - \frac{1}{2} ((\epsilon_i^x)^2 + (\epsilon_i^y)^2 + (\epsilon_j^x)^2 + (\epsilon_j^y)^2) J_{ij} (\hat{\mathbf{z}}_i \cdot \hat{\mathbf{z}}_j) \right), \quad (10.3.26)$$

which can be written in a more compact form after introducing the abbreviation

$$\gamma_i = \frac{1}{2} \sum_j J_{ij} (\hat{\mathbf{z}}_i \cdot \hat{\mathbf{z}}_j) \quad (10.3.27)$$

as

$$\begin{aligned} H &= E_{\text{GS}} + \frac{1}{2} \sum_{ij} \left( \epsilon_i^x J_{ij} (\hat{\mathbf{x}}_i \cdot \hat{\mathbf{x}}_j) \epsilon_j^x + \epsilon_i^y J_{ij} (\hat{\mathbf{y}}_i \cdot \hat{\mathbf{y}}_j) \epsilon_j^y - \delta_{ij} (\epsilon_i^x 2\gamma_i \epsilon_j^x + \epsilon_i^y 2\gamma_i \epsilon_j^y) \right) \\ &= E_{\text{GS}} + \frac{1}{2} \begin{pmatrix} \boldsymbol{\epsilon}^x & \boldsymbol{\epsilon}^y \end{pmatrix} \begin{pmatrix} M^x & 0 \\ 0 & M^y \end{pmatrix} \begin{pmatrix} \boldsymbol{\epsilon}^x \\ \boldsymbol{\epsilon}^y \end{pmatrix}, \end{aligned} \quad (10.3.28)$$

where the sum now extends over all spin pairs  $i$  and  $j$ ,  $\boldsymbol{\epsilon}^{x/y} = (\epsilon_1^{x/y}, \dots, \epsilon_N^{x/y})$  and

$$\begin{aligned} M_{ij}^x &= J_{ij} (\hat{\mathbf{x}}_i \cdot \hat{\mathbf{x}}_j) - 2\gamma_i \delta_{ij}, \\ M_{ij}^y &= J_{ij} (\hat{\mathbf{y}}_i \cdot \hat{\mathbf{y}}_j) - 2\gamma_i \delta_{ij}. \end{aligned} \quad (10.3.29)$$

In the above matrix notation it becomes clear that the in-plane and out-of-plane excitations are not coupled in the harmonic approximation.

The next step is to exploit the translation symmetry of the lattice by performing a Fourier transform of the matrices  $M^x$  and  $M^y$  to momentum space. Before one proceeds, it is however useful to simplify all equations by specifying the relative spin positions in the ground state explicitly. Using Fig. 10.1.3, one finds for two *neighboring* kagome spins  $i$  and  $j$

$$(\hat{\mathbf{x}}_i \cdot \hat{\mathbf{x}}_j) = \begin{cases} 1 & i, j \in \text{same bipyramid} \\ -1/2 & i, j \in \text{same intermediate triangle} \end{cases}, \quad (10.3.30)$$

$$(\hat{\mathbf{y}}_i \cdot \hat{\mathbf{y}}_j) = 1, \quad (10.3.31)$$

$$(\hat{\mathbf{z}}_i \cdot \hat{\mathbf{z}}_j) = \begin{cases} 1 & i, j \in \text{same bipyramid} \\ -1/2 & i, j \in \text{same intermediate triangle} \end{cases} \quad (10.3.32)$$

whereas one finds

$$\begin{aligned} (\hat{\mathbf{x}}_i \cdot \hat{\mathbf{x}}_j) &= -1 \\ (\hat{\mathbf{y}}_i \cdot \hat{\mathbf{y}}_j) &= +1 \\ (\hat{\mathbf{z}}_i \cdot \hat{\mathbf{z}}_j) &= -1 \end{aligned} \quad (10.3.33)$$

if one of the two spins is located on the triangular lattice. All matrix products between non-neighboring spins vanish. With these definitions,  $\gamma_i$  becomes

$$\gamma_i = \begin{cases} J_1/2 - J_2 & i \in \text{kagome lattice} \\ -3J_2 & i \in \text{triangular lattice} \end{cases} . \quad (10.3.34)$$

Transforming to momentum space by

$$\epsilon_i^{x/y} = \frac{1}{\sqrt{N/8}} \sum_{\mathbf{k}} \epsilon_{\mathbf{k}}^{x/y} e^{i\mathbf{k}\cdot\mathbf{r}_i} \quad (10.3.35)$$

yields two  $8 \times 8$  matrices  $M_{\mathbf{k}}^x$  and  $M_{\mathbf{k}}^y$ , whose matrix elements are given in appendix A. By construction, the eigenvalues of  $M_{\mathbf{k}}^x$  correspond the energies associated with in-plane deviations of the spins out of their ground state position, whereas the eigenvalues of  $M_{\mathbf{k}}^y$  correspond the excitation energies for out-of-plane excitations. These energies are shown in Fig. 10.3.11 along a path connecting high symmetry points in the Brillouin zone separately for in-plane and out-of-plane excitations and for various values of  $J_2/J_1$ . The fact that there are no excitations with negative energy yields a cross-check for correctness of the spin-wave calculation.

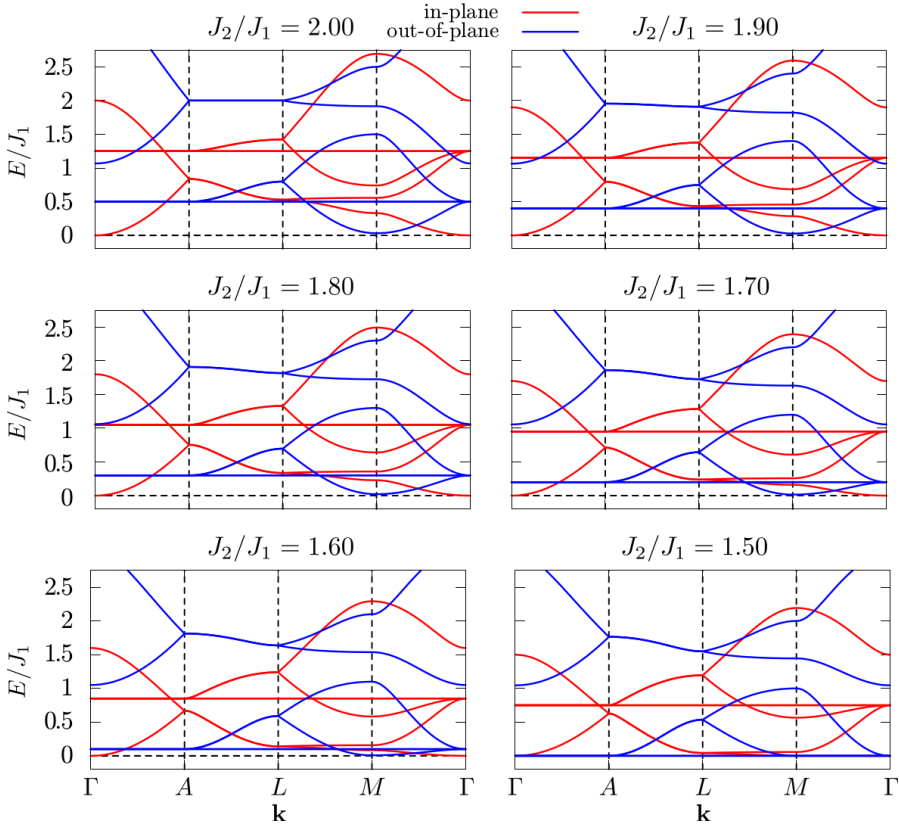
One finds that there is a doubly degenerate completely flat band corresponding to out-of-plane excitations that is continuously shifted to lower energies as  $J_2/J_1$  is reduced and becomes gapless exactly at  $J_2/J_1 = 3/2$ . One thus recovers the previous result from the simple spin-wave analysis for a single hexagon of spins where it was also found that the mode shown in Fig. 10.3.10 becomes soft at this point. For the in-plane excitations, there is no such flat band, indicating that these excitations never go soft.

Based on the above spin-wave analysis, one can also calculate the expected reduction of the specific in the limit  $T \rightarrow 0$  for  $J_2/J_1 = 3/2$ . Since there are in total eight quadratic in-plane and six quadratic and two quartic out-of-plane modes, one would expect the specific heat in the low-temperature limit to be

$$c_V = \underbrace{\left(\frac{8}{8} \times \frac{1}{2}\right)}_{\text{in-plane}} + \underbrace{\left(\frac{6}{8} \times \frac{1}{2} + \frac{2}{8} \times \frac{1}{4}\right)}_{\text{out-of-plane}} = \frac{15}{16} \quad (10.3.36)$$

according to the discussion in Sec. 7.4. It will be shown in Sec. 10.4 that this value agrees excellently with the numerical results from the classical Monte Carlo simulation.

**Fluctuations around an arbitrary coplanar state** It is also possible to describe the out-of-plane fluctuations around an *arbitrary* coplanar ground state



**Figure 10.3.11.:** The harmonic excitation spectrum around the unique ground state for  $J_2/J_1 \geq 3/2$ . Red and blue lines correspond to in-plane and out-of-plane excitations, respectively. There is a doubly degenerate dispersionless band belonging to out-of-plane excitations that becomes soft exactly at  $J_2/J_1 = 3/2$ .

for  $J_2/J_1 < 3/2$  in the same way as before, even though the ground state is not unique anymore. This is rooted in the fact that, in the local basis with mutually parallel  $\hat{\mathbf{y}}_i$ , the product  $(\hat{\mathbf{y}}_i \cdot \hat{\mathbf{y}}_j)$  that enters the matrix  $M_{\mathbf{k}}^y$  always equals 1 for neighboring spins. Additionally, the  $\gamma_i$ 's that enter  $M_{\mathbf{k}}^y$  also do not depend on the particular ground state: For an arbitrary spin  $\mathbf{S}_T$  on the triangular lattice, one finds (c. f. Fig. 10.3.12 for the numbering of the spins)

$$\begin{aligned}\gamma_T &= \frac{1}{2} \sum_j J_{ij} \mathbf{S}_T \cdot \mathbf{S}_j \\ &= \frac{1}{2} J_2 \mathbf{S}_T \cdot (\mathbf{S}_K^1 + \mathbf{S}_K^2 + \mathbf{S}_K^3 + \mathbf{S}_K^4 + \mathbf{S}_K^5 + \mathbf{S}_K^6)\end{aligned}\quad (10.3.37)$$

Using the ground state constraints Eq. (10.1.3) and (10.1.4), which in this notation read

$$\begin{aligned}\mathbf{S}_K^1 + \mathbf{S}_K^2 + \mathbf{S}_K^3 &= -2 \frac{J_2}{J_1} \mathbf{S}_T, \\ \mathbf{S}_K^4 + \mathbf{S}_K^5 + \mathbf{S}_K^6 &= -2 \frac{J_2}{J_1} \mathbf{S}_T,\end{aligned}\quad (10.3.38)$$

one can reduce  $\gamma_T$  to the universal value

$$\gamma_T = -2 \frac{J_2^2}{J_1}, \quad (10.3.39)$$

which is independent of the particular spin configuration in the ground state. The same is also possible for  $\gamma_K$ , which is in the notation of Fig. 10.3.13 given by

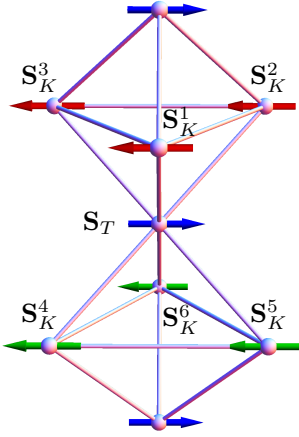
$$\begin{aligned}\gamma_K &= \frac{1}{2} \sum_j J_{ij} \mathbf{S}_K \cdot \mathbf{S}_j \\ &= \frac{1}{2} \left( J_1 \mathbf{S}_K \cdot (\mathbf{S}_K^1 + \mathbf{S}_K^2 + \mathbf{S}_K^3 + \mathbf{S}_K^4) \right. \\ &\quad \left. + J_2 \mathbf{S}_K \cdot (\mathbf{S}_T^1 + \mathbf{S}_T^2) \right).\end{aligned}\quad (10.3.40)$$

The  $120^\circ$  angles on the intermediate triangles imply  $\mathbf{S}_K \cdot \mathbf{S}_K^3 = \mathbf{S}_K \cdot \mathbf{S}_K^4 = -1/2$  and one is left with

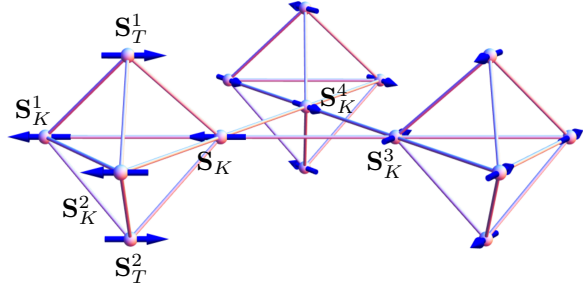
$$\gamma_K = -\frac{J_1}{2} + \frac{J_1}{2} \mathbf{S}_K \cdot \left( \mathbf{S}_K^1 + \mathbf{S}_K^2 + \frac{J_2}{J_1} (\mathbf{S}_T^1 + \mathbf{S}_T^2) \right). \quad (10.3.41)$$

Using once again the ground state constraint Eq. (10.1.4), in this notation given by

$$\mathbf{S}_K^1 + \mathbf{S}_K^2 + \frac{J_2}{J_1} (\mathbf{S}_T^1 + \mathbf{S}_T^2) = -\mathbf{S}_K, \quad (10.3.42)$$



**Figure 10.3.12.:** Spin numbering used for the determination of  $\gamma_T$ .



**Figure 10.3.13.:** Spin numbering used for the determination of  $\gamma_K$ .

one finally obtains

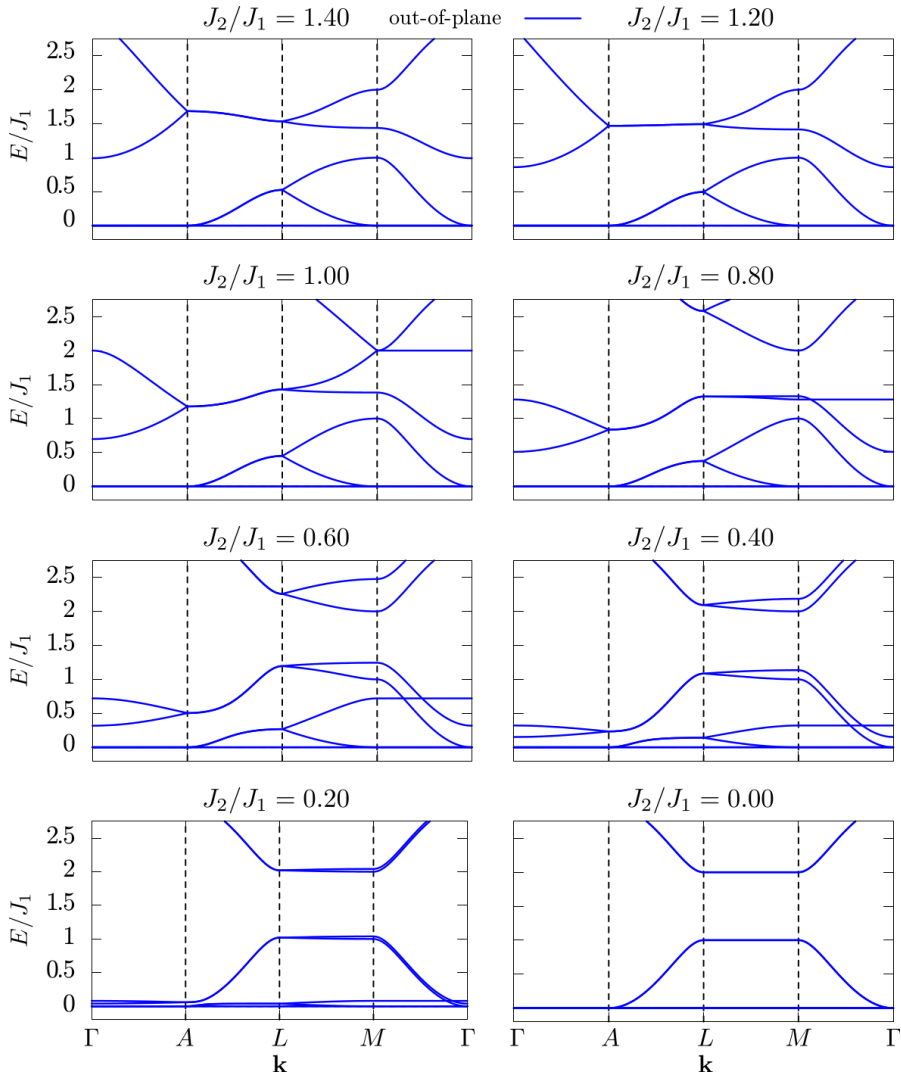
$$\gamma_K = -J_1. \quad (10.3.43)$$

Unfortunately, the in-plane fluctuation matrix  $M_{\mathbf{k}}^x$  depends on the products  $(\hat{\mathbf{x}}_i \cdot \hat{\mathbf{x}}_j)$ , which are in contrast to  $(\hat{\mathbf{y}}_i \cdot \hat{\mathbf{y}}_j)$  different for each ground state. It is therefore not possible to give a general result for the in-plane excitation spectrum and I will hence focus only on the out-of-plane excitations.

Fig. 10.3.14 shows the out-of-plane excitation spectrum around an arbitrary coplanar ground state for various values  $J_2/J_1$ .

The doubly degenerate flat band that appeared at  $J_2/J_1 = 3/2$  is still present for *all* values  $J_2/J_1$  down to 0, implying that coplanar ground states *always* feature soft excitations in this regime. Based on this powerful result, one can conclude that the corresponding order-by-disorder transition must exist for all  $J_2/J_1 \leq 3/2$  as well, which allows further insight into the regime  $J_2/J_1 \lesssim 1.2$ , where the transition is strongly first-order and cannot be equilibrated anymore in Monte Carlo simulations, c. f. Sec. 10.2.

As  $J_2/J_1$  is lowered towards 0, the excitation spectrum collapses continuously into a two-fold degenerate spectrum. This spectrum simply represents the two independent kagome planes, each having a soft excitation according to Sec. 7.4, and two additional flat bands corresponding to the non-interacting triangular spins per unit cell.



**Figure 10.3.14.:** The harmonic excitation spectrum for out-of-plane excitations around an arbitrary coplanar ground state for  $J_2/J_1 < 3/2$ . There is always a doubly degenerate flat band at  $E = 0$ , indicating that all coplanar ground states have two soft modes.



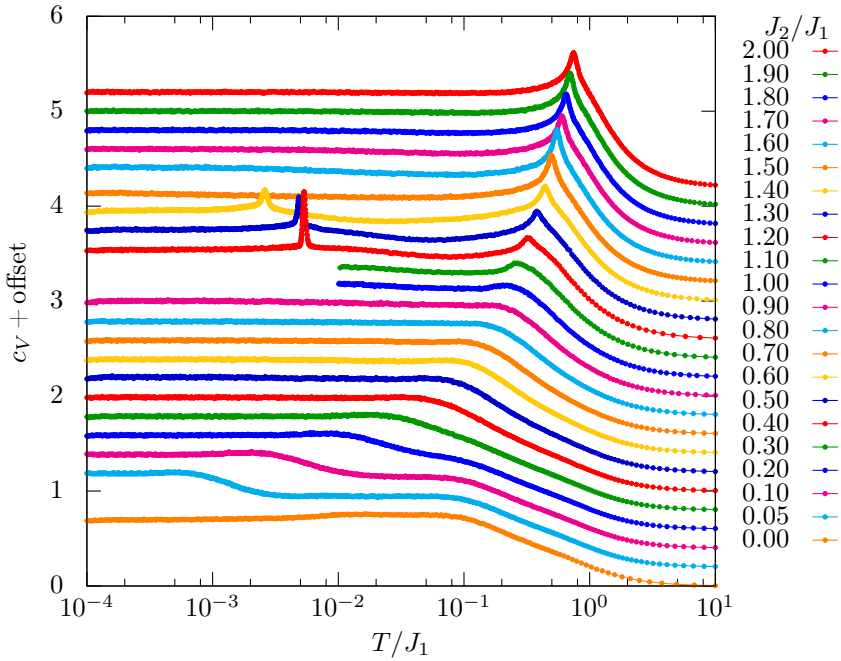
## 10.4. Specific heat

Another interesting quantity besides the order parameter is the specific heat since it allows the identification of phase transitions and crossovers without knowing the corresponding order parameter. In addition to that, its low-temperature behavior yields information about the presence of soft modes and provides thus an unbiased way to find order-by-disorder transitions. Fig. 10.4.15 shows the specific heat for various ratios  $J_2/J_1$  over five orders of magnitude in temperature. The different observed features are explained separately in the following.

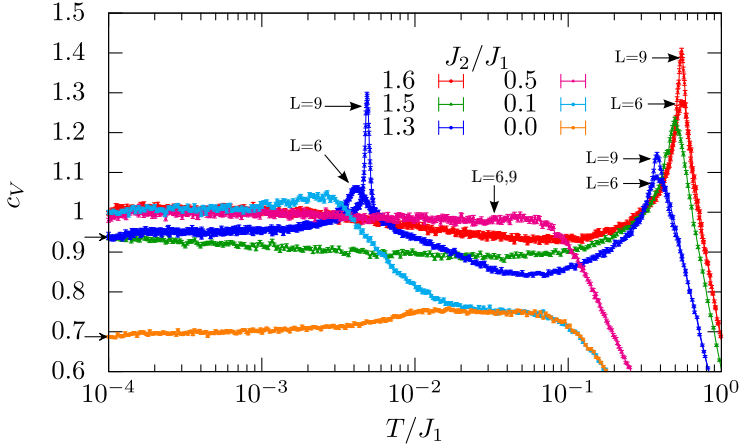
**Phase transition/crossover at high temperatures** Starting at the largest simulated value  $J_2/J_1 = 2$ , one finds a peak in the specific heat at  $T/J_1 = 10^{-1} \dots 10^0$  whose height continuously decreases as  $J_2/J_1$  is decreased. At  $J_2/J_1 \approx 1$ , this peak has vanished completely and for ratios lower than  $J_2/J_1 \approx 1$ , the specific heat rises straight to one without showing any features.

Following the discussion of the ground state degeneracy in Sec. 10.1, the ground state is unique and long-range ordered for  $J_2/J_1 \geq 3/2$ , whereas it is degenerate for  $J_2/J_1 < 3/2$ . The observed peak in specific heat for  $J_2/J_1 \geq 3/2$  thus indicates a true thermodynamic singularity corresponding to a second order phase transition. For  $J_2/J_1 < 3/2$ , on the other hand, the system only enters a spin-liquid regime where it is governed by local constraints and there is consequently no long-range order. The observed hump in the specific heat for values  $J_2/J_1 \lesssim 3/2$  thus corresponds to a *crossover* instead of a phase transition.

Although this statement is obvious from the discussion of the ground state degeneracy in Sec. 10.1, it is difficult to prove numerically. In principle, one would measure the specific heat for different system sizes and analyze the scaling behavior of the peak: if the peak originates from a true phase transition with a diverging correlation length, it would become narrower and sharper with increasing system size, c. f. Sec. 1.4. On the other hand, if the peak originates from a crossover, in which the correlation length only grows to a *finite* value, one would observe that the peak does not scale any more once the linear system size exceeds this correlation length. Following the discussion in Sec. 10.1, the correlation length is still very large if  $J_2/J_1$  is close to  $3/2$  and it is thus impossible to simulate system sizes large enough to see this effect. For smaller values  $J_2/J_1$ , however, one indeed observes that the specific heat is independent of the system size already between a linear system size of  $L = 6$  and  $L = 9$ , see e. g. the curve for  $J_2/J_1 = 0.5$  in Fig. 10.4.16. Since the whole regime  $J_2/J_1 < 3/2$  is conceptual equivalent, c. f. Sec. 10.1, one can expect that this effect could in principle also be observed for  $J_2/J_1$  close to  $3/2$ , provided that one could simulate larger systems.



**Figure 10.4.15.:** The specific heat for different values  $J_2/J_1$  at  $L = 9$ . Different curves have been shifted by an offset of 0.2 for visibility. The two curves for  $J_2/J_1 = 1.1$  and 1.0 end at  $T/J_1 = 0.01$  because the first-order transition could not be equilibrated any more for these values. For  $J_2/J_1 \leq 0.9$ , the first-order transition is pushed to very low temperatures  $T/J_1 < 10^{-4}$  and equilibration could be achieved in the whole temperature range  $T/J_1 \geq 10^{-4}$ .



**Figure 10.4.16.:** The specific heat  $c_V$  for selected ratios  $J_2/J_1$  and  $L = 6$  (as well as  $L = 9$  for  $J_2/J_1 = 0.5, 1.3, 1.6$ ). In the limit  $T \rightarrow 0$ , the curve for  $J_2 = 1.6$  approaches 1 while the ones for  $J_2/J_1 = 1.5$  and  $1.3$  approach  $15/16$ . For  $J_2/J_1 = 0.1$  and  $0.5$ , the specific heat seemingly approaches 1, but the first-order transition is pushed to very low temperatures. The arrows on the  $c_V$ -axis mark the values  $15/16$  and  $11/16$ , see main text.

**Order-by-disorder transition and low-temperature behavior** For  $J_2/J_1 < 3/2$ , the specific heat shows an additional peak at the temperature of the order-by-disorder transition, c. f. Sec. 10.2. Already for  $L = 9$ , this peak is very sharp pronounced and has a shape close to a delta distribution, the expected shape for a first-order transition in the thermodynamic limit, c. f. Fig. 10.4.16. For ratios  $J_2/J_1 < 1.20$ , it was not possible to equilibrate this transition anymore and the corresponding curves are hence only shown for  $T/J_1 \geq 0.01$  in Fig. 10.4.15. For  $J_2/J_1 \lesssim 0.9$  the transition temperature is pushed below  $T/J_1 = 10^{-4}$ , the smallest temperature analyzed in the simulations. It should again be emphasized that the existence of the order-by-disorder transition is guaranteed for *all*  $J_2/J_1 < 3/2$  by the spin-wave analysis, c. f. Sec. 10.3.

Based on this analysis and a mode counting argument, it was also predicted in Sec. 10.3 that the specific heat should approach the value  $15/16$  in the limit  $T \rightarrow 0$ . This value, marked by the upper black arrow on the  $c_V$ -axis in Fig. 10.4.16, agrees remarkably well with the numerical data and lends further support to the previous analyses. For values  $J_2/J_1 > 3/2$ , the specific heat clearly approaches

the value 1 as  $T \rightarrow 0$ , proving the absence of soft modes in this regime. Exactly at  $J_2/J_1 = 3/2$ , the specific heat approaches the predicted value of  $15/16$  without showing any further features after the high-temperature peak. The absence of an additional peak at low temperatures is rooted in the fact that there is no order-by-disorder transition since the unique ground state for  $J_2/J_1 = 3/2$  is already coplanar.

**Behavior for small  $J_2/J_1$**  The curve for  $J_2/J_1 = 0$  essentially reproduces the known result from the 2d kagome lattice with the specific heat being rescaled by a factor of  $6/8$  to account for the two effectively non-interacting kagome spins. This modifies the low-temperature value of the specific heat from  $11/12$  to  $11/16$ .

If the out-of plane coupling is finite but sufficiently small, i.e.  $J_2/J_1 \lesssim 0.3$ , one finds that at high temperatures, the system first behaves as if the kagome plane were completely decoupled in the sense that the corresponding specific heat curves do not deviate from each other (compare curves for  $J_2/J_1 = 0.1$  and  $0.0$  in Fig. 10.4.16). The first plateau in the specific heat signals that the different kagome planes enter their respective ground state manifold and form independent 2d spin-liquids. In this regime, the six kagome spins per unit cell have purely quadratic excitations in the two directions perpendicular to the respective ground state orientation, whereas the two triangular spins are effectively non-interacting. Following Sec. 7.4, the low-temperature value of the specific heat per spin in this regime should therefore be

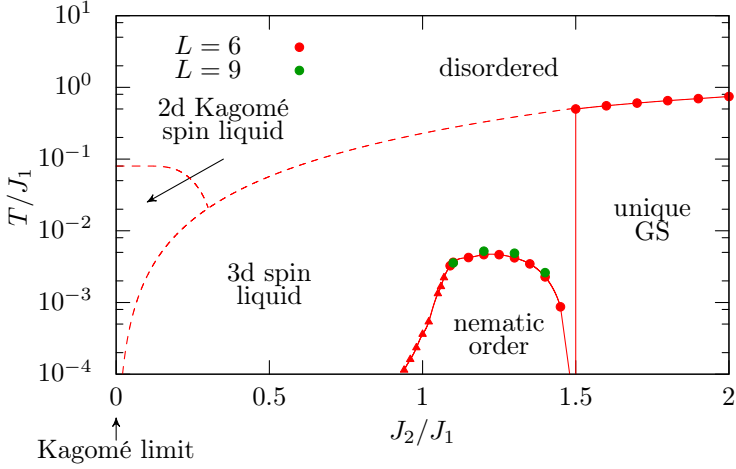
$$c_V = 2 \times \left( \frac{6}{8} \times \frac{1}{2} + \frac{2}{8} \times 0 \right) = \frac{3}{4}, \quad (10.4.44)$$

which agrees again well with the numerical data.

Upon lowering the temperature further, the out-of-plane coupling becomes relevant and the system crosses over into the 3d spin-liquid regime governed by the local constraint on the bipyramids. The triangular spins now also feel a quadratic potential and the specific heat consequently approaches 1 as  $T \rightarrow 0$ . As predicted by the spin-wave analysis, the system will also undergo a first-order transition to a coplanar ground state at some small temperature (that was not reached in the Monte Carlo simulations), which eventually reduces the specific heat to  $15/16$  again.

## 10.5. Phase diagram

Fig. 10.5.17 shows the finite temperature phase diagram in dependence on the ratio  $J_2/J_1$ . In the following, I discuss how the different phase boundaries and crossover lines have been determined.



**Figure 10.5.17.:** Phase diagram: For  $J_2/J_1 \geq 3/2$ , there is a unique ground state which is selected after a second-order transition. For  $J_2/J_1 < 3/2$ , the dashed line continues the second-order transition but is a crossover line instead (set by the scale  $J_2^2/J_1$ ), separating a standard paramagnet from a 3d classical spin liquid. At low  $T$ , there is a first-order transition to a nematically ordered phase. The dots emerge from an analysis of the specific heat, whereas the triangles are determined from the diffusivity of the replicas, see the main text for more explanations. The nematic phase extends all the way to  $J_2 = 0$  but is not shown due to the logarithmic temperature scale.

The phase boundary that separates the unique ground state from the paramagnetic phase was obtained from the corresponding peak in the specific heat. Alternatively, one could have also analyzed the peak in the susceptibility

$$\chi = \frac{\langle M^2 \rangle - \langle M \rangle^2}{T}, \quad (10.5.45)$$

of the corresponding order parameter, given by the staggered magnetization at  $\mathbf{Q} = (4\pi/3, 0, 0)^T$ , which would have led to the same result.

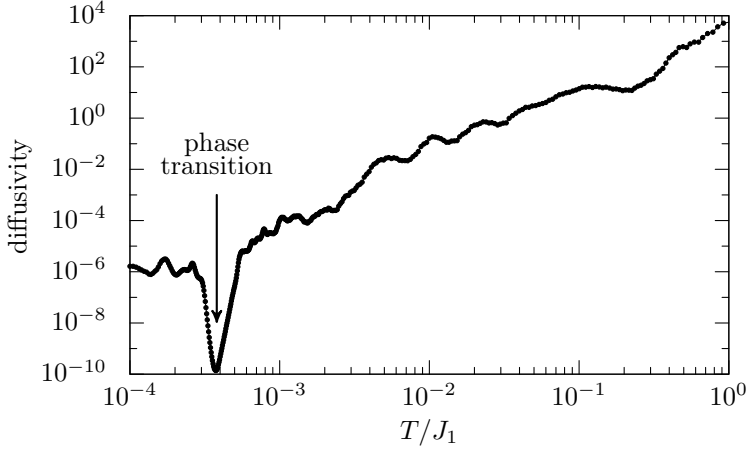
For  $J_2/J_1 < 3/2$ , the crossover temperature was determined from the hump in the specific heat down to  $J_2/J_1 \approx 1$ , where the hump vanishes. For smaller ratios  $J_2/J_1$ , the point at which the specific heat approaches 1 was used instead.

For very small  $J_2/J_1 \lesssim 0.3$ , it was shown in Sec. 10.4 that the specific heat first rises to a plateau at  $c_V = 3/4$ , indicating that the individual Kagome layers have entered their respective ground state manifold. The triangular spins, on the other hand, remain disordered until a much lower temperature, where the specific heat finally rises to 1. The intermediate regime with the plateau at  $c_V = 3/4$  can

thus be interpreted as 2d kagome spin-liquid. The corresponding crossover lines have again been determined from the temperatures at which the specific heat approaches  $3/4$  and  $1$ , respectively.

Interestingly, the temperature that separates the paramagnetic regime from the unique ground state for  $J_2/J_1 \geq 3/2$  and the spin liquid regime for  $J_2/J_1 < 3/2$ , scales proportional to  $J_2^2/J_1$ , which is the effective ferromagnetic coupling between the triangular spins along  $c$ -direction, c. f. Eq. (10.1.1).

The determination of the first-order phase boundary separating the nematic phase from the spin liquid is not that easy since the corresponding phase transition could only be equilibrated for  $J_2/J_1 \geq 1.20$ . Nevertheless, it is possible to initialize all replicas of the parallel tempering simulation in a coplanar ground state and to monitor the diffusivity of these replicas through temperature space. Since the phase transition is according to the discussion in Sec. 2.3 a bottleneck for the diffusion of the replicas, one finds that the diffusivity is strongly suppressed at the transition temperature. Fig. 10.5.18 shows the diffusivity according to Eq. (2.3.9) for  $J_2/J_1 = 1$  at  $L = 6$ . At the critical temperature, the diffusivity drops by about four orders of magnitude, which allows to determine the transition temperature with sufficient accuracy to continue the phase separation line in Fig. 10.5.17 for  $J_2/J_1 < 1.20$ . It should again be emphasized that the corresponding phase transition exists all the way down to  $J_2/J_1 \rightarrow 0$ , even though the line is only shown down to  $T/J_1 = 10^{-4}$  on the logarithmic temperature scale in the phase diagram.



**Figure 10.5.18.:** The diffusivity according to Eq. (2.3.9) for  $J_2/J_1 = 1$  at  $L = 6$ . The sharp drop in the diffusivity of about four orders of magnitude at  $T_c \approx 3.610^{-4} J_1$  indicates a phase transition.

## 10.6. Structure factors and correlations

As already discussed for the Ising model in Sec. 9.4, correlations are best analyzed in momentum space. The magnetic structure factor

$$S(\mathbf{q}) = \frac{1}{N} \sum_{ij} \langle \mathbf{S}_i \cdot \mathbf{S}_j \rangle e^{i\mathbf{q}(\mathbf{r}_i - \mathbf{r}_j)} \quad (10.6.46)$$

at  $T/J_1 = 0.01$  is shown for various ratios  $J_2/J_1$  in the  $(q_x, q_y, q_z = 0)$  and  $(q_{xy}, q_{xy}, q_z)$  planes in Fig. 10.6.19 and Fig. 10.6.20, respectively.

For  $J_2/J_1 = 0.1$ , the system is in the 2d spin-liquid phase at  $T/J_1 = 0.01$  (c. f. phase diagram in Fig. 10.5.17), i. e. the triangular spins are not yet ordered along  $c$ -direction, resulting in vanishing correlations along this direction, whereas the structure factor in the  $q_x - q_y$  plane basically resembles the result for the kagome lattice, c. f. Fig. 7.4.13. As  $J_2/J_1$  is increased above  $\sim 0.2$ , the triangular spins order along  $c$ -direction, leading to sharp Bragg spots along  $q_z$  direction.

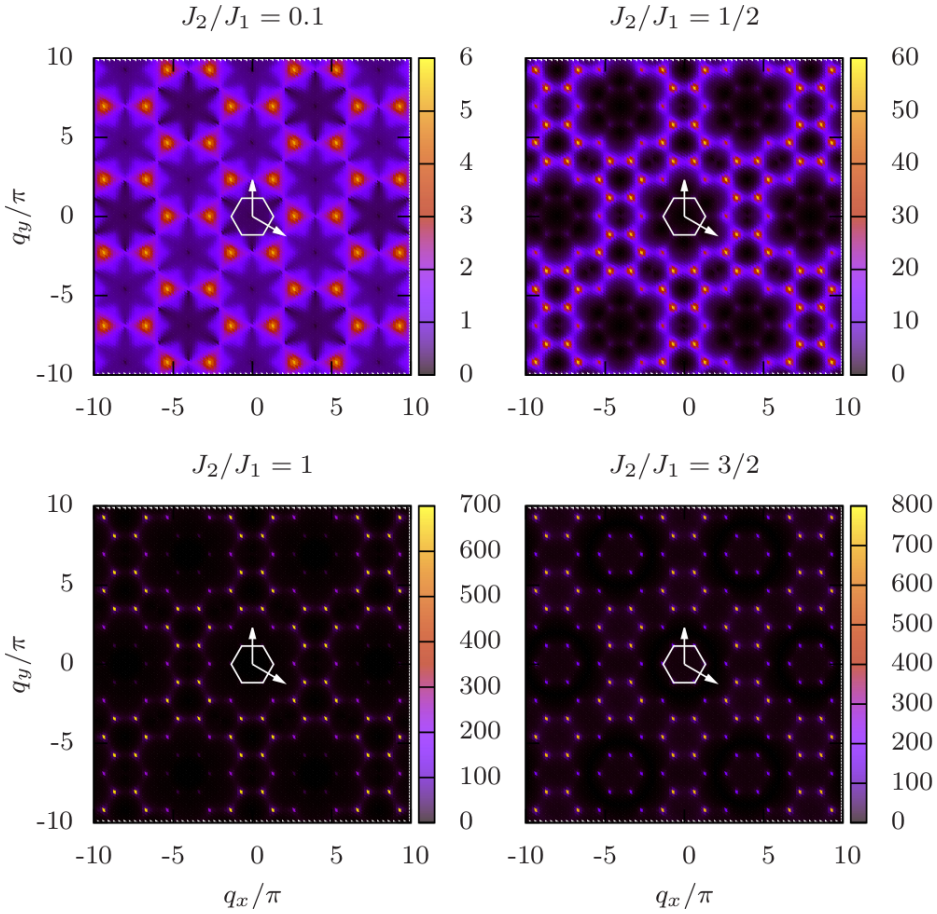
According to the discussion in Sec. 10.1, an increase of the out-of-plane interaction leads also to stronger correlations in the  $ab$ -plane. This is in agreement with the observation that the Bragg peaks in the  $q_x - q_y$  plane become sharper as  $J_2/J_1$  is increased.

For  $J_2/J_1 \geq 3/2$ , the Bragg peaks are not broadened anymore due to the long-range ordered unique ground state. Interestingly, it is very difficult to distinguish

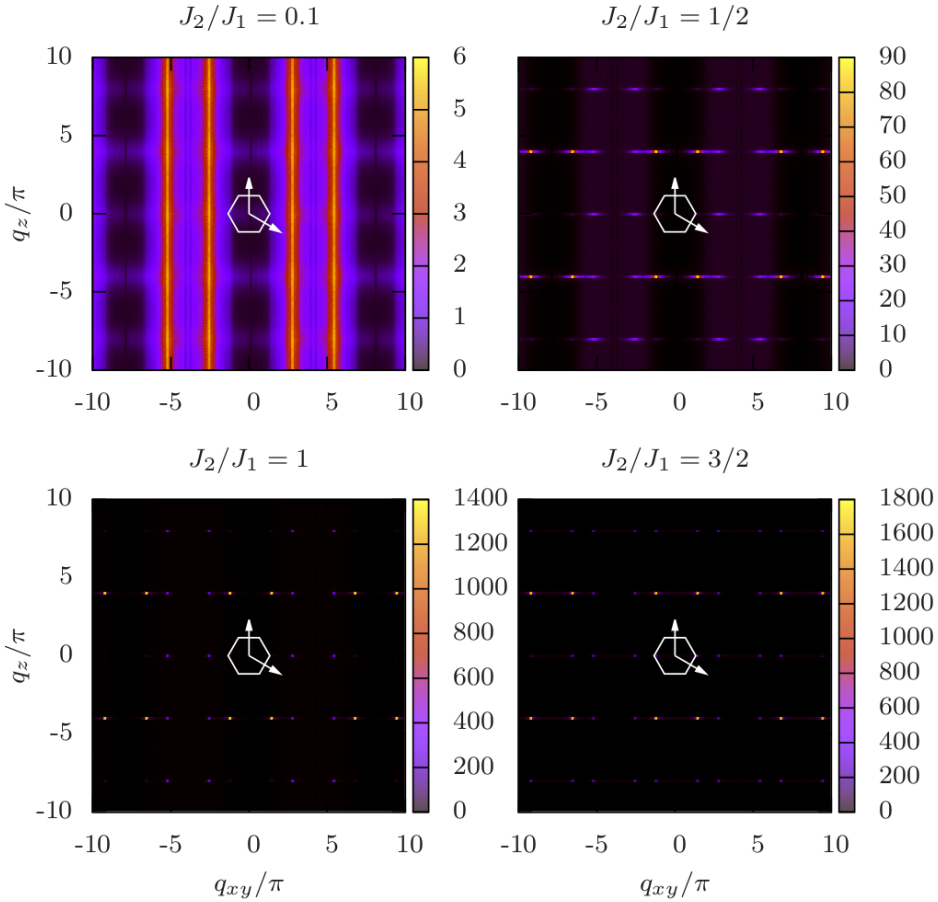
the structure factor for  $1 \lesssim J_2/J_1 \lesssim 3/2$  from  $J_2/J_1 \geq 3/2$ . Since the correlation length in the first regime is already very large compared to the simulated linear lattice size of  $L = 12$ , the structure factor gives the impression that the ground state is already long-range ordered, which contradicts the discussion of the ground state degeneracy in Sec. 10.1. If one could simulate larger lattice sizes, one would observe a small broadening of the Bragg peaks in this regime as well.

For the 2d kagome antiferromagnet, it was shown in Sec. 7.4 that one can observe additional features in the structure factor once coplanar ground states have been selected. It is an interesting question whether such additional features can also be observed in the coplanar ordered phases on the swedenborgite lattice. Fig. 10.6.21 shows the structure factor for  $J_2/J_1 = 1.3$  at  $T/J_1 = 10^{-2}$  and  $T/J_1 = 10^{-4}$ , i. e. before and after the order-by-disorder transition, c. f. Fig. 10.5.17), on a logarithmic intensity scale. One can clearly observe that additional very weak correlations at the reciprocal wave vectors  $\mathbf{k}_1 = 2\pi(1, -1/\sqrt{3}, 0)^T$ ,  $\mathbf{k}_2 = 2\pi(0, 2/\sqrt{3}, 0)^T$  and wave vectors related by symmetry occur below the transition temperature. Since the structure factor is in contrast to the nematic order parameter an experimentally accessible quantity, the presence or absence of these features in neutron scattering experiments can be used as a guidance to decide whether a coplanar ground state is realized in a certain compound. Together with the information about the specific heat, this provides an important assistance for the experimental verification of an order-by-disorder transition.

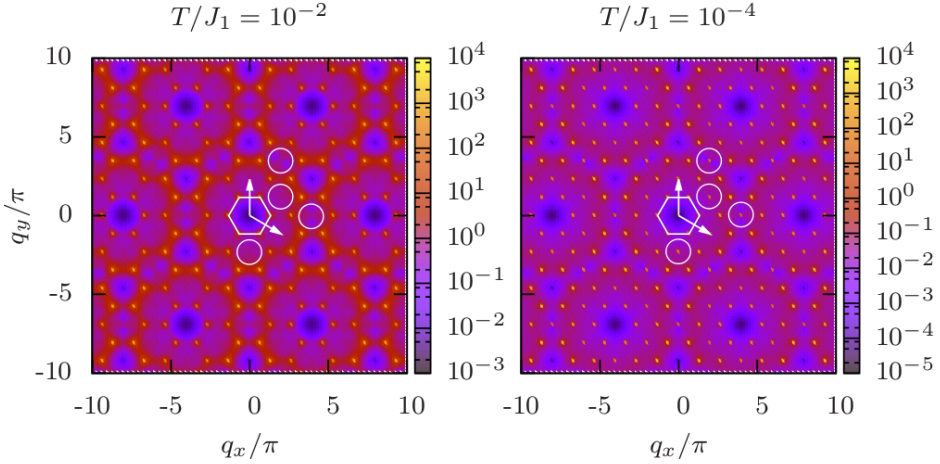




**Figure 10.6.19.:** The magnetic structure factor in the  $(q_x, q_y, q_z = 0)$  plane for various ratios  $J_2/J_1$  at  $T/J_1 = 0.01$  and  $L = 12$ . Note the different scales of the color code in the different images.



**Figure 10.6.20.:** The magnetic structure factor in the  $(q_{xy}, q_{xy}, q_z)$  plane for various ratios  $J_2/J_1$  at  $T/J_1 = 0.01$  and  $L = 12$ . Note the different scales of the color code in the different images.

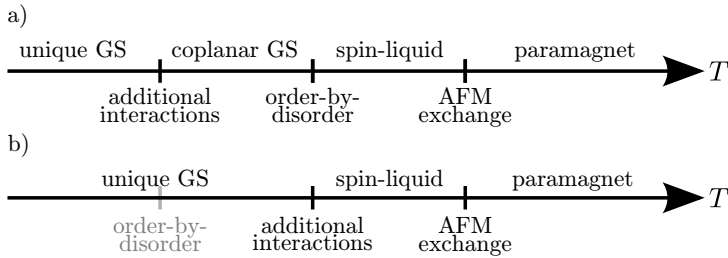


**Figure 10.6.21.:** The magnetic structure factor for  $J_2/J_1 = 1.3$  above (left) and below (right) the temperature of the order-by-disorder transition in the  $(q_x, q_y, q_z = 0)$  plane. The white circles denote some of the positions of the additional features in the nematic phase.

## 10.7. Conclusion and experimental verification

Swedenborgites are very promising candidates for an experimental observation of the predicted order-by-disorder transition. As it was already mentioned in Ch. 8, it is possible to synthesize compounds with various magnetic and non-magnetic ions, which translates to a very desirable tunability of the ratio  $J_2/J_1$  in the simplified model Eq. (8.1.2). By tuning this ratio to the interval 1.2 to 1.4, the transition temperature of the order-by-disorder transition can be maximized to a value of  $T_c \approx 5 \cdot 10^{-3} J_1$ , a value which is well within experimental reach, considering that the exchange interactions in many compounds are of the order  $\mathcal{O}(2000 \text{ K})$  [111, 114].

An experimental observation also depends on how much the simplified model, Eq. (8.1.2), which considers only two distinct nearest neighbor interactions, deviates from the true model, which incorporates all interaction effects. Any perturbation to the Hamiltonian usually lifts the ground state degeneracy and leads to a unique ground state at zero temperature. Such a perturbation is e. g. given by the Dzyaloshinskii-Moriya interaction, which one can expect to be present here due to the lack of inversion symmetry in the lattice structure, c. f. Fig. 8.1.2. Nevertheless, the presence of these interactions does not necessarily exclude the existence of an order-by-disorder transition at finite temperatures, provided that the energy scale  $\Delta E$  set by these interactions is small enough. This is the case



**Figure 10.7.22.:** Possible hierarchies of energy scales: **a)** The additional interactions are weak enough that the entropic selection of a coplanar ground state can take place before a unique ground state is eventually selected. **b)** A unique ground state is selected due to the relatively strong additional interactions before the order-by-disorder transition to coplanar ground states can place.

if the transition temperature  $T_c$  of the order-by-disorder transition is sufficiently large compared to  $\Delta E$ , i. e. if the additional interactions are not yet relevant at the temperature of the order-by-disorder transition. In this scenario, one would first observe the order-by-disorder transition to coplanar ground states followed by a second transition to the unique ground state at lower temperatures. On the other hand, if  $T_c$  is smaller or of the same size as  $\Delta E$ , the unique ground state is selected before the order-by-disorder transition can take place and consequently, one will observe only one transition. Both scenarios are shown in Fig. 10.7.22. Which scenario is eventually realized might differ from compound to compound, but a realization of the first scenario seems likely in compounds with large exchange interactions and a ratio  $J_2/J_1$  in the range of approximately 1.2 to 1.4. Further experimental studies might also be performed with compounds which are synthesized specifically to meet to these demands.

Finally, the presence of a structural phase transition that relieves the geometric frustration (and is found e. g. in  $\text{YBaCo}_4\text{O}_7$  [117]) could also exclude the observation of an order-by-disorder transition. One should thus concentrate on compounds that do not show such a transition in the search for suitable compounds for further studies.

Following the discussion of the previous sections, an experiment with the aim to confirm the predicted order-by-disorder transition could consist of neutron diffraction and high-temperature susceptibility measurements to find compounds with a suitable ratio  $J_2/J_1$  and a large Curie-Weiss temperature (i. e. large exchange interactions). For these compounds, one could measure the low-temperature specific heat and look for a first-order phase transition at a temperature that can be estimated from the phase diagram presented in Fig. 10.5.17. If such

a transition is found, one should further check whether it goes along with the predicted change of the magnetic structure factor according to Sec. 10.6 to verify that it corresponds indeed to the selection of a common spin plane.

Due to the unique tunability of energy scales and the large exchange interactions, one can conclude that it is very likely that an experimental observation of the order-by-disorder transition is possible and one can expect that the results of this chapter will stimulate both experimental and theoretical follow up works.



Part IV.

Appendices





# A. Matrix elements for the spin-wave calculation

Only the non-vanishing matrix elements  $M_{ij}$  with  $i \leq j$  are stated here for compactness. Matrix elements  $M_{ij}$  with  $i > j$  follow from the given elements as  $M_{ij} = M_{ji}^*$ .

## Matrix elements for $\mathbf{J}_2/\mathbf{J}_1 \geq 3/2$

$$\begin{aligned}
 M_{11}^x &= \frac{J_1}{2} - J_2 & M_{45}^x &= J_2 e^{-i(-k_x/6 - k_y/6 + k_z/4)} \\
 M_{12}^x &= J_1 \left( e^{-ik_y/2} - \frac{1}{2} e^{ik_y/2} \right) & M_{46}^x &= J_2 e^{-i(k_x/3 - k_y/6 + k_z/4)} \\
 M_{13}^x &= J_1 \left( e^{i(k_x - k_y)/2} - \frac{1}{2} e^{-i(k_x - k_y)/2} \right) & M_{47}^x &= J_2 e^{-i(-k_x/6 + k_y/3 + k_z/4)} \\
 M_{14}^x &= J_2 e^{-i(-k_x/6 + k_y/3 + k_z/4)} & M_{55}^x &= \frac{J_1}{2} - J_2 \\
 M_{18}^x &= J_2 e^{-i(-k_x/6 + k_y/3 - k_z/4)} & M_{56}^x &= J_1 \left( e^{-ik_x/2} - \frac{1}{2} e^{ik_x/2} \right) \\
 M_{22}^x &= \frac{J_1}{2} - J_2 & M_{57}^x &= J_1 \left( e^{-ik_y/2} - \frac{1}{2} e^{ik_y/2} \right) \\
 M_{23}^x &= J_1 \left( e^{ik_x/2} - \frac{1}{2} e^{-ik_x/2} \right) & M_{58}^x &= J_2 e^{-i(k_x/6 + k_y/6 + k_z/4)} \\
 M_{24}^x &= J_2 e^{-i(-k_x/6 - k_y/6 + k_z/4)} & M_{66}^x &= \frac{J_1}{2} - J_2 \\
 M_{28}^x &= J_2 e^{-i(-k_x/6 - k_y/6 - k_z/4)} & M_{67}^x &= J_1 \left( e^{i(k_x - k_y)/2} - \frac{1}{2} e^{-i(k_x - k_y)/2} \right) \\
 M_{33}^x &= \frac{J_1}{2} - J_2 & M_{68}^x &= J_2 e^{-i(-k_x/3 + k_y/6 + k_z/4)} \\
 M_{34}^x &= J_2 e^{-i(k_x/3 - k_y/6 + k_z/4)} & M_{77}^x &= \frac{J_1}{2} - J_2 \\
 M_{38}^x &= J_2 e^{-i(k_x/3 - k_y/6 - k_z/4)} & M_{78}^x &= J_2 e^{-i(k_x/6 - k_y/3 + k_z/4)} \\
 M_{44}^x &= -3J_2 & M_{88}^x &= -3J_2
 \end{aligned}$$

## A. Matrix elements for the spin-wave calculation

---

$$\begin{aligned}
M_{11}^y &= \frac{J_1}{2} - J_2 & M_{45}^y &= J_2 e^{-i(-k_x/6 - k_y/6 + k_z/4)} \\
M_{12}^y &= J_1 \left( e^{ik_y/2} + e^{-ik_y/2} \right) & M_{46}^y &= J_2 e^{-i(k_x/3 - k_y/6 + k_z/4)} \\
M_{13}^y &= J_1 \left( e^{i(k_x - k_y)/2} + e^{-i(k_x - k_y)/2} \right) & M_{47}^y &= J_2 e^{-i(-k_x/6 + k_y/3 + k_z/4)} \\
M_{14}^y &= J_2 e^{-i(-k_x/6 + k_y/3 + k_z/4)} & M_{55}^y &= \frac{J_1}{2} - J_2 \\
M_{18}^y &= J_2 e^{-i(-k_x/6 + k_y/3 - k_z/4)} & M_{56}^y &= J_1 \left( e^{ik_x/2} + e^{-ik_x/2} \right) \\
M_{22}^y &= \frac{J_1}{2} - J_2 & M_{57}^y &= J_1 \left( e^{ik_y/2} + e^{-ik_y/2} \right) \\
M_{23}^y &= J_1 \left( e^{ik_x/2} + e^{-ik_x/2} \right) & M_{58}^y &= J_2 e^{-i(k_x/6 + k_y/6 + k_z/4)} \\
M_{24}^y &= J_2 e^{-i(-k_x/6 - k_y/6 + k_z/4)} & M_{66}^y &= \frac{J_1}{2} - J_2 \\
M_{28}^y &= J_2 e^{-i(-k_x/6 - k_y/6 - k_z/4)} & M_{67}^y &= J_1 \left( e^{i(k_x - k_y)/2} + e^{-i(k_x - k_y)/2} \right) \\
M_{33}^y &= \frac{J_1}{2} - J_2 & M_{68}^y &= J_2 e^{-i(-k_x/3 + k_y/6 + k_z/4)} \\
M_{34}^y &= J_2 e^{-i(k_x/3 - k_y/6 + k_z/4)} & M_{77}^y &= \frac{J_1}{2} - J_2 \\
M_{38}^y &= J_2 e^{-i(k_x/3 - k_y/6 - k_z/4)} & M_{78}^y &= J_2 e^{-i(k_x/6 - k_y/3 + k_z/4)} \\
M_{44}^y &= -3J_2 & M_{88}^y &= -3J_2
\end{aligned}$$

## Matrix elements for $J_2/J_1 \geq 3/2$

For  $J_2/J_1 < 3/2$ , only the matrix elements for out-of-plane excitations are stated here since these are universal for all coplanar states. The matrix elements for in-plane excitations depend on the specific ground state used in the spin-wave expansion, c. f. Sec. 10.3.

$$\begin{aligned}
M_{11}^y &= -J_1 & M_{45}^y &= J_2 e^{-i(-k_x/6 - k_y/6 + k_z/4)} \\
M_{12}^y &= J_1 \left( e^{ik_y/2} + e^{-ik_y/2} \right) & M_{46}^y &= J_2 e^{-i(k_x/3 - k_y/6 + k_z/4)} \\
M_{13}^y &= J_1 \left( e^{i(k_x - k_y)/2} + e^{-i(k_x - k_y)/2} \right) & M_{47}^y &= J_2 e^{-i(-k_x/6 + k_y/3 + k_z/4)} \\
M_{14}^y &= J_2 e^{-i(-k_x/6 + k_y/3 + k_z/4)} & M_{55}^y &= -J_1 \\
M_{18}^y &= J_2 e^{-i(-k_x/6 + k_y/3 - k_z/4)} & M_{56}^y &= J_1 \left( e^{ik_x/2} + e^{-ik_x/2} \right) \\
M_{22}^y &= -J_1 & M_{57}^y &= J_1 \left( e^{ik_y/2} + e^{-ik_y/2} \right)
\end{aligned}$$

---

$$M_{23}^y = J_1 \left( e^{ik_x/2} + e^{-ik_x/2} \right)$$

$$M_{24}^y = J_2 e^{-i(-k_x/6 - k_y/6 + k_z/4)}$$

$$M_{28}^y = J_2 e^{-i(-k_x/6 - k_y/6 - k_z/4)}$$

$$M_{33}^y = -J_1$$

$$M_{34}^y = J_2 e^{-i(k_x/3 - k_y/6 + k_z/4)}$$

$$M_{38}^y = J_2 e^{-i(k_x/3 - k_y/6 - k_z/4)}$$

$$M_{44}^y = -2 \frac{J_2^2}{J_1}$$

$$M_{58}^y = J_2 e^{-i(k_x/6 + k_y/6 + k_z/4)}$$

$$M_{66}^y = -J_1$$

$$M_{67}^y = J_1 \left( e^{i(k_x - k_y)/2} + e^{-i(k_x - k_y)/2} \right)$$

$$M_{68}^y = J_2 e^{-i(-k_x/3 + k_y/6 + k_z/4)}$$

$$M_{77}^y = -J_1$$

$$M_{78}^y = J_2 e^{-i(k_x/6 - k_y/3 + k_z/4)}$$

$$M_{88}^y = -2 \frac{J_2^2}{J_1}$$



# Bibliography

- [1] E. Ising, “Beitrag zur Theorie des Ferromagnetismus”, *Zeitschrift für Physik* **31**, 253 (1925).
- [2] L. Onsager, “Crystal Statistics. I. A Two-Dimensional Model with an Order-Disorder Transition”, *Phys. Rev.* **65**, 117 (1944).
- [3] M. E. J. Newman and G. T. Barkema, *Monte Carlo Methods in Statistical Physics* (Oxford University Press, USA, 1999).
- [4] N. Metropolis *et al.*, “Equation of State Calculations by Fast Computing Machines”, *The Journal of Chemical Physics* **21**, 1087 (1953).
- [5] W. K. Hastings, “Monte Carlo sampling methods using Markov chains and their applications”, *Biometrika* **57**, 97 (1970).
- [6] W. Nolting, *Grundkurs Theoretische Physik 6: Statistische Physik* (Springer, 2005).
- [7] O. Melchert, “autoScale.py - A program for automatic finite-size scaling analyses: A user’s guide”, arXiv:0910.5403 (2009).
- [8] M. H. Gerlach, “Directional Ordering in the Classical Compass Model in Two and Three Dimensions”, diploma thesis, Universität Leipzig (2012).
- [9] H. Shinaoka and Y. Motome, “Loop algorithm for classical Heisenberg models with spin-ice type degeneracy”, *Phys. Rev. B* **82**, 134420 (2010).
- [10] U. Wolff, “Collective Monte Carlo Updating for Spin Systems”, *Phys. Rev. Lett.* **62**, 361 (1989).
- [11] K. Hukushima and K. Nemoto, “Exchange Monte Carlo Method and Application to Spin Glass Simulations”, *J. Phys. Soc. Jpn.* **65**, 1604 (1996).
- [12] C. Predescu, M. Predescu, and C. V. Ciobanu, “The incomplete beta function law for parallel tempering sampling of classical canonical systems”, *The Journal of Chemical Physics* **120**, 4119 (2004).
- [13] D. A. Kofke, “On the acceptance probability of replica-exchange Monte Carlo trials”, *The Journal of Chemical Physics* **117**, 6911 (2002).
- [14] D. A. Kofke, “Comment on The incomplete beta function law for parallel tempering sampling of classical canonical systems [J. Chem. Phys. 120, 4119 (2004)]”, *The Journal of Chemical Physics* **121**, 1167 (2004).

- [15] D. A. Kofke, “Erratum: On the acceptance probability of replica-exchange Monte Carlo trials [J. Chem. Phys. 117, 6911 (2002)]”, *The Journal of Chemical Physics* **120**, 10852 (2004).
- [16] H. G. Katzgraber, S. Trebst, D. A. Huse, and M. Troyer, “Feedback-optimized parallel tempering Monte Carlo”, *Journal of Statistical Mechanics: Theory and Experiment* **2006**, P03018 (2006).
- [17] A. Kone and D. A. Kofke, “Selection of temperature intervals for parallel-tempering simulations”, *The Journal of Chemical Physics* **122**, 206101 (2005).
- [18] S. Trebst, D. A. Huse, and M. Troyer, “Optimizing the ensemble for equilibration in broad-histogram Monte Carlo simulations”, *Phys. Rev. E* **70**, 046701 (2004).
- [19] N. Henze, *Irrfahrten und verwandte Zufälle - Ein elementarer Einstieg in die stochastischen Prozesse*, 2013 ed. (Springer, 2013).
- [20] W. H. Press, S. A. Teukolsky, W. T. Vetterling, and B. P. Flannery, *Numerical Recipes 3rd Edition: The Art of Scientific Computing* (Cambridge University Press, 2007).
- [21] P. Bak and M. H. Jensen, “Theory of helical magnetic structures and phase transitions in MnSi and FeGe”, *Journal of Physics C: Solid State Physics* **13**, L881 (1980).
- [22] Y. Ishikawa and M. Arai, “Magnetic Phase Diagram of MnSi near Critical Temperature Studied by Neutron Small Angle Scattering”, *J. Phys. Soc. Jpn.* **53**, 2726 (1984).
- [23] B. Lebech *et al.*, “Magnetic phase diagram of MnSi”, *Journal of Magnetism and Magnetic Materials* **140–144 (Part 1)**, 119 (1995).
- [24] S. Mühlbauer *et al.*, “Skyrmion Lattice in a Chiral Magnet”, *Science* **323**, 915 (2009).
- [25] T. Schulz *et al.*, “Emergent electrodynamics of skyrmions in a chiral magnet”, *Nature Physics* **8**, 301 (2012).
- [26] N. Romming *et al.*, “Writing and deleting single magnetic skyrmions”, *Science* **341**, 636 (2013).
- [27] I. Dzyaloshinsky, “A thermodynamic theory of “weak” ferromagnetism of antiferromagnetics”, *Journal of Physics and Chemistry of Solids* **4**, 241 (1958).
- [28] T. Moriya, “Anisotropic Superexchange Interaction and Weak Ferromagnetism”, *Phys. Rev.* **120**, 91 (1960).
- [29] Y. Ishikawa, G. Shirane, J. A. Tarvin, and M. Kohgi, “Magnetic excitations in the weak itinerant ferromagnet MnSi”, *Phys. Rev. B* **16**, 4956 (1977).

- 
- [30] J. Waizner, “Dynamics in chiral magnets: Magnetic and electric excitations of helices and skyrmions”, diploma thesis, Universität zu Köln (2013).
- [31] K. Everschor, “Current-Induced Dynamics of Chiral Magnetic Structures”, PhD Thesis, Universität zu Köln (2012).
- [32] W. Münzer *et al.*, “Skyrmion lattice in the doped semiconductor  $\text{Fe}_{1-x}\text{Co}_x\text{Si}$ ”, *Phys. Rev. B* **81**, 041203 (2010).
- [33] C. Pfleiderer *et al.*, “Skyrmion lattices in metallic and semiconducting B20 transition metal compounds”, *Journal of Physics: Condensed Matter* **22**, 164207 (2010).
- [34] T. Adams *et al.*, “Long-Wavelength Helimagnetic Order and Skyrmion Lattice Phase in  $\text{Cu}_2\text{OSeO}_3$ ”, *Phys. Rev. Lett.* **108**, 237204 (2012).
- [35] X. Yu *et al.*, “Near room-temperature formation of a skyrmion crystal in thin-films of the helimagnet FeGe”, *Nature Materials* **10**, 106 (2011).
- [36] Yu X. Z. *et al.*, “Real-space observation of a two-dimensional skyrmion crystal”, *Nature* **465**, 901 (2010).
- [37] P. Milde *et al.*, “Unwinding of a Skyrmion Lattice by Magnetic Monopoles”, *Science* **340**, 1076 (2013).
- [38] G. Lynn, *Animate Form*, 1st ed. (Princeton Architectural Press, 1999).
- [39] D. J. Thouless, M. Kohmoto, M. P. Nightingale, and M. den Nijs, “Quantized Hall Conductance in a Two-Dimensional Periodic Potential”, *Phys. Rev. Lett.* **49**, 405 (1982).
- [40] M. Z. Hasan and C. L. Kane, “Colloquium: Topological insulators”, *Rev. Mod. Phys.* **82**, 3045 (2010).
- [41] N. Goldenfeld, *Lectures on phase transitions and the renormalization group* (Addison-Wesley, Advanced Book Program, 1992).
- [42] L. D. Landau and E. Lifschitz, *Lehrbuch der theoretischen Physik Bd.5: Statistische Physik Teil I*, 7th ed. (Akademie Verlag, 1987).
- [43] S. Mühlbauer *et al.*, “Skyrmion Lattice in a Chiral Magnet”, *Science* **323**, 915 (2009), online supplement, available at <http://www.sciencemag.org/content/323/5916/915>.
- [44] T. Adams *et al.*, “Long-Range Crystalline Nature of the Skyrmion Lattice in MnSi”, *Phys. Rev. Lett.* **107**, 217206 (2011).
- [45] S. Tewari, “Blue Quantum Fog: Chiral Condensation in Quantum Helimagnets”, *Phys. Rev. Lett.* **96**, 047207 (2006).
- [46] I. A. Fischer, “Crystalline phases in chiral ferromagnets: Destabilization of helical order”, *Phys. Rev. B* **77**, 024415 (2008).

- [47] U. K. Röfler, “Spontaneous skyrmion ground states in magnetic metals”, *Nature* **442**, 797 (2006).
- [48] A. Bogdanov and D. Yablonskii, “Thermodynamically stable “vortices” in magnetically ordered crystals. The mixed state of magnets”, *Journal of Experimental and Theoretical Physics* **68**, 101 (1989).
- [49] A. Bogdanov and A. Hubert, “Thermodynamically stable magnetic vortex states in magnetic crystals”, *Journal of Magnetism and Magnetic Materials* **138**, 255 (1994).
- [50] S. D. Yi, S. Onoda, N. Nagaosa, and J. H. Han, “Skyrmions and anomalous Hall effect in a Dzyaloshinskii-Moriya spiral magnet”, *Phys. Rev. B* **80**, 054416 (2009).
- [51] S. Buhandt and L. Fritz, “Skyrmion lattice phase in three-dimensional chiral magnets from Monte Carlo simulations”, *Phys. Rev. B* **88**, 195137 (2013).
- [52] A. Hamann *et al.*, “Magnetic Blue Phase in the Chiral Itinerant Magnet MnSi”, *Phys. Rev. Lett.* **107**, 037207 (2011).
- [53] A. Bauer, M. Garst, and C. Pfleiderer, “Specific Heat of the Skyrmion Lattice Phase and Field-Induced Tricritical Point in MnSi”, *Phys. Rev. Lett.* **110**, 177207 (2013).
- [54] D. Vollhardt, “Characteristic Crossing Points in Specific Heat Curves of Correlated Systems”, *Phys. Rev. Lett.* **78**, 1307 (1997).
- [55] S. M. Stishov *et al.*, “Heat capacity and thermal expansion of the itinerant helimagnet MnSi”, *Journal of Physics: Condensed Matter* **20**, 235222 (2008).
- [56] S. A. Brazovskii, “Phase transition of an isotropic system to a nonuniform state”, *Journal of Experimental and Theoretical Physics* **41**, 85 (1975).
- [57] M. Janoschek *et al.*, “Fluctuation-induced first-order phase transition in Dzyaloshinskii-Moriya helimagnets”, *Phys. Rev. B* **87**, 134407 (2013).
- [58] S. M. Stishov *et al.*, “Magnetic phase transition in the itinerant helimagnet MnSi: Thermodynamic and transport properties”, *Phys. Rev. B* **76**, 052405 (2007).
- [59] D. Lamago, R. Georgii, and P. Böni, “Magnetic susceptibility and specific heat of the itinerant ferromagnet MnSi”, *Physica B: Condensed Matter* **359–361**, 1171 (2005).
- [60] A. Van Oosterom and J. Strackee, “The Solid Angle of a Plane Triangle”, *Transactions on Biomedical Engineering* **BME-30**, 125 (1983).
- [61] C. D. Christ, A. E. Mark, and W. F. van Gunsteren, “Basic ingredients of free energy calculations: A review”, *Journal of Computational Chemistry* **31**, 1569 (2010).



- 
- [62] S. Zhang and S. S.-L. Zhang, “Generalization of the Landau-Lifshitz-Gilbert Equation for Conducting Ferromagnets”, *Phys. Rev. Lett.* **102**, 086601 (2009).
- [63] C. Pfleiderer and A. Rosch, “Single skyrmions spotted”, *Nature* **465**, 880 (2010).
- [64] M. V. Berry, “Quantal Phase Factors Accompanying Adiabatic Changes”, *Proc. Roy. Soc. A* **392**, 45 (1984).
- [65] K. Everschor *et al.*, “Rotating skyrmion lattices by spin torques and field or temperature gradients”, *Phys. Rev. B* **86**, 054432 (2012).
- [66] A. Neubauer *et al.*, “Topological Hall Effect in the *A* Phase of MnSi”, *Phys. Rev. Lett.* **102**, 186602 (2009).
- [67] P. Milde *et al.*, “Unwinding of a Skyrmion Lattice by Magnetic Monopoles”, *Science* **340**, 1076 (2013), online supplement, available at <http://www.sciencemag.org/content/340/6136/1076>.
- [68] C. Schütte, “Skyrmions and Monopoles in Chiral Magnets & Correlated Heterostructures”, PhD Thesis, Universität zu Köln (2014).
- [69] J. L. García-Palacios and F. J. Lázaro, “Langevin-dynamics study of the dynamical properties of small magnetic particles”, *Phys. Rev. B* **58**, 14937 (1998).
- [70] C. Castelnuovo, R. Moessner, and S. L. Sondhi, “Magnetic monopoles in spin ice”, *Nature* **451**, 42 (2008).
- [71] D. J. P. Morris *et al.*, “Dirac Strings and Magnetic Monopoles in the Spin Ice  $\text{Dy}_2\text{Ti}_2\text{O}_7$ ”, *Science* **326**, 411 (2009).
- [72] P. Dirac, “Quantised Singularities in the Electromagnetic Field”, *Proc. Roy. Soc. A Contain. Pap. Math. Phys. Character* **133**, 60 (1931).
- [73] C. Pfleiderer, “Experimental studies of weakly magnetic transition metal compounds”, *Journal of Magnetism and Magnetic Materials* **226–230**, Part 1, 23 (2001).
- [74] C. Pfleiderer, S. R. Julian, and G. G. Lonzarich, “Non-Fermi-liquid nature of the normal state of itinerant-electron ferromagnets”, *Nature* **414**, 427 (2011).
- [75] R. Ritz *et al.*, “Formation of a topological non-Fermi liquid in MnSi”, *Nature* **497**, 231 (2013).
- [76] Han T.-H. *et al.*, “Fractionalized excitations in the spin-liquid state of a kagome-lattice antiferromagnet”, *Nature* **492**, 406 (2012).
- [77] J. Villain, R. Bidaux, J. P. Carton, and R. Conte, “Order as an effect of disorder”, *Journal de Physique* **41**, 1263 (1980).

- [78] J. T. Chalker, P. C. W. Holdsworth, and E. F. Shender, “Hidden order in a frustrated system: Properties of the Heisenberg Kagomé antiferromagnet”, *Phys. Rev. Lett.* **68**, 855 (1992).
- [79] R. Moessner and J. T. Chalker, “Low-temperature properties of classically frustrated antiferromagnets”, *Phys. Rev. B* **58**, 12049 (1998).
- [80] R. Moessner and J. T. Chalker, “Properties of a classical spin liquid: the Heisenberg pyrochlore antiferromagnet”, *Phys. Rev. Lett.* **80**, 2929 (1998).
- [81] D. Bergman *et al.*, “Order by disorder and spiral spin liquid in frustrated diamond lattice antiferromagnets”, *Nature Physics* **3**, 487 (2007).
- [82] A. P. Ramirez, “Strongly geometrically frustrated magnets”, *Annual Review of Materials Science* **24**, 453 (1994).
- [83] L. Balents, “Spin liquids in frustrated magnets”, *Nature* **464**, 199 (2010).
- [84] G. H. Wannier, “Antiferromagnetism. The Triangular Ising Net”, *Phys. Rev.* **79**, 357 (1950).
- [85] R. Houtappel, “Order-disorder in hexagonal lattices”, *Physica* **16**, 425 (1950).
- [86] Y. L. Loh, D. X. Yao, and E. W. Carlson, “Thermodynamics of Ising spins on the triangular kagome lattice: Exact analytical method and Monte Carlo simulations”, *Phys. Rev. B* **77**, 134402 (2008).
- [87] K. Kanô and S. Naya, “Antiferromagnetism. The Kagomé Ising Net”, *Progress of Theoretical Physics* **10**, 158 (1953).
- [88] C. Lacroix, P. Mendels, and F. Mila, *Introduction to Frustrated Magnetism - Materials, Experiments, Theory*, 2011 ed. (Springer Berlin Heidelberg, 2013).
- [89] J. N. Reimers, “Absence of long-range order in a three-dimensional geometrically frustrated antiferromagnet”, *Phys. Rev. B* **45**, 7287 (1992).
- [90] M. E. Zhitomirsky, “Octupolar ordering of classical kagome antiferromagnets in two and three dimensions”, *Phys. Rev. B* **78**, 094423 (2008).
- [91] S. T. Bramwell and M. J. P. Gingras, “Spin Ice State in Frustrated Magnetic Pyrochlore Materials”, *Science* **294**, 1495 (2001).
- [92] Y. Yamashita and K. Ueda, “Spin-driven Jahn-Teller distortion in a pyrochlore system”, *Phys. Rev. Lett.* **85**, 4960 (2000).
- [93] M. Y. Veillette, J. T. Chalker, and R. Coldea, “Ground states of a frustrated spin-1/2 antiferromagnet:  $\text{Cs}_2\text{CuCl}_4$  in a magnetic field”, *Phys. Rev. B* **71**, 214426 (2005).
- [94] C. L. Henley, “Ordering by disorder: Ground-state selection in fcc vector antiferromagnets”, *Journal of Applied Physics* **61**, 3962 (1987).

- 
- [95] C. L. Henley, “Ordering due to disorder in a frustrated vector antiferromagnet”, *Phys. Rev. Lett.* **62**, 2056 (1989).
- [96] N. D. Mermin and H. Wagner, “Absence of Ferromagnetism or Antiferromagnetism in One- or Two-Dimensional Isotropic Heisenberg Models”, *Phys. Rev. Lett.* **17**, 1133 (1966).
- [97] G.-W. Chern and R. Moessner, “Dipolar Order by Disorder in the Classical Heisenberg Antiferromagnet on the Kagome Lattice”, *Phys. Rev. Lett.* **110**, 077201 (2013).
- [98] S. Sachdev, “Kagome- and triangular-lattice Heisenberg antiferromagnets: Ordering from quantum fluctuations and quantum-disordered ground states with unconfined bosonic spinons”, *Phys. Rev. B* **45**, 12377 (1992).
- [99] C. L. Henley, “The “Coulomb Phase” in Frustrated Systems”, *Annual Review of Condensed Matter Physics* **1**, 179 (2010).
- [100] J. D. Bernal and R. H. Fowler, “A Theory of Water and Ionic Solution, with Particular Reference to Hydrogen and Hydroxyl Ions”, *The Journal of Chemical Physics* **1**, 515 (1933).
- [101] T. Fennell *et al.*, “Magnetic Coulomb Phase in the Spin Ice  $\text{Ho}_2\text{Ti}_2\text{O}_7$ ”, *Science* **326**, 415 (2009).
- [102] M. E. Fisher, “On the Dimer Solution of Planar Ising Models”, *Journal of Mathematical Physics* **7**, 1776 (1966).
- [103] E. Sela, H.-C. Jiang, M. H. Gerlach, and S. Trebst, “Order-by-disorder and spin-orbital liquids in a distorted Heisenberg-Kitaev model”, *Phys. Rev. B* **90**, 035113 (2014).
- [104] G. Aminoff, “Über ein neues Mineral von Langban”, *Zeitschrift für Kristallographie, Mineralogie und Petrographie* **60**, 262 (1924).
- [105] M. Valldor, Y. Sanders, and W. Schweika, “High spin frustration in Co based Swedenborgites”, *J. Phys.: Conf. Ser.* **145**, 012076 (2009).
- [106] L. C. Chapon, P. G. Radaelli, H. Zheng, and J. F. Mitchell, “Competing magnetic interactions in the extended Kagomé system  $\text{YBaCo}_4\text{O}_7$ ”, *Phys. Rev. B* **74**, 172401 (2006).
- [107] M. Soda *et al.*, “Magnetic Structure of  $\text{YBaCo}_4\text{O}_7$  with Kagome and Triangular Lattices”, *J. Phys. Soc. Jpn.* **75**, 054707 (2006).
- [108] M. Valldor and M. Andersson, “The structure of the new compound  $\text{YBaCo}_4\text{O}_7$  with a magnetic feature”, *Solid State Sciences* **4**, 923 (2002).

- [109] P. Manuel *et al.*, “Magnetic Correlations in the Extended Kagome  $\text{YBaCo}_4\text{O}_7$  Probed by Single-Crystal Neutron Scattering”, *Phys. Rev. Lett.* **103**, 037202 (2009).
- [110] D. D. Khalyavin, P. Manuel, J. F. Mitchell, and L. C. Chapon, “Spin correlations in the geometrically frustrated  $\text{RBaCo}_4\text{O}_7$  antiferromagnets: Mean-field approach and Monte Carlo simulations”, *Phys. Rev. B* **82**, 094401 (2010).
- [111] W. Schweika, M. Valldor, and P. Lemmens, “Approaching the Ground State of the Kagomé Antiferromagnet”, *Phys. Rev. Lett.* **98**, 067201 (2007).
- [112] M. Valldor, “Remnant magnetization above room temperature in the semiconductor  $\text{Y}_{0.5}\text{Ca}_{0.5}\text{BaCo}_4\text{O}_7$ ”, *Solid State Sciences* **8**, 1272 (2006).
- [113] M. Valldor, “Syntheses and structures of compounds with  $\text{YBaCo}_4\text{O}_7$ -type structure”, *Solid State Sciences* **6**, 251 (2004).
- [114] M. Valldor *et al.*, “Spin correlations in the extended kagome system  $\text{YBaCo}_3\text{FeO}_7$ ”, *Phys. Rev. B* **84**, 224426 (2011).
- [115] E. Rosén, “Magnetische Eigenschaften und Spinkorrelationen in Co- und Fe-basierten Swedenborgiten”, diploma thesis, RWTH Aachen (2011).
- [116] J. Reim, “Spindynamik im Swedenborgit  $\text{CaBaCo}_2\text{Fe}_2\text{O}_7$ : Untersuchung mit Neutronenstreuung und Spinwellentheorie”, diploma thesis, RWTH Aachen (2011).
- [117] A. Huq *et al.*, “Structural and magnetic properties of the Kagomé antiferromagnet  $\text{YbBaCo}_4\text{O}_7$ ”, *Journal of Solid State Chemistry* **179**, 1136 (2006).
- [118] J. R. Stewart *et al.*, “Spin dynamics, short-range order, and spin freezing in  $\text{Y}_{0.5}\text{Ca}_{0.5}\text{BaCo}_4\text{O}_7$ ”, *Phys. Rev. B* **83**, 024405 (2011).
- [119] S. Buhrandt and L. Fritz, “Antiferromagnetic Ising model on the swedenborgite lattice”, *Phys. Rev. B* **90**, 094415 (2014).
- [120] S. V. Isakov, K. S. Raman, R. Moessner, and S. L. Sondhi, “Magnetization curve of spin ice in a [111] magnetic field”, *Phys. Rev. B* **70**, 104418 (2004).
- [121] S. Buhrandt and L. Fritz, “Spin-liquid phase and order by disorder of classical Heisenberg spins on the swedenborgite lattice”, *Phys. Rev. B* **90**, 020403 (2014).
- [122] L. Seabra, T. Momoi, P. Sindzingre, and N. Shannon, “Phase diagram of the classical Heisenberg antiferromagnet on a triangular lattice in an applied magnetic field”, *Phys. Rev. B* **84**, 214418 (2011).
- [123] H. Kawamura and S. Miyashita, “Phase transition of the Heisenberg Antiferromagnet on the Triangular Lattice in a Magnetic Field”, *J. Phys. Soc. Jpn.* **54**, 4530 (1985).

- [124] P. M. Chaikin and T. C. Lubensky, *Principles of Condensed Matter Physics* (Cambridge University Press, 2000).
- [125] D. Andrienko, “Introduction to liquid crystals”, Lecture notes, available at [http://www2.mpip-mainz.mpg.de/~andrienk/teaching/IMPRS/liquid\\_crystals.pdf](http://www2.mpip-mainz.mpg.de/~andrienk/teaching/IMPRS/liquid_crystals.pdf) (20.06.2014).
- [126] M. Gvozdikova and M. Zhitomirsky, “A Monte Carlo study of the first-order transition in a Heisenberg FCC antiferromagnet”, *Journal of Experimental and Theoretical Physics Letters* **81**, 236 (2005).



# Statement of authorship / Selbständigkeitserklärung

Ich versichere, dass ich die von mir vorgelegte Dissertation selbständig angefertigt, die benutzten Quellen und Hilfsmittel vollständig angegeben und die Stellen der Arbeit - einschließlich Tabellen, Karten und Abbildungen -, die anderen Werken im Wortlaut oder dem Sinn nach entnommen sind, in jedem Einzelfall als Entlehnung kenntlich gemacht habe; dass diese Dissertation abgesehen von der Universität Utrecht noch keiner anderen Fakultät oder Universität zur Prüfung vorgelegen hat; dass sie - abgesehen von unten angegebenen Teilpublikationen - noch nicht veröffentlicht worden ist, sowie, dass ich eine solche Veröffentlichung vor Abschluss des Promotionsverfahrens nicht vornehmen werde. Die Bestimmungen der Promotionsordnung sind mir bekannt. Die von mir vorgelegte Dissertation ist von Prof. Dr. Achim Roch (Köln), Prof. Dr. H. Stoof (Utrecht) und Dr. L. Fritz (Utrecht) betreut worden.

.....  
(Stefan Buhrandt)

## Teilpublikationen

- **S. Buhrandt** und L. Fritz, “Skyrmion lattice phase in three-dimensional chiral magnets from Monte Carlo simulations”, *Phys. Rev. B* **88**, 195137 (2013).
- P. Milde, D. Köhler, J. Seidel, L. M. Eng, A. Bauer, A. Chacon, J. Kindervater, S. Mühlbauer, C. Pfleiderer, **S. Buhrandt**, C. Schütte und A. Rosch, “Unwinding of a Skyrmion Lattice by Magnetic Monopoles”, *Science* **340**, 1076 (2013).
- **S. Buhrandt** und L. Fritz, “Spin-liquid phase and order by disorder of classical Heisenberg spins on the swedenborgite lattice”, *Phys. Rev. B* **90**, 020403(R) (2014).
- **S. Buhrandt** und L. Fritz, “Antiferromagnetic Ising model on the swedenborgite lattice”, *Phys. Rev. B* **90**, 094415 (2014).





# Curriculum vitae

## Personal data

Name	Stefan Buhrandt
Address	Clemens-August Str. 20-22, 53115 Bonn, Germany
Date of birth	30.10.1986
Place of birth	Troisdorf
Nationality	German
eMail	stefan.buhrandt@googlemail.com

## Academic education

10/2006-09/2009	Studies of physics at the University of Bonn
09/2009	Bachelor degree
10/2009 - present	Member of the Bonn-Cologne Graduate School of Physics and Astronomy
09/2011	Master degree
11/2011 - 01/2014	PhD studies at the University of Cologne
02/2014 - present	PhD studies at Utrecht University

## School education

08/1993 - 06/1997	Grundschule Donrath
08/1997 - 06/2006	Gymnasium Lohmar
06/2006	Abitur

## Working experience

04/2011 - 09/2011	Student research assistant at the University of Bonn
07/2006 - 10/2006	Packet sorter at UPS, Cologne-Bonn airport
2004 - 2011	Private tutor